

# **Abstract of thesis entitled**

## **Design, modeling, control, and implementation of bi-copter UAVs**

Submitted by

**Qin Youming**

For the degree of Doctor of Philosophy

Department of Mechanical Engineering

at The University of Hong Kong

in April 2022

Unmanned aerial vehicles (UAVs) emerged as the premier platform for data collection tasks due to their superior mobility and mechanical simplicity. When performing those tasks, UAVs usually operate in confined spaces while carrying professional sensors that are precise but heavy. The bi-copter UAV is the optimal choice when there is a simultaneous demand for large payload capacity, long operating time, and size restriction.

The first problem this thesis focuses on is the designing, modeling, controlling, and implementation of compact yet efficient bi-copter UAV platforms. Through theoretical analysis of the efficiency and practicality of 12 common configurations, we show that bi-copter has 30% higher efficiency than quad-copters of the same



width. Moreover, we demonstrate the feasibility of a servo-based tandem rotor bi-copter approach through an exemplary design, Gemini mini. Such a 10 inches bi-copter can carry a 380 g LiDAR and hover for 13 minutes (the equivalent quad-copters can barely operate for more than 10 minutes). Besides presenting the design process, we also demonstrate its flight performance under external disturbances and during a 40 cm narrow gap fly-through.

The second issue that we engage in is improving the UAV operation efficiency through aerial-ground locomotion. Since flying UAVs' primary power consumption is the thrust generated to counteract gravity, obtaining force support from the ground will save the majority of hovering power. We integrated a single passive wheel into the bi-copter, Gemini W. After adopting the ground locomotion approach, Gemini W saves up to 77% battery by adding merely 1% to the original UAV weight.

The third difficulty that we tackle is to further improve the agility of the bi-copter UAV by addressing the drawback brought by servo motors, which is for vectoring the motor thrust direction. Issues such as non-linearity, response lag, non-minimum phase, and backlash in servo motors and their contained gearboxes seriously restrict the bi-copter's performance. Moreover, when servo-based bi-copters have a large size or heavy payload capacity, the servo motors will become heavy, bulky, and hard to maintain. To resolve these challenges, we first adopt the swashplate approach, which failed to be validated by experiments due to safety concerns caused by the severe vibration of the rotating swashplate mechanism. Next, we innovatively embrace the swashplate-less cyclic pitch-varying technique instead. The swashplate-less mechanism decouples the vectorized thrust using sinusoidal motor thrust and three passive hinges. This novel method not only resolves the issues caused by servo motors, but also makes the system mechanically simpler, more reliable, and cost-effective. We build a swashplate-less based bi-copter, Gemini II, and achieve full attitude control with only two actuators. Lastly, we demonstrate the validity and flight performance of Gemini II by conducting tests, including a power consumption test, poking disturbance test, gust wind disturbance test, step response test, and agile trajectory tracking.

This thesis systematically exhibits a series of bi-copter designs, including de-



tailed mechanical designs, avionics, motor tests, and each design's modeling, control, and implementation. Overall, our proposed bi-copter platforms possess multiple virtues in terms of compactness, efficiency, agility, and robustness.

(497 words)





# **Design, modeling, control, and implementation of bi-copter UAVs**

by

**Qin Youming**

Department of Mechanical Engineering

The University of Hong Kong

Supervisor: Dr. Zhang Fu

A thesis submitted in partial fulfilment of the requirements for  
the Degree of Doctor of Philosophy  
at The University of Hong Kong.

April 2022





# Dedication

“So you think you can tell?

Heaven from hell?

Blue skies from pain?

Can you tell a green field?

From a cold steel rail?

A smile from a veil?

Do you think you can tell?

Did they get you to trade?

Your heroes for ghosts?

Hot ashes for trees?

Hot air for a cool breeze?

Cold comfort for change?

Did you exchange?

A walk-on part in the war?

For a leading role in a cage?”

— *Wish you were here* by Pink Floyd

May the drones are used for saving life rather than taking life.



May the bi-copters be used to make this world a better place.

To the world peace



# Declaration

I declare that this thesis represents my own work, except where acknowledgement is made, and that it has not been previously included in a thesis, dissertation or report submitted to this University or to any other institution for a degree, diploma or other qualifications.

Signed .....  


Qin Youming



# Acknowledgements

I would like to take this opportunity to show my great appreciation to all the people who have assisted me in completing the research works described in the dissertation.

First and foremost, I want to express my sincerest gratitude to my supervisor, Professor Zhang Fu. He has meticulously supported me, persistently guided me, and constantly inspired me during my whole Ph.D. career. I respect his enthusiasm for knowledge, availability for student questions, and ability to dissect complicated concepts into logical and easy-to-understand forms. He is very down-to-earth. During weekly group meetings, he patiently addresses his feedback and concerns upon every students' questions, even sometimes it requires him to derive equations and debug side by side with students. On the other hand, he also has high-level industry insights. Because of his broad and profound knowledge base, every constructive feedback he provides expands my vision and imagination. His guidance goes far beyond merely being an academic advisor. He values students' soft skills as much as hard skills. Whenever he discovers opportunities for improving presentation skills, writing skills, communications skills, professionalism, and other transferable skills, he would kindly encourage me to participate. Instead of giving orders and bossing me around, he always uses his wisdom to explain to me the logic and reasoning behind his decision-making process and then leaves the choices for the students to decide. When designing the novel Gemini II mechanism encountered problems, he meticulously guided me to tackle the potential causes behind thousands of failures and shepherd me through the darkest valley of my Ph.D. career. The success of my experiments will never have come true without Professor Zhang's encouragement and patience.



My special thanks also go to Professor James Lam for his generosity in granting me lab access and accelerating my experiment. I also appreciate the Mechanical Engineering department for other resources supporting my work.

I also want to extend my appreciation to my friends and colleagues at the MaRS lab. I witnessed this lab-grown from 3 students to almost 30 people. It is a pleasure to work with everyone, and I've learned so much from each person.

I'd also like to show my gratefulness to Professor Wong Ngai, Lu Peng, Kwok Ka Wai, Zhang Youmin, and Lyu Ximin for my qualification or dissertation committees.

Last but not least, my friends and family are always there for me, stand with me and support me. I would like to thank my family for patiently supporting my feeling and mental health; thank Miss Xi and Mr. Shu for taking care of my sickness during this COVID-19 great pandemic time; thank my labmate and soon-to-be Dr. Xu taught me hand by hand how to tune and fly a UAV. I also learned a lot by collaborating with Mr. Li, Mr. Chen, and Mr. Cai. Their expectations and support are the biggest motivation along my journey of pursuing scientific research and a Ph.D. degree.



# Contents

<i>Dedication</i> .....	7
<i>Declaration</i> .....	9
<i>Acknowledgements</i> .....	10
<i>Table of Contents</i> .....	16
<i>List of Figures</i> .....	34
<i>List of Tables</i> .....	35
<i>List of Publications and Patents</i> .....	36
<b>1 Introduction</b>	<b>37</b>
1.1 Historical Evolution of UAVs .....	37
1.2 UAVs Classification .....	40
1.3 Contemporary UAVs Civilian Applications .....	43
1.4 UAV Application Gaps .....	45
1.5 Our Approach .....	47
1.6 Design Method .....	49
1.7 Thesis Organization .....	49



<b>2 Gemini mini: Servo-based Bi-copter</b>	<b>54</b>
2.1 Introduction .....	54
2.2 Working Principle .....	56
2.3 Literature Review .....	57
2.4 Aerodynamic Analysis .....	58
2.4.1 Momentum Theory .....	59
2.4.2 Experiment Verification .....	62
2.4.3 Efficiency Comparison .....	63
2.5 System Design, Optimization, and Implementation .....	66
2.5.1 Design Goal .....	67
2.5.2 Avionics .....	68
2.5.3 Layout .....	70
2.5.4 Designed Parts .....	72
2.6 Control .....	74
2.6.1 Dynamics .....	74
2.6.2 Control System .....	75
2.7 Experiment Results .....	78
2.7.1 Hovering Flight .....	78
2.7.2 Flying Through a 40 cm Gap .....	82
2.8 Discussion and Conclusion .....	82
2.9 Related Publication .....	84



<b>3 Gemini W: Aerial-ground Locomotion Bi-copter</b>	<b>85</b>
3.1 Introduction .....	85
3.2 Literature Review .....	87
3.3 System Design and Implementation .....	90
3.3.1 Propulsion System .....	91
3.3.2 Airframe .....	92
3.3.3 Single Passive Wheel .....	112
3.3.4 Integrated PMU Board .....	112
3.4 Control .....	114
3.4.1 Dynamics Modeling .....	114
3.4.2 Controller Design .....	117
3.5 Experiment Validation .....	120
3.5.1 Feasibility Validation .....	120
3.5.2 Efficiency Demonstration .....	125
3.6 Discussion and Conclusion .....	126
3.7 Related Publications .....	127
<b>4 Hong Sun: Swashplate-based Bi-copter</b>	<b>128</b>
4.1 Introduction .....	128
4.2 Related Works .....	129
4.3 Working Principle .....	130



4.4	Hong Sun: Swashplate Bi-copter .....	131
4.4.1	Propulsion System Test .....	133
4.4.2	Fuselage Design .....	137
4.4.3	Overall Specification .....	138
4.5	Conclusion .....	140
<b>5</b>	<b>Gemini II: Swashplate-less Bi-copter</b>	<b>142</b>
5.1	Introduction .....	142
5.2	Literature Review .....	144
5.3	System Architecture and Mechanical Design .....	147
5.3.1	Fuselage .....	149
5.3.2	Avionics .....	155
5.3.3	Swashplate-less Cyclic Blade Pitch Control Mechanism ..	156
5.3.4	Overall Specification .....	161
5.4	System Modeling and Control .....	163
5.4.1	Modeling .....	163
5.4.2	Control .....	165
5.5	Experiment results .....	169
5.5.1	Actuators Evaluation .....	170
5.5.2	Model Identification and Disturbance Rejection Analysis ..	175
5.5.3	Disturbance Test .....	180
5.5.4	Trajectory Tracking Following a “3D Figure 8” Pattern ..	186



5.6	Conclusion and Discussion .....	188
5.7	Related Publication .....	189
<b>6</b>	<b>Conclusion and Future Works</b>	<b>190</b>
6.1	Conclusion .....	190
6.2	Future Works .....	191
<b>References</b>	.....	<b>204</b>



# List of Figures

## Figure 1.1

UAVs during World Wars (a) The Austrian balloon (1849): the first disposable UAVs used in the war; (b) November Kettering Bug plane (1917): the world's first radio wave controlled UAVs. **Image Source:**[1, 2] 38

## Figure 1.2

UAVs after the World Wars (a) Northrop P-61 black widow (1946): the weather data gathering UAV; (b) Lockheed D-21 (1969): high-altitude and high-speed reconnaissance unmanned aerial vehicle. **Image Source:** [3, 4] ..... 38

## Figure 1.3

UAVs after the Cold War (a) Global Hawk (HALE UAV, 1998): the unmanned surveillance and reconnaissance aerial vehicle. (b) RoboBee X-Wing MAV (2013): a coin-sized unmanned aerial vehicle. **Image Source:** [5, 6] ..... 39

## Figure 1.4

Contemporary UAV classification with two examples given for each class [7] (a) Lighter-than-air UAVs; (b) Fixed-wing UAVs; (c) Multi-rotor UAVs (with 12 common multi-rotor configurations); (d) Flapping-wing UAVs; (e) Hybrid UAVs. **Image Source:** [8–14] ..... 41



## Figure 1.5

UAVs application examples (a) Firefighting; (b) Emergency relay communications; (c) Inspection; (d) Agriculture. **Image Source:** [15–18] .. 43

## **Figure 1.6**

Commercial quad-copter UAV examples **(a)** DJI Matrice 100 quad-copter;

**(b)** Crazyflie 2.0 Micro Aerial Vehicle (MAV) quad-copter. **Image**

**Source:** [19, 20] ..... 45

## **Figure 1.7**

Existing solutions for UAVs to fly through narrow gaps **(a)** Quad-copter flying through narrow gap; **(b)** Morphing-based approach to fly through narrow gap; **(c)** Agile morphing approach to fly through narrow gap; **(d)** Passive morphing approach to fly through narrow gap. **Image Source:**

[21, 21–23] ..... 46

## **Figure 1.8**

Our bi-copter approach achieves full controllability of the UAV with a minimal set of actuators (only two brush-less motors). Its horizontal width is the size of the propeller, and it can efficiently navigate in confined spaces while carrying a heavy payload such as 600 g LiDAR. ..... 48

## **Figure 1.9**

UAV system design process. **Image Source:** [24] ..... 49

## **Figure 1.10**

Thesis structure ..... 50

## **Figure 2.1**

The Gemini mini at hovering. The propeller size is 10 inches (25.4 cm),

and the total system weights 1.8 Kg. It is capable of flying up to 13

minutes. Video available at: <https://youtu.be/i7n0w0HonMM> ..... 55

## **Figure 2.2**

Bi-copter working principle: The pitch is controlled by the differential

thrust. Roll and yaw are controlled by tilting servo motors in the same

and opposite directions, respectively. **Image Source:** [25] ..... 56



### **Figure 2.3**

Previous tilt-rotor bi-copters **(a)** T-Phoenix tilt-rotor bi-copter with a non-linear controller; **(b)** Bi-copter that moves in different moving direction than Gemini mini. **Image Source:** [26, 27] ..... 58

### **Figure 2.4**

Other previous bi-copters **(a)** Bi-copter without any tilting mechanism; **(b)** Bi-copter that uses reaction wheels to provide the roll and yaw torque **Image Source:** [28, 29]. ..... 58

### **Figure 2.5**

The definitions of physical parameters in idea momentum theory. **Image Source:** edited figure based on [30] ..... 59

### **Figure 2.6**

The relationship between disk loading and hover efficiency: the hover efficiency is inversely proportional to the square root of disk loading. **Image Source:** [31] ..... 61

### **Figure 2.7**

Hover efficiency versus disk loading predicted by the momentum theory and from actual propeller data provided by APC propeller official website <https://www.apcprop.com/technical-information/performance-data/>. The red dashdotted line remarks the upper envelope of the propeller data. ..... 62



### **Figure 2.8**

The propeller radius of a bi-copter versus a quad-copter with the same effective size. The bi-copter configuration has a larger effective disk area than quad-copters, therefore higher hovering efficiency. ..... 63

### **Figure 2.9**

Efficiency comparison among multi-rotor UAVs (The Gemini mini's bi-copter configuration has the highest efficiency among the single propeller configurations, and it is also the most practical and mechanically simplest one among all configurations). ..... 65

### **Figure 2.10**

Various other unconventional UAV configurations that are not practical for indoor applications (a) Triangular Quadrotor. (b) "Stackrotor" platform [32]. (c) Aerial robot dragon. **Image Source:** [33–35] ..... 66

### **Figure 2.11**

Gemini mini framework: the off-the-shelf avionics (marked in black); the off-the-shelf air-frame parts (marked in magenta); and the designed parts (marked in blue). ..... 67

### **Figure 2.12**

Power consumption of all APC propellers below 10 inches. The propeller loading constraint is 0.9 Kg. The APC10x45MR achieves the highest power efficiency and thus is chosen. ..... 69

### **Figure 2.13**

The static thrust of the chosen propulsion system at different PWM inputs. Each actuator is capable of generating 1266g thrust, and the hover duty will be around 73% throttle. ..... 69

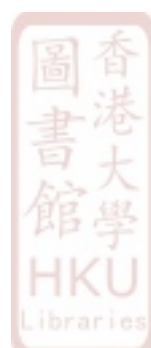


### **Figure 2.14**

Gemini mini fixed avionics layout (actuators, LiDAR, flight controller, on-board computer, battery, and radio station). The critical design decisions mentioned in the text are marked in red squared boxes. ..... 71

### **Figure 2.15**

Gemini mini weight distribution chart. ..... 72

**Figure 2.16**

Gemini mini motor base with secondary hinge (marked in red) for strengthening. .... 73

**Figure 2.17**

Gemini mini designed model versus actual aircraft side-by-side comparison **(a)** The Gemini mini CAD model; **(b)** The final assembled Gemini mini. .... 73

**Figure 2.18**

Gemini mini dynamics **(a)** The generation of roll control moment  $\tau_x$ :  $\tau_x = T_1 D \sin \delta_1 + T_2 D \sin \delta_2$  ( $\delta = \delta_1 = \delta_2$  in this circumstance); **(b)** The generation of pitch control moment  $\tau_y$ :  $\tau_y = (T_1 \cos \delta_1 - T_2 \cos \delta_2)L$ ; **(c)** The generation of yaw control moment  $\tau_z$ :  $\tau_z = (T_1 \sin \delta_1 - T_2 \sin \delta_2)L$ . . 74

**Figure 2.19**

The proposed controller structure. .... 76

**Figure 2.20**

**(a)** Gemini mini hovering flight; **(b)** The voltage, current, and power consumption data during the hovering flight. .... 79

**Figure 2.21**

Gemini mini poking test **(a)** Applying poking disturbances while Gemini mini is hovering; **(b)** The position and attitude data during the hovering flight. .... 80

**Figure 2.22**

Gemini mini angular rate and mixer output during a single poking test **(a)** Pitch angular rate; **(b)** Roll angular rate; **(c)** Yaw angular rate; **(d)** Mixer output of brush-less motors and servo motors (because of the two servo motors' physical installation angles, servo motor tilt in same directions when command are the opposite); **(e)** Attitude response closeup. .... 81



### **Figure 2.23**

Gemini mini flying through a 40 cm gap **(a)** Top, side and back view of the Gemini flying through gap; **(b)** The position and attitude data when crossing the gap. .... 83

### **Figure 3.1**

Gemini W: Hybrid aerial-ground locomotion UAV with a single passive wheel at: <https://youtu.be/22SXYY39KjM> .... 86

### **Figure 3.2**

Example perching and resting actions in nature: Flying animals such as birds or bats often make use of structures in the environment to save energy. In choosing, they select locations that can be approached and evacuated by simply maneuvering in the air, while still allowing them to execute a mission - such as observing the environment or looking for prey. **Image Source:** [36]. .... 87

### **Figure 3.3**

Other perching mechanisms and methods **(a)** Dry-adhesive gecko-inspired grippers perching; **(b)** Dry-adhesive pads perching. **Image Source:** [37, 38] .... 88

### **Figure 3.4**

Transformable ground-air vehicle. **Image Source:** [39] .... 88

### **Figure 3.5**

Hybrid multi-terrain vehicles **(a)** Multi-terrain Multi-utility robot (MT-MUR); **(b)** Air-ground amphibious agricultural information collection robot. **Image Source:** [40, 41] .... 89

### **Figure 3.6**

Small mobile robot with a hybrid locomotion mechanism of passive wheels and multi-rotors **(a)** WAMORN (WAseda MOnitoring dRoNe). **(b)** Parrot Rolling Spider. **Image Source:** [42, 43] .... 89



### **Figure 3.7**

5S APC 1045MR bench test with motors of three different Kv ratings.  
The 740 Kv motor is chosen for its highest efficiency performance when  
hovering with takeoff weight at 1950 g (975 g per actuator). . . . . 91

### **Figure 3.8**

Sideview of common bi-copter crashes (Vehicle falls to the ground following the direction marked by blue arrows. The damaged parts are marked in red and need to be strengthened) (a) The head crash (Upon collision, forces will react on the servo holder as marked by yellow arrows. The momentum of the battery and on-board computer will create another force load to the fuselage as marked by a green arrow); (b) The hard touchdown (Upon collision, momentum from all the parts above the fuselage will create a force load on the fuselage at the locations marked by green arrow). . . . . 93

### **Figure 3.9**

Workflow of topology optimization. Based on the pre-assigned workspace and load setting conditions, this process generated the structure with minimized material (thus minimized weight) and maximized stiffness. . . 95

### **Figure 3.10**

Servo holder part for optimization (a) Servo holder model before topology optimization; (b) Servo holder design space and load condition locations based on the previous model. The designed space can be optimized through topology optimization, while the non-designed space is pre-determined due to installation constraints. The load conditions assumptions are based on previously discussed crash scenarios. . . . . 97



**Figure 3.11**

Servo holder Altair Inspire topology optimization (a) Altair Inspire topology optimization with “maximize stiffness” setting; (b) Altair Inspire servo holder topology optimization result. The non-design space (gray parts) are kept due to installation constraints, and the design space has been optimized. .... 98

**Figure 3.12**

Servo holder part optimization structure redrawn process (a) Servo holder topology optimization result overlay onto design space; (b) Servo holder CAD structure redrawn; (c) Servo holder part optimized CAD sketch. ... 99

**Figure 3.13**

Servo holder ANSYS Workbench analysis (a) Servo holder after fine meshing in ANSYS Workbench; (b) Servo holder ANSYS Workbench constraints and load setting with two remote forces with both vertical and horizontal directions to simulate the crash scenarios. The surfaces marked in red represent the surface where remote forces have been applied to. ... 100

**Figure 3.14**

Servo holder ANSYS Workbench simulation result (a) Total Deformation; (b) Equivalent Stress; (c) Strain Energy; (d) Safety Factor. The safety factor has a minimum value of 12.14 but a weight 42.15 g, thus the model is safe but overweight. .... 101

**Figure 3.15**

Servo holder topology optimization iteration (a) Inspire topology optimization with 24g weight constraints (only the materials to be retained are shown, and the material suggested to be removed is circled in red); (b) ANSYS stress distribution and strain energy distribution analysis (only the less stressed materials are shown, and the materials could be removed with the corresponding method are circled in red). .... 102

**Figure 3.16**

Servo holder final deliverable after topology optimization, weight reduction iteration, and cable tray features added. .... 103

**Figure 3.17**

Servo holder final deliverable simulation analysis (a) Total Deformation (b) Equivalent Stress (c) Strain Energy (d) Safety Factor. The safety factor has the minimum value of 9.199 and the weight is reduced to 24 g. The weight is halved and met the requirement, while the safety factor is still desirably high. The optimization is successful in simulation. .... 103

**Figure 3.18**

Servo holder experimental validation (a) The weight of the optimized servo holder is 25 g. (b) The final aluminum 3D printed servo holder in use. The final servo holder successfully surpasses the experiment validation, and has never been wrecked upon crashes ever after. .... 104

**Figure 3.19**

The optimized servo holder comparison with the previous model. The newly improved model surpasses the previous model in every physical performance aspect, including stress distribution (26.63 MPa maximum vs. 198.19 MPa maximum previously), safety factor (9.19 minimum vs. 1.22 minimum previously), weight (25 g vs. 44 g previously), and useability (easy installation features added). .... 106



**Figure 3.20**

Gemini W main fuselage with load settings. Assume the carbon fiber rod and LiDAR as the fixed mounts constraints (tagged with A), and apply a load that is equivalent to the gravitational force of battery, flight controller, power module, and the on-board computer to the remote installation holes that is the farthest from the mounting points (tagged with B). .... 107

### **Figure 3.21**

Main fuselage simulation analysis (a) Total Deformation (with maximum deformation of 0.89 mm); (b) Equivalent Stress; (c) Strain Energy; (d) Safety Factor (with the minimum value of 2.01). The deformation is high under current load settings, and the weak spots are circled in red. Besides high deformation, the fuselage weights 67 g and needs to be reduced. .... 108

### **Figure 3.22**

Gemini W main fuselage structure strengthings and features for easy installation. .... 109

### **Figure 3.23**

Gemini W main fuselage simulation analysis after optimization (a) Total Deformation (with maximum deformation of 0.53 mm, and evenly distributed across the affected sections); (b) Equivalent Stress (c) Strain Energy (d) Safety Factor (2.5). The deformation and safety factor have been greatly improved, and the weight of the fuselage is reduced to 50 g with installation holes and ESC installtion panel features added. .... 110

### **Figure 3.24**

Gemini W improved main fuselage safety factor comparison (safety factor of sections less than 5 are displayed, the improved result show significantly fewer weak spots) (a) The original design for comparison; (b) The improved result after optimization. .... 110

### **Figure 3.25**

The improved fuselage comparison with the previous model. The newly improved model surpasses the previous model in every physical performance aspect, including maxmimum deformation structure (0.53 mm vs. 0.83 mm previously), equivalent stress (16.98 MPa maximum. vs. 21.87 MPa maximum previously), strain energy (0.028 mJ vs. 0.143 mJ previously), safety factor (2.59 minimum vs. 2.01 minimum previously), and weight (50 g vs. 67 g previously). .... 111



**Figure 3.26**

By changing the attitude and making use of the friction, the vehicle is able to move in any direction following an S-shaped curve. .... 112

**Figure 3.27**

(a) Original PX4 power distribution system; (b) Customized highly integrated PMU board. The original PX4 power distribution system weights 95 g and requires complicated installation, while the customized board integrates all these components into a single PCB board and weights only 50 g. Besides, the installation can be done in one minute. .... 113

**Figure 3.28**

The definition of body frame ( $x^B y^B z^B$ ) and inertial frame ( $x^I y^I z^I$ ). .... 115

**Figure 3.29**

The generation of the torque ( $\tau_x \tau_y$ ) in rolling mode. .... 115

**Figure 3.30**

Different phases of the hybrid aerial-ground locomotion: above  $D_H$  is the aerial mode, below  $D_L$  is the ground locomotion, and between them is the transition. .... 118

**Figure 3.31**

Controller block diagrams: black blocks are used in normal aerial flight, red blocks are turned on when in transition mode and blue blocks are for control when rolling on the ground. .... 118

**Figure 3.32**

(a) Aerial-ground transition process; (b) The vertical position, velocity, and acceleration during aerial-ground transition. .... 122

**Figure 3.33**

The attitude response during the aerial-ground transition. .... 123

### **Figure 3.34**

(a) Attitude response when rolling on ground. (b) Velocity response when rolling on ground. .... 124

### **Figure 3.35**

Rolling on the ground following a pattern “8”. .... 125

### **Figure 3.36**

The power consumption comparison among different states: hovering state (H), rolling on the ground state (R), sitting on the wheel state (S).  
The numbers above each bar are the mean power consumption of the state over 10 seconds. .... 126

### **Figure 4.1**

Boeing CH-47 Chinook military bi-copter: (a) Aircraft [44]; (b) Swashplate mechanism [45]. .... 129

### **Figure 4.2**

Flybar-less swashplate mechanism (a) The assembled flybar-less swashplate mechanism example; (b) Simplified schematic of the proposed swashplate mechanism with the essential joints. **Image Source:** [46] ... 130

### **Figure 4.3**

The Hong Sun bi-copter concept. Hong Sun is a bi-copter powered by two FBL swashplate propulsion systems. The Hong Sun has a wingspan of 155 cm and is designed for 5 Kg takeoff weight. With a 50000 mAh 12s battery on board, it is expected to hover for around 30 minutes or level flight for even longer flight efficiency. .... 131



### **Figure 4.4**

Controlling the Hung Sun propulsion system heave with servo motor (a) Maximum AOA for maximum heave; (b) Minimum AOA for minimum heave. .... 132

**Figure 4.5**

Hong Sun propulsion system test setup. The power consumption and force generation are monitored through this setup. .... 133

**Figure 4.6**

Hong Sun propulsion system test data. The force and power consumption of the combinations of all three actuator inputs during operating zone is logged. Colors and bars are added to the cell backgrounds for value reflection. .... 135

**Figure 4.7**

The long motor shaft in Hong Sun propulsion system. Due to non-ideal factors such as manufacturing error or wastage, the long shaft tends to bend and causes vibrations when rotating at high speed. .... 136

**Figure 4.8**

Hong Sun interior avionics. .... 138

**Figure 4.9**

Hong Sun fuselage validation (a) Top view; (b) Side closeup. The fuselage (including 3D printed body, nylon parts and carbon fiber parts) weights 811 g. .... 138

**Figure 4.10**

(a) Hong Sun hovering test rig with protecting foam box; (b) Hong Sun test rig interior closeup. .... 139

**Figure 4.11**

Propulsion system test fails. Huge vibrations of the brush-less motor (shown in the lower right corner) cause the motor base (circled in green) to disassemble itself during testing. .... 140



### **Figure 5.1**

Gemini II servo-less bi-copter performing agile maneuvering (Gemini II achieves 6-DoF with two motors as the only actuators). The propeller size is 13 inches (33.02 cm), and the total system weights 1.87 Kg. It is capable of flying up to 22 minutes. The video is available at: <https://youtu.be/qGhQbPtp7Sw> ..... 143

### **Figure 5.2**

Dual rolls swashplate-less mechanism that is able to generate pitching and rolling torque without extra servo motors. **Image Source:** [47] ..... 145

### **Figure 5.3**

Swashplate-less mechanism with flap hinges to reduce vibrations. **Image Source:** [48] ..... 146

### **Figure 5.4**

Scalability of swashplate-less mechanism. ..... 147

### **Figure 5.5**

Gemini II mechanical design detail and avionics. Each propulsion system consists of only one motor and swashplate mechanism with extension stands augmenting roll and yaw control authorities. Gemini II is also equipped with Livox Avia LiDAR and an on-board computer for future autonomous flying capability. ..... 148



### **Figure 5.6**

Gemini II design space design **(a)** Avionics layout (LiDAR payload, battery, on-board computer, flight controller, PMU); **(b)** Design space and constrains setting (Draw the basic geometric shape and apply load with assumptions). ..... 150

### **Figure 5.7**

Gemini II fuselage sketching process **(a)** Topology optimization result; **(b)** Importing the result into CATIA; **(c)** Do a new sketch on top of the topology optimization result, and repeat the process for top, side, and front views; **(d)** Fuselage sketch deliverable. .... 151

### **Figure 5.8**

Gemini II fuselage sketch analysis **(a)** Mesh analysis; **(b)** Constrains and load condition settings; **(c)** Total Deformation (The most dramatical change of deformation happens in the weak structure circled in magenta); **(d)** Equivalent Stress (The weak structure experience the greatest amount of stress, and is circled in magenta); **(e)** Strain Energy (The weak structure bear the largest amount of strain energy, and is circled in magenta); **(f)** Safety Factor (The weak structure is a continuous chunk rated with safety factors less than 9, and is circled in magenta). .... 152

### **Figure 5.9**

Gemini II fuselage weak structures and corresponding remedy **(a)** Tendon strengthener method; **(b)** Pillar rib strengthener method. .... 154



### **Figure 5.10**

Gemini II fuselage analysis after iteration **(a)** Total Deformation (5.51 mm maximum vs. 7.96 mm maximum previously); **(b)** Equivalent Stress (211.71 MPa maximum vs. 370.68 MPa maximum previously); **(c)** Strain Energy (0.10 mJ maximum vs. 0.17 mJ maximum previously); **(d)** Safety Factor (1.16 minimum vs. 0.76 minimum previously). Every aspect mentioned above suggests the fuselage has higher stiffness against shocks, and is much less likely to break upon crash. .... 155

**Figure 5.11**

Gemini II fuselage safety factor improvement (a) Before iteration, multiple chunks of structures have a safety factor of less than three (circled in red); (b) After iteration, safety factor is greatly improved with no risky structure that has safety factor less than one and no huge chunk of structure has safety factor less than three. .... 156

**Figure 5.12**

swashplate-less cyclic blade pitch control mechanism (a) Mechanism diagram (brush-less motor rotates following the direction indicated by the magenta arrow); (b) Magnetic encoder closeup. .... 157

**Figure 5.13**

Blade dynamic reaction on the counterclockwise spinning motor (a) Lagging behavior of the two blades. (b) Tilting of the propeller disk. ... 158

**Figure 5.14**

Different mechanical bearings (a) Tapered roller bearing (b) Ball bearing (c) Thrust bearing. .... 160

**Figure 5.15**

One rotation cycle of the swashplate-less mechanism under high speed camera. The instantaneous pitch at one location is controlled by the phase of the torque modulation (a)  $0^\circ$ ; (b)  $90^\circ$ ; (c)  $180^\circ$ ; (d)  $270^\circ$ . .... 161

**Figure 5.16**

Gemini II's definition of coordinate frames (the black coordinate represents the world frame, the magenta coordinate represents the body frame, and the two orange coordinate represents two motor frames respectively)  
(a) Front view. (b) Side view. (c) Top view. .... 162

**Figure 5.17**

Control system structure of the Gemini II. .... 166

**Figure 5.18**

Actuator evaluation setup. ATI 6-axis force sensor is used along with 3D printed structure for testing. .... 170

**Figure 5.19**

Effect of the swashplate-less mechanism on the power efficiency. The swashplate-less mechanism barely has any effect on the power efficiency. 171

**Figure 5.20**

Gemini II hovering power consumption. The Gemini II consumes around 193 W of power on average while hovering. .... 172

**Figure 5.21**

(a) Our improved mechanism: Tilting angle vs. sinusoidal amplitude response near operating point (highly linear with no actuator deadband).  
(b) Previous swashplate-less work: Moment magnitude vs. sinusoidal amplitude response at three different operating speeds. **Image Source:** [47] .... 173

**Figure 5.22**

Roll angle step response comparison. The swashplate-less bi-copter Gemini II performs twice as fast as the servo-based bi-copter Gemini mini, and is 64 ms slower than the corresponding quad-copter. .... 174

**Figure 5.23**

y-axis position control system structure of the Gemini II. The upper diagram inside of the red box represents the closed-loop roll angle control system and the lower diagram indicates the complete closed-loop y-axis position control system. .... 176

**Figure 5.24**

Gemini II identified model evaluation. The roll rate measurement and identified model output comparison are highly overlapping, proving the accuracy of the model. .... 178



**Figure 5.25**

Frequency domain analysis of the Gemini II (a) Bode diagram of the closed-loop position control transfer function; (b) Bode diagram of the external force disturbance rejection transfer function. .... 179

**Figure 5.26**

Gemini II poking test (a) Test setup (b) The attitude and position setpoint vs. feedback during the poking test. .... 181

**Figure 5.27**

Closeup data during the first poke (a) Desired angular rate vs. actual angular rate during the first poke (boxed in green); (b) Mixer output during the first poke; (c) Attitude setpoint vs. feedback during the first poke. .... 182

**Figure 5.28**

Gemini II wind disturbance test (a) Test setup (b) attitude and position setpoint vs. feedback during the gust wind disturbance test. .... 184

**Figure 5.29**

Closeup data of a gust of wind hit (a) Desired angular rate vs. actual angular rate of a gust of wind hit (boxed in green); (b) Mixer output of a gust of wind hit; (c) Attitude setpoint vs. feedback of a gust of wind hit. .... 185

**Figure 5.30**

Gemini II trajectory test (a) following a “3D Figure 8” pattern trajectory (b) “3D Figure 8” trajectory track setpoint vs. feedback (c) Velocity and position setpoint vs. feedback while following a “3D Figure 8” pattern. .... 187

**Figure 5.31**

Gemini II two-way spring-damper mechanism for alleviating vibration issues. .... 188



# List of Tables

**Table 2.1**

The Gemini mini's Specifications .....	74
--	----

**Table 4.1**

The Hong Sun's Specifications .....	138
-------------------------------------	-----

**Table 5.1**

The Gemini II's Specifications .....	161
--------------------------------------	-----

**Table 5.2**

Gemini II y-axis Control Parameters .....	177
---	-----



# List of Publications and Patents

## Published works:

- [1] **Qin Y.**, Chen N., Cai Y., Xu W., and Zhang F., “Gemini II: Design, Modeling, and Control of a Compact Yet Efficient Servo-less Bi-copter,” *IEEE/ASME Transactions on Mechatronics*, doi: 10.1109/TMECH.2022.3153587, 2022.
- [2] **Qin Y.**, Xu W., Lee A., and Zhang F., “Gemini: A compact yet efficient bi-copter UAV for indoor applications,” *IEEE Robotics and Automation Letters*, 5(2), 3213-3220, 2020.
- [3] **Qin Y.**, Li Y., Xu W., and Zhang F., “Hybrid aerial-ground locomotion with a single passive wheel,” in *IEEE/RSJ International Conference on Intelligent Robots and Systems (IROS)*, 2020.
- [4] Li Y., **Qin Y.**, Xu W., and Zhang F., “Modeling, Identification, and Control of Non-minimum Phase Dynamics of Bi-copter UAVs,” in *IEEE/ASME International Conference on Advanced Intelligent Mechatronics (AIM)*, pp. 1249-1255, July 2020.
- [5] Xu W., Gu H., **Qin Y.**, Lin J., and Zhang F., “Full Attitude Control of an Efficient Quadrotor Tail-sitter VTOL UAV,” in *International Conference on Unmanned Aerial Systems (ICUAS)*, 2019.
- [6] **Qin Y.**, and **Zhang F.**, “Compact yet efficient bi-copter UAV for indoor mapping,” US Prov. Patent: US63/018,529, 2019.



# Chapter 1

## Introduction

The introduction chapter introduces the background of unmanned aerial vehicles (UAV) and our work motivations and methods. Starting with a brief history of the development of unmanned aerial vehicles, we exhibit all the common classifications and applications of unmanned aerial vehicles. After covering the background, we analyze the gaps between contemporary unmanned aerial vehicles and the real-world application demands, followed by how our work can resolve the issues. The outline of the whole thesis is presented at the end of the chapter.

### 1.1 Historical Evolution of UAVs

Humans crave to conquer the sky existed since the dawn of history. The western myth of Daedalus and Icarus [49], along with the eastern Chinese tale of Shun's aircraft [50], could both be traced back to far ancient times. In the middle age, the early shape of modern aircraft was taken by scientists such as Leonardo Da Vinci (1452-1519) [51]. Unmanned aerial vehicles, also referred to as drones, emerged in the 19th century. The historical evolution of UAVs starts from myths and concepts and is catalyzed by the era of wars.

Instead of requiring a human pilot onboard, UAVs are ideal weapons to do damage while preventing casualties during wartime. Since the beginning of the



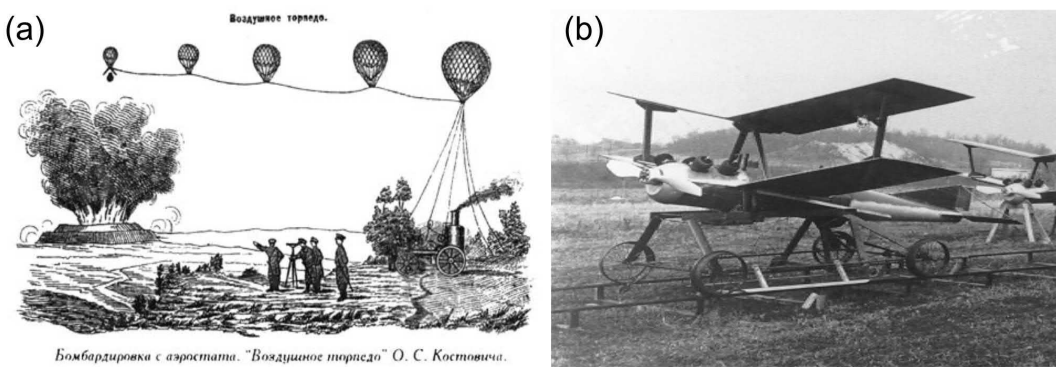


**Figure 1.1** UAVs during World Wars **(a)** The Austrian balloon (1849): the first disposable UAVs used in the war; **(b)** November Kettering Bug plane (1917): the world's first radio wave controlled UAVs. **Image Source:**[1, 2]

World Wars, the military demands for disposable UAVs drastically increased. In 1849, the unmanned combat air vehicle was first used when Austrians attacked the Italian city of Venice with 200 timber bombs loaded balloons, as shown in Figure 1.1a. The attack caused little damage, but Venice surrendered two days later [52]. This event marks the first military application of UAVs.

On April 16th, 1867, the Wright brothers invented, built, and successfully piloted the world's first motor-operated airplane [53]. Not long after the dawn of airplanes, In 1917, the U.S. military unmanned system November Kettering Bug plane was able to fly under radio wave control, representing the early UAVs system, as shown in Figure 1.1b.

Right after the world wars ended in 1945, the military demands for unmanned

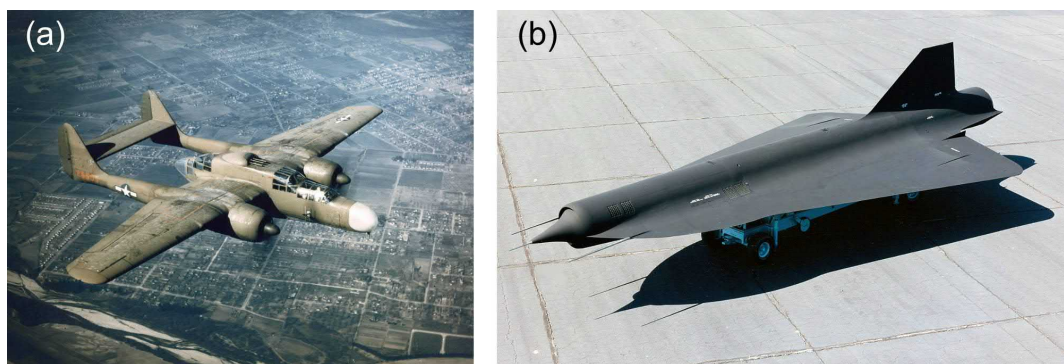


**Figure 1.2** UAVs after the World Wars **(a)** Northrop P-61 black widow (1946): the weather data gathering UAV; **(b)** Lockheed D-21 (1969): high-altitude and high-speed reconnaissance unmanned aerial vehicle. **Image Source:** [3, 4]



aerial vehicles dropped dramatically. Instead of carrying weapons and bombs, UAVs became popular in data gathering tasks. In April 1946, Northrop P-61 black widow was the first UAV for scientific research purposes (shown in [Figure 1.2a](#)). It serves as a weather data-gathering drone for the U.S. Weather Bureau [3].

During the cold war period (March 12, 1947 to December 26, 1991) [54], espionage missions boosted the field study of UAVs. Military companies such as Lockheed Martin developed a series of supersonic unpiloted detection UAVs. As shown in [Figure 1.2b](#), the high-altitude and high-speed reconnaissance drones, D-21-ShunkWorks, carry a high-resolution photographic camera over the preprogrammed path, then release the camera module into the air for retrieval, after which the drone would self-destruct [55].

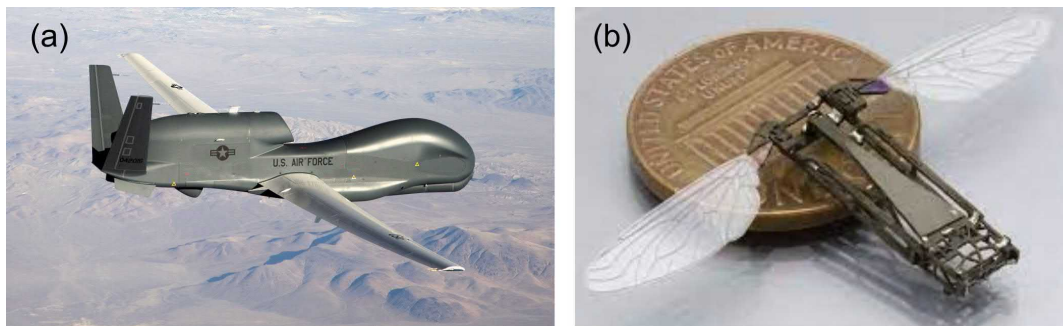


**Figure 1.3** UAVs after the Cold War **(a)** Global Hawk (HALE UAV, 1998): the unmanned surveillance and reconnaissance aerial vehicle. **(b)** RoboBee X-Wing MAV (2013): a coin-sized unmanned aerial vehicle. **Image Source:** [5, 6]

After the cold war, the development of UAVs mainly aims to enhance UAV's performance envelop and shrink the vehicle size [56]. The unmanned combat air vehicles (UCAV) were designed for high speed and high maneuverability. As shown in [Figure 1.3a](#), the Global Hawk is a high-altitude long endurance (HALE) UAV, and it is representative of such a type [5]. The coin-sized micro aerial vehicles (MAVs) were developed to carry small sensors and perform tasks [6]. As shown in [Figure 1.3b](#), the RoboBee X-Wing MAV uses a piezoelectric bimorph material as actuators to generate mechanical deformation using inverse piezoelectric effect. This lift-enhancing design of mimicking the flapping mechanism of a fly's 2 cm wingspan enabled the 80 mg FWMAV to fly autonomously. The Robobee was fitted with various individual sensors for onboard feedback. Pitch and yaw control of the



RoboBee using an on-board magnetometer was presented with the robot constrained to rotate only about its principal axes. The integration of a MEMS gyroscope onto the RoboBee to provide attitude feedback in flight.

In the 21 century, with the maturity of electronic components hardware such as batteries and mini radios and sensors such as inertial measurement units (IMUs), the price of UAVs, especially that of the quad-copters, has decreased significantly [57]. At the same time, UAVs started to change into more miniaturized and low-power versions [58]. The merging of autonomous robotics technology largely enhanced the level of intelligence of UAVs. With the camera sensor becoming more and more mature, commercial drones are able to perform professional images with user-friendly operations. Spanning from applications such as aerial photography, inspection, and movie making, the civilian and consumer UAV market boomed during the past decade. The applications and common contemporary UAV classification will be discussed in the following subsections.

## 1.2 UAVs Classification

The common contemporary UAVs can be categorized into five types, lighter-than-air UAVs, fixed-wing UAVs, multi-rotor UAVs, flapping wing UAVs, and hybrid UAVs [56, 59], as shown in [Figure 1.4](#).

Lighter-than-air UAVs: this category of UAVs is lighter than air, such as airships (unmanned 5G airship [8] in [Figure 1.4a\(i\)](#)) and balloons (indoor robotic airship [9] in [Figure 1.4\(ii\)](#)). Since the lighter-than-air utilize inflated low-density air to counteract gravity, the endurance of such aircrafts is long, but the volume of the aircrafts is unavoidably huge, making the drag relatively large and fundamentally restricting the agility of the aircraft.

Fixed-wings UAV: the fixed-wing UAVs is mostly used for military purpose and usually require a runway to take off (General Atomics MQ-1 “Predator” [10] in [Figure 1.4b\(i\)](#)) or require a shoot off to deploy (Airbus “SMDM” [11] in [Figure 1.4b\(ii\)](#)).



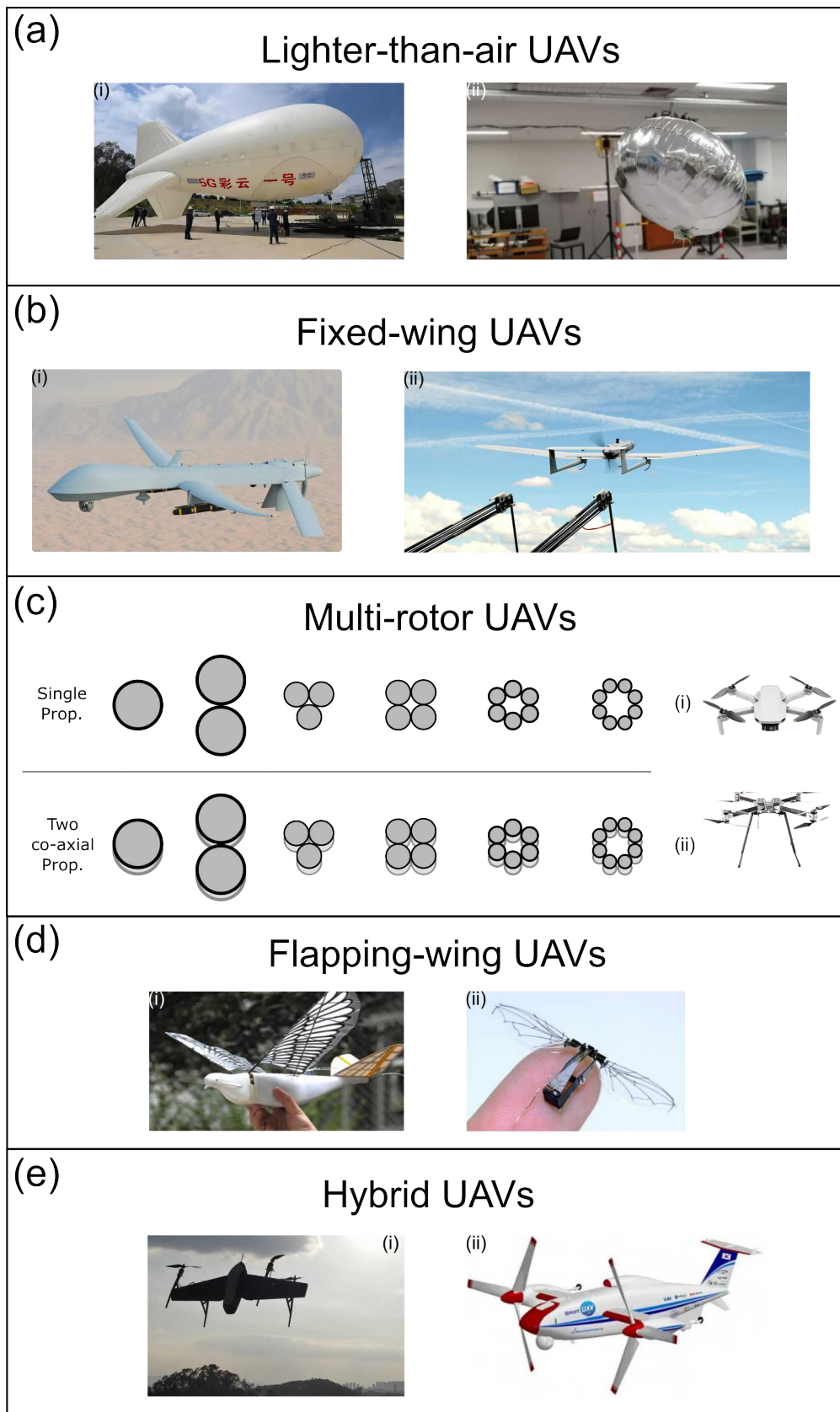


**Figure 1.4** Contemporary UAV classification with two examples given for each class [7] (a) Lighter-than-air UAVs; (b) Fixed-wing UAVs; (c) Multi-rotor UAVs (with 12 common multi-rotor configurations); (d) Flapping-wing UAVs; (e) Hybrid UAVs. **Image Source:** [8–14]

They typically have long endurance and can operate at high speed.

Multi-rotors UAVs: in general, these types of UAVs have the advantage of being small in size, low cost, high maneuverability, and high capacity but suffer short endurance as a drawback. Due to the relatively low cost, this type of UAV is the most popular one in the civilian and consumer market. As shown in the left hand side of [Figure 1.4c](#), a rotorcraft UAV has 12 common configurations, including helicopter, tandem rotors, co-axial rotors, etc. As shown in [Figure 1.4c\(i\)](#), the single propeller quad-copters are most commonly seen. Two co-axial propeller configuration is sometimes adopted for greater maximum thrust and maneuverability but comes at the cost of lower hovering efficiency and even shorter endurance, as shown in [Figure 1.4c\(ii\)](#). Theoretically, the larger number of motors adds redundancy and therefore improves stability and safety. However, the more motors onboard, the heavier and larger the aircraft is going to be [12].

Flapping-wing UAVs: this type of UAV is usually small in size and is able to morph like birds (bird-like surveillance drone [13] in [Figure 1.4d\(i\)](#)) and flying insects (Harvard insect-sized robot that can both fly and swim [14] in [Figure 1.4d\(ii\)](#)). This type of UAV has the drawback of relatively higher cost and low or no payload capacity.

Hybrid UAVs: these hybrid configurations usually combine fixed-wing UAVs and multi-rotor UAVs, such as Vertical Take-off and Landing (VTOL) UAVs (“Hong Hu” VTOL UAV [60] in [Figure 1.4e\(i\)](#)) and (tilt-rotor UAV [61] in [Figure 1.4e\(ii\)](#)). By adopting these configurations, the UAVs are able to take advantage of the high-efficiency cruising brought by the wings and the flexibility of the multi-rotor UAVs, i.e. being able to hover in place. However, the flexibility comes at a higher manufacturing cost and lower maneuverability and efficiency at hovering mode when compared to traditional multi-rotor UAVs.



### 1.3 Contemporary UAVs Civilian Applications

Nowadays, the civilian multi-rotor UAVs market is emerging at an astonishing speed. The multi-rotor UAVs have been considered the perfect platform for the aerial view of areas in confined airspace when manned helicopters cannot operate [62]. The multi-rotor UAVs can access structures using autonomous navigation systems in the abundance of a new class of applications. These structures, such as the top of the banks or bottom of the valley, are too small, tall, and inaccessible for manned aircraft or satellite multi-spectral imaginaries to get up close [62]. With exploding electronic intriguing and fresh autonomous navigation and localization technologies, the rapidly expanding market in civilian swashplate-less UAVs such as rescuing tasks and environmental monitoring are taking place. According to the global civil drone market outlook, 2019-2027, published by Statista Research Department on Oct 19, 2021, “The global civil drone industry is expected to reach about 21.6 billion U.S. dollars by 2027. Military use has previously accounted for much of drone use, but the industry is increasingly entering commercial, scientific, and agricultural usage [63].”

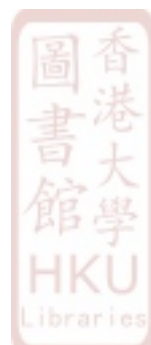
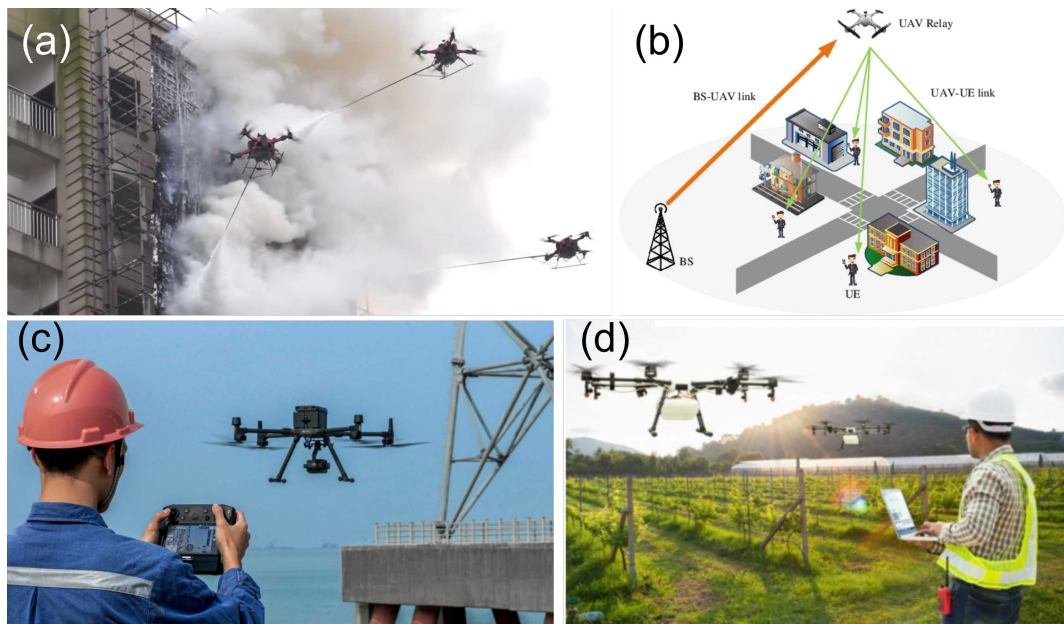


**Figure 1.5** UAVs application examples **(a)** Firefighting; **(b)** Emergency relay communications; **(c)** Inspection; **(d)** Agriculture. **Image Source:** [15–18]

As multi-rotor UAVs become smaller, lighter, and more intelligent, they are able to carry different payloads. Contemporary UAVs can be used for wide applications that traditional manned aircraft have no access to. As shown in [Figure 1.5](#), when performing firefighting tasks, emergency relay communications, inspections, and agriculture, UAVs carry overwhelming advantages over humans. First and foremost, the UAVs are flexible and easily deployable. They could be placed in the most harshed working environment and even some spaces that are unsuitable for humans, such as contaminated nuclear wasteland. Besides, by using swashplate-lesson-board sensors such as GPS, UAVs can operate with high precision. Moreover, the cost of drone operations is usually significantly cheaper than human operations. In addition, UAVs usually could fly faster than most ground vehicles, which makes them ideal for emergency tasks such as firefighting. In summary, advantages such as the superior flexibility, relatively low cost, high precision, and outstanding mobility of UAVs make them the most popular choices in tasks such as:

1. Inspection and surveying of terrain, pipelines, utilities, buildings, etc.
2. Aerial photography and filming
3. Law enforcement and security surveillance
4. Environmental monitoring
5. Agriculture and forestry
6. Firefighting
7. Relay communications
8. Cave and tunnel explorations
9. And many other applications that are either repetitive or operating in harsh environments that are unsuitable for humans.



## 1.4 UAV Application Gaps

Due to the inherent mechanical simplicity and superior mobility, quad-copters have emerged as the premier platform for a multitude of tasks such as inspection, indoor construction site mapping, exploration, post-disaster search & rescuing [64–66]. Though the tasks mentioned above are often performed by on-board sensors such as LiDAR and professional cameras, these sensors tend to be as heavy as they are precise, thus decreasing the overall maneuverability of the UAV. While most quad-copters increase the size of their propellers to compensate for the extra mass, their ability to operate indoors or in tight spaces is in turn severely compromised.

Indoor applications usually demand high payload capacity, small size yet still having long enough endurance to finish the tasks [67]. Many tasks require a few hundred grams payload of 3D LiDAR, the size of a corridor or of a human body width (with necessary safety clearance) and more than 10 minutes of fly time. These three requirements are conflicting with each other and fundamentally limit the applicability of quad-copters.

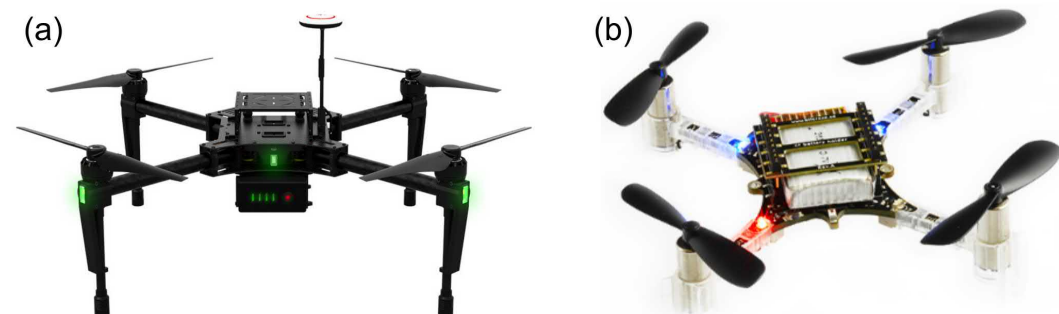


**Figure 1.6** Commercial quad-copter UAV examples **(a)** DJI Matrice 100 quad-copter; **(b)** Crazyflie 2.0 Micro Aerial Vehicle (MAV) quad-copter.  
**Image Source:** [19, 20]

For example, the DJI Matrice M100, as shown in Figure 1.6a, is able to carry up to 0.9 Kg of extra payloads, yet it has a wingspan of 806 mm [19], which is considerably larger than the average width of a door in indoor operations. An intuitive approach may seem to reduce the size of the UAV such that it can fit through a door frame, yet, the UAV has to be able to carry a sufficiently heavy payload, and decreasing its

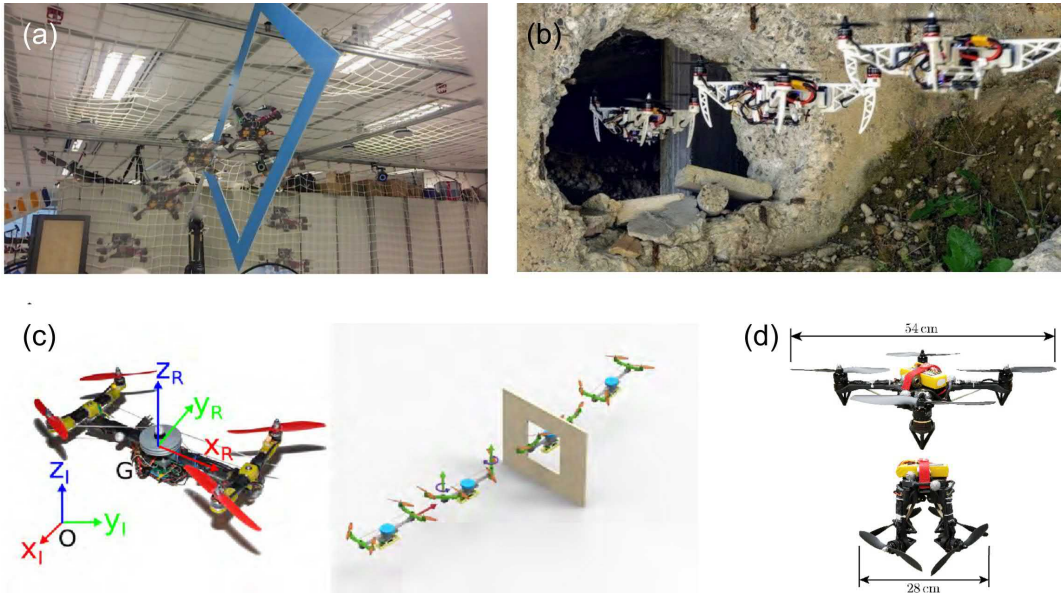


**Figure 1.7** Existing solutions for UAVs to fly through narrow gaps **(a)** Quad-copter flying through narrow gap; **(b)** Morphing-based approach to fly through narrow gap; **(c)** Agile morphing approach to fly through narrow gap; **(d)** Passive morphing approach to fly through narrow gap. **Image Source:** [21, 21–23]

size will greatly diminish its ability to do so. Take another example, Crazyflie 2.0, as shown in Figure 1.6b, a miniature quad-copter UAV, that is obviously capable of fitting through extremely small gaps [20]. However, its maximum payload mass is a meager 15 g, making it impossible to carry most of the usable payloads, and has a very limited flight time of a few minutes.

Previous solutions to the problem of flying through confined spaces have been done. One simple solution is making use of the flat geometry of a quad-copter and rolling the whole UAV to fit a narrow gap [21, 68], as shown in Figure 1.7a. Besides requiring accurate trajectory calculation and tracking, this maneuver cannot be constantly maintained (e.g., flying through a long narrow corridor) as rolling will inevitably cause lateral movement. In addition, the nature of this approach also limits the amount of space below the UAV that payloads can be mounted on, as the height of a UAV would surely interfere with the maneuver. Adaptive morphology is another solution of enabling a UAV to adapt to confined spaces. D. Falanga *et al.* [22] transform the frame of the UAV into different configurations to allow it to fit through a space that it may not have been able to previously, and it is illustrated in Figure 1.7b. This solution allowed UAVs to maintain their size without sacrificing



power and efficiency. However, the degree of deformation and the overall UAV size are still constrained by the many propellers being used. Moreover, the four additional servomotors also increase the mechanical complexity and UAV weight. To even decrease the UAV size, Reiviere *et al.* [69] proposed an agile morphing mechanism that arranges all the four rotors in a row, reducing the UAV size to the size of a single propeller, as shown in Figure 1.7c. However, with such a transformation, the roll axis is not controllable. Another application of such adaptive morphology can be found in [23]. Whereas the research above morphed the UAV across a single plane, that being lateral, the design of [23] contracts the arms of the UAV downwards into a ball, allowing it to halve its effective size (shown in Figure 1.7d). This configuration proves to be simpler than the previous one, as the morphing mechanism is totally passive, requiring no additional servomotors. However, similar to [22], the UAV in the morphed shape is inherently unstable and cannot be constantly maintained due to the loss of controllability.

In summary, indoor UAV applications simultaneously pose high demands for payload capacity, size, and endurance. Most contemporary solutions tend to rely on unconventional concepts and mechanical prowess, which is generally not a reliable combination for practical uses in the current stage. Maximizing the aforementioned three high demands without practical compromises is the focus of our approach.

## 1.5 Our Approach

When compared to the deformable quad-copter mentioned previously, bi-copter configurations are mechanical simpler (with a minimal set of actuators), smaller (reducing the UAV size to that of a single propeller), fully controllable (attaining full controllability in all flights), and more practical (carrying significant payloads for a prolonged time).

In this thesis, we propose a series of bi-copter approaches that address the issue of building compact yet efficient bi-copter UAVs. Unlike the existing work, which focuses more on the control of such bi-copter UAVs, we focus on the overall



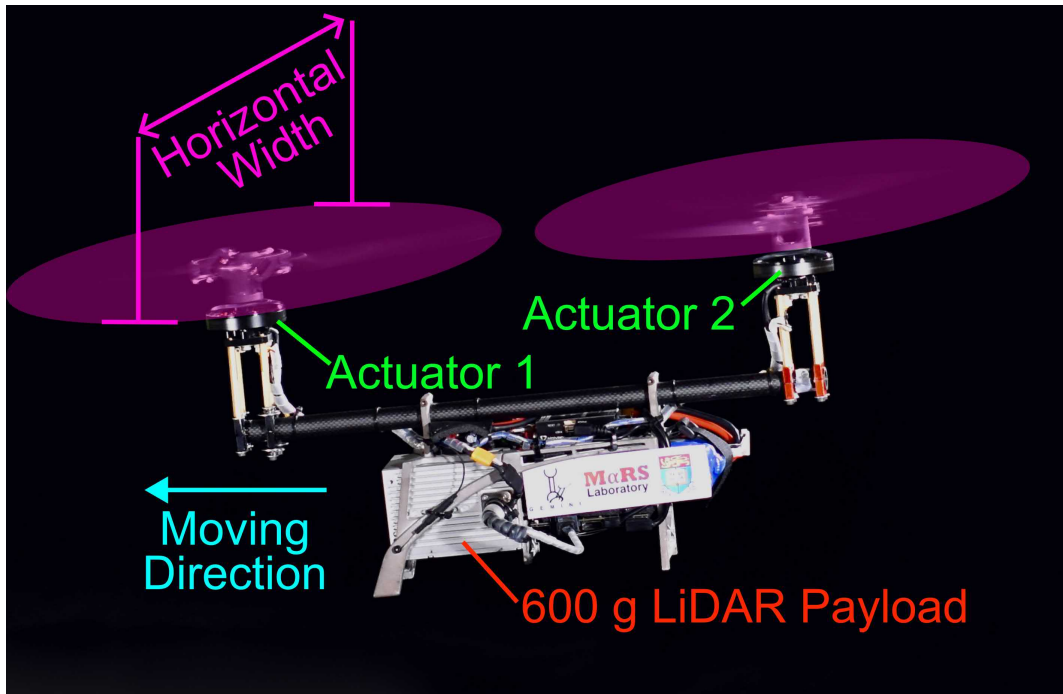


**Figure 1.8** Our bi-copter approach achieves full controllability of the UAV with a minimal set of actuators (only two brush-less motors). Its horizontal width is the size of the propeller, and it can efficiently navigate in confined spaces while carrying a heavy payload such as 600 g LiDAR.

aircraft design (overall system architecture, implementation, controller design, power consumption, and the flight performance of the bi-copter) to increase its usability (maximum takeoff weight, UAV size, and efficiency optimization).

As shown in Figure 1.8, our bi-copter approach pushes the limit of each design aspect with aerodynamic optimization under specific design criteria. These special bi-copter arrangements allow for the preservation of propeller size, meaning that we can effectively halve the horizontal width of the quad-copter UAV whilst only slightly decreasing its payload carrying capability.

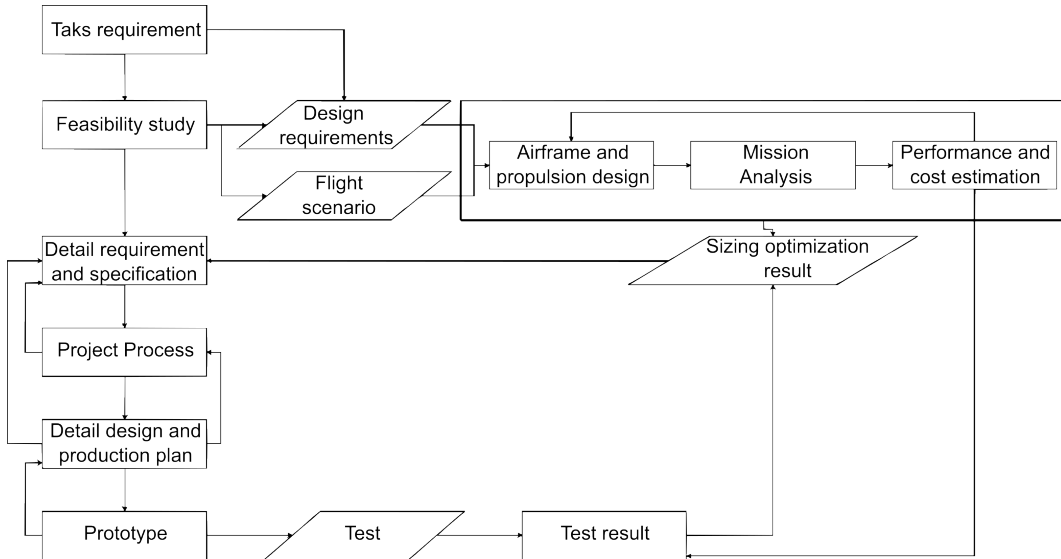


**Figure 1.9** UAV system design process. **Image Source:** [24]

## 1.6 Design Method

The system engineering design is tightly coupled with mission objectives. As illustrated in [Figure 1.9](#), rather than imposing special required performance to the platform for each specific application or mission, the mission objective requirements shall be defined according to the interaction between payload and platform.

As mentioned earlier in the chapter, vehicle size, payload capacity, and cruising time are the three-factors conundrum that is conflicting with each other. In this thesis, we focus on resolving this fundamental conundrum while keeping practicality in mind. We clarify the design requirement first and then optimize the performance through testing and iterations.

## 1.7 Thesis Organization

The thesis is composed of six chapters in total. The thesis organization and flow are structured as [Figure 1.10](#). The main focus of each chapter is further illustrated in the following secessions.



## Design, modeling, control, and implementation of bi-copter UAVs

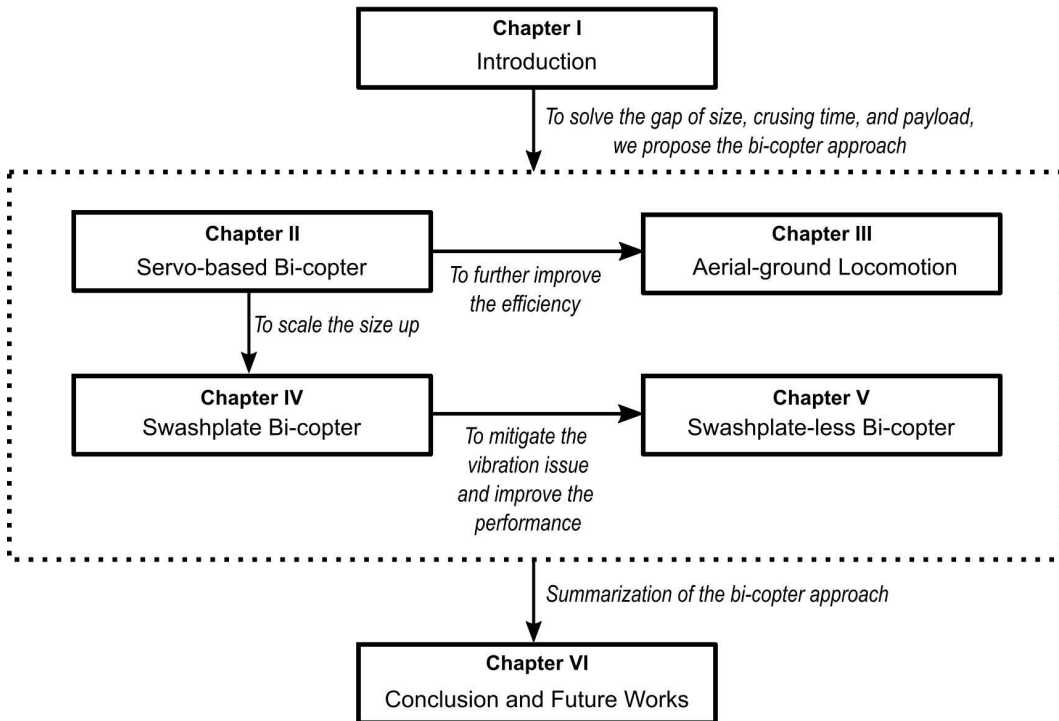


**Figure 1.10** Thesis structure

### *Chapter I - Introduction*

The first chapter went through the background of UAVs, started with the historical revolution of UAVs from ancient times till the post-world-war era when civilian use of UAVs boomed. Furthermore, the UAVs classification and contemporary UAVs civilian applications were introduced. Then chapter one also pointed out the gap between contemporary UAVs and their applications, followed by how our method resolved the gap with a brief introduction on our approaches. At the end of chapter I, the organizational outline of the thesis is listed.

### *Chapter II - Gemini mini: servo-based bi-copter*

The second chapter focuses on is the designing, modeling, controlling, and implementation of a compact yet efficient bi-copter UAV platform. The exemplary design of our proposed bi-copter UAV platform is named Gemini mini. We firstly illustrate the aerodynamic analysis and comparison against various motor-rotor UAV configurations and the process of optimizing the efficiency of the bi-copter



method. Using momentum theory, we theoretically prove the superiority of bi-copter operations in confined spaces, followed by experimental validation of the presumptions.

Moreover, in order to optimize the efficiency, power consumption, and propulsion system, tests were conducted for picking the critical off-the-shelf on-board elements that allow the Gemini mini to work seamlessly. The reasoning process behind the chosen layout and the design decisions are also illustrated, especially the customized designed parts.

The control system design is also presented, with the hovering test, attitude poking experiment, and flying through 40 cm gap experiment to validate the whole system design.

### ***Chapter III - Gemini W: aerial-ground locomotion bi-copter***

Chapter III engages in improving the UAV swashplate-less operation efficiency through aerial-ground locomotion. We start with reviewing the existing aerial-ground locomotion UAVs work, then elaborates on the system design, core components onboard, and implementation process of our aerial-ground locomotion bi-copter approach with our exemplary design known as the Gemini W. Besides, our iteration process using the topology optimization method has also been exploited.

Furthermore, the controller and the program logic that enables the air-ground transition are also presented. More specifically, the dynamic model of the Gemini W rolling on the ground will be presented, along with the condition that triggers the UAV to enter transition mode and rolling mode.

To validate the Gemini W system design, we present feasibility experiment validation during the aerial-ground transition and ground locomotion. Last but not least, to emphasize the benefit of ground locomotion, the power consumption analysis among different modes will also be discussed.

### ***Chapter IV - Hong Sun: swashplate based bi-copter***

To further enhance the agility of the bi-copter UAV by addressing the disadvan-



tage brought by servo motors, Chapter IV illustrates the whole process of our attempt to build the swashplate-based bi-copter we call Hong Sun.

Starting with the motivation, we first discussed the limitation of the servo-based approach proposed in previous chapters. Then we discussed the process of our design, from the propulsion system to the fuselage design.

During tests, severe vibration issues cause the propulsion system to disassemble itself, and the attempt is aborted for practical reasons and safety concerns. At the end of the chapter, we meticulously listed the limitations and issues with the current swashplate approach.

### ***Chapter V - Gemini II: swashplate-less bi-copter***

After the failed attempt with the swashplate-based bi-copter, Chapter V seeks the solution by adopting the swashplate-less cyclic blade pitch technique to replace the servo motors, and validates this technique by building a swashplate-less based bi-copter called Gemini II. Firstly, we summarize all the drawbacks of the servo-based and swashplate-based methods, and then we review the previous works that have been conducted relating to the swashplate-less design.

Secondly, we elucidate the Gemini II system architecture and mechanical design details, including the fuselage, avionics, and the swashplate-less mechanism. Since the swashplate-less mechanism is a relatively new concept, we will explain the working principle behind the mechanism and reveal our implementation details on how we resolved the issues existed in the previous swashplate-less mechanism, especially the vibration issue caused by the propulsion system, and other factors that affect the system stability.

Thirdly, we explicate the system models, controller, and mixers logic that is behind the Gemini II. The topology optimization method is adopted again for more durable, lighter-weight structures. The design process follows the topology optimization iteration method, and the design is verified with optimization software such as ANSYS.



In the end, we validate the system design through a series of experiments. To verify the feasibility and performance of the swashplate-less bi-copter design, we first test the actuators on a test bench. The actuator evaluations, including power consumption test, sinusoidal throttle test, and agility comparison against quad-copters and Gemini mini bi-copter actuator, were conducted. Using the well-tuned parameters, we identify the external force disturbance rejection model. Then we conduct two disturbance tests, along with a trajectory tracking experiment on Gemini II, proving the robustness of the controller and the performance of our novel bi-copter design.

### ***Chapter VI - Conclusion and future works***

Chapter VI concludes the thesis with the content summary and contribution highlights. Future works and other potentials will be discussed in the end.



# Chapter 2

## Gemini mini: Servo-based Bi-copter

### 2.1 Introduction

Quad-copters are the premier platform for data collection tasks, yet their ability to collect data in narrow indoor spaces is severely compromised due to their huge size when carrying heavy sensors. Compared with quad-copters, bi-copters are equipped with fewer rotors, making them have smaller sizes, lower costs, higher efficiency, and lower mechanical complexity [70]. In this chapter, we propose a bi-copter UAV configuration that has similar levels of versatility as that of the quad-copter and improves compactness or efficiency at the same time. Such an arrangement allows for the preservation of propeller size, meaning that we can effectively reduce the horizontal width of the UAV while still maintaining the same payload capacity. Furthermore, pitch, roll, and yaw control can also be achieved through mechanically simple means, increasing the UAV reliability and operation precision. We also theoretically prove that the bi-copter platform is a more power-efficient yet practical solution for indoor applications among twelve common UAV configurations. This chapter will detail the entire process of creating the platform, from picking the ideal propeller through aerodynamic analysis, system design, optimization, implementation, control, and real flight tests that demonstrate its ability to function seamlessly.

The design requirement for the Gemini mini is to be able to carry a 3D LiDAR



(380 g Ouster-16) and operate for more than 10 minutes flying time with a size smaller than human body width (with necessary safety clearance).

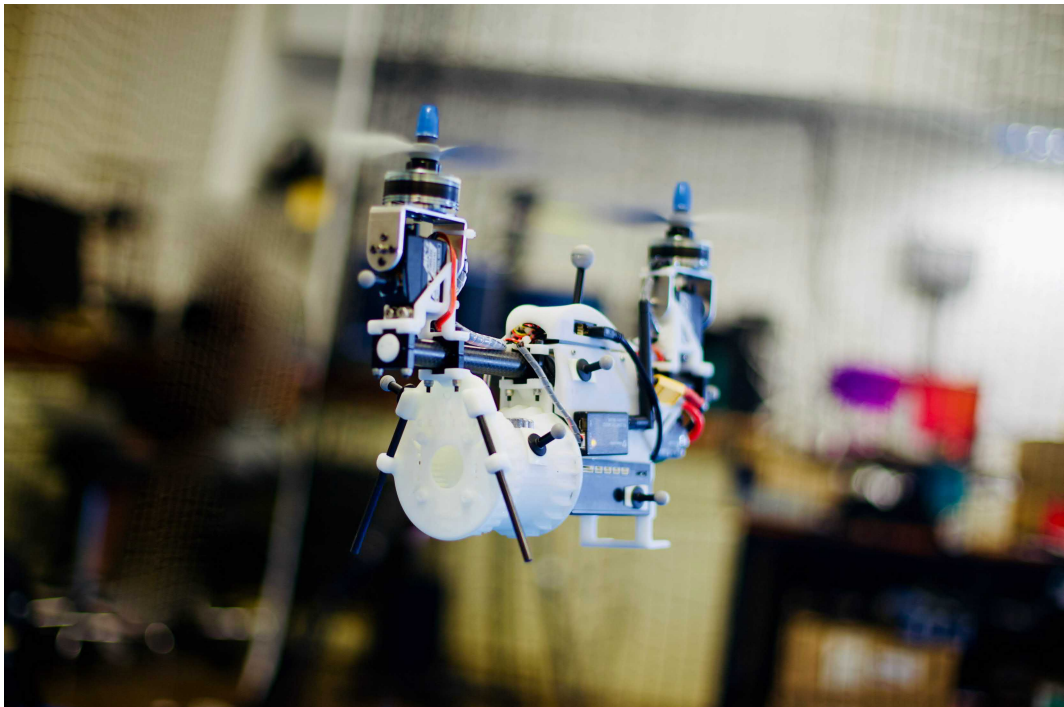


**Figure 2.1** The Gemini mini at hovering. The propeller size is 10 inches (25.4 cm), and the total system weights 1.8 Kg. It is capable of flying up to 13 minutes. Video available at: <https://youtu.be/i7n0wOHonMM>

**Figure 2.1** shows the Gemini mini at hovering. The Gemini mini has a compact size of propeller diameter, making it suitable for flying in congested indoor environments. It carries a 3D LiDAR sensor and a powerful on-board computer, which allows it to perform tasks like real-time 3D LiDAR mapping.

The contributions of this work are:

1. We conduct comprehensive aerodynamic analysis and show that the bi-copter UAV is a more power-efficient yet practical solution for indoor applications
2. We implement the concept of Gemini mini bi-copter UAV by systematically selecting its components (e.g., propeller, motors). The bi-copter prototype, known as Gemini, has a compact size (10 inches), high payload capacity (able to carry 0.4 Kg 3D LiDAR), and prolonged flight time (over 13 minutes).



3. We design a simple yet effective control system for Gemini mini bi-copter UAVs. The designed system is composed of cascaded PID controllers with accurate control mixing: the position loop, attitude loop, and angular rate loop all shows good tracking performance, and the disturbance rejection is fast and robust.
  
4. We demonstrate the Gemini mini system through real flight tests.

## 2.2 Working Principle

As shown in [Figure 2.2](#), we define the direction of moving (front direction) of the bi-copter to align with the positive roll axis and assume the center of gravity is located at the origin of the coordinate.

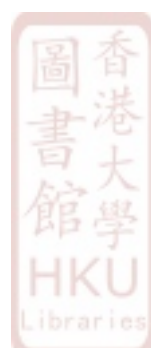
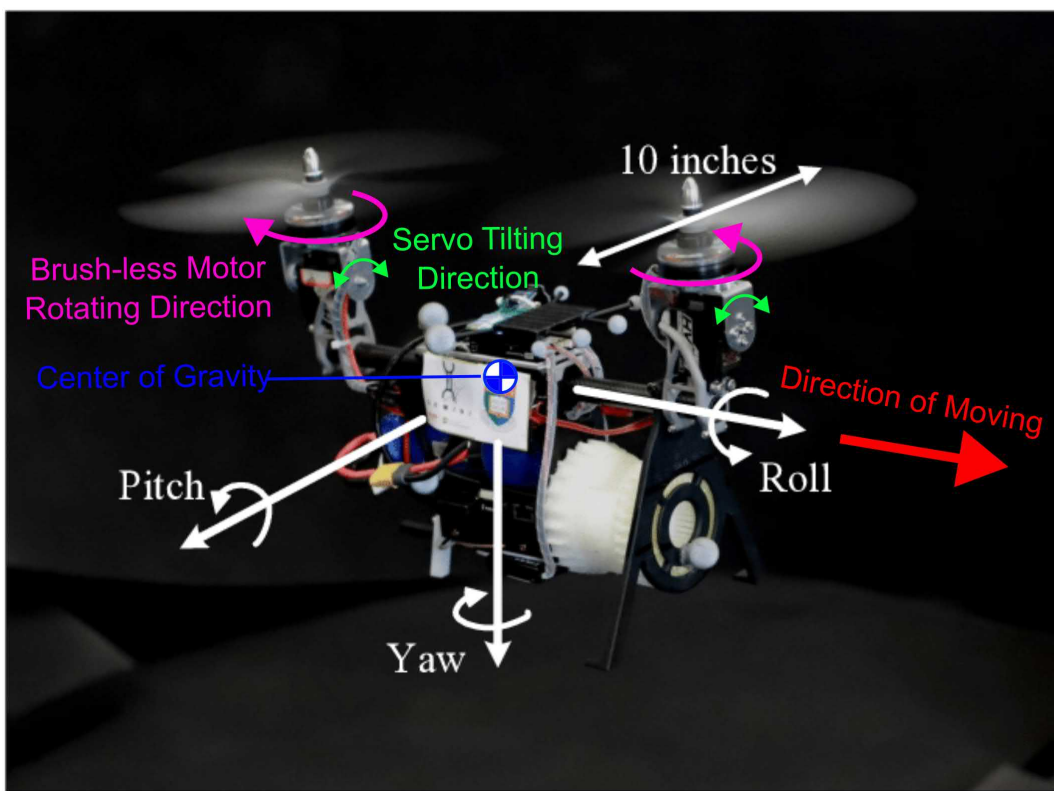


**Figure 2.2** Bi-copter working principle: The pitch is controlled by the differential thrust. Roll and yaw are controlled by tilting servo motors in the same and opposite directions, respectively. **Image Source:** [25]

The two propellers of a bi-copter UAV rotate in the opposite direction, generating vertical thrust while canceling out the torque with each other. When the front and back brush-less motor rotates at different speeds, the tilting of the pitch angle can be achieved through the differential thrust. The roll angle attitude can also be controlled by tilting the servo motors in the same direction. When the motors tilt in the same direction, the thrust generated by the two propellers will have a displacement from the center of gravity, generating torque in the roll direction. Similarly, when the tilting direction of the two servo motors is in different directions, the torque will be generated on the bi-copter along the yaw direction. Therefore, the bi-copter is able to control both its attitudes.

## 2.3 Literature Review

The concept of bi-copters with tilt-rotors is not new, besides a variety of large manned aircraft of the bi-copter configuration [71–75], a vast amount of prior work can be found on small scale bi-copters, especially on their modeling and control. Sanchez *et al.* [26] first developed a prototype of such a bi-copter UAV concept, called T-Phoenix (shown in Figure 2.3a), and demonstrated its hover flight with a nonlinear controller. Papachristos *et al.* [76], Hrečko *et al.* [27], and Zhang *et al.* [77] focus on the attitude control of a model of Bell Boeing V-22 Osprey, which has two tilt-rotors like Gemini but different moving direction (shown in Figure 2.3b). The position control in these works was not considered. Gonçalves *et al.* [78] presented a conceptual design of a similar bi-copter UAV, but with no actual prototype or test.

While these works are all based on bi-copter UAVs with tilt-rotors, Blouin *et al.* [28] proposed a UAV without any tilting mechanism (shown in Figure 2.4a). Due to the insufficient number of DOF in control, the UAV is not able to hover, which is essential for practical indoor applications. Siddhardha *et al.* [29] also presented a bi-copter UAV, which uses reaction wheels instead of servo motors to provide the roll and yaw torque (shown in Figure 2.4b). As claimed by the author, it is suitable for UAVs with a very small moment of inertia on the roll axis. However, the



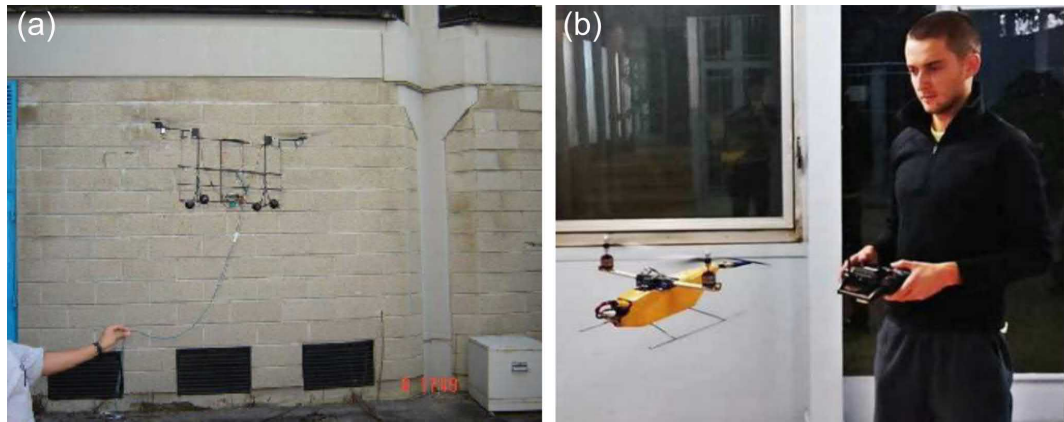


**Figure 2.3** Previous tilt-rotor bi-copters (a) T-Phoenix tilt-rotor bi-copter with a nonlinear controller; (b) Bi-copter that moves in different moving direction than Gemini mini. **Image Source:** [26, 27]

work did not supply neither actual test nor prototype of this design. Moreover, for actual bi-copter UAVs with payload, the moment of inertia on the roll axis is much more significant and the torque provided by the reaction wheel is far sufficient for satisfactory control performance.

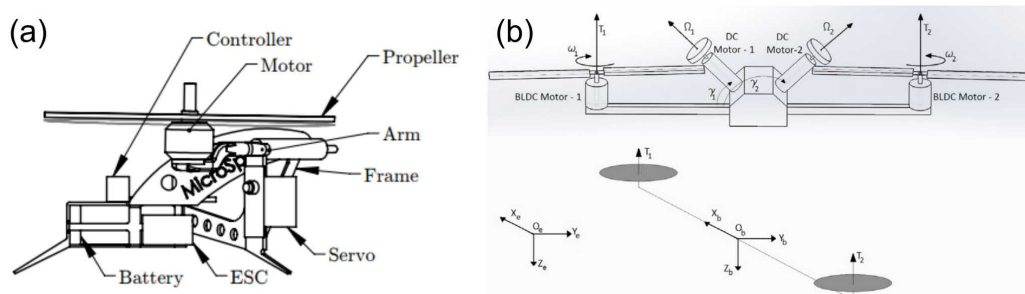


**Figure 2.4** Other previous bi-copters (a) Bi-copter without any tilting mechanism; (b) Bi-copter that uses reaction wheels to provide the roll and yaw torque **Image Source:** [28, 29].

## 2.4 Aerodynamic Analysis

This section analyzes the hovering efficiency of common UAVs. Starting from aerodynamical momentum theory, we determine the factors that affect UAV hovering efficiency. Afterward, we compare the theoretical hovering efficiency among the twelve common UAVs and illustrate the efficiency superiority of the bi-copter

platform when operating in the same effective size.

### 2.4.1 Momentum Theory

When the flow of air is axisymmetric, and the flow-through rotors are either upward or downward, the flow regime is easily predictable by mathematical models. However, accurate prediction of hovering performance is not straightforward, even with the help of modern mathematical models. The actual physical flow of motors includes a complicated vortical wake structure, but the basic performance of the rotor can be simplified with the Rankine-Froude momentum theory. The momentum theory provides a first-order mathematical model prediction of an ideal actuator's thrust and power [30].

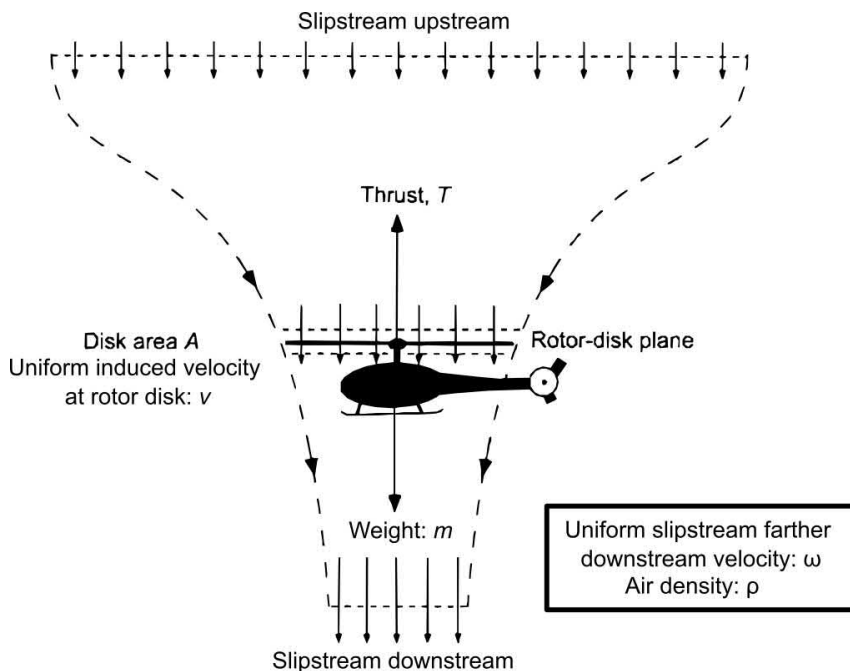


**Figure 2.5** The definitions of physical parameters in idea momentum theory.  
Image Source: edited figure based on [30]

Assume the air flow to be ideal (the airflow through the rotor is one-dimensional, quasi-steady, incompressible, and inviscid) with the density  $\rho$ . As shown in Figure 2.5, let the uniform induced velocity to be  $v$  at the rotor disk,  $m$  be the aircraft mass, and  $A$  (also known as disk area) be the area swept by the blades of a rotor, the mass flow rate  $\dot{m}$  of the air will be

$$\dot{m} = \rho A v \quad (2.1)$$

The mass flow rate  $\dot{m}$  shall be constant throughout the slipstream upstream and downstream of the disk due to the conservation of mass. When the UAV is hovering in place, the starting energy, momentum, and velocity are zero. According to the conservation of momentum, if the homogeneous slipstream far downstream has a velocity of  $\omega$ , the motor thrust  $T$  is equal to the rate of change of momentum:

$$T = \dot{m}\omega \quad (2.2)$$

By conservation of energy, the amount of energy change in the slipstream shall be equivalent to the work done by the rotor:

$$Tv = \frac{\dot{m}\omega^2}{2} \quad (2.3)$$

Substituting Eq. 2.2  $T$  into Eq. 2.3, we have:

$$v = \frac{\omega}{2} \quad (2.4)$$

With Eq. 2.1, Eq. 2.2 and Eq. 2.4, the thrust is equivalent to:

$$T = \dot{m}\omega = 2\dot{m}v = 2\rho Av^2 \quad (2.5)$$

The induced velocity is:

$$v = \sqrt{\frac{T}{2A\rho}} \quad (2.6)$$

Therefore the power required for hover is:



$$P = T v = T \cdot \sqrt{\frac{T}{2A\rho}} \quad (2.7)$$

In characterizing the efficiency of an aircraft lifted by propellers (e.g., helicopter), the hover efficiency,  $HE$ , and disk loading,  $DL$ , are commonly used. They are defined as

$$DL = \frac{m}{A} \quad (2.8)$$

$$HE = \frac{m}{P} \quad (2.9)$$

At hovering in place, the propeller thrust is equal to the gravity due to the conservation of mass, then, substituting Eq. 2.8 and Eq. 2.9 into Eq. 2.7 yields

$$HE = \frac{1}{g \cdot \sqrt{\frac{g}{2\rho} \cdot DL}} \quad (2.10)$$

Eq. 2.10 implies that the hover efficiency is inversely proportional to the square root of disk loading: a lower disk loading leads to higher efficiency. This theoretical prediction has also been confirmed with real-world examples [31].

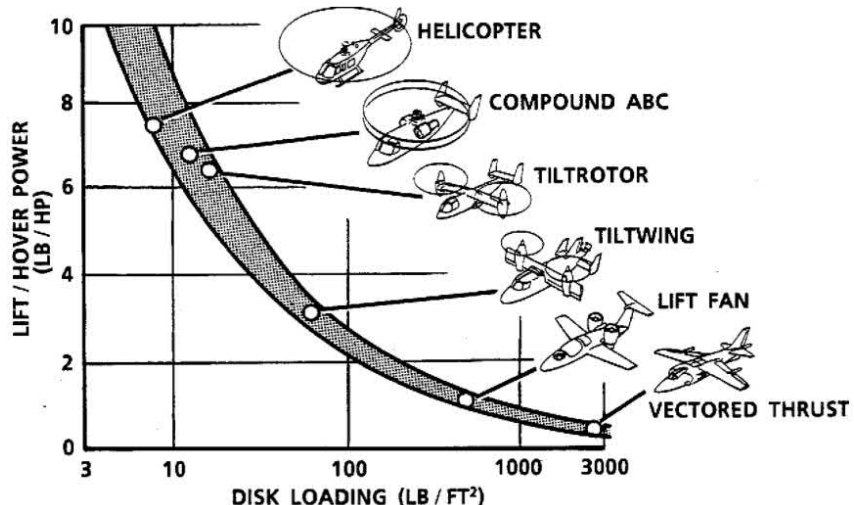


**Figure 2.6** The relationship between disk loading and hover efficiency: the hover efficiency is inversely proportional to the square root of disk loading. **Image Source:** [31]



### 2.4.2 Experiment Verification

The relation predicted by the momentum theory in Eq. 2.10 did not consider any of the ground effects as shown in [79]. Many of the key propeller parameters such as airfoil, blade pitch, twist, rotation speed, etc. are not modeled either. To verify this relation, we compare it to actual test data provided by the propeller manufacturers. In this paper, we restrict our attention to APC propellers due to the availability of its propeller data [80]. Figure 2.7 summarizes how the hover efficiency changes with the disk loading from the theoretical predictions by Eq. 2.10 (the black curve) and actual propeller data (marked as “x”).

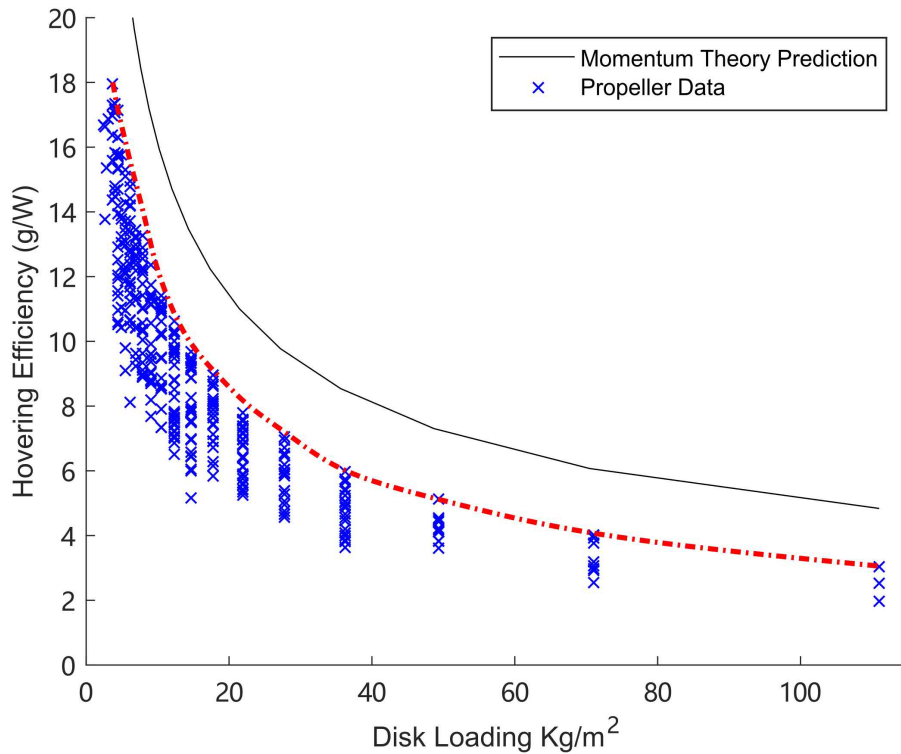


**Figure 2.7** Hover efficiency versus disk loading predicted by the momentum theory and from actual propeller data provided by APC propeller official website <https://www.apcprop.com/technical-information/performance-data/>. The red dash-dotted line remarks the upper envelope of the propeller data.

When plotting the data points for actual propeller data, we fix the propeller thrust to 0.9 Kg and compute the hover efficiency for all APC propellers. For propellers of



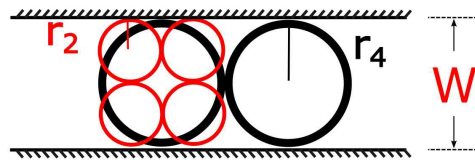


**Figure 2.8** The propeller radius of a bi-copter versus a quad-copter with the same effective size. The bi-copter configuration has a larger effective disk area than quad-copters, therefore higher hovering efficiency.

the same size, they have different power consumption (thus different hover efficiency) due to the variation in airfoils, twist, pitch angles, etc., but the same disk loading, forming a perfect column of data points as shown in [Figure 2.7](#).

From [Figure 2.7](#), we notice that the envelope comprised of the highest data point in each column forms a curve that is almost parallel to the theoretical predictions by [Eq. 2.10](#), meaning that the momentum theory can successfully predict the actual performance of a properly designed propeller, and provide a simple yet effective model for our subsequent efficiency analysis. A constant gap between the envelope and the theoretical predictions is observed due to the unmodeled propeller parameters (e.g., airfoil, blade pitch, and twist). Nevertheless, this constant gap does not change the relative efficiency among different propellers.

### 2.4.3 Efficiency Comparison

Based on the momentum theory explained and verified in the previous sections, we conduct a thorough comparison of our bi-copter against other possible UAV configurations. As an example, we analyze the power consumption of the Gemini mini bi-copter against a quad-copter with the same takeoff weight and effective size.

In this case, the thrust produced by each propeller for a bi-copter at hovering  $T_2$ , and that of a quad-copter  $T_4$  are related as

$$T_2 = 2 \cdot T_4 \quad (2.11)$$

Since the bi-copter moves along its longitudinal direction, the effective size of the whole UAV size is counted as one propeller diameter (as shown in [Figure 2.8](#)). Then with the same effective size, the propeller radius of a bi-copter,  $r_2$ , and a quad-copter,  $r_4$ , are related as

$$r_2 = 2 \cdot r_4 \quad (2.12)$$

Substituting (5) and (6) into (1), and noticing that the total power is the power of a single propeller time the number of propellers, we have

$$\frac{P_2}{P_4} = \frac{\sqrt{2}}{2} \approx 0.71 < 1 \quad (2.13)$$

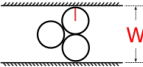
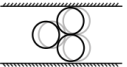
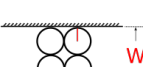
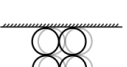
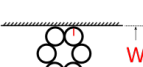
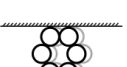
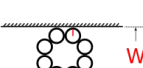
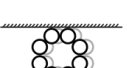
where  $P_2$  and  $P_4$  are the total power consumption of the bi-copter and the quad-copter configuration, respectively. [Eq. 2.13](#) implies that, with the same takeoff weight and UAV size, a bi-copter UAV consumes 30% less power than a quad-copter, theoretically. Or equivalently, with the same power consumption and takeoff weight, the bi-copter is 30% smaller than that of a quad-copter.

More generally, we extend this analysis to other common multi-rotor configurations, including helicopter (one-propeller), tri-copter, hexa-copter, and octo-copter, each with a single propeller and two co-axial propellers along each axis. The power consumption of all the multi-rotor configurations under the same size and take-off weight is summarized in [Figure 2.9](#), where all the power is normalized by the single propeller helicopter configuration.

For UAVs that have only one propeller on an axis, it is clear that bi-copter consumes the least power. When considering the two co-axial propellers option, the co-axial bi-copter achieves even less power consumption than our bi-copter. Unfortunately, such configuration is not practically implementable: the two co-axial propellers (and associated motors) are too chunky to be installed on the same servo motor without any mechanical interference.

The next optimal configurations among the co-axial option are the co-axial helicopter and co-axial quad-copters, which achieve the same efficiency as that of our bi-copter. However, since two co-axial propellers are usually less efficient than



Radius	Single Prop.	Power	Two co-axial Prop.	Power
$r=W/2$		1		0.7071
$r=W/2$		0.7071		0.5
$r=W/4$		1.1547		0.8165
$r=W/4$		1		0.7071
$r=W/(4*\sin(60^\circ)+2)$ $\approx 0.183W$		1.1154		0.7887
$r=W/(4+4*\sin(45^\circ))$ $\approx 0.146W$		1.2071		0.8536

**Figure 2.9** Efficiency comparison among multi-rotor UAVs (The Gemini mini's bi-copter configuration has the highest efficiency among the single propeller configurations, and it is also the most practical and mechanically simplest one among all configurations).

two individual propellers (like our bi-copter) because one propeller is operating in the downstream of another [81], the power efficiency of these two configurations is usually considerably lower than the theoretical prediction in [Figure 2.9](#).

Additionally, the co-axial helicopter has its propeller downstream being easily blocked by the payload and other mounting structures, and co-axial quad-copters suffer from various energy losses in motor and ESC due to the many propellers being used. Therefore, we conclude that the bi-copter is the most efficient configuration among these common UAV configurations under the same takeoff weight and size.

Finally, the hexa-copter and octo-copter configurations listed in [Figure 2.9](#) are not considered in practice for indoor applications, not just because more motors bring down the efficiency [34], but also the many propellers (and motors) bring too much weight and the size of each propeller needs to be impractically small to fit in the whole UAV size.



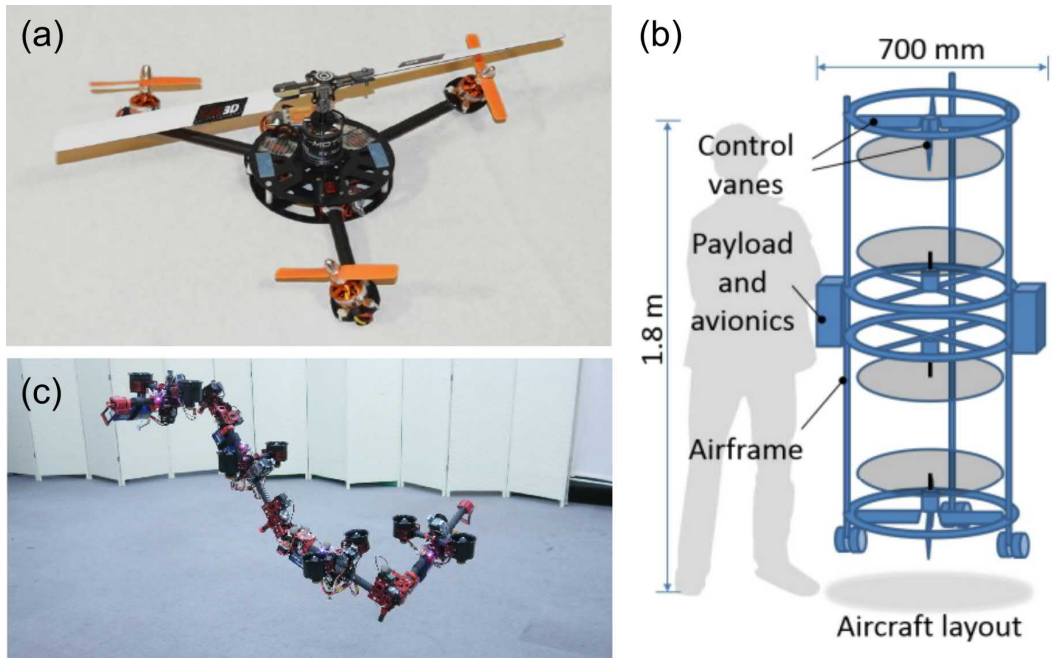


**Figure 2.10** Various other unconventional UAV configurations that are not practical for indoor applications (a) Triangular Quadrotor. (b) “Stackrotor” platform [32]. (c) Aerial robot dragon. **Image Source:** [33–35]

It is important to mention that, Figure 2.9 only summarizes the commonly seen UAV configurations. There are various other unconventional configurations, such as the Triangular Quadrotor (shown in Figure 2.10a) in [33], “Stackrotor” platform (shown in Figure 2.10b) in [32] and the aerial robot dragon (shown in Figure 2.10c) in [35]. Even with the chosen bi-copter configuration, one can always keep increasing its efficiency by adding more rotors on the servo motor. Nevertheless, the bi-copter UAV is the minimal implementation, which simplifies the mechanical design and increases the maneuverability in tight spaces like turning in sharp corners.

## 2.5 System Design, Optimization, and Implementation

This section details the design, optimization, and implementation of the bi-copter UAV concept proposed in the previous section. The framework of the Gemini mini UAV is mainly consists of three categories: the off-the-shelf avionics (marked in



black); the off-the-shelf air-frame parts (marked in magenta); and the designed parts (marked in blue). The detailed design process will be further illustrated in the following subsections.

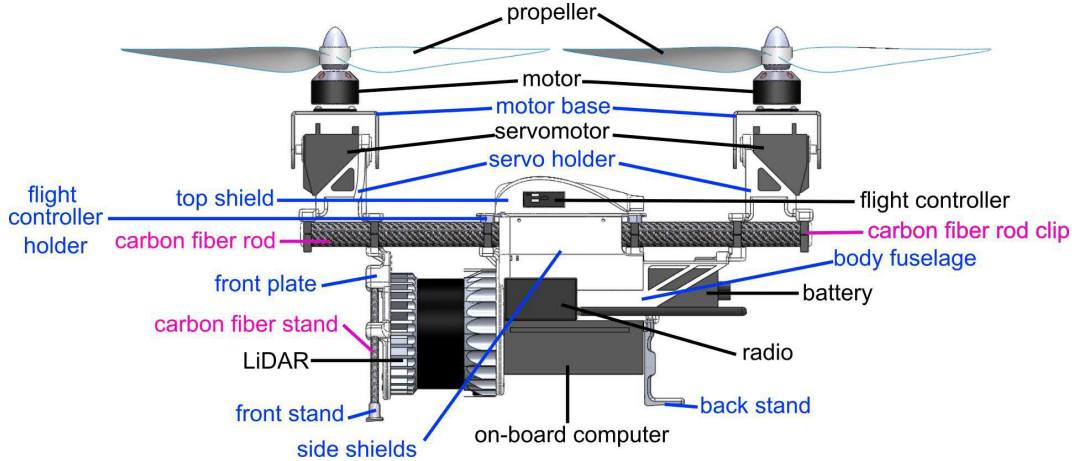


**Figure 2.11** Gemini mini framework: the off-the-shelf avionics (marked in black); the off-the-shelf air-frame parts (marked in magenta); and the designed parts (marked in blue).

### 2.5.1 Design Goal

First and foremost, the layout of the current design has a few goals. The first one is to protect the battery during crashing since it is explosive and may cause hazards during experiments. The second goal is to protect the LiDAR during crashing because it is the most expensive device on-board. The third goal is to make sure that the center of gravity is located at the center of the carbon fiber rod so that the two propulsion systems can generate the minimum amount of thrust difference during hovering and extend the pitch control bandwidth. The fourth goal is to place the flight controller as close to the center of gravity as possible, maximizing control performance. The last goal is to make the bi-copter modularized so that single part wreckage or wearing will only need replacing that specific part. To be more specific, the back stand, front stand, side shields, and top shields are all easily replaceable.

At first, we list out all the crucial avionics, and then we model all the components in the computer-aided design software such as Dassault Systèmes Solidworks for



effective and efficient layout planning.

## 2.5.2 Avionics

We use Pixhawk 4 mini as the flight controller hardware, but replaced the key controller software including the mixer (see section IV). A DJI Manifold 2 on-board computer is used to receive position feedback from motion capture systems and send this position feedback to the flight controller for position control. This on-board computer will also be used to process the LiDAR data and camera images to enable autonomous indoor operation in the future. The CUAV on-board radio provides real time altitude flight data to the ground station, and is working at 900 MHz. We use a 4S 5000 mAh battery, Dualsky 30 C. Its high C rating allows a large current to be drained, as is the case of Gemini. Considering the 25 W of power consumption from other electronics such as on-board computer, the estimated flight time is 15 minutes.

### 2.5.2.1 Propulsion System

According to the momentum theory, the bigger size of the propeller means higher efficiency, but also restricts the maneuverability of the UAV due to size increment. To enable the UAV to operate in congested indoor environments with narrow doors, windows, and other unstructured spaces, we restrict the UAV size (i.e., the propeller diameter) below 10 inches. [Figure 2.12](#) shows the power consumption for all APC propellers when providing 0.9 Kg thrust. The data are drawn from the manufacturer [80]. It is seen that the APC10x45MR achieves the smallest power consumption. We also considered three-blades propellers in choosing the propeller. As shown in [Figure 2.12](#), three-blade propellers provide large thrusts with very small sizes (i.e., below 5 inches). However, when the propeller size increases, they are less efficient than two-blade propellers [81].

We use a T-Motor MT3506 650KV brush-less motor after a few trial tests. [Figure 2.13](#) shows the static thrust with the chosen motor and propeller. It is seen



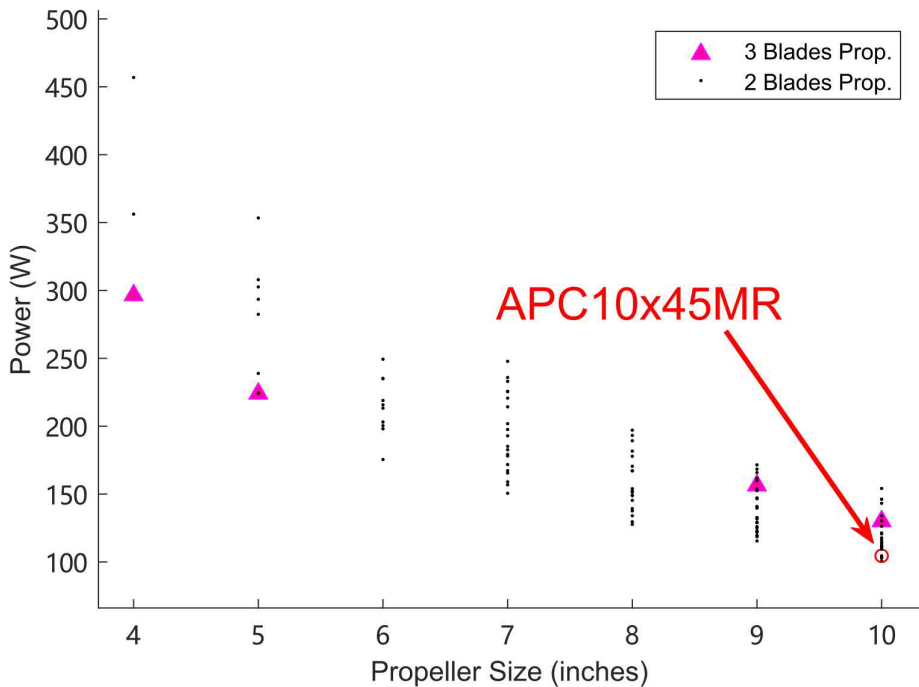


**Figure 2.12** Power consumption of all APC propellers below 10 inches. The propeller loading constraint is 0.9 Kg. The APC10x45MR achieves the highest power efficiency and thus is chosen.

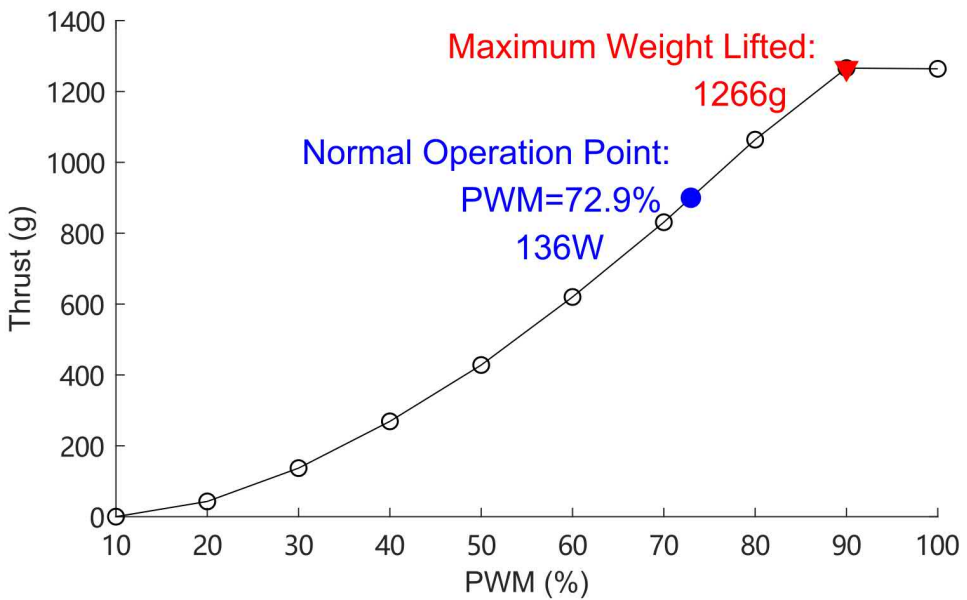


**Figure 2.13** The static thrust of the chosen propulsion system at different PWM inputs. Each actuator is capable of generating 1266g thrust, and the hover duty will be around 73% throttle.



that by providing a maximal thrust of up to 1.25 Kg per propeller, the hover duty is 73%, leaving a sufficient margin for maneuvering. The power consumption at hovering is  $2 \times 136 = 272$  W. To show the effectiveness of the bi-copter, we make a trivial comparison to a quad-copter with well-designed propellers such as DJI snail 5048S propellers [82]. This propeller has a 5 inches diameter and leads to the same size if four are used. Reading data from [82], we obtain that a single DJI snail 5048S propeller consumes 142 W when providing 0.45 Kg thrust. As a consequence, the quad-copter will consume 568 W, more than twice of a bi-copter.

For the fast response of the Gemini, a servo motor with a short response time is necessary. We chose the MKS HV1220, which has 0.115 seconds of response time and allows a higher control bandwidth. The titanium gearbox inside the motor also prevents malfunctioning from violent shocks. It is also able to overcome the Coriolis torque caused by propeller rotation by providing a torque up to 23 Kg\*cm.

### 2.5.3 Layout

After the settlement of avionics lists, we modeled them in CAD and arranged them in the following layout according to our design goals. The main engineering decisions a to d are marked inside of the red boxes in [Figure 2.14](#).

Decision a is related to the length of the aircraft. The blade length is 10 inches wide, so we left 1.5 inch gap for the possibility to extend propeller size in order to adapt to heavier load or the demands for trading off the size for higher efficiency.

Decision b is about the motor base. Due to the limitation of the available servo motor choices on the market, we have not found any servo motors with two servo hinges. Therefore, we customized the servo holder and motor base and designed a secondary connection hinge in order to maintain a strong connection between the brush-less motor and servo motor and counter the potential wreckage upon crashes. More details will be illustrated in the next subsection.

Decision c is the placement of the flight controller. The flight controller is placed



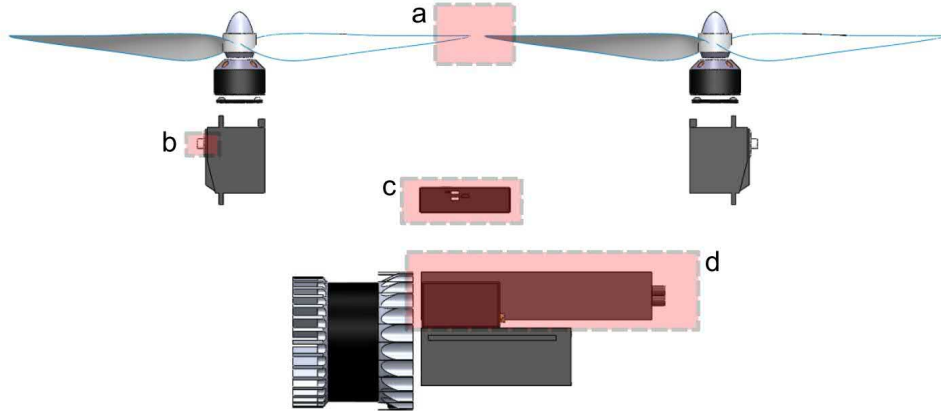
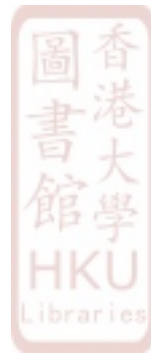


**Figure 2.14** Gemini mini fixed avionics layout (actuators, LiDAR, flight controller, on-board computer, battery, and radio station). The critical design decisions mentioned in the text are marked in red squared boxes.

at the center of the vehicle. Due to the mechanical nature of the px4 flight controller inertial measurement unit (IMU), the closer it has been placed to the center of the vehicle, the IMU will produce a better estimate.

The battery is placed at the specified location in decision d, but not the very bottom. This decision is to ensure that the battery will not collide with any sharp surfaces and trigger an explosion upon crash. Meanwhile, lowering the heavy part will lower the center of gravity. The weight distribution chart of specific components is shown in [Figure 2.15](#). As shown in the weight distribution chart, the battery, LiDAR, and the on-board computer take the majority of the total weight. The longer the distance the center of gravity is from the actuator, the higher the UAV roll and yaw control authority will be gained. The working principle of such will be further illustrated in the control section.

In the current exemplary design, the payload is a 16-line LiDAR (Ouster-16, weighing 380 grams) for indoor mapping uses. At the size of only 10 inches (25.4 cm), the rated UAV takeoff weight is up to 1.8 Kg and flies more than 13 minutes with a Dualsky 5000 mAH 4s battery.



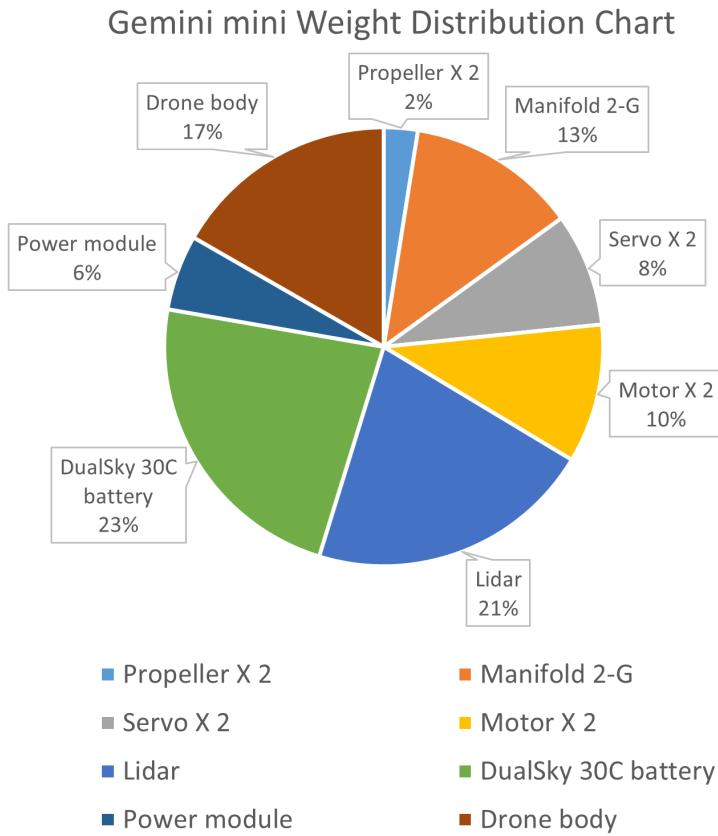


**Figure 2.15** Gemini mini weight distribution chart.

#### 2.5.4 Designed Parts

The designed parts include 3D printed the main air-frame and CNC bent metal motor base. The 3D-printed main air-frame serves the purpose of holding all the parts and also covering up and protecting the wires and avionics. Note that a bearing is embedded inside the servo holder and provides a secondary connection hinge (as shown in [Figure 2.16](#), the servo hinge is marked in blue, while the secondary connection hinge is marked in red) for the motor base and the servo motor, reinforcing the connection strength while minimizing the metal bent caused by stress. The bent metal part in [Figure 2.16](#) is a 5 mm aluminum plate cut with a CNC machine, and bended to fit the width of the two connection hinges.

After the parts arrive, we validate the assembling and do iterations through trial and error. The process repeats until all the mechanical issues are resolved. Everything



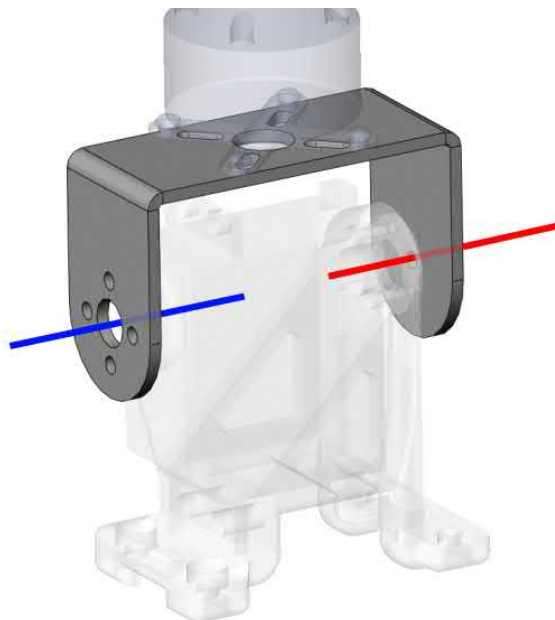


**Figure 2.16** Gemini mini motor base with secondary hinge (marked in red) for strengthening.

else besides the designed parts is all off-the-shelf commercial products, such as the battery, propellers, motors, servo motor, on-board computer, and exemplary LiDAR payload. The side-by-side comparison between the CAD model and the final assembled Gemini mini is shown in [Figure 2.17](#). [Table 2.1](#) summarizes the Gemini mini design specifications.

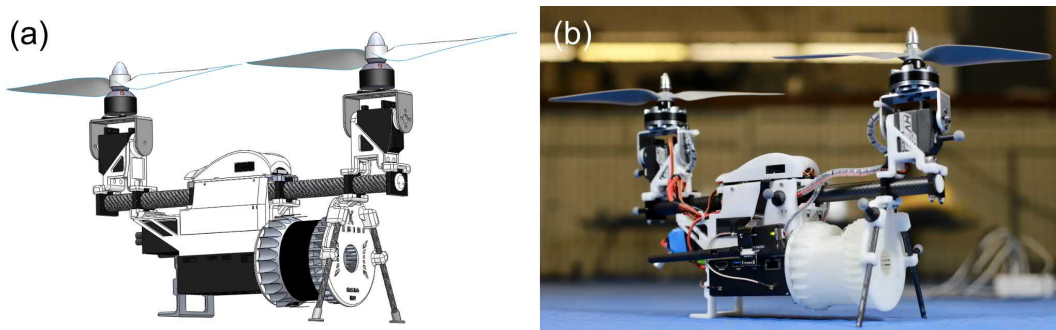


**Figure 2.17** Gemini mini designed model versus actual aircraft side-by-side comparison **(a)** The Gemini mini CAD model; **(b)** The final assembled Gemini mini.

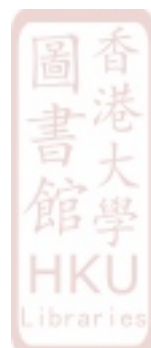


**Table 2.1** The Gemini mini's Specifications

Width	Power	Takeoff Weight	Flight Time (estimated)
25.4 cm	297 W	1.8 Kg	15 min

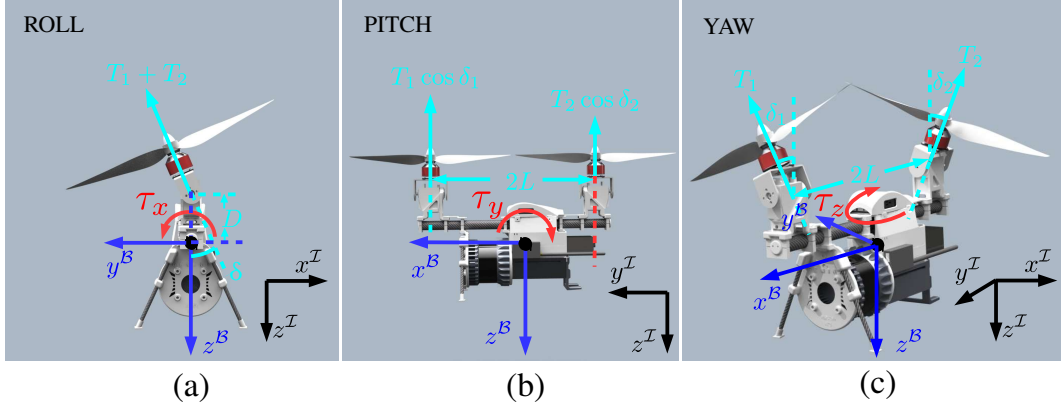


**Figure 2.18** Gemini mini dynamics **(a)** The generation of roll control moment  $\tau_x$ :  $\tau_x = T_1 D \sin \delta_1 + T_2 D \sin \delta_2$  ( $\delta = \delta_1 = \delta_2$  in this circumstance); **(b)** The generation of pitch control moment  $\tau_y$ :  $\tau_y = (T_1 \cos \delta_1 - T_2 \cos \delta_2)L$ ; **(c)** The generation of yaw control moment  $\tau_z$ :  $\tau_z = (T_1 \sin \delta_1 - T_2 \sin \delta_2)L$ .

## 2.6 Control

### 2.6.1 Dynamics

Figure 2.18 shows the definition of the inertial frame ( $x^T y^T z^T$ ) and body frame ( $x^B y^B z^B$ )<sup>1</sup>. The inertial frame is in the convention of North-East-Down (NED). The UAV dynamics follow a standard rigid-motion:

$$\begin{bmatrix} mI & 0 \\ 0 & J^B \end{bmatrix} \begin{bmatrix} \dot{\mathbf{v}}^T \\ \dot{\boldsymbol{\omega}}^B \end{bmatrix} + \begin{bmatrix} 0 \\ \hat{\boldsymbol{\omega}}^B J^B \boldsymbol{\omega}^B \end{bmatrix} = \begin{bmatrix} \mathbf{f}_g \\ 0 \end{bmatrix} + \begin{bmatrix} R f_T^B \\ \boldsymbol{\tau}^B \end{bmatrix} + \begin{bmatrix} \mathbf{f}_{dist} \\ \boldsymbol{\tau}_{dist} \end{bmatrix} \quad (2.14a)$$



$$\mathbf{R} = \mathbf{R}_z(\eta) \mathbf{R}_y(\theta) \mathbf{R}_x(\varphi) \quad (2.14b)$$

<sup>1</sup>Throughout the text the superscript  $T$  and  $B$  will be used to denote the inertial and body frame, respectively.

where  $m$ ,  $\mathbf{I}$ , and  $\mathbf{J}^{\mathcal{B}}$  stand for the mass, the identity matrix in  $\mathbb{R}^{3 \times 3}$  and the inertia matrix,  $\boldsymbol{\omega}^{\mathcal{B}}$  is the angular velocity vector represented in the body frame while  $\hat{\boldsymbol{\omega}}^{\mathcal{B}}$  is the skew-symmetric cross product matrix of  $\boldsymbol{\omega}^{\mathcal{B}}$ ,  $\mathbf{v}^{\mathcal{I}}$  is the velocity vector represented in the inertial frame,  $\mathbf{f}_g = [0 \ 0 \ mg]^T$  stands for the gravity in the inertial frame,  $\mathbf{R}$  is the rotation matrix from the inertial frame to the body frame following the Z-Y-X Tait-Bryan order where  $\eta$ ,  $\theta$ , and  $\varphi$  stand for the yaw, pitch, and roll Euler angle, respectively,  $\boldsymbol{\tau}^{\mathcal{B}} = [\tau_x \ \tau_y \ \tau_z]^T$  is the moment vector produced by rotors in body frame, where  $\tau_x$ ,  $\tau_y$ ,  $\tau_z$  are detailed in [Figure 2.18](#), the force vector is  $\mathbf{f}_T^{\mathcal{B}} = [0 \ 0 \ T]^T$ , where  $T = T_1 \cos \delta_1 + T_2 \cos \delta_2$ . The external force and torque disturbances are represented by  $\mathbf{f}_{dist}$  and  $\boldsymbol{\tau}_{dist}$  respectively.

It should be noted that there are three simplifications in the above modeling process. (1) The reactive torque of servo motor, which comes from the angular acceleration of its rotor, is not modeled because the rotor inertia is quite small when compared to the whole aircraft. (2) The propeller torque is also ignored in  $\boldsymbol{\tau}^{\mathcal{B}}$  as it is usually small when compared to the torque caused by thrusts. (3) In the calculation for the force vector  $\mathbf{f}_T^{\mathcal{B}}$ , the thrust projected to the y-axis of the body frame during the tilt of the two servo motors is neglected. This force is only present in the transient response of roll rotation and is zero when the roll angle converges to the desired value. The neglected torque and force will bring additional dynamics to the UAV rotation and translation and require careful modeling [26]. In this paper, we focus on designing the baseline controller that aims to stabilize the overall system. For this purpose, the three simplifications are valid, as shown in the actual experiments.

## 2.6.2 Control System

The whole control structure of Gemini mini is shown in [Figure 2.19](#). The navigation module produces the target position  $\mathbf{p}_d$  and yaw angle  $\psi_d$  for the position controller to track. The position controller will generate the desired attitude  $\mathbf{R}_d$  and body-Z axis force  $T_d$ . The attitude controller will calculate the desired moment  $\boldsymbol{\tau}_d^{\mathcal{B}}$  based on the desired attitude. And finally, the mixer will calculate the motor thrust commands and servo angle commands based on the  $\boldsymbol{\tau}_d^{\mathcal{B}}$  and  $T_d$ .



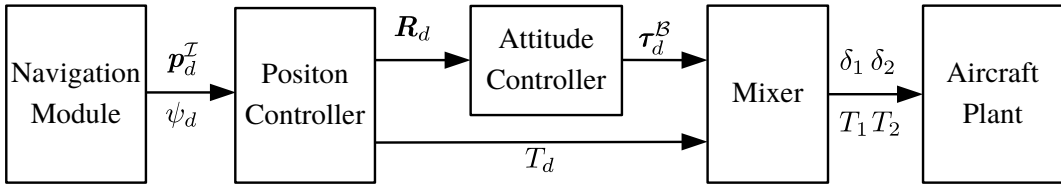


**Figure 2.19** The proposed controller structure.

### 2.6.2.1 Position Controller

The position controller of Gemini mini is a cascaded controller with proportional gain  $K^P$ . It calculates the desired velocity  $\mathbf{v}_d^T$  as follows:

$$\mathbf{v}_d^T = K^P \cdot \mathbf{p}_e^T = K_p \cdot (\mathbf{p}_d^T - \mathbf{p}^T) \quad (2.15)$$

where  $\mathbf{p}_e^T$ ,  $\mathbf{p}_d^T$  and  $\mathbf{p}^T$  are the position error, desired position, and current position, respectively. The inner velocity loop will calculate the desired acceleration  $\mathbf{a}_d^T$  through a PID controller:

$$\mathbf{v}_e^T = \mathbf{v}_d^T - \mathbf{v}^T \quad (2.16a)$$

$$\mathbf{a}_d^T = K_p^v \cdot \mathbf{v}_e^T + K_i^v \cdot \int \mathbf{v}_e^T + K_d^v \cdot \dot{\mathbf{v}}_e^T \quad (2.16b)$$

where  $\mathbf{v}_e^T$  and  $\mathbf{v}^T$  are the velocity error and current velocity, respectively,  $K_p^v$ ,  $K_i^v$  and  $K_d^v$  are the gains of PID terms. Note that the integral action undertakes the obligation of suppressing the force disturbance  $\mathbf{f}_{dist}$  previously mentioned in Eq. 2.14a. The desired attitude  $\mathbf{R}_d$  and force  $\mathbf{f}_{Td}^B = [0 \ 0 \ T_d]^T$  can be uniquely solved from the below equation following the method in [83]:

$$m\mathbf{a}_d^T = \mathbf{f}_g + \mathbf{R}_d \mathbf{f}_{Td}^B \quad (2.17)$$

### 2.6.2.2 Attitude Controller



The attitude controller is also a cascaded controller. The outer loop (i.e., angular loop) is a proportional controller to track the desired attitude  $\mathbf{R}_d$ . The quaternion ( $\mathbf{q} = [\eta, \boldsymbol{\epsilon}]$ ) is used to represent the attitude, where  $\boldsymbol{\epsilon}$  and  $\eta$  denote the vector and scalar part of the quaternion, respectively. With the quaternion representation, the attitude error  $\mathbf{q}_e$  and desired angular velocity  $\boldsymbol{\omega}_d^B$  are calculated based on the “Quaternion linear” method in [84]:

$$\mathbf{q}_e = \mathbf{q}_d^* \otimes \mathbf{q} = \begin{bmatrix} \eta_e & \boldsymbol{\epsilon}_e^T \end{bmatrix}^T \quad (2.18a)$$

$$\varphi = 2 \cdot \text{atan2}(\|\boldsymbol{\epsilon}_e\|, \eta_e) \quad (2.18b)$$

$$\boldsymbol{\omega}_d^B = K^a \cdot \boldsymbol{\xi}_e^B = K^a \cdot \text{sign}(\eta_e) \frac{\varphi}{\sin(\frac{\varphi}{2})} \boldsymbol{\epsilon} \quad (2.18c)$$

where  $\mathbf{q}_d$ ,  $\mathbf{q}$  are the desired and actual attitude;  $K^a$  is the gain from attitude error  $\boldsymbol{\xi}_e^B$  to desired angular velocity  $\boldsymbol{\omega}_d^B$ . The inner loop (i.e., angular rate loop) is a PID controller Eq. 5.13 to track the desired angular velocity  $\boldsymbol{\omega}_d^B$ :

$$\boldsymbol{\omega}_e^B = \boldsymbol{\omega}_d^B - \boldsymbol{\omega}^B \quad (2.19a)$$

$$\boldsymbol{\tau}_d^B = K_p^r \cdot \boldsymbol{\omega}_e^B + K_i^r \cdot \int \boldsymbol{\omega}_e^B + K_d^r \cdot \dot{\boldsymbol{\omega}}_e^B \quad (2.19b)$$

where  $\boldsymbol{\omega}_e^B$  and  $\boldsymbol{\omega}^B$  are the angular velocity error and current angular velocity, respectively.  $K_p^r$ ,  $K_i^r$  and  $K_d^r$  are the gains of PID terms. Note that the integral action undertakes the obligation of suppressing the torque disturbance  $\boldsymbol{\tau}_{dist}$  previously mentioned in Eq. 2.14a. The output of the inner loop is the desired moment  $\boldsymbol{\tau}_d^B = [\tau_{xd} \ \tau_{yd} \ \tau_{zd}]^T$ .

### 2.6.2.3 Mixer

As shown in Figure 2.18, the relationship between moments ( $\tau_x$ ,  $\tau_y$ ,  $\tau_z$ ), body-Z



force  $T$  and actuator output ( $\delta_1, \delta_2, T_1, T_2$ ) is as below:

$$\begin{bmatrix} 0 & 1 & 0 & 1 \\ D & 0 & D & 0 \\ 0 & L & 0 & -L \\ L & 0 & -L & 0 \end{bmatrix} \begin{bmatrix} T_1 \sin \delta_1 \\ T_1 \cos \delta_1 \\ T_2 \sin \delta_2 \\ T_2 \cos \delta_2 \end{bmatrix} = \begin{bmatrix} T \\ \tau_x \\ \tau_y \\ \tau_z \end{bmatrix} \quad (2.20)$$

Given desired moments  $\boldsymbol{\tau}_d^B = [\tau_{xd} \ \tau_{yd} \ \tau_{zd}]^T$  and desired body-Z force  $T_d$ , the actuator outputs  $\delta_1, \delta_2$  and motor thrust outputs  $T_1, T_2$  can be solved from Eq. 5.7 as:

$$\delta_1 = \text{atan} \left( \frac{L \cdot \tau_{xd} + D \cdot \tau_{zd}}{D \cdot L \cdot T_d + D \cdot \tau_{yd}} \right) \quad (2.21a)$$

$$\delta_2 = \text{atan} \left( \frac{L \cdot \tau_{xd} - D \cdot \tau_{zd}}{D \cdot L \cdot T_d - D \cdot \tau_{yd}} \right) \quad (2.21b)$$

$$T_1 = \frac{1}{2} \sqrt{\left( \frac{\tau_{xd}}{D} + \frac{\tau_{zd}}{L} \right)^2 + \left( T_d + \frac{\tau_{yd}}{L} \right)^2} \quad (2.21c)$$

$$T_2 = \frac{1}{2} \sqrt{\left( \frac{\tau_{xd}}{D} - \frac{\tau_{zd}}{L} \right)^2 + \left( T_d - \frac{\tau_{yd}}{L} \right)^2} \quad (2.21d)$$

## 2.7 Experiment Results

To validate the performance of the Gemini, a hovering flight with a disturbance test and a flying through a 40 cm gap test were conducted. This section presents the experiment results obtained with our design and proposed controller.

### 2.7.1 Hovering Flight

Figure 2.20 shows that the actual power consumption is around 335 W, which is 12.8% higher than our prediction of 297 W. The error is due to the downwash purling induced by the UAV body. With this power consumption, the estimated hovering time is 13.3 minutes with the 5000 mAh battery. The actual hovering time also depends on the battery discharging capabilities, the optimization of which is beyond



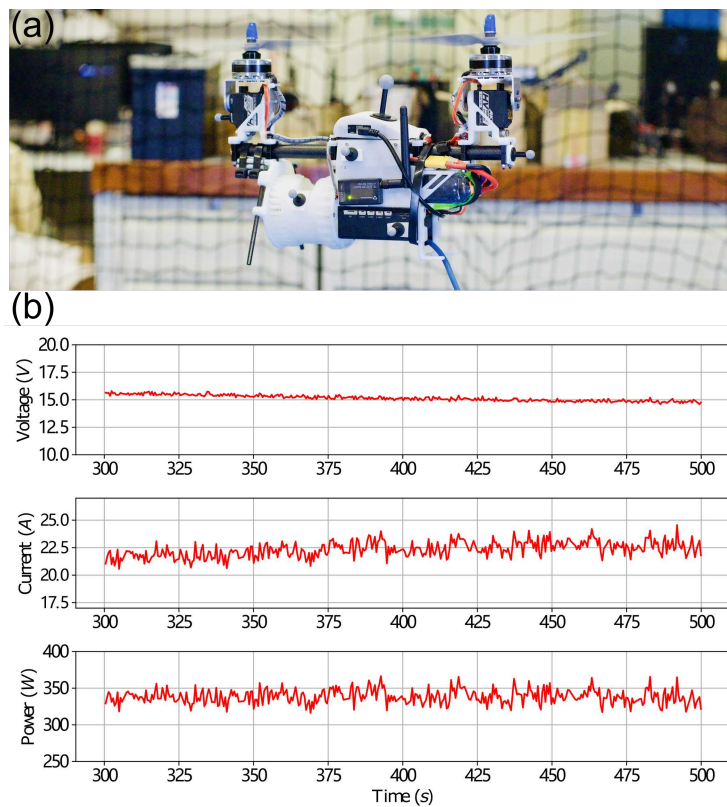


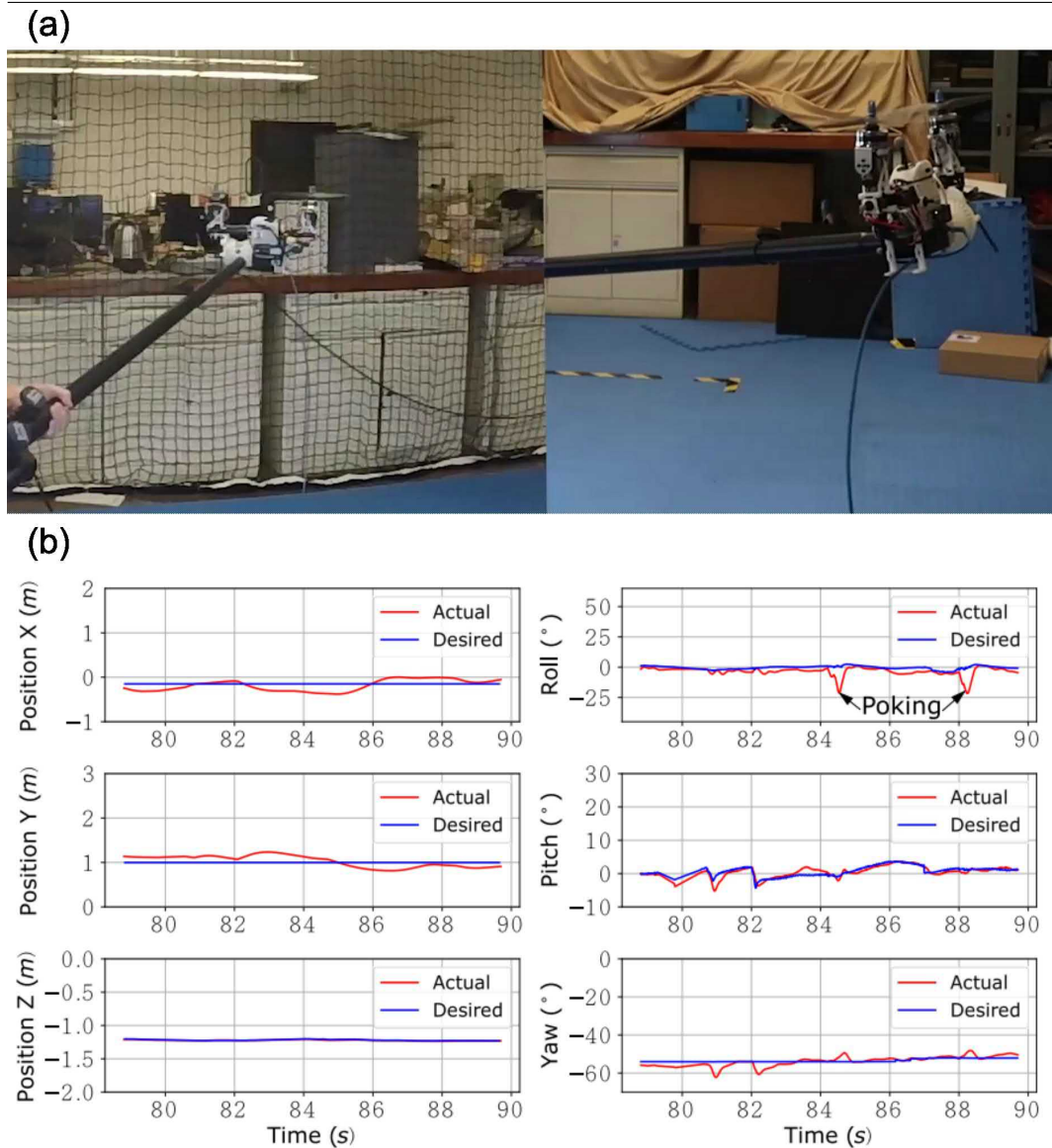
**Figure 2.20** (a) Gemini mini hovering flight; (b) The voltage, current, and power consumption data during the hovering flight.

the scope of this paper.

Figure 2.21 shows that the position control is robust to external disturbances. As shown in Figure 2.21a, two firm pokes were made on the Gemini mini roll direction while hovering. In the roll position graph from Figure 2.21b it can be seen that two peaks appear between 84s to 90s, and Gemini mini recovered within half a second and robustly suppressed the disturbances.

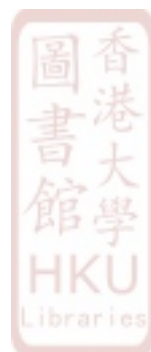
Figure 2.22 explicitly shows the detailed angular rate data and mixer output during a single poke. From Figure 2.22(a) to (c), we can see that from 84.5s to 84.6s, the actual angular rates all breach the desired command. Thus, the poke injected disturbances in all three angular directions, especially on roll rate at  $-2 \text{ m/s}^2$ . As the error between the desired roll rate and actual roll rate accumulates, the integrator in the inner control loop increases the roll command value and is mapped onto the mixer output. As shown in Figure 2.22d, the output of two brushless motors and servo motors is exhibited. The command for brush-less motors ranges from 0 to 2000, and





**Figure 2.21** Gemini mini poking test (a) Applying poking disturbances while Gemini mini is hovering; (b)The position and attitude data during the hovering flight.

a higher value will generate greater thrusts. The command for servo motors ranges from 1000 to 2000. Due to servo motor gear plate installation, the middle point of each servo motor (brush-less motor facing vertically up) has different offset values and requires calibrations before each flight (In this case, the middle point is around 1250 for both servo motors). Because of the two servo motors' physical installation angles, the same command will make the servo motor tilt in different directions. When a negative roll rate disturbance is detected, the desired roll rate command goes up, and two servo motors tilt to the corresponding positive roll direction (the front servo motor decreases the command value while the rear servo motor increases



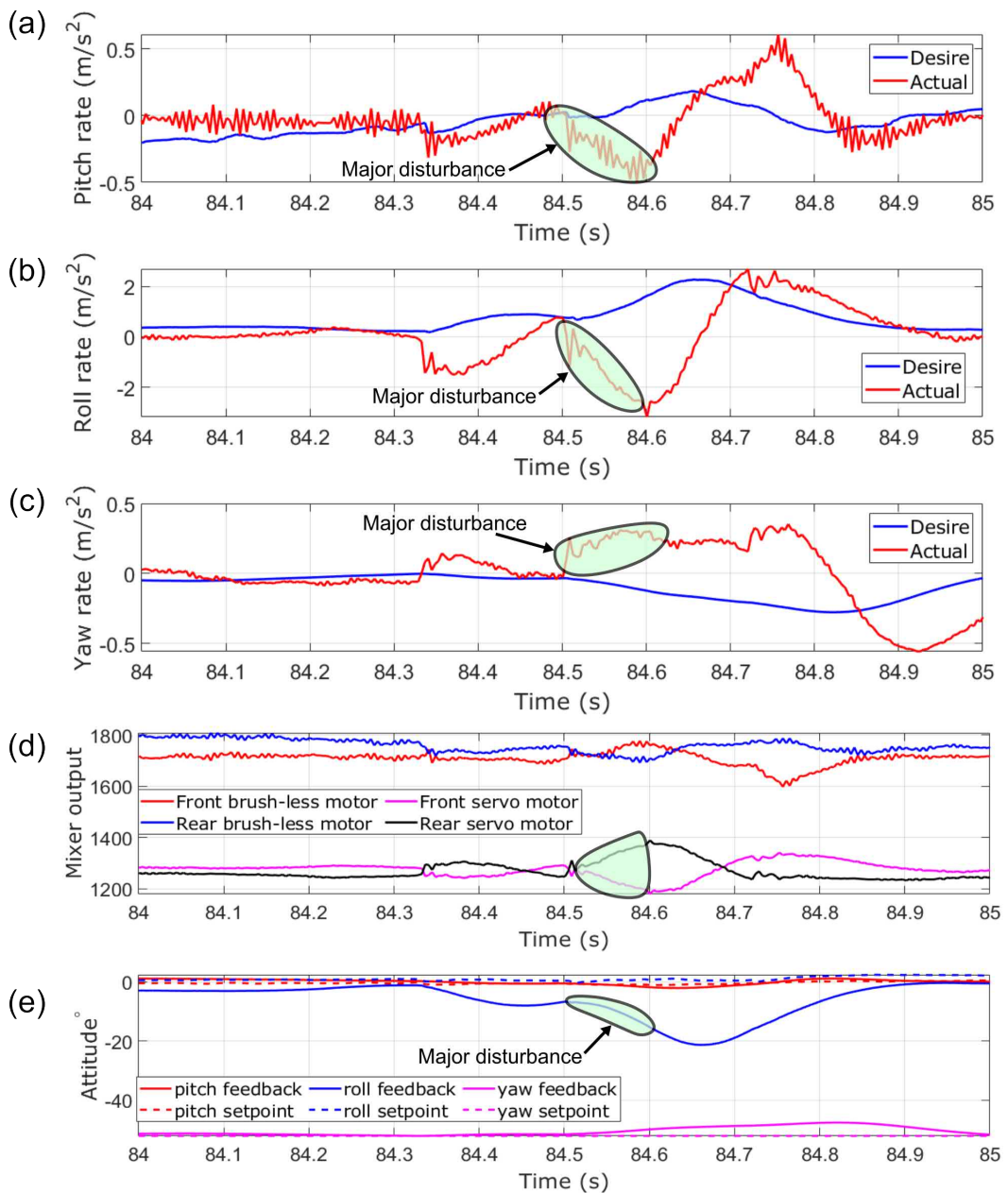


**Figure 2.22** Gemini mini angular rate and mixer output during a single poking test **(a)** Pitch angular rate; **(b)** Roll angular rate; **(c)** Yaw angular rate; **(d)** Mixer output of brush-less motors and servo motors (because of the two servo motors' physical installation angles, servo motor tilt in same directions when command are the opposite); **(e)** Attitude response closeup.



the command value). As a result, the actuator generates enough thrust on the roll direction, which is enough to counteract the disturbance and return the attitude back to the setpoint as shown in [Figure 2.22e](#).

The success of this experiment marks the validity of the controller design and the control logic for the actuators. The successful suppression of disturbance demonstrated the robustness of the controller.

### 2.7.2 Flying Through a 40 cm Gap

To validate the preciseness and the stability of the Gemini, we challenged it to fly through a gap with a full payload. As shown in [Figure 2.23a](#), two tall tripods are put together with a 40 cm distance, and a motion capture system is used to give position feedback to the Gemini. The test process is to let the UAV hover in front of the two poles and accelerate in the  $x$  direction. The success of this experiment marks its ability to perform tasks in narrow spaces with no previous adaptations.

[Figure 2.23b](#) shows the flight data when crossing the gap. The Gemini mini accelerated toward the  $x$  direction for 1 meter, while the other direction stays constant. The success of this challenge demonstrates the maneuverability of the Gemini.

## 2.8 Discussion and Conclusion

This chapter presents the design, analysis, implementation, and control of a bi-copter UAV. As demonstrated by flight experiments, the bi-copter platform proves to be stable in hover flight and is capable of carrying a significant payload. Our approach achieves similar levels of efficiency and maneuverability common amongst quad-copters and multi-rotor while allowing it to perform stable flight through small gaps.

It should be noted that there are still multiple aspects of this design that can be improved upon. Immediately noticeable is the jerky yaw and roll control, which is



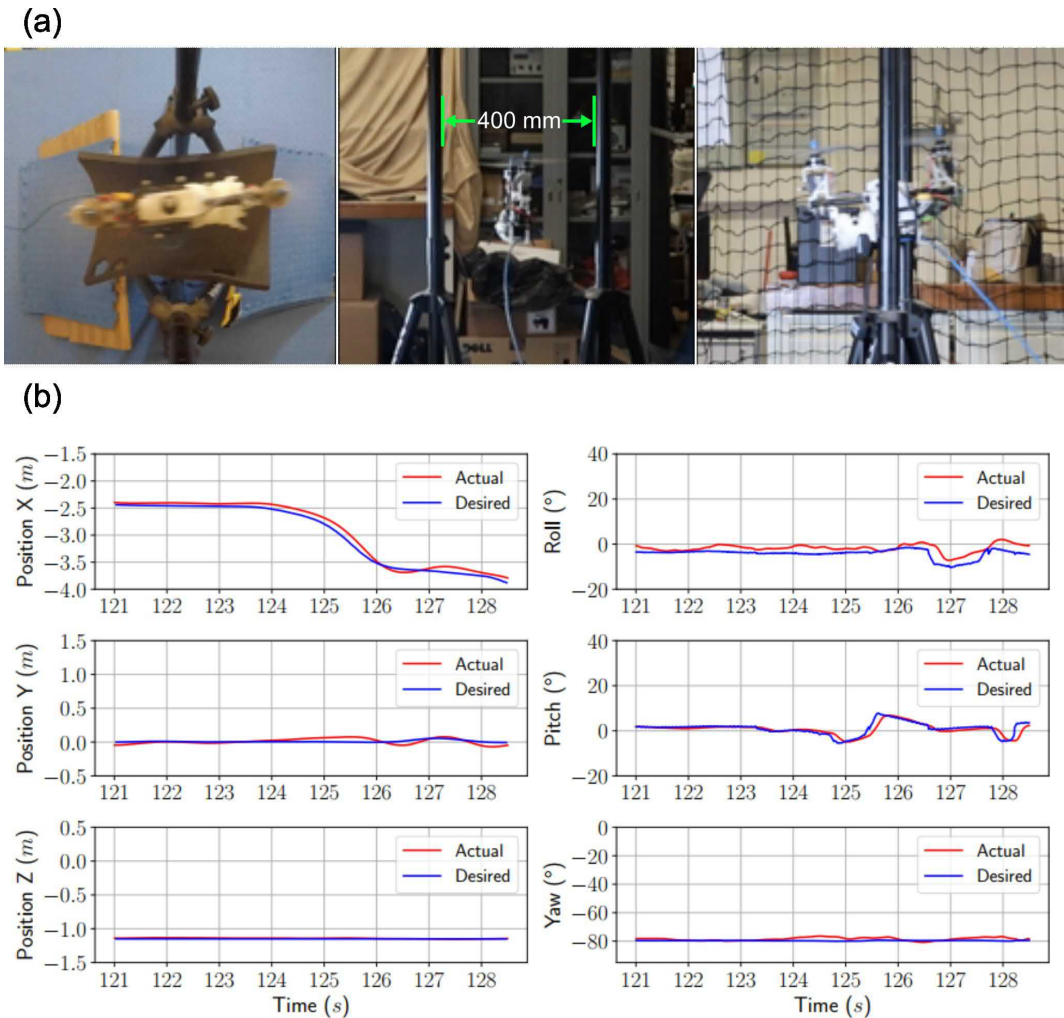


**Figure 2.23** Gemini mini flying through a 40 cm gap **(a)** Top, side and back view of the Gemini flying through gap; **(b)** The position and attitude data when crossing the gap.

undoubtedly a result of a tandem-rotor bi-copter design. Also, the two additional dynamics, as pointed out in the main texts, need to be carefully modeled and compensated to achieve accurate and robust control of such a bi-copter UAV. Last but not least, the fuselage has huge room for optimization. Throughout experiments, crashes usually would result in total wreckage of the UAV. Adopting stronger material and topology optimization methods could improve the stiffness while minimizing the weight. The remedy and further improvement on the Gemini mini will be further discussed in the future chapters.



## 2.9 Related Publication

Qin Y., Xu W., Lee A., and Zhang F., “Gemini: A compact yet efficient bi-copter UAV for indoor applications,” *IEEE Robotics and Automation Letters*, 5(2), 3213-3220, 2020.



# Chapter 3

## Gemini W: Aerial-ground Locomotion Bi-copter

### 3.1 Introduction

Even with the highly efficient bi-copter method we proposed in the last chapter, the bi-copter UAV's full potential still hasn't been unleashed. The limited on-board power dramatically decreases UAV flight time, especially at large payloads [85]. Even stationary hovering with a multirotor is energetically expensive as it requires constant motor actuation (hence power consumption) [30]. Increasing the size of UAV propellers mitigates the problem, but its mobility in tight spaces will be seriously jeopardized [86].

In nature, insects with the ability to fly can constantly perch and rest to restore energy. Similarly for UAVs, exploiting contacts with environmental structures could provide extra force support and reduce the required motor actuation, hence saving power and extending cruising time. The design objective for the Gemini W bi-copter is to exploit a novel aerial-ground hybrid locomotion on a flat surface environment with only a single passive wheel.

As shown in [Figure 3.1](#), this design is a single passive wheel integrated at the



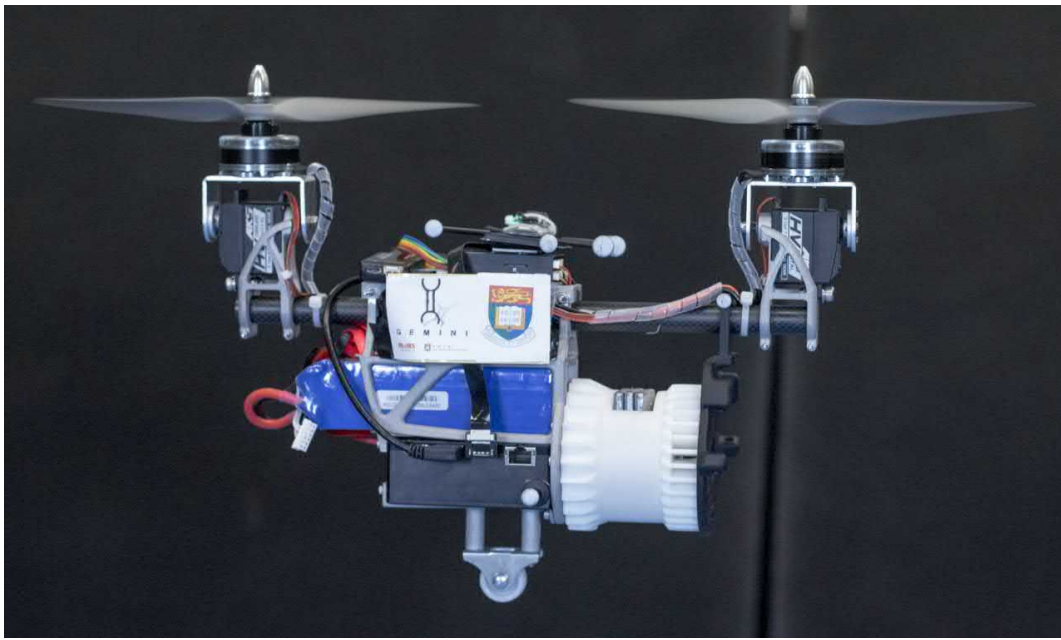


**Figure 3.1** Gemini W: Hybrid aerial-ground locomotion UAV with a single passive wheel at: <https://youtu.be/22SXYY39KjM>

UAV bottom, serving the minimal design for hybrid aerial-ground locomotion to date. Results show that our minimal design allows successful aerial-ground hybrid locomotion even with a less-controllable bi-copter UAV. The ground locomotion saves up to 77% battery without much tuning effort.

In this chapter, we adopt this locomotion method and take the Gemini mini bi-copter efficiency to the next level. Moreover, the detailed fuselage optimization and iteration process will be meticulously discussed, including but not limited to the crash proofing, topology optimization, and on-board avionics integrations. The main contributions of this work are:

1. We propose an aerial-ground hybrid locomotion method with a single passive wheel, which is the minimal design so far.
2. We implement the aerial-ground hybrid locomotion onto the Gemini W and demonstrate its feasibility of enabling aerial-ground hybrid locomotion via real flight experiments
3. We conduct actual flight tests to validate the power saving enabled by the aerial-ground hybrid locomotion.



## 3.2 Literature Review

In order to extend the UAV operating time, a widely researched approach is to perch a UAV on elevated locations (e.g., ceilings, walls, and others), mimicking the birds resting on tree branches or power lines [36, 87, 88]. For example, Hang *et al.* [36] designed a transformable landing gear with specially designed grippers that enable a multirotor to perch on different objects, poles, rooftops, branches, etc., as shown in Figure 3.2. H. Zhang *et al.* [89] propose a compliant bistable gripper that enables a micro quad-rotor Crazyflie 2.0 to perch on cylindrical objects.

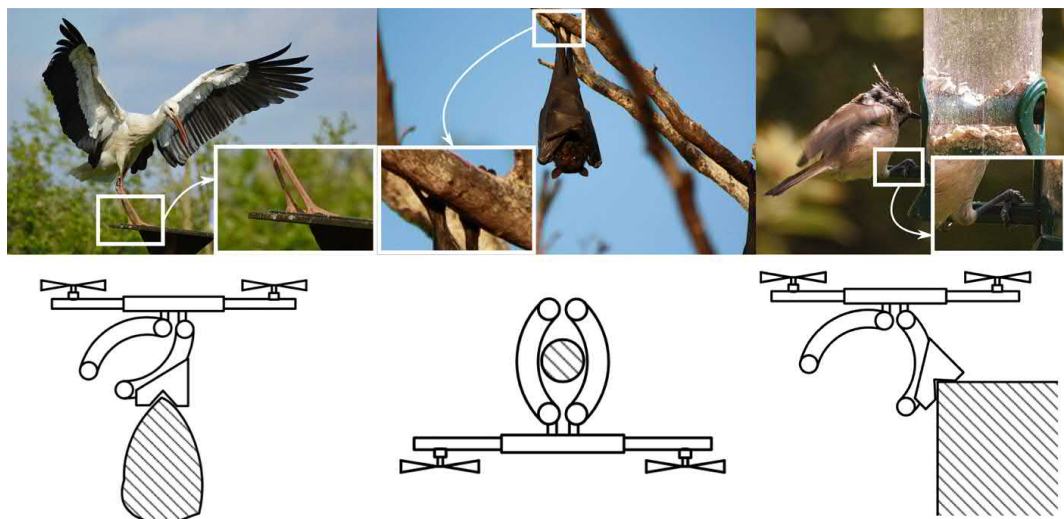


**Figure 3.2** Example perching and resting actions in nature: Flying animals such as birds or bats often make use of structures in the environment to save energy. In choosing, they select locations that can be approached and evacuated by simply maneuvering in the air, while still allowing them to execute a mission - such as observing the environment or looking for prey. **Image Source:** [36].

Other perching mechanisms such as dry-adhesive gecko-inspired grippers (shown in Figure 3.3a) [37, 90, 91], fiber-adhesive grippers [92], and dry-adhesive pads (shown in Figure 3.3b) [38] have also been actively researched. Regardless of the exact implementation, a notable limitation of perching is that the UAV has to stay at the perching location. Traveling between those perching locations is still energetically expensive.

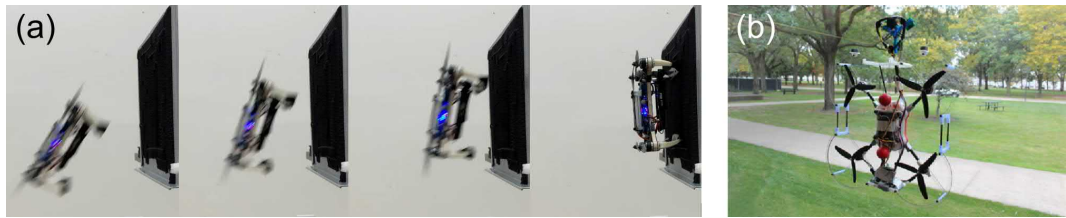


**Figure 3.3** Other perching mechanisms and methods **(a)** Dry-adhesive gecko-inspired grippers perching; **(b)** Dry-adhesive pads perching. **Image Source:** [37, 38]

Another approach is to obtain force support from the ground, leading to aerial-ground hybrid locomotion. Compared with perching, UAVs moving on the ground cannot maintain a high vantage point but preserves mobility, which is indeed necessary for tasks such as mobile mapping, exploration, search, and rescue. Although this concept is quite straightforward and long-existing in our lives, such as aircrafts landing gears for takeoff/landing, its formal application in aerial robots seems scarce. Most of the current work was motivated to improve the mobility of ground robots constrained by rough terrains in disaster relief [39–42] or out of entertainment or safety [43]. Specifically, Morton *et al.* [39] presented a novel wheel-based locomotion (see Figure 3.4). With a worm gear as an actuator embedded in the middle, the robot can transform from driving mode to quad-rotors.

Adarsh *et al.* [40] proposed an air-land-water vehicle concept with a wall maneuvering capability named Multi-terrain Multi-utility robot (MTMUR)(see Figure 3.5a). The various functionality makes the design quite complicated, four wheels, two servo

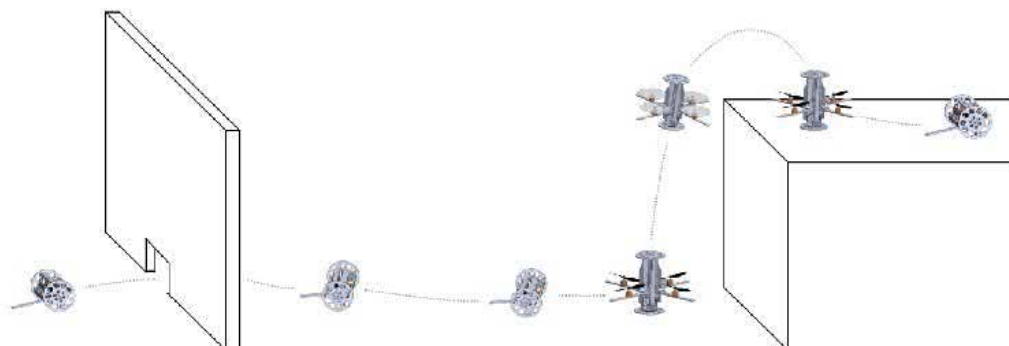


**Figure 3.4** Transformable ground-air vehicle. **Image Source:** [39]



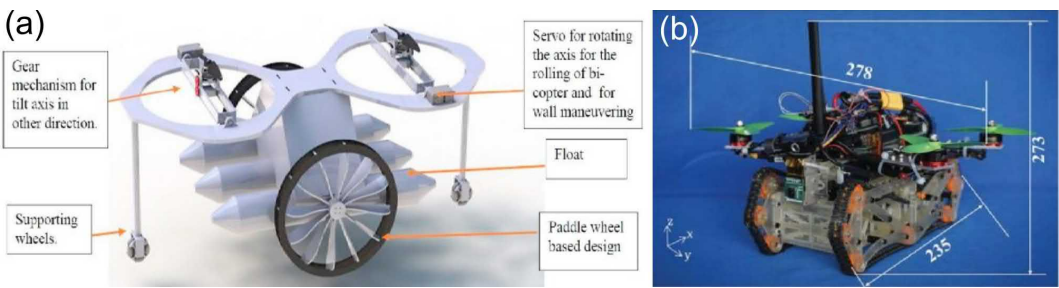


**Figure 3.5** Hybrid multi-terrain vehicles **(a)** Multi-terrain Multi-utility robot (MTMUR); **(b)** Air-ground amphibious agricultural information collection robot. **Image Source:** [40, 41]

motors, and a chassis. It is a unique lightweight design similar to a bi-copter and capable of moving on the ground and water using specially designed wheels with the help of float. This concept has applications that include search and rescue, mapping, surveillance, and military purposes. Unfortunately, it has not come true to our best knowledge. Wang *et al.* [41] proposed a similar work of combining quad-rotors with chassis (see Figure 3.5b). This air-ground amphibious robot is aiming at operating in complex farmland terrains.

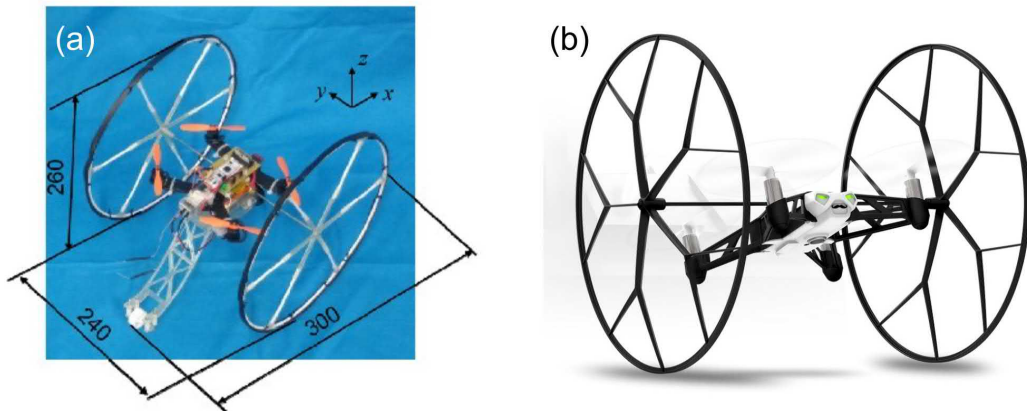


**Figure 3.6** Small mobile robot with a hybrid locomotion mechanism of passive wheels and multi-rotors **(a)** WAMORN (WAseDA MOnitoring dRoNe). **(b)** Parrot Rolling Spider. **Image Source:** [42, 43]

Tanaka *et al.* [42] developed a small mobile robot with a hybrid locomotion mechanism of wheels and multi-rotors, WAMORN (see Figure 3.6a). The design is very similar to the Parrot Rolling Spider [43], where two wheels are placed at the two sides of a quad-rotor (see Figure 3.6b). The two wheels of the Parrot Rolling



spider, however, weigh 18% of the total takeoff weight. A third wheel was also used for stabilizing the robot during running and allowing recovery from the flipping state.

All the prior work mentioned above uses either at least two wheels or caterpillar chassis. Although they are able to move on rough terrains as expected, the driving mechanism adds up a significant weight to the system, leading to increased power consumption when moving in the air [30].

We take another view of the aerial-ground hybrid locomotion as a measure to improve UAV power efficiency while maintaining its mobility. Unlike the previous work, our approach is a single passive wheel installed at the bottom of the UAV, the minimal design among all others. Such a design simplifies the implementation and reduces the add-on weight: our preliminary implementation is 20 grams, adding merely 1% to the UAV weight and minimizing the effect on flight power consumption. Moreover, it leads to a clear side view (i.e., a spinning LiDAR has a clear view on two sides, hence maximizing mapping efficiency). The efficiency, flexibility, heavy payload capacity, and compactness make this platform ideal for applications like cave explorations or oil pipeline inspection.

### 3.3 System Design and Implementation

In principle, the aerial-ground hybrid locomotion mechanism based on a single passive wheel is applicable to generic multi-rotor UAVs. In this chapter, we implement such a method onto the Gemini mini bi-copter introduced in the last chapter. This section illustrates the system design process and implementation details of the Gemini W aerial-ground locomotion bi-copter, including the propulsion system details, airframe redesign with optimization, and iteration based on the previous Gemini mini design, the single passive wheel design, and the avionics integration work.



### 3.3.1 Propulsion System

The Gemini mini designed in the previous chapter used a 4S battery, limiting the maximum thrust produced by the two brush-less motors and hence the UAV maneuverability. To overcome this, we use a 5000 mAH 10C 5S battery with a higher voltage in the current platform. According to the motor test data from the APC propeller official website, this upgrade of voltage theoretically will result in a 300 g higher maximum thrust on each motor, which adds more agility and upon adopting frictions from the ground and extra weight from heavier components.

The “Kv” rating of a motor refers to the motor’s velocity constant, and it is measured by the number of revolutions per minute (RPM) that a motor turns when 1 V (one volt) is applied with no load attached to that motor [93]. With the change in power voltage and takeoff weight, the optimal propulsion system proposed in the last chapter no longer applies. In order to find out the highest efficient motor under 5S voltage, we conduct a bench drag test among motors with different Kv values.

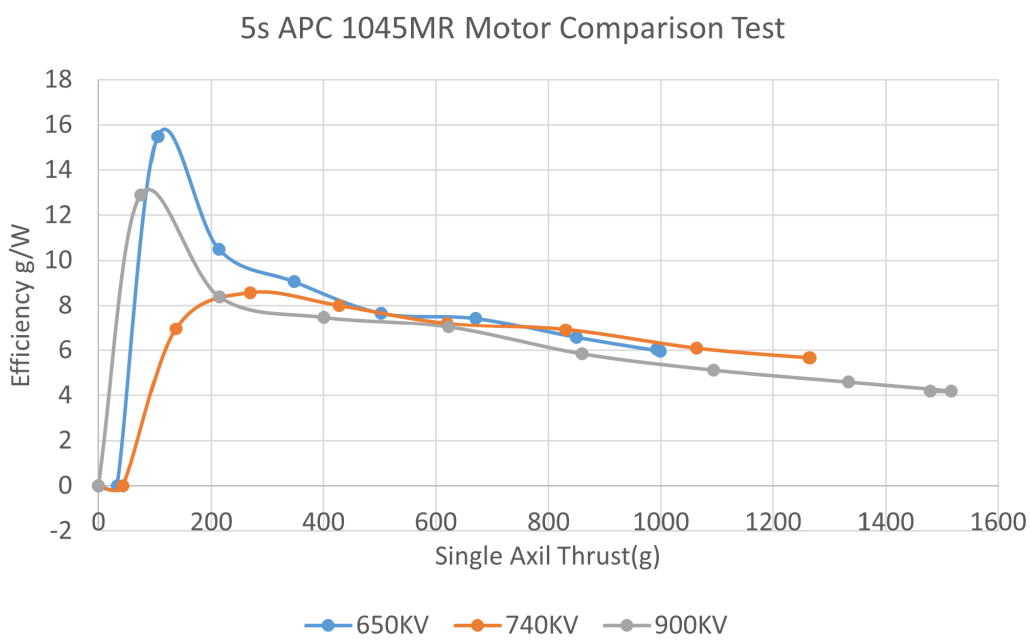


**Figure 3.7** 5S APC 1045MR bench test with motors of three different Kv ratings. The 740 Kv motor is chosen for its highest efficiency performance when hovering with takeoff weight at 1950 g (975 g per actuator).



Three motors with close Kv values are equipped with identical propellers and sweep from zero to full throttles with ten steps. The efficiency is calculated with the thrust generated by the motor divided by the power consumption at the time. Since the total takeoff weight is 1950 g (weight difference among motors with different Kv is negligible), the thrust required to generate by each rotor at a hovering state will be 975 g. Higher Kv value results in higher motor RPM (therefore higher thrust) under the same voltage and such a trend is verified with the maximum thrust data from [Figure 3.7](#). Through the curve fitting, the 740 Kv motor has the highest efficiency among all and is chosen to replace the original 650Kv motor.

### 3.3.2 Airframe

The Gemini mini was previously printed with plastic Stereolithography (SLA). Such material is cheap and fast to manufacture but has a tensile strength of merely 33 Mpa. Due to the working principle, bi-copters do not have propulsion system redundancy. As a result, the UAV airframe will scatter into pieces upon every propulsion system or control failure.

To strengthen the rigidity of the UAV, we first replace the SLA plastic material. The whole airframe and servo holders have also been rebuilt with Selective Laser Sintering (SLS) 3D printed aluminum alloys (7075-T6). It usually takes more than two weeks to build, and the cost is relatively low (around 2000 RMB) for each part, but this material is able to ensure sufficient rigidity (7075-T6 has a tensile strength of 330 Mpa). As a result of the aluminum body and other added components, the total takeoff weight (with other components such as payload, wheels, and markers) increased to 1950 g. The following subsections explain the detailed decision-making procedure of the new design.

#### 3.3.2.1 Original Airframe Failure Analysis

According to the author's testing experience, the failures of the Gemini mini bi-copter will most commonly result in two different types of crashes, the head crash



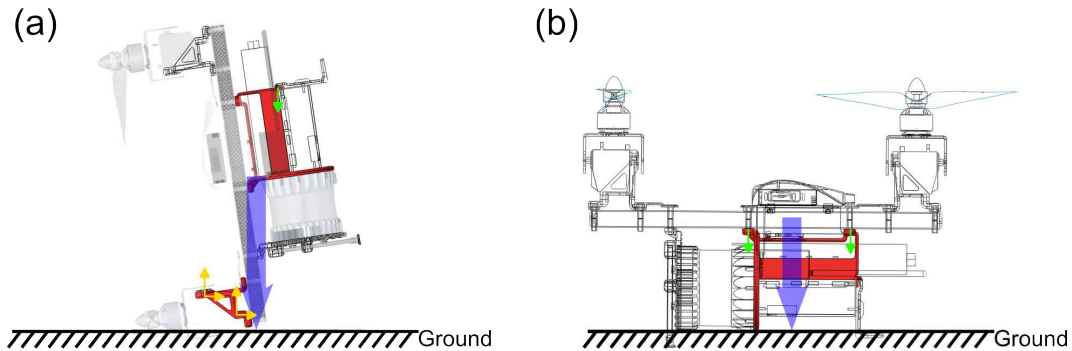


**Figure 3.8** Sideview of common bi-copter crashes (Vehicle falls to the ground following the direction marked by blue arrows. The damaged parts are marked in red and need to be strengthened) **(a)** The head crash (Upon collision, forces will react on the servo holder as marked by yellow arrows. The momentum of the battery and on-board computer will create another force load to the fuselage as marked by a green arrow); **(b)** The hard touchdown (Upon collision, momentum from all the parts above the fuselage will create a force load on the fuselage at the locations marked by green arrow).

(the bi-copter pitches down and hits the ground with the front head, as shown in [Figure 3.8a](#)) and the hard touchdown (the bi-copter loses altitude and hits the ground with the bottom body, as shown in [Figure 3.8b](#)). In [Figure 3.8](#), propellers are ignored due to their fragility and trivial mass, while the damaged parts are painted red. When the head crash happens, forces will react on the servo holder as marked by yellow arrows. The momentum of the battery and on-board computer will create another force load to the fuselage as marked by a green arrow. When the hard touchdown is taken place, momentum from all the parts above the fuselage will create a force load on the fuselage at the locations marked by the green arrow, damaging mainly the upper part of the main fuselage upon the first shock.

During testing, crashes resulting from mechanical failures and control failures are unavoidable. The cause of crashes is usually either caused by one propulsion system or caused by altitude controls. Upon every crashing, the red part indicated in [Figure 3.8](#) will have a high chance of wreckage, delaying the experiment, costing expensive manufacturing fees, and consuming much repairing time. In order to resolve this problem, besides replacing the previous material with aluminum that is

more rigid, the topology optimization method was used to strengthen the part while reducing the weight at the same time.

As shown in [Figure 3.9](#), the entire optimization process is done through model analysis and iterations by using software such as Altair Inspire, Ansys Fluent, SolidWorks, and CATIA. The general process can be divided into three parts:

The first part is applying topology optimization commercial software Inspire for topology optimization. Firstly, according to the layout avionics, the design space of the part is determined. With the given materials, the load value of the falling impact condition is obtained based on the flight height and attached to the contact point in the design space. Finally, set the maximum stiffness as the optimization objective and uses Inspire to solve for the optimal structure.

The second part is to redraw the CAD model based on the optimized structure solved in the previous step.

The third part is to assign materials to the model and then apply the load settings for finite element simulation analysis to analyze its structural strength, stiffness, and safety factor and check if it meets the initial design requirements. Then size optimization and shape optimization will be carried out through software such as Ansys Fluent. In order to meet all the standards, repetitive iterations are necessary sometimes. The CAD models will have to be modified according to analysis results.

### 3.3.2.2 Optimization: Servo Motor Holder

The optimization objective for the Gemini W structure focuses on its endurance and stiffness. The expectation of the servo motor is to be able to withhold 80N horizontal force and 40N vertical force, and withstand torque load that is caused by the secondary bearing axis.

Assume the scenario where the bi-copter is originally hovering at the altitude  $h$  of 2 meters and suddenly loses control of the pitch, is diving down with  $-90^\circ$  of pitch angle, and the acceleration due to gravity ( $g = 9.8 \text{ m/s}^2$ ). Since the altitude is



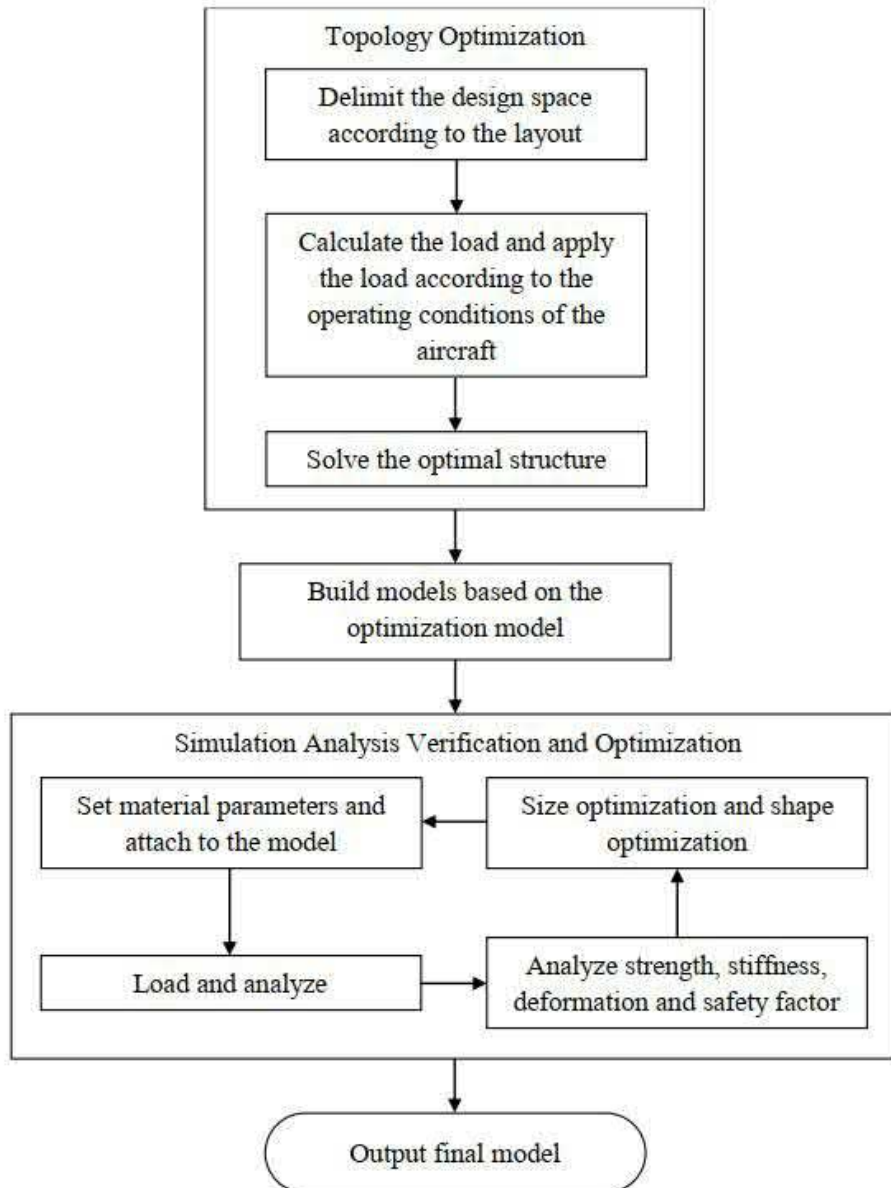


**Figure 3.9** Workflow of topology optimization. Based on the pre-assigned workspace and load setting conditions, this process generated the structure with minimized material (thus minimized weight) and maximized stiffness.



relatively small, the velocity just before impact using simplified can be estimated with the free-falling model:

$$v = \sqrt{2gh} \quad (3.1)$$

the weight  $m$  of the UAV is 1950 g, and the  $v$  is estimated to be 6.26 m/s. Assume the landing contacting time to an experimental value of 0.14 s, according to the conservation of momentum, the impact force can be calculated as:

$$F = m \frac{\Delta v}{\Delta t} = 76.29N \quad (3.2)$$

According to author's experience, the contact area during the head crashing is usually less than 1 cm<sup>3</sup>, therefore the pressure can easily go higher than:

$$P = \frac{F}{A} = 76.29Mpa \quad (3.3)$$

which totally exceeds the limitation of 33 Mpa of the plastic SLA material. During actual testing, the servo holder breaks every time upon the bi-copter head crash, and experimentally has half the chance to crash upon the hard touchdown. After the wreckage, it is a very labor-heavy task to replace the servo holder and repair the propulsion system.

Topology optimization has been widely used by mechanical and civil engineers for decades. In order to minimize the amount of used material and the strain energy of structures while maintaining their mechanical strength, this method is usually adopted [94]. This method uses a mathematical method that spatially optimizes the distribution of material within a defined domain by fulfilling given constraints previously established and minimizing the cost function that has been defined previously.

Shape optimization can be performed with Altair Inspire using gradient-based optimization methods enabled by the adjoint solver. The adjoint solver in Altair Inspire is a smart shape optimization tool that enables the creation of designs with minimal mass and maximal stiffness. [95].

[Figure 3.10a](#) shows the servo holder part that needs to be topology optimized.



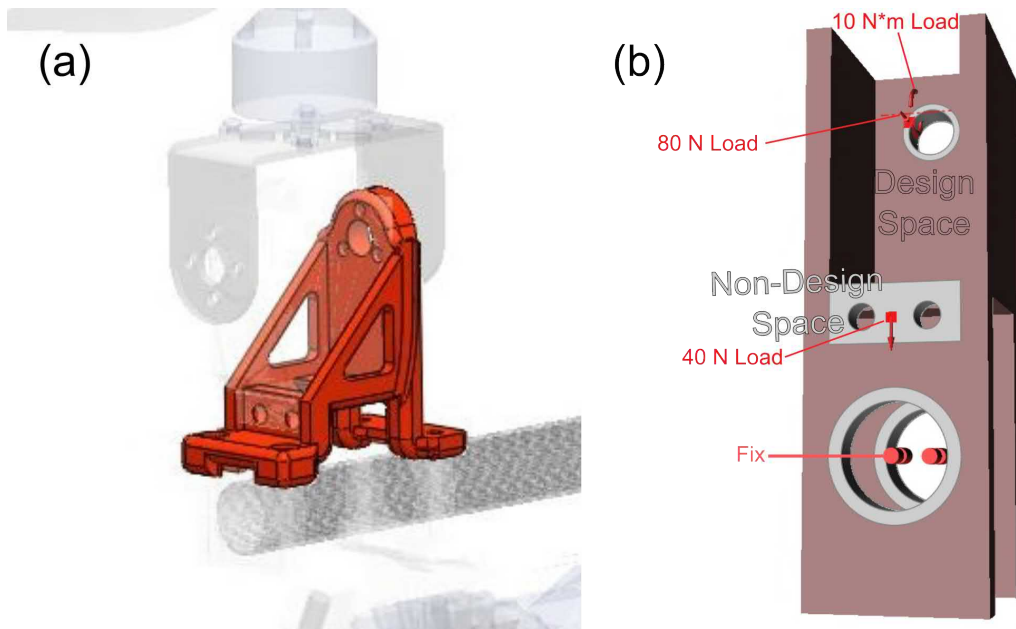


**Figure 3.10** Servo holder part for optimization **(a)** Servo holder model before topology optimization; **(b)** Servo holder design space and load condition locations based on the previous model. The designed space can be optimized through topology optimization, while the non-designed space is pre-determined due to installation constraints. The load conditions assumptions are based on previously discussed crash scenarios.

Since the installation position of the servo motor and the fuselage (id east the carbon fiber rod) will remain in the same relative position, the initial design space of the optimized deliverable can be established according to the previous installation position. As shown in Figure 3.10b, the model is divided into the design space area (shown in red) and non-design space area (shown in grey). The material in the design space area will run through the topology optimization, while the non-design space area will remain unchanged due to installation constraints. The fixed constraints are fixed at the two lower circular holes simulating the fixed connection between the servo motor support part and the main carbon fiber rod. The load condition is set on the two contact surfaces of the servo motor support with 40N and 80N, respectively, under the two crash scenario assumption we made earlier. A 10 N\*m torque load is also added to simulate the torque acted upon the secondary bearing axis.

After importing the part and setting the load constraint, we run the “topology”



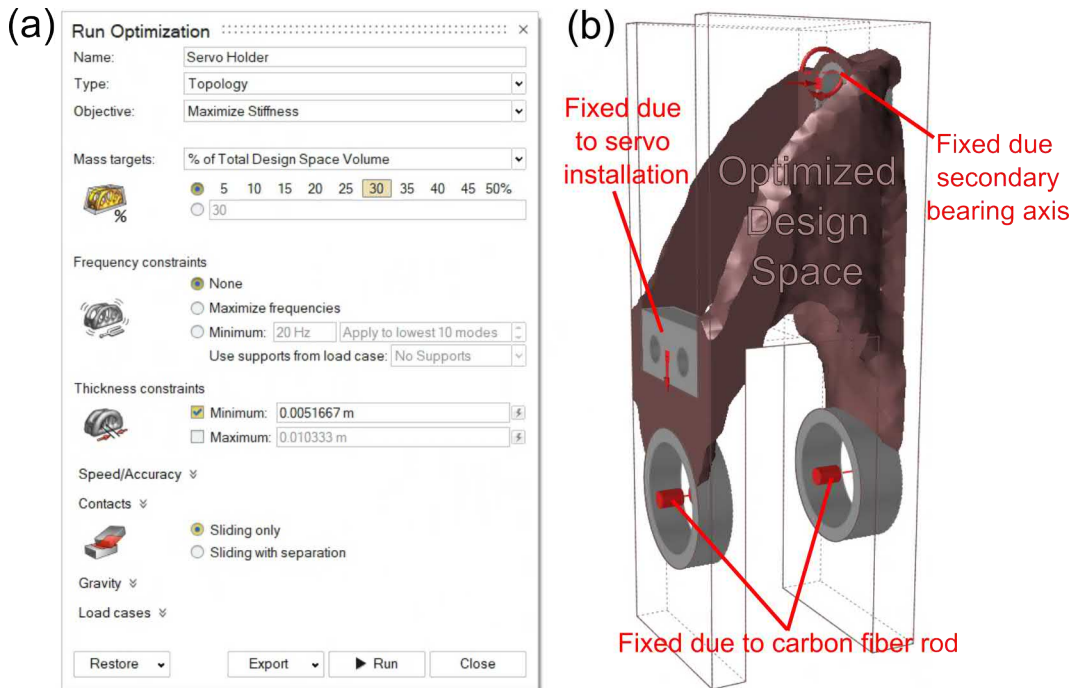


**Figure 3.11** Servo holder Altair Inspire topology optimization (a) Altair Inspire topology optimization with “maximize stiffness” setting; (b) Altair Inspire servo holder topology optimization result. The non-design space (gray parts) are kept due to installation constraints, and the design space has been optimized.

function with “maximum stiffness” as the target and “total volume of design space” at the mass target (shown in Figure 3.11a). Set the minimum thickness constraints to be slightly bigger than 0.005 m to satisfy the 3D printing requirement, and retain everything else as default. After running the analysis, the optimized model result is shown in Figure 3.11b. It can be seen that the structure converges into a triangular shape, with three bifurcations accumulating near the two joints of the servo motor support and the main carbon fiber rod. The left lower and right upper bifurcations are thicker compared to the lower bifurcations at the right lower corners. The left lower and right upper bifurcations become the main branch during the force transmission path, and the right lower bifurcations connect this main force transmission path with the connection joint at the lower right with the carbon fiber rod.

The topology optimization simulation result above is only able to provide the general idea of structure optimization. Previously, we used Dassault Systèmes Solidworks to build the servo holder part, but this software is not good at drawing



curved surfaces, especially the shape similar to the topology optimization simulation result. On the other hand, the Dassault Systèmes CATIA is a Computer-aided design (CAD) software famous for its curvilinear features. To improve the design, we import the side view of the Altair Inspire servo holder optimization simulation result into CATIA modeling software as shown in [Figure 3.12a](#).

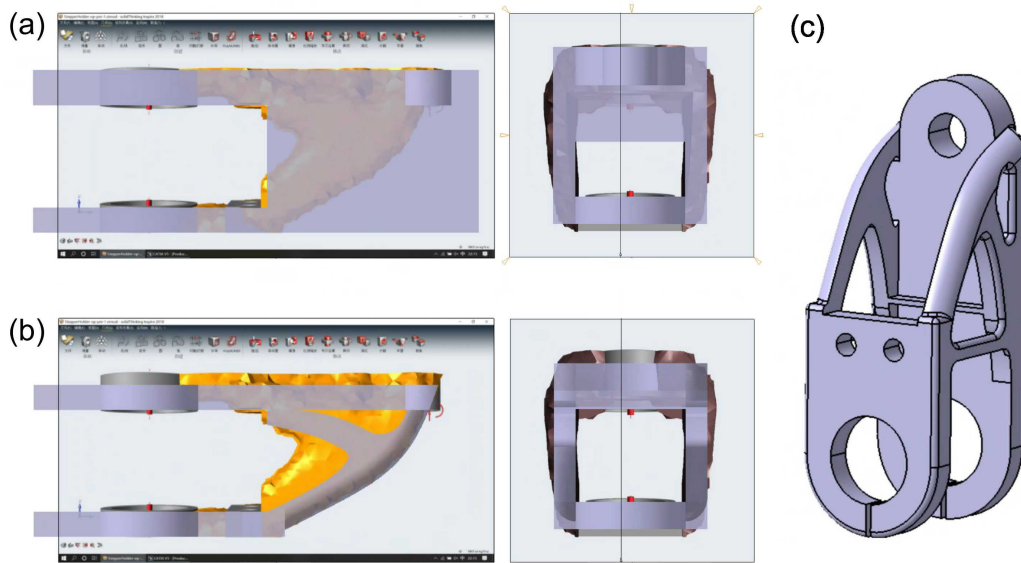


**Figure 3.12** Servo holder part optimization structure redrawn process **(a)** Servo holder topology optimization result overlay onto design space; **(b)** Servo holder CAD structure redrawn; **(c)** Servo holder part optimized CAD sketch.

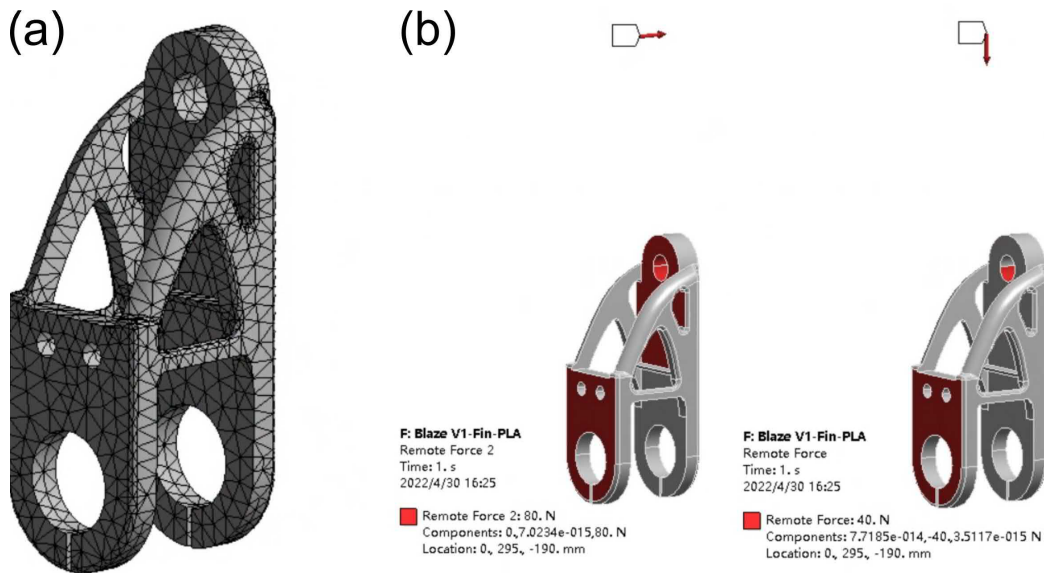
After adjusting the size and proportion of the picture, overlay the picture onto the design space. Do the same for the three surfaces and redraw the structure based on the optimization simulation contour (shown in [Figure 3.12b](#)) using mainly “boss” and “groove” commands. Continue doing the same for the rest of the three surfaces, and add a non-design space area into the new rebuilt model. The optimized servo holder CAD redrawn is shown in [Figure 3.12c](#).

After the redrawn, we use ANSYS Workbench to validate the redrawn part. Ansys Mechanical enables solving complex structural engineering problems with the finite element analysis (FEA) solvers available in the suite and allows customizing and automating solutions for structural mechanics problems and parameterizing them to analyze multiple design scenarios [96].

Import the model into the ANSYS Workbench software and choose the corre-

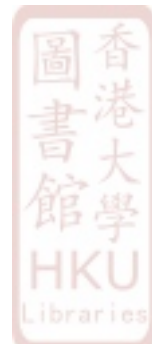


sponding material, then mesh the model with the maximum relevance setting of 100 for the highest precision (shown in [Figure 3.13a](#)). Meshing the model will dissect the whole part into tiny pieces of triangular shapes. The larger the meshing number is, the finer triangular shapes will be, and the more precise analysis will be delivered.



**Figure 3.13** Servo holder ANSYS Workbench analysis **(a)** Servo holder after fine meshing in ANSYS Workbench; **(b)** Servo holder ANSYS Workbench constraints and load setting with two remote forces with both vertical and horizontal directions to simulate the crash scenarios. The surfaces marked in red represent the surface where remote forces have been applied to.

The next step is to constrain the load application. As shown in [Figure 3.13b](#), by using the identical load constraints as [Figure 3.11a](#), we apply remote force on the area marked in red as shown in [Figure 3.8a](#) to simulate the head crash scenario. Upon head crash scenarios, the servo holder is not mostly like to be hit on the head perpendicularly. If east, the contact might have an angle if the contact happens while the pitch angle is slightly larger than  $-90^\circ$  (such as  $-80^\circ$ ), the force will mainly act on the strong carbon fiber rod, however, if the contact happens while the pitch angle is slightly less than  $-90^\circ$  (such as  $-100^\circ$ ), a downward force component will be acted onto the servo holder. Assume the headcrash force to be 80N according to [Eq. 3.2](#), and assume the vertical force to be half of the horizontal force from our experience. Apply the remote forces in both vertical and horizontal directions to simulate the head crash.



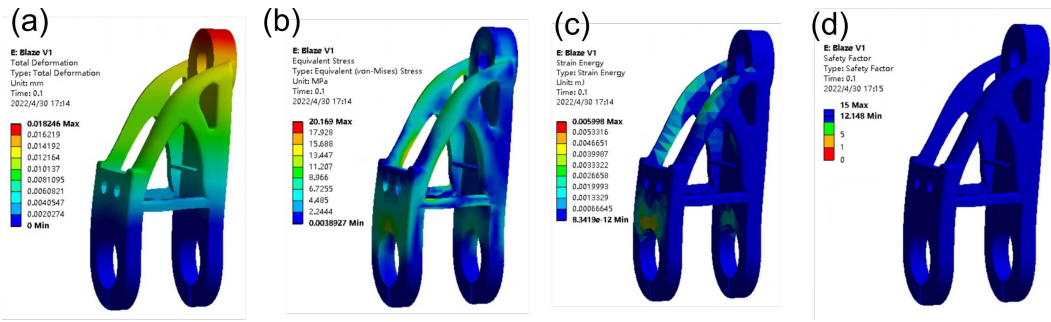


**Figure 3.14** Servo holder ANSYS Workbench simulation result **(a)** Total Deformation; **(b)** Equivalent Stress; **(c)** Strain Energy; **(d)** Safety Factor. The safety factor has a minimum value of 12.14 but a weight 42.15 g, thus the model is safe but overweight.

After applying constraints, we run the simulation and observe the deformation, equivalent stress, strain energy of the frame, and the safety factor of the rebuilt structure. As shown in [Figure 3.14](#), after applying the load conditions, the deformation is minor throughout most of the structure. The stress is mostly below 4.4 MPa, and the strain energy is universally smaller than 0.02 mJ. The safety factor has a minimum value of 12.14, which goes far above the high safety standard of 9 by the software default. This performance overkill is not necessary. However, due to the change of heavier material, the estimated mass became 42.15 g. The previous model merely has a 24 g mass, and the optimization goal of the new part is to make the part stronger under the constraint of not adding extra weight.

In order to reduce the weight of the part, lowering the minimum constraint size of the topology optimization, observing the simulated stress distribution cloud, and removing the less energy distributed parts are the two most common approaches. We first adjusted the new model to the Inspire, and the minimum constraint size is set to the model mass at 24 g. The optimized material to be retained is shown in [Figure 3.15a](#). The stress distribution of the rear carbon fiber rod holder and its surrounding part structure is minimal, suggesting these corresponding parts can be made thinner.

After the first approach, we use ANSYS to analyze the stress distribution and strain energy distribution in the cloud image (shown in [Figure 3.15b](#)). The visible parts all have equivalent stress less than 2MPa and strain energy less than 0.15 nJ selected by capped isosurface. [Figure 3.15b](#) also indicates that the stress distribution



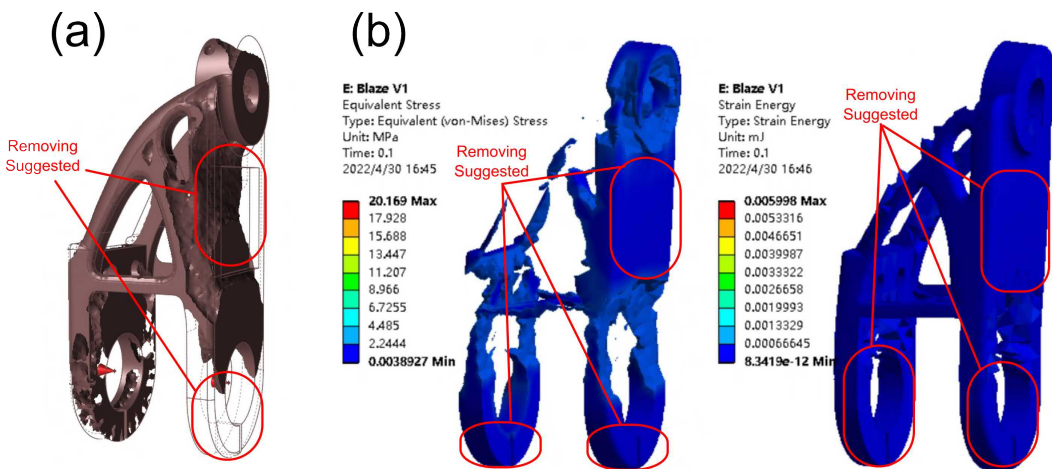


**Figure 3.15** Servo holder topology optimization iteration **(a)** Inspire topology optimization with 24g weight constraints (only the materials to be retained are shown, and the material suggested to be removed is circled in red); **(b)** ANSYS stress distribution and strain energy distribution analysis (only the less stressed materials are shown, and the materials could be removed with the corresponding method are circled in red).

and transfer function of the rear fixed plate and small parts on two sides of the structure is minimal, suggesting that removing the corresponding materials in these parts won't affect the stress distribution and strain energy distribution much. Since this conclusion is similar to the result of topology optimization, we can make changes to the mentioned parts.

With the conclusion drawn from the two methods mentioned above, another iteration is made with reduced material. The final CAD deliverable of the servo motor holder is shown in Figure 3.16. In the final deliverable, the redundant part, especially the back and bottom servo holder support, are reduced significantly. The less stressed materials, especially the part that holds the carbon fiber rod, were made thinner. Extra design features such as cable trays are added for easy installation.

To verify the result of the iteration, we run another round of simulation with the same load settings and constraints, which are shown in Figure 3.17. From the simulation result, the safety factor is still retained in the desirable range. The shape deformation is reasonably tiny, and both stress and strain energy are uniformly dis-



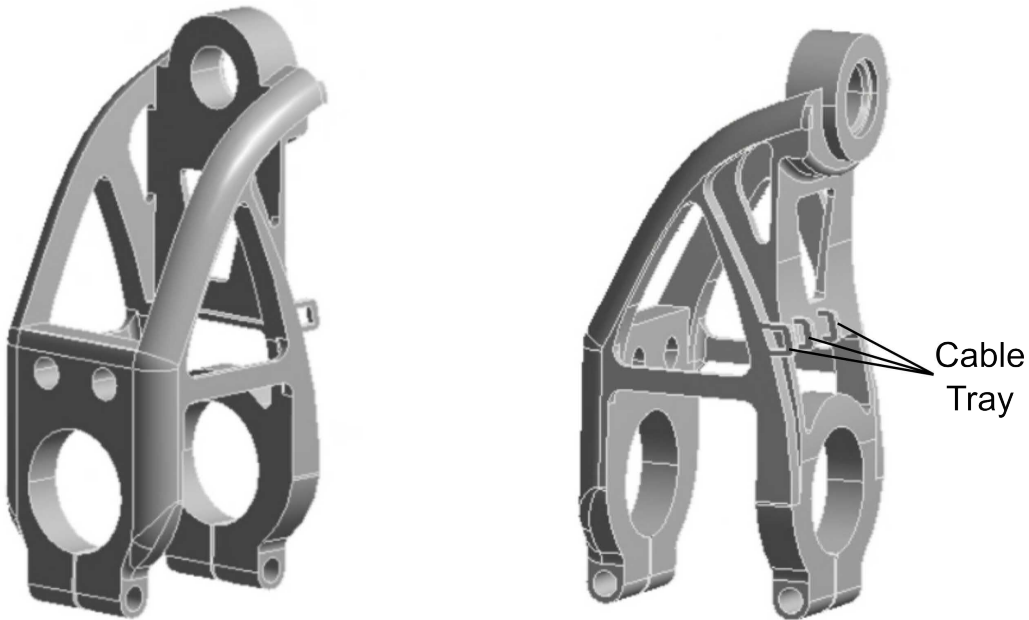


**Figure 3.16** Servo holder final deliverable after topology optimization, weight reduction iteration, and cable tray features added.

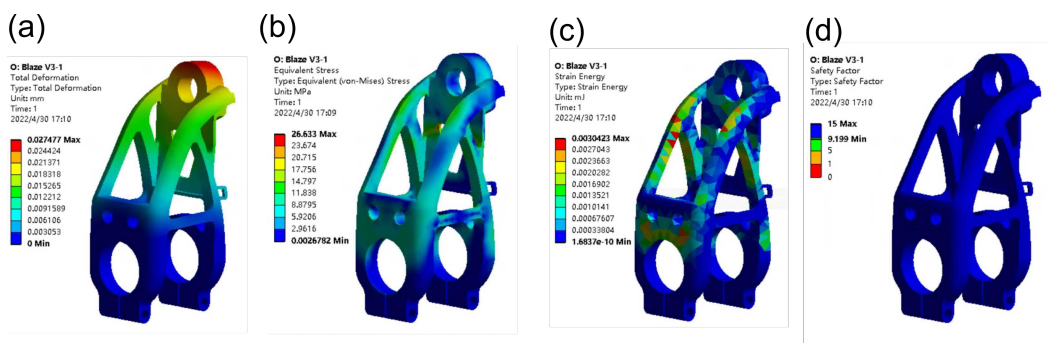


**Figure 3.17** Servo holder final deliverable simulation analysis **(a)** Total Deformation **(b)** Equivalent Stress **(c)** Strain Energy **(d)** Safety Factor. The safety factor has the minimum value of 9.199 and the weight is reduced to 24 g. The weight is halved and met the requirement, while the safety factor is still desirably high. The optimization is successful in simulation.



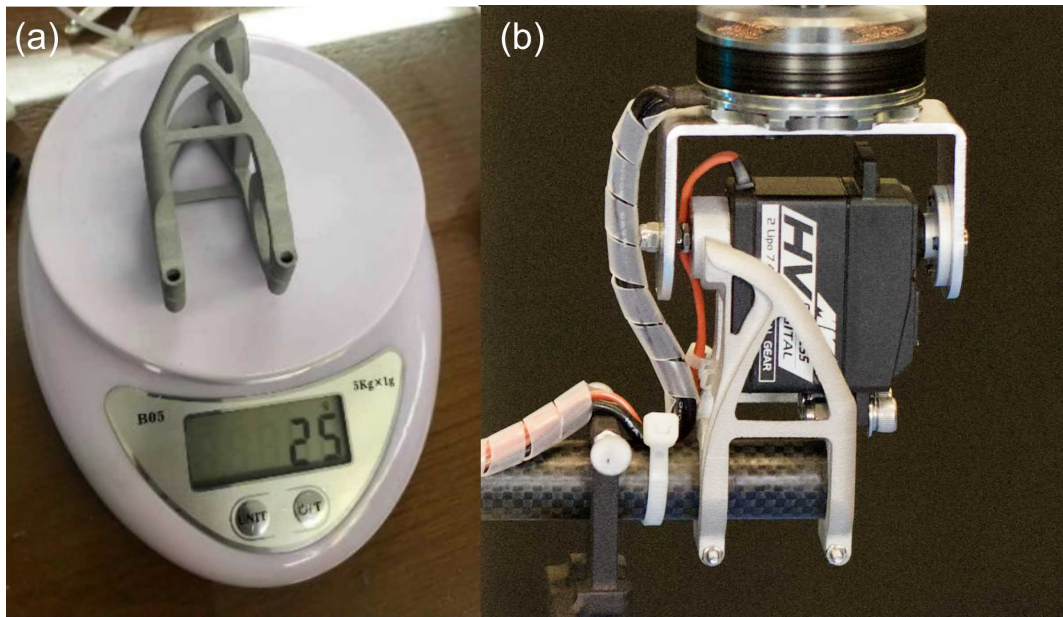
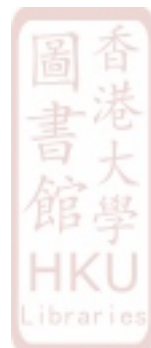


**Figure 3.18** Servo holder experimental validation **(a)** The weight of the optimized servo holder is 25 g. **(b)** The final aluminum 3D printed servo holder in use. The final servo holder successfully surpasses the experiment validation, and has never been wrecked upon crashes ever after.

tributed around the part. The safety factor has a minimum value of 9.19, which is empirically highly acceptable. Throughout a series of trial and errors, the finalized model has the simulated weight reduced to 24 g, yet the stiffness has been significantly improved and is predicted to be durable upon head crash. Even though the deformation result increased from 0.018 mm to 0.027 mm, the difference is still trivial for this relatively large part.

Compared to the previous design, the new servo holder part no longer needs off-the-shelf carbon fiber rod clips, reducing the need for interference fit assembly procedures and saving assembly time and labor cost. However, without the carbon fiber rod clips, the servo holder part can no longer be disassembled except for the two ends of the carbon fiber rod. Nevertheless, since this servo holder will only be installed at the two ends of the carbon fiber rods, it does not affect the installation and debugging procedure very much when other parts need to be disassembled.

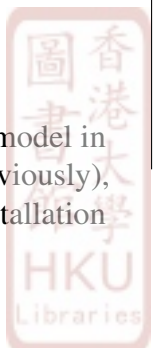
To verify the feasibility of the CAD design and accuracy of weight prediction, we printed the part out and the actual weight is 25 g (shown in [Figure 3.18a](#)), which is



very accurate and merely 1 g of error occurs. The selective laser sintering aluminum 3D printing will unavoidably leave residues on the surface, therefore affecting the precision of the part and causing trouble while assembling. In order to resolve this issue, electrical grinding tools and drills are usually needed to manually adjust the part before assembling. In actual testings, the final assembled part has never been wrecked ever after (shown in [Figure 3.18a](#)).

[Figure 3.19](#) summarizes the comparison of the original servo holder vs. the optimized model. The old part is made from SLS plastic, and has maximum equivalent stress distribution of 198.19 MPa with sharp transitions especially around the edges. The minimum safety factor is only 1.22, but weights 44 g totally. The newly designed aluminum alloy part has uniformly distributed equivalent stress distribution, with a maximum value of only 26.63 MPa. The minimum safety factor is 9.19, and weights 25 g totally. Besides features for easy installations such as cable tray, the optimized model has 7.6 times less maximum equivalent stress, uniformly distributed stress, and the whole part is smash proof with a high safety factor.





Model	Material	Equivalent Stress Distribution	Safety Factor	Weight and Volume	Features
Servoholder plus	SLS plastic	Max: 198.19 MPa Sharp transitions	Min: 1.22	Total: 44 g (part: 24 g clamp: 20 g)  16213 mm <sup>3</sup>	None
Blaze V3-1	Aluminum Alloy	Max: 26.63 MPa Uniformly distributed	Min: 9.19	Total: 25 g  8779.8 mm <sup>3</sup>	Cable tray  No need to use 20g carbon fiber clamp

**Figure 3.19** The optimized servo holder comparison with the previous model. The newly improved model surpasses the previous model in every physical performance aspect, including stress distribution (26.63 MPa maximum. vs. 198.19 MPa maximum previously), safety factor (9.19 minimum vs. 1.22 minimum previously), weight (25 g vs. 44 g previously), and usability (easy installation features added).

### 3.3.2.3 Optimization: Main Fuseluge

The main fuselage is one of the essential parts of the UAV. It is responsible for attaching most of the avionics, including LiDAR payload, on-board PC, battery, etc. Upon hard touchdown scenario or switching from aerial mode to ground locomotion mode, this part will be most likely to undertake a tremendous amount of stress and scatters, and it is a labor heavy task to repair upon wreckage. Besides the requirement of rigidity, weight is also an uncompromisable concern since the weight. Since the central fuselage part is the most significant 3D printing part, controlling its weight is the most effective way to control the whole bi-copter weight. The optimization objective for the fuselage is to reinforce the weak structure during two crash scenarios mentioned previously and aerial-ground locomotion during the switching process, while minimizing the weight as much as possible at the same time.

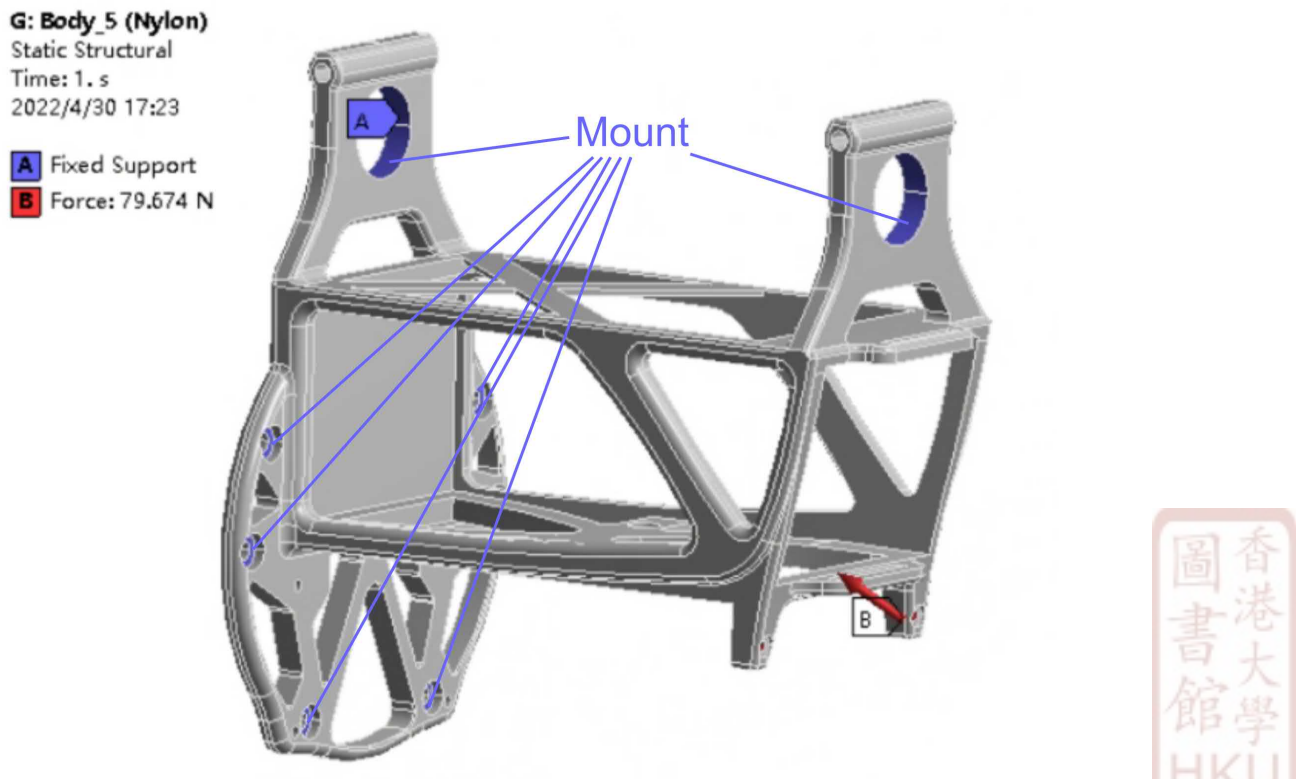


**Figure 3.20** Gemini W main fuselage with load settings. Assume the carbon fiber rod and LiDAR as the fixed mounts constraints (tagged with A), and apply a load that is equivalent to the gravitational force of battery, flight controller, power module, and the on-board computer to the remote installation holes that is the farthest from the mounting points (tagged with B).

**Figure 3.20** shows the CAD model of the main fuselage frame in the ANSYS Workbench. To maximize the stiffness of the structure, we simulate the worst-case scenario of free falling head crash. The components that need to be installed in the main fuselage mainly include the battery, flight controller, power module, and the on-board computer. In the case of impact and fall, it can be regarded as the inertial force of these components applied to the main fuselage. Set the rigid body that is attached to the main fuselage (LiDAR and carbon fiber rod) as a fixed amount (tagged with A), and apply a load that is equivalent to the gravitational force of the battery, flight controller, power module, and the on-board computer to the remote installation holes that is the farthest from the mounting points (tagged with B). The longer the distance between the mount and the applying force, the larger deformation will be taken place. Therefore, applying the force at point B will simulate the worst-case upon free falling. The equivalent gravitational force of the modules mentioned above is equivalent to 79.67N in the XYZ direction.

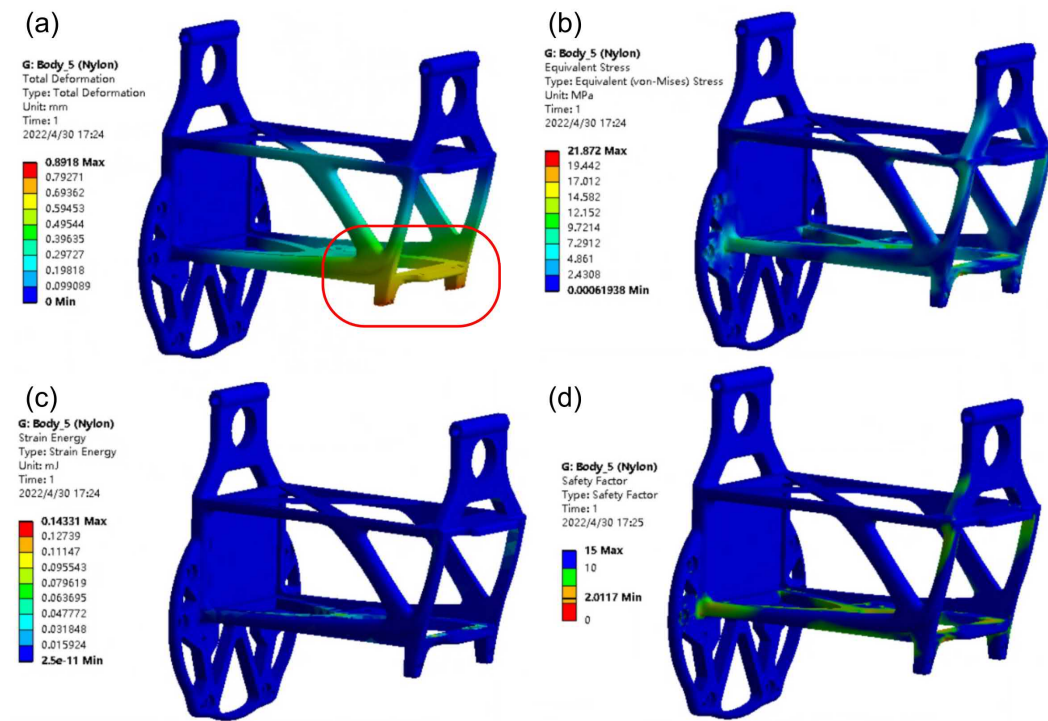
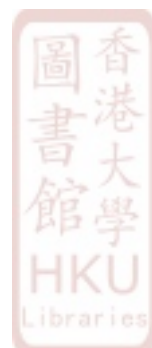


**Figure 3.21** Main fuselage simulation analysis **(a)** Total Deformation (with maximum deformation of 0.89 mm); **(b)** Equivalent Stress; **(c)** Strain Energy; **(d)** Safety Factor (with the minimum value of 2.01). The deformation is high under current load settings, and the weak spots are circled in red. Besides high deformation, the fuselage weights 67 g and needs to be reduced.



Similar to the simulation process of the servo holder part, we run the simulation to analyze the design. As shown in [Figure 3.21](#). It is obvious that the lower right area of the main fuselage suffers from visible deformations up to 0.8 mm. Besides, the bottom structure is weak and suffers a large amount of stress. On the other hand, the weight of such a part is 67 g, which increases the demand for actuator thrust and jeopardizes the control authority.

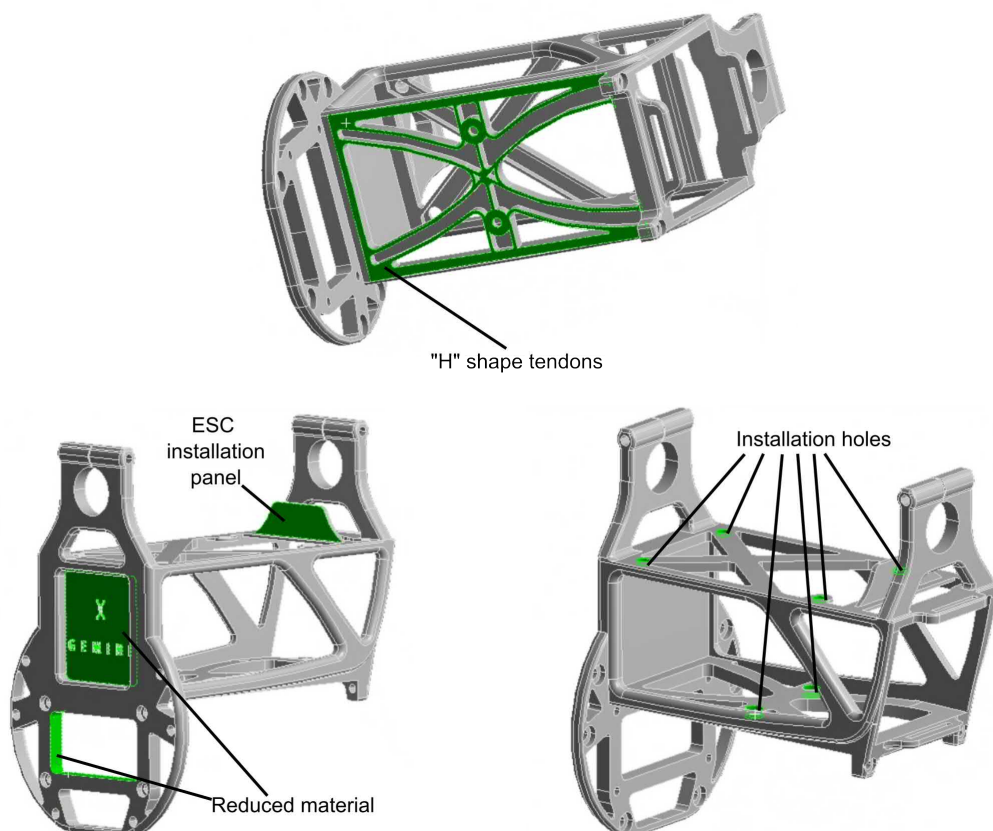


**Figure 3.22** Gemini W main fuselage structure strengthenings and features for easy installation.

We adopt the “H” shape structure with tendons added as strengtheners (shown in green). Besides the structure improvement, we also manipulated the original structure into a more space-efficient one by cutting down the non-stress-bearing structure at the LiDAR holding side. As shown in [Figure 3.22](#), the material is cut out in order to reduce the weight. A vertical plate is designed for pasting two electrical speed controllers, and multiple installation holes are for easy on-board computer and power management unit installation purposes.

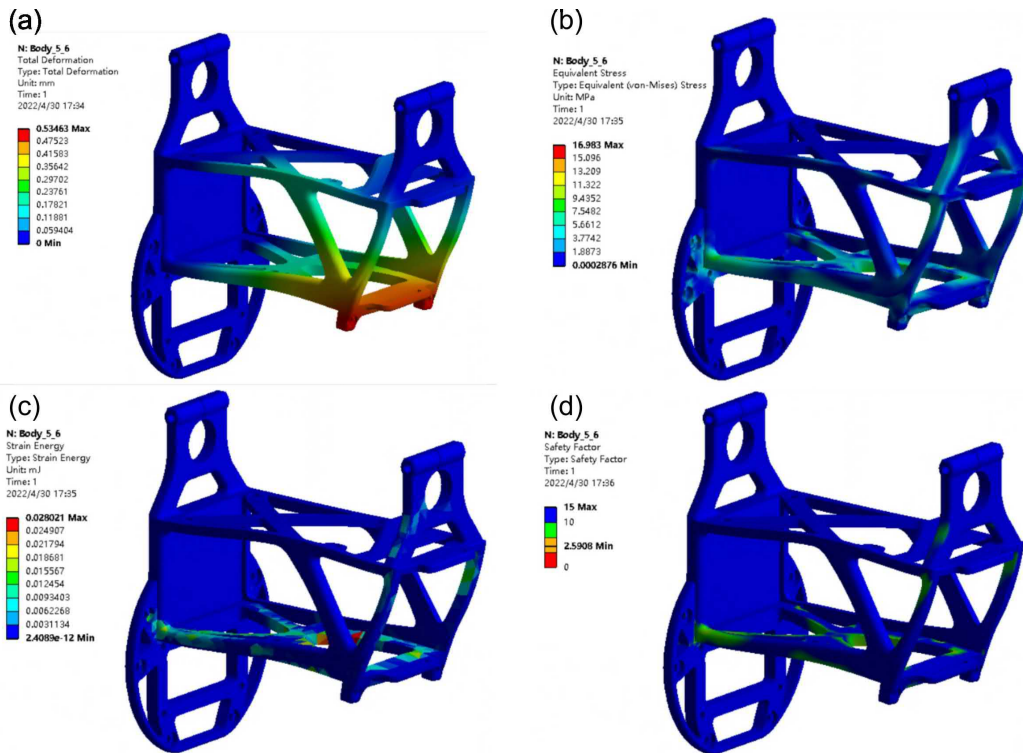


**Figure 3.23** Gemini W main fuselage simulation analysis after optimization  
**(a)** Total Deformation (with maximum deformation of 0.53 mm, and evenly distributed across the affected sections); **(b)** Equivalent Stress **(c)** Strain Energy **(d)** Safety Factor (2.5). The deformation and safety factor have been greatly improved, and the weight of the fuselage is reduced to 50 g with installation holes and ESC installation panel features added.

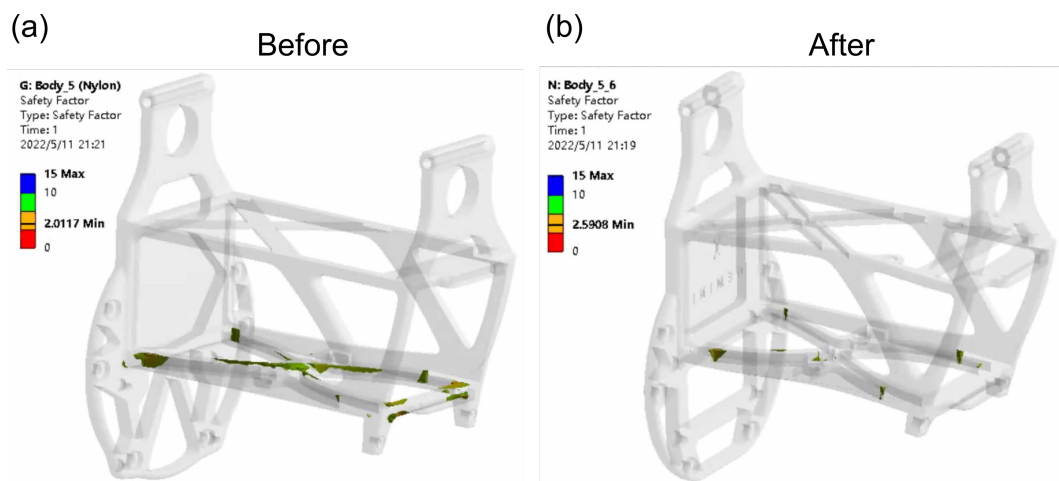
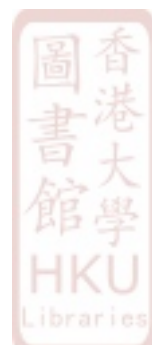


**Figure 3.24** Gemini W improved main fuselage safety factor comparison (safety factor of sections less than 5 are displayed, the improved result show significantly fewer weak spots) **(a)** The original design for comparison; **(b)** The improved result after optimization.



Model	Maximum Deformation Structure	Equivalent Stress	Strain Energy	Safety Factor	Weight and Volume
	0.83 mm	Max: 21.87 MPa Median: 9.72 MPa Unevenly distributed	Max: 0.143 mJ Average: 0.030 mJ Unevenly distributed	Min: 2.01	67g
	0.53 mm	Max: 16.98 MPa Median: 7.55 MPa Uniformly distributed	Max: 0.028 mJ Average: 0.005 mJ Uniformly distributed	Min: 2.59	50g

**Figure 3.25** The improved fuselage comparison with the previous model. The newly improved model surpasses the previous model in every physical performance aspect, including maximum deformation structure (0.53 mm vs. 0.83 mm previously), equivalent stress (16.98 MPa maximum. vs. 21.87 MPa maximum previously), strain energy (0.028 mJ vs. 0.143 mJ previously), safety factor (2.59 minimum vs. 2.01 minimum previously), and weight (50 g vs. 67 g previously).

After iterations, we analyze the model using the same method illustrated before. From Figure 3.23 we can see that the maximum deformation structure section has decreased from 0.83 mm to 0.53 mm. The stress distribution is more uniformly distributed when compared with the previous design, with significantly less median (the average stress dropped from 9.7 MPa to 7 MPa). By adopting the “H” shaped structure, the average strain energy also dropped greatly from 0.03 mJ to 0.005 mJ, with the maximum number being 0.02 mJ (marked in red). The safety factor improved from 2.01 to 2.5. In order to make the safety factor differences more easily visible to the eye, the safety factor of sections less than five is marked in Figure 3.24. It can see that the areas that are less safe have been greatly reduced. Besides the strength improvement, the weight is also reduced to 50 g, which is a 25% improvement when compared with the previous version of 67 g.

Similar to servo holder optimization, the fuselage design has also been 3D printed and tested. The actual printed part has the identical 50 g weight as the prediction, and the part has never been damaged during crashes that happened in experiments. Figure 3.25 summarizes the side by side comparison of original model vs. the improved version of the fuselage. Even though the new part and old one both uses the same nylon material, the improved version surpasses the previous one in every aspect.



### 3.3.3 Single Passive Wheel

In order to achieve aerial-ground hybrid locomotion with minimal implementation, we picked an off-the-shelf nylon wheel of proper size. The wheel weighs 20 g and can roll along its shaft (see [Figure 3.26](#)). The wheel is attached to the UAV bottom right below the center of mass, minimizing the thrust difference between two brush-less motors when operating on the ground. [Figure 3.26](#) shows the working principle of the ground locomotion with a closeup look of the wheel. With the single wheel, the vehicle is able to move in any direction following an S-shaped curve by adjusting its attitude: the vehicle moves forward with the wheel rolling on the ground by pitching down and making turns by changing the yaw directions. When making turns on the ground, the friction between the wheel and the ground will provide the centripetal force. Adjusting the UAV’s attitude both in the air and on the ground is achieved by actuating the propeller thrust and servo angle (see [86]).



**Figure 3.26** By changing the attitude and making use of the friction, the vehicle is able to move in any direction following an S-shaped curve.

### 3.3.4 Integrated PMU Board

The power management unit (PWM) that comes with the PX4 unit is shown in the upper left corner of [Figure 3.27a](#). This board is able to measure the current



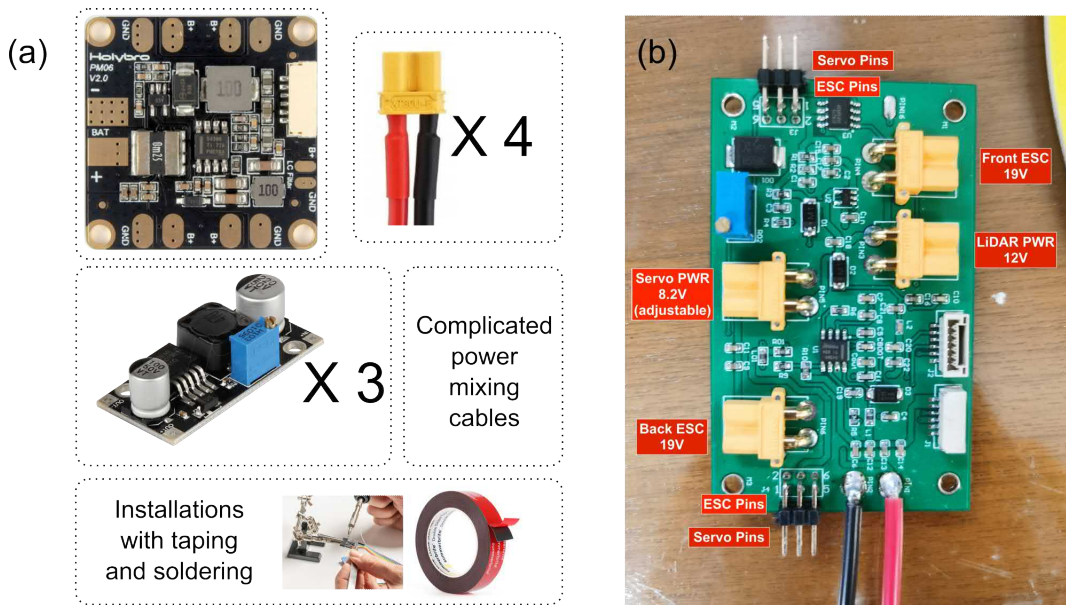
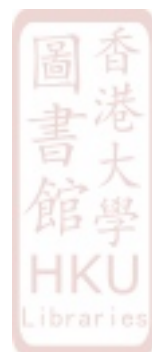


**Figure 3.27** (a) Original PX4 power distribution system; (b) Customized highly integrated PMU board. The original PX4 power distribution system weights 95 g and requires complicated installation, while the customized board integrates all these components into a single PCB board and weights only 50 g. Besides, the installation can be done in one minute.

and voltage of the battery and send the battery power information to the PX4 flight controller. However, this board only does a 500 mA small current DC step down 5V voltage for powering up the flight controller, and the main power distribution is identical to the battery voltage. Besides delivering battery voltage to two motors and a step-down buck DC to DC voltage converter, the Gemini W also requires two more different voltages for powering up the LiDAR and servo motors. Note the voltage supply for the servo motor is adjustable. Depending on the desired performance, the higher the voltage is, the faster the reaction will be. The fastest reaction speed for our chosen servo motor HV1220 is 0.115 sec per 60 degrees at no load [97], and the corresponding power supply is 8.2V. The LiDAR also demands a 12V power supply with a current that could go up to 2A.

In sum, the Gemini W requires five different voltages: 21 18V, 12V, 8.2V, and 5V. Having multiple DC buck converters is chunky in size, and the weight is heavy. Therefore, we developed a highly integrated PMU board as shown in Figure 3.27b. This board has two fixed voltage DC Buck converters (a 12 V 3 A output for LiDAR



load with a 1 A safety margin and a 5 V 500 mA output for powering up PX4) and one adjustable DC Buck converter for servo motors. A similar hall sensor and voltage sensing circuit board is adopted as what is currently used on the PX4 official PMU. Besides, the three pins servo and three pins ESC signals have both been mapped to a dedicated board.

The original PMU weights over 30 g and requires soldering for four plugs that weigh around 5 g each, three DC to DC converters that weigh around 10 g each, and complicated mixing cables that weigh around 15 g. In total, the original power distribution system weighs around 95 g. The customized PCB board not only lowered the weight to 50 g but also cut down the installation time and maintenance process. Before the new PMU, the assembling process of the Gemini mini requires manually tuning three DC buck converters, sticking them together, soldering plugs for motors, and extending the servo motor wires. The whole process usually takes more than 8 hours. With the new PMU design, the assembling is as easy as plug and play, and the only tuning parameter is tuning the potentiometer for a specific payload, which could be done in less than one minute. The mounting of the PCB is as simple as screwing it on the pre-designed mounting holes shown in [Figure 3.22](#).

## 3.4 Control

This chapter discusses the dynamic modeling and controller design behind our aerial-ground locomotion approach, especially the working principles and logic that enable the aerial-ground transition to perform seamlessly.

### 3.4.1 Dynamics Modeling

[Figure 3.28](#) shows the definition of body frame ( $x^B y^B z^B$ ) and N-E-D inertial frame ( $x^I y^I z^I$ )<sup>1</sup>. Since the vehicle dynamics in the air is identical to a bi-copter

<sup>1</sup>Throughout the text the superscript  $I$  and  $B$  will be used to denote the inertial and body frame, respectively.



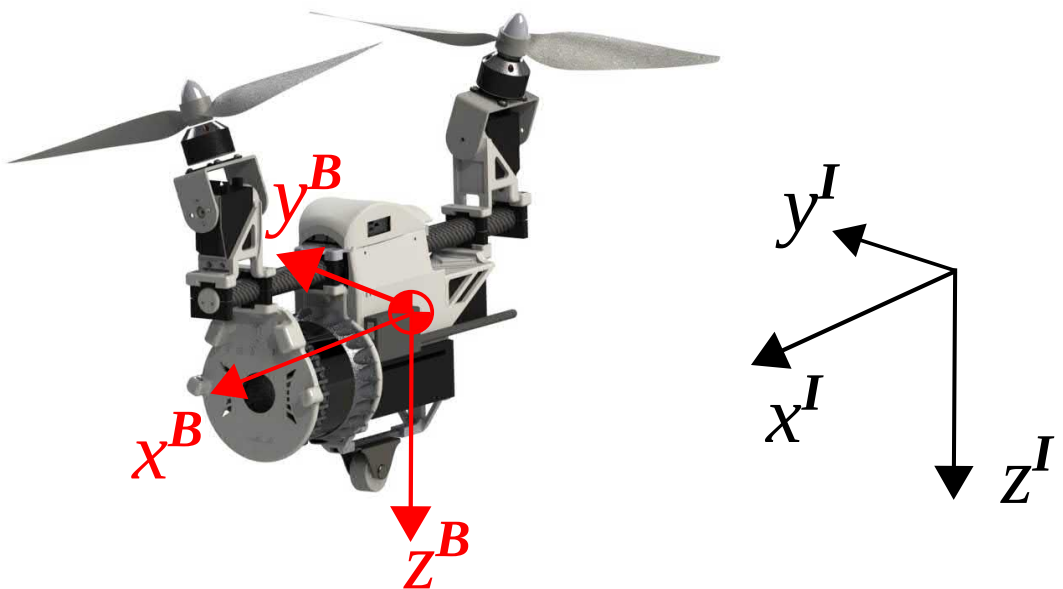


**Figure 3.28** The definition of body frame ( $x^B y^B z^B$ ) and inertial frame ( $x^I y^I z^I$ ).

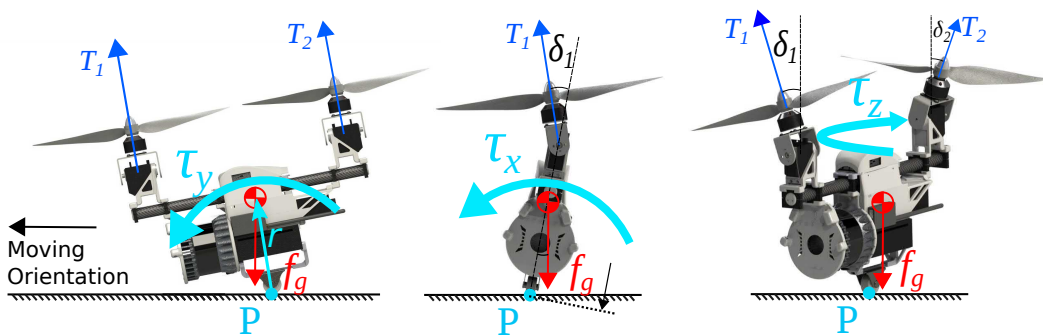


**Figure 3.29** The generation of the torque ( $\tau_x \tau_y \tau_z$ ) in rolling mode.



UAV, here we focus on the vehicle dynamics when rolling on the ground. The related notations are shown in Figure 3.29.

Assuming there is no slip between the wheel and the ground, the UAV rotates with respect to the contact point with the ground (the point P in Figure 3.29). The dynamic model of this vehicle is as below:

$$m\dot{\mathbf{v}}_{CM}^I = \mathbf{f}^I \quad (3.4a)$$

$$\mathbf{J}_P^B \dot{\boldsymbol{\omega}} + \hat{\boldsymbol{\omega}} \mathbf{J}_P^B \boldsymbol{\omega} = \boldsymbol{\tau}^B \quad (3.4b)$$

where the  $m$  is the mass; the  $\mathbf{v}_{CM}^I$  denotes the velocity of the Center of Mass (CoM); the  $\boldsymbol{\omega}$  stands for the angular rate represented in the body frame while the  $\hat{\boldsymbol{\omega}}$  is its skew-symmetric cross product matrix; the  $\mathbf{f}^I$  is the total force applied to the UAV including the gravity, thrust and other possible forces (e.g., frictions with the ground); the  $\mathbf{J}_P^B$  and  $\boldsymbol{\tau}^B = [\tau_x \quad \tau_y \quad \tau_z]^T$  denote the inertia matrix and total torque with respect to the point P; Here denotes the torque generated by thrusts ( $T_1$  and  $T_2$  in Figure 3.29) as  $\boldsymbol{\tau}_t^B$  whose detail can be found in our previous work [86]. One of the main difference between the rolling dynamic and hovering dynamic is that the gravity will produce extra torque, as shown in Figure 3.29 and Eq. 3.5:

$$\boldsymbol{\tau}^B = \boldsymbol{\tau}_t^B + \hat{\mathbf{r}}^B \mathbf{f}_g^B \quad (3.5)$$

where  $\mathbf{r}^B$  stands for the distance vector from point P to CoM that is a constant vector in body frame. For the translational motion on the rolling mode, the velocity of CoM (i.e.,  $\mathbf{v}_{CM}^I$ ) should be:

$$\mathbf{v}_{CM}^I = \mathbf{R} (\mathbf{v}_P^B + \hat{\boldsymbol{\omega}} \mathbf{r}^B) \quad (3.6)$$

where  $\mathbf{R}$  denotes the rotation matrix from the inertial frame to the body frame following the Z-Y-X Tait-Bryan order where  $\eta$ ,  $\theta$ , and  $\varphi$  stand for the yaw, pitch, and roll Euler angle, respectively,  $\mathbf{v}_P^B = [v_{Px}^B \quad v_{Py}^B \quad v_{Pz}^B]^T$  is the velocity of point P represented in body frame. It should be noted that no slipping between the wheel and the ground means  $\mathbf{v}_P^B = v_{Px}^B \mathbf{e}_1$  where  $\mathbf{e}_1 = [1 \quad 0 \quad 0]^T$ . Therefore, the derivation



of CoM velocity is:

$$\dot{\mathbf{v}}_{CM}^T = \mathbf{R} \left( \dot{v}_{Px}^B \mathbf{e}_1 + \hat{\boldsymbol{\omega}} \mathbf{r}^B + \hat{\boldsymbol{\omega}} v_{Px}^B \mathbf{e}_1 + \hat{\boldsymbol{\omega}}^2 \mathbf{r}^B \right) \quad (3.7)$$

Next, the total force consists of the friction force  $\mathbf{f}_f$ , support force  $\mathbf{f}_N$ , gravity force  $\mathbf{f}_g$  and thrust force  $\mathbf{f}_T$  as below

$$\mathbf{f}^T = \mathbf{f}_f^T + \mathbf{f}_N^T + \mathbf{f}_g^T + \mathbf{R} \mathbf{f}_T^B \quad (3.8)$$

Putting [Eq. 3.5](#), [Eq. 3.7](#) and [Eq. 3.8](#) back into [Eq. 3.4](#), we can get the detailed dynamic model of rolling mode:

$$m\mathbf{R} \left( \dot{v}_{Px}^B \mathbf{e}_1 + \hat{\boldsymbol{\omega}} \mathbf{r}^B + \hat{\boldsymbol{\omega}} v_{Px}^B \mathbf{e}_1 + \hat{\boldsymbol{\omega}}^2 \mathbf{r}^B \right) = \mathbf{f}_f^T + \mathbf{f}_N^T + \mathbf{f}_g^T + \mathbf{R} \mathbf{f}_T^B \quad (3.9a)$$

$$\mathbf{J}_P^B \hat{\boldsymbol{\omega}} + \hat{\boldsymbol{\omega}} \mathbf{J}_P^B \boldsymbol{\omega} = \boldsymbol{\tau}_t + \hat{\mathbf{r}}^B \mathbf{f}_g^B \quad (3.9b)$$

### 3.4.2 Controller Design

In order to implement automatic switching from aerial mode to rolling mode, additional control needs to be implemented. This section illustrates the detail of the control process in each stage of the aerial-ground locomotion.

#### 3.4.2.1 Aerial Mode

As shown in [Figure 3.30](#), the bi-copter is in aerial mode when it flies over a height  $D_H$  or where no ground effect is present. Its velocity and attitude are controlled through a cascaded controller as shown in [Figure 3.31](#). The details about the velocity controller and aerial attitude controller has been illustrated in our previous paper [86]. Throughout the experiment, the velocity controller is robust enough for the whole transition process. The aerial attitude controller can stabilize the bi-copter in aerial mode and transition modes but will fail in rolling mode, where a change of



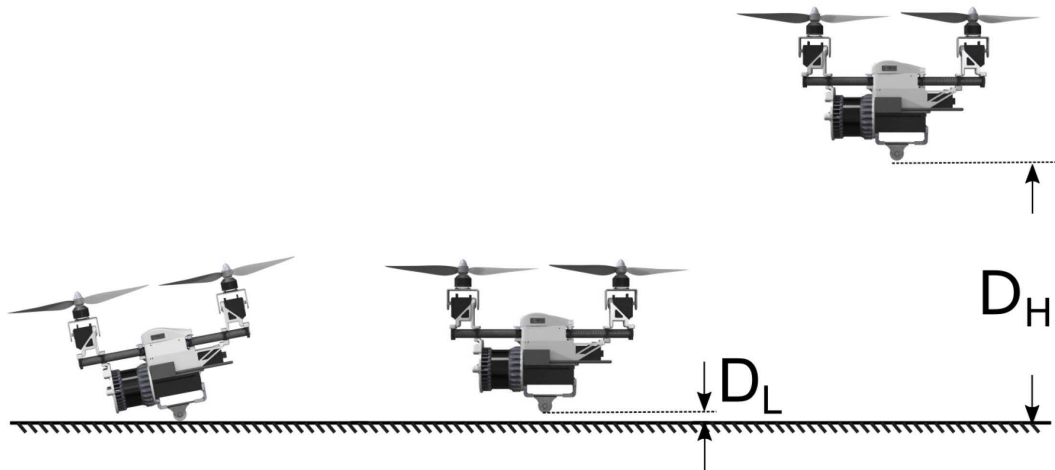


**Figure 3.30** Different phases of the hybrid aerial-ground locomotion: above  $D_H$  is the aerial mode, below  $D_L$  is the ground locomotion, and between them is the transition.

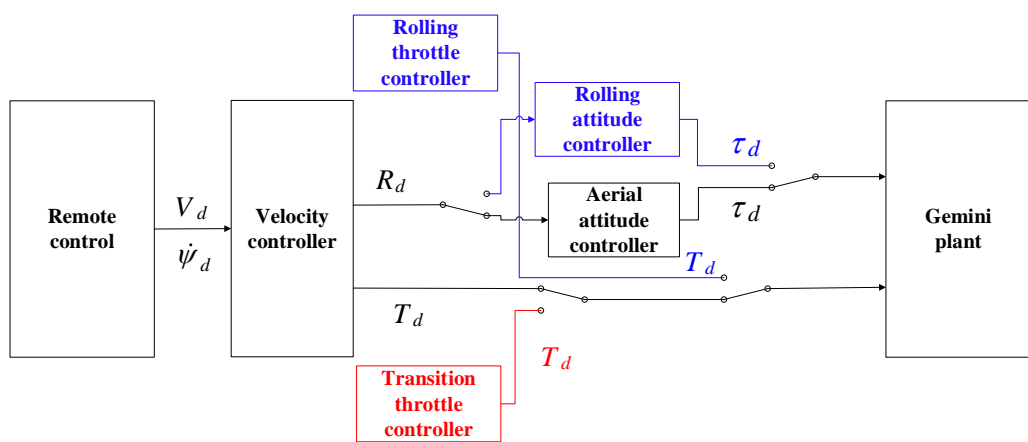


**Figure 3.31** Controller block diagrams: black blocks are used in normal aerial flight, red blocks are turned on when in transition mode and blue blocks are for control when rolling on the ground.



attitude controller will occur.

### 3.4.2.2 Transition Mode

When the pilot turns on the transition switch, transition mode will be entered if the aircraft's height is lower than  $D_H$ . Once entered, the throttle command is controlled automatically in this mode. The aircraft approaches the ground by gravity when the throttle is lowered. To prevent a sudden falling, we set the throttle command to gradually decrease. Because the ground effect increases as the vehicle approaches the ground surface [98], the throttle has to be decreased further to balance the additional lift caused by ground effect. The precise identification of the ground effect is not our primary concern at this stage of work. We found the simple linear decrease of the total throttle applied on  $z^B$  direction works well in practice, and the relation is the following:

$$T_d = T_h(1 - Kt) \quad (3.10)$$

where  $T_h$  is hovering throttle near the ground, and  $K$  is the decreasing rate. Landing is automatically detected if the wheel touches the ground surface (i.e., the height of the wheel is below  $D_L$  in [Figure 3.30](#)) for a certain time. After this, the controller will switch to rolling mode.

### 3.4.2.3 Rolling Mode

As mentioned previously, the dynamics of the rolling mode are considerably different from the aerial mode. The attitude can not be controlled using the same attitude control parameters as in aerial mode. Otherwise, the vehicle will go unstable and crashes within seconds. To overcome this, we use a new set of attitude controller parameters with the same structure (i.e., PID) as the aerial mode, which can be found in [86]. The PID parameters are re-tuned based on our previous dynamics analysis. Due to additional torque caused by gravity in [Eq. 3.9b](#), the aircraft by itself is an unstable system like an inverted pendulum. As a result, the controller needs to have higher actuator values to compensate for the changes. Therefore we mainly



tuned P and I and quickly got a good performance. The agility of rolling motion is determined by the throttle command, and the ideal parameter is also obtained from the trial and error method.

## 3.5 Experiment Validation

In order to validate the feasibility of our design in enabling aerial-ground hybrid locomotion, we conduct various flight experiments. We present the results in aerial-ground transition and ground locomotion and refer readers to our prior work [86] for detailed aerial locomotion results. The experiments are conducted in an indoor environment equipped with OptiTrack motion capture systems providing the position feedback. An ultra wide-band module is used to transfer the position data to the on-board Pixhawk 4 mini flight controller. A full payload of 500 g is used to simulate the weight of a 16-line LiDAR (Ouster-16, weighing 380 g) and its connectors. The total takeoff weight of the whole UAV is 1950 g. Besides mobility tests, energy efficiency is also a core feature of hybrid locomotion. Therefore, we conduct a comparison study on power consumption in various conditions such as normal hovering, standing still on the ground, and rolling on the ground.

### 3.5.1 Feasibility Validation

To test the feasibility and performance of our design, we conduct the aerial-ground transition test and the ground locomotion test. The position, velocity, attitude, and acceleration data is provided.

#### 3.5.1.1 Aerial-ground Transition

By using trial and error method during flight tests, we conclude that these following parameters has 90% chance of soft touchdown among 10 tests:  $D_H = 0.2m$



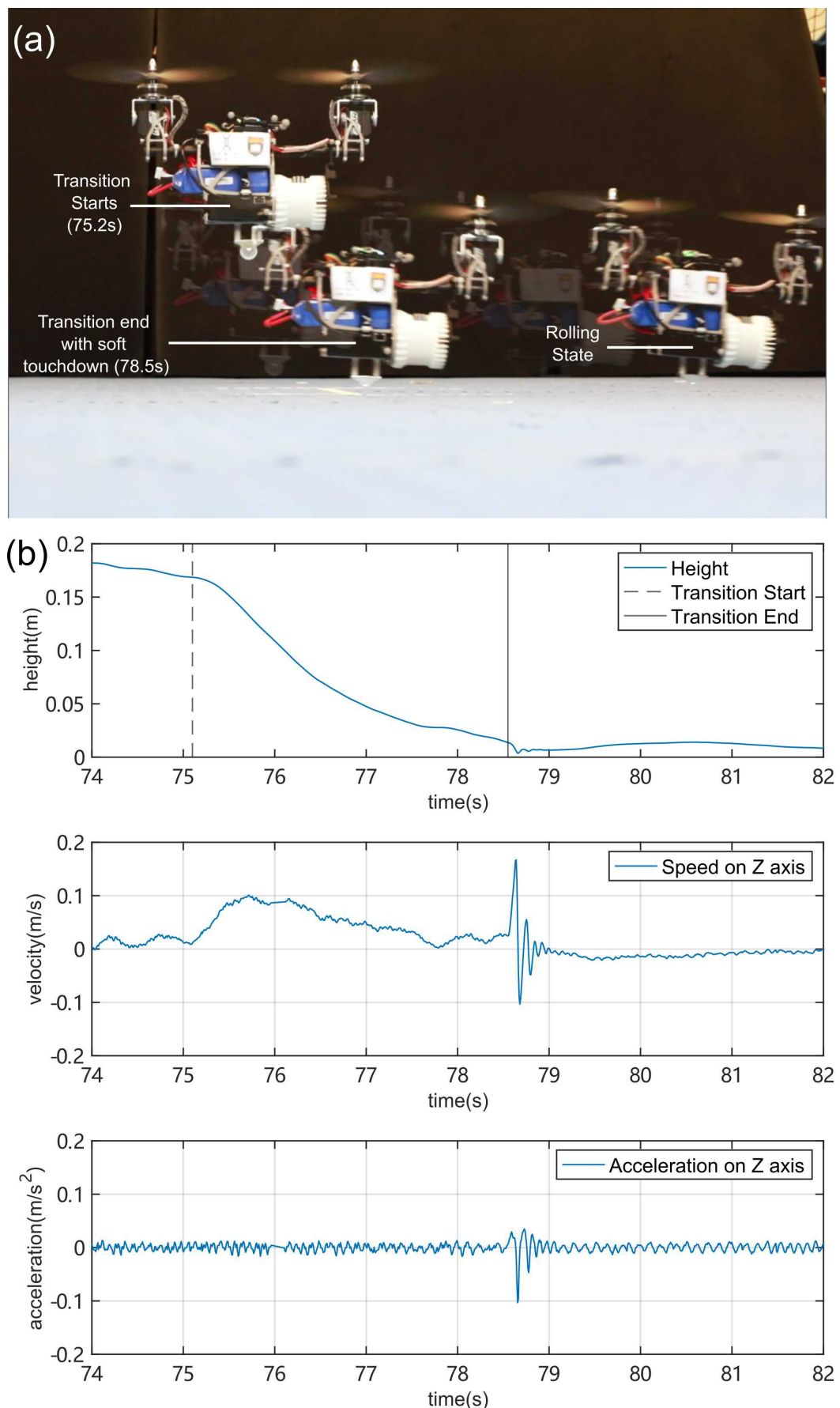
$D_L = 0.01m$   $K = 0.35\% / s$   $\delta t = 0.15s$ . Figure 3.32a shows the UAV poses at different times during the transition process overlaid together. The aircraft is initially hovering at the height of 15 cm above the ground and initiates a transition (at around 57.2 s). It can be seen that the UAV successfully completes the transition and continues to move on the ground without interruption. Figure 3.32b and Figure 3.33 report the vertical translation and rotation during the landing process. After the landing command is sent out to the flight controller, the velocity in the Z direction increases to lower the height, and then decelerates until it reaches the ground surface to give the landing a soft touchdown. Due to the imprecision of the position feedback, the system received the signal of reaching the ground surface while it is actually a little bit above, throttle drops immediately, resulting in a spike oscillation afterward. The oscillation soon drops down and back to normal in half a second. The height data shows a little bounce back after the lowest point, but the whole transition process went on smoothly, and the bounce oscillation is barely observable by the eyes.

Attitude control is close to the idea. Even though the touchdown shocks the roll angle, resulting in an 8 degrees angle disturbance, it rapidly recovered to normal within half a second. The soft touchdown barely has any effect on the yaw angle, and the pitch angle almost stays intact except for a trivial disturbance of around 3 degrees. The success of this experiment proves the feasibility of the concept of hybrid aerial-ground locomotion with a single passive wheel on a bi-copter.

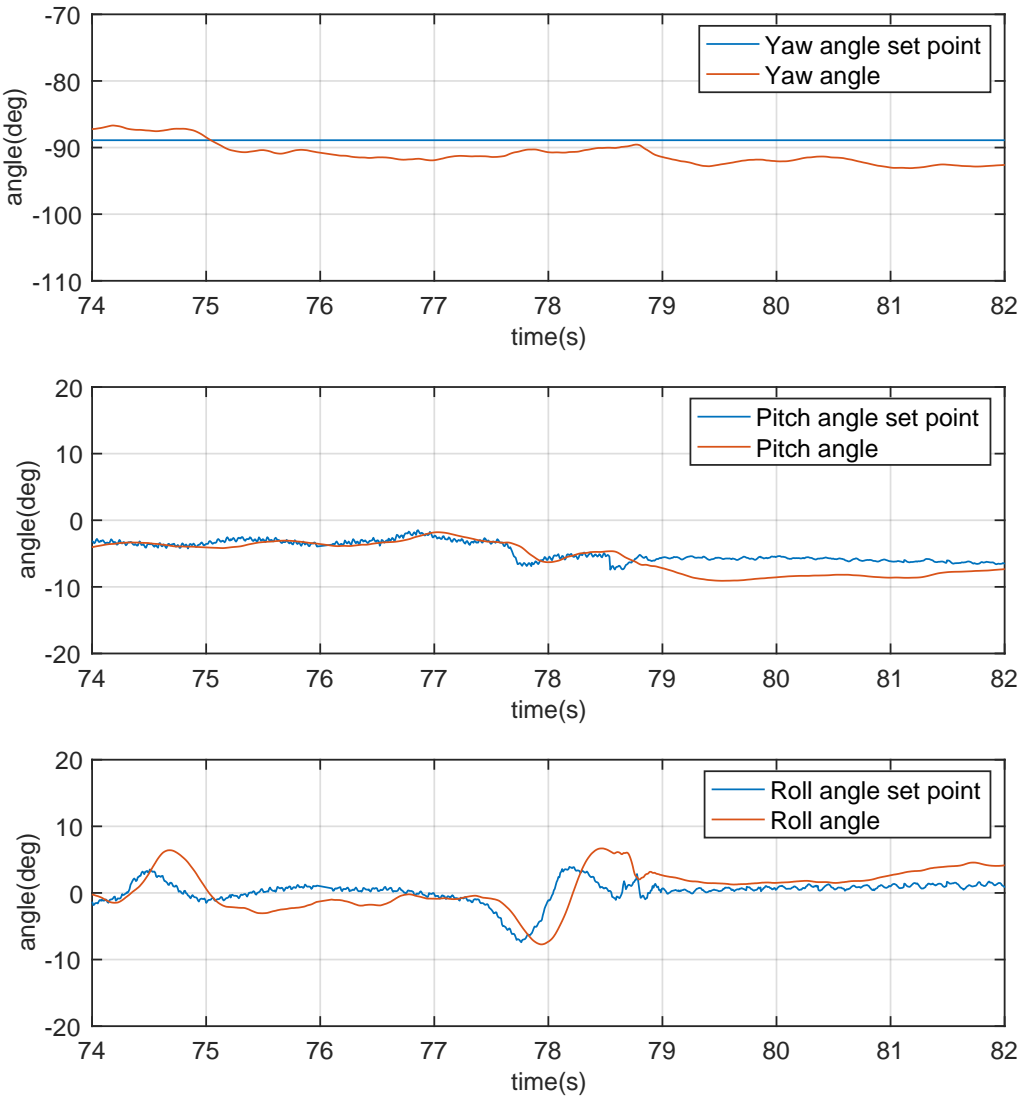
### 3.5.1.2 Ground Locomotion

Figure 3.34 shows the attitude and velocity response when the aircraft is rolling on the ground back and forward. Velocity in the body X direction is commanded while the rest are set to zero. As expected, the velocity profiles in all three directions are tracked well. Inspecting the attitude responses, we found that the pitch command is varying to achieve the translation along that direction while the rests are around zero;





**Figure 3.32** (a) Aerial-ground transition process; (b) The vertical position, velocity, and acceleration during aerial-ground transition.

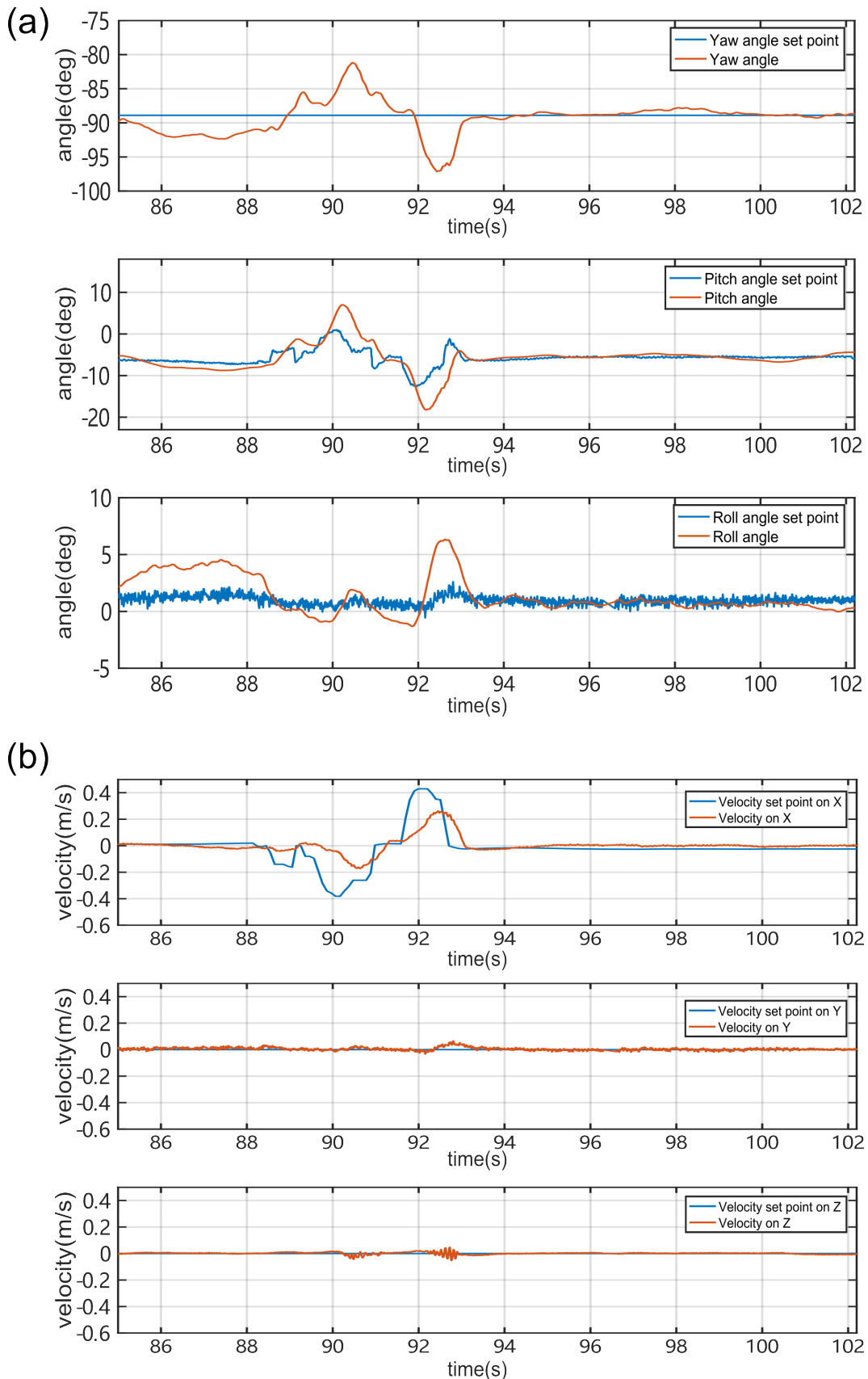


**Figure 3.33** The attitude response during the aerial-ground transition.

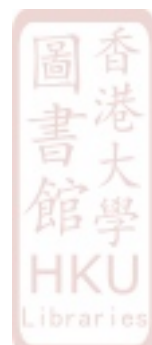
all are within our expectation. The attitude responses suffer from some fluctuations, especially in yaw and roll, but overall remain stable. The roll suffered around 5 degrees of fluctuations after the rolling stops; the yaw has 10 degrees of fluctuations towards the right while accelerating and 10 degrees of fluctuations towards the left while the rolling stops. These fluctuations are due to the friction between the wheel and ground, which is not seriously compensated in our attitude controller. Improving the attitude controller performance by carefully modeling and exploiting these contact forces will be interesting future work.

Besides following a straight line, we also command the vehicle to follow an “8” figure on the ground. The whole process is overlaid and shown in [Figure 3.35](#).





**Figure 3.34** (a) Attitude response when rolling on ground. (b) Velocity response when rolling on ground.



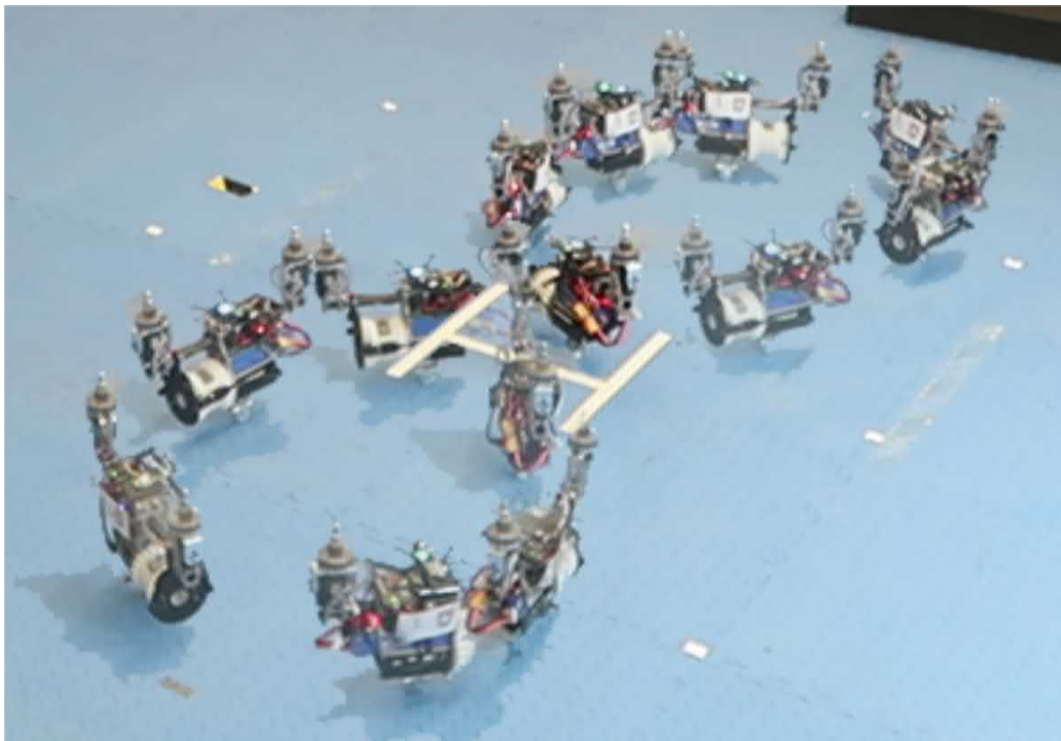


**Figure 3.35** Rolling on the ground following a pattern “8”.

### 3.5.2 Efficiency Demonstration

To test the efficiency of the ground locomotion approach, we tested the UAV to roll on the ground following the radio controller command and predesigned pattern. The attitude and velocity data during the rolling state are provided.

#### 3.5.2.1 Power Consumption Comparison

Empirical power consumption comparisons among different flight phases are reported in [Figure 3.35](#). The power consumption data are gathered when the aircraft is hovering high above the ground surface with no ground effect (H state), rolling on the ground surface (R state), and sitting still on the ground surface, respectively (S state). It can be seen from the figure that sitting on the ground consumes the least power. Rolling on the ground costs a bit more energy than sitting as the aircraft has



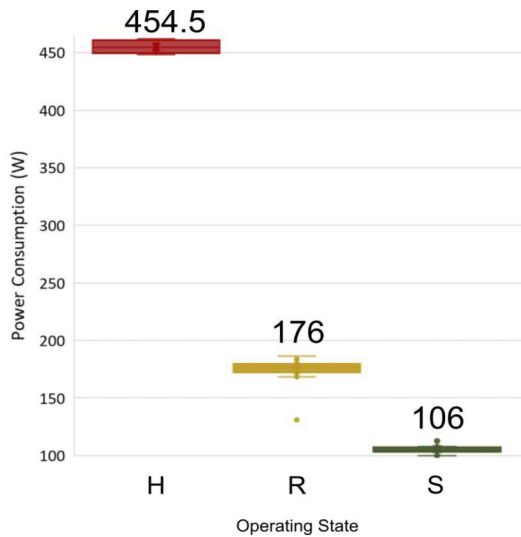


**Figure 3.36** The power consumption comparison among different states: hovering state (H), rolling on the ground state (R), sitting on the wheel state (S). The numbers above each bar are the mean power consumption of the state over 10 seconds.

to overcome the friction. In conclusion, when comparing the H state, R state, and S states save 61, and 77% power, respectively. This proves the considerable energy saving with the ground locomotion.

## 3.6 Discussion and Conclusion

This chapter proposes novel aerial-ground hybrid locomotion with a single passive wheel based on the Gemini mini bi-copter presented in the previous chapter. The design iteration, implementation optimization, control, and flight experiment are presented. Unlike previous aerial-ground locomotion works that sacrifice weight for heavy chassis to achieve hybrid locomotion, our approach achieves great power efficiency advantages of the ground locomotion with the minimal addition of a single wheel that weighs only 1% of the total takeoff weight. Flight experiments validated the feasibility and efficiency of our proposal.

A drawback of the Gemini W single-wheel design is that the system is inherently unstable and cannot land on the ground. An extra landing station is required for parking. As shown in the video, a white topless cardboard box is used for takeoff



and landing. The inherently unstable system dynamics may also lower the vehicle stability when moving on rough terrains. Even with flat ground, the current control strategy involves complicated switching strategies and relies on many human tuning efforts.

### 3.7 Related Publications

**Qin Y.**, Li Y., Xu W., and Zhang F., “Hybrid aerial-ground locomotion with a single passive wheel,” in *IEEE/RSJ International Conference on Intelligent Robots and Systems (IROS)*, 2020.

Li Y., **Qin Y.**, Xu W., and Zhang F., “Modeling, Identification, and Control of Non-minimum Phase Dynamics of Bi-copter UAVs,” in *IEEE/ASME International Conference on Advanced Intelligent Mechatronics (AIM)*, pp. 1249-1255, July 2020.



# Chapter 4

## Hong Sun: Swashplate-based Bi-copter

### 4.1 Introduction

The Gemini bi-copters introduced in previous chapters are highly efficient for small-scale UAVs. However, when scaling up the UAVs, huge servo motors usually have the limitation of being bulky in size, heavy in weight, and requiring constant maintenance. Servo motors use a gearbox to achieve large torque. The weariness of the gearbox, however, will become more and more severe as the weight of the aircraft increases. Since the servo motor is constantly tilting with a large load, the gaps between gears increase, thus introducing non-linearity to the UAV system and decreasing its flight performance. Moreover, according to Xian *et al.*, the frequent tilting of the servo will increase the risk of its stuck fault greatly [99], putting the stability of the aircraft at risk.

The larger the aircraft is, the more critical role the safety factor will play. As a result, large-sized bi-copter aircraft usually adopt the swashplate mechanism. This chapter introduces our attempt to build a swashplate-based bi-copter, including its corresponding propulsion system design and testing.



## 4.2 Related Works

The swashplate mechanism is a complex nonlinear system with three degrees of freedom (DOF) that produces pitch, roll, and heave motions [46]. Many previous researches have been done on the swashplate topic. Lange et al. derived a complete kinematic model of the swashplate employed at the CL-327 Guardian unmanned helicopter using parallel robotic manipulators' forward and inverse kinematics framework [100], and conducted the dynamic analysis of this mechanism with the derivation of the equations of motion free of constraint wrenches using the method of the natural orthogonal complement (NOC) [101]. Using the principle of virtual work and the concept of link Jacobian matrices, Sabaapour et al. achieved another systematic research regarding the swashplate mechanism with a Bell-Hiller mixer [102]. The work mentioned above requires a flybar mechanism to improve the cyclic stability and make the cyclic control much more manageable. However, such a mechanism is complex and adds extra weight to the system.

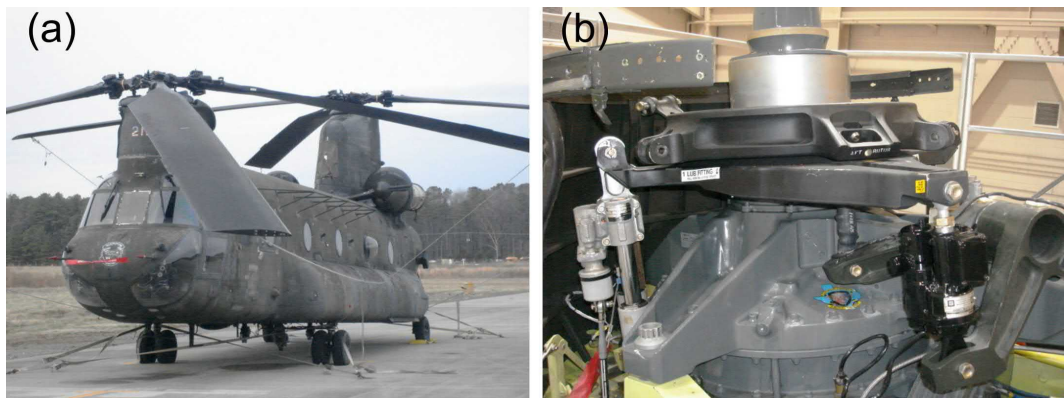


**Figure 4.1** Boeing CH-47 Chinook military bi-copter: (a) Aircraft [44]; (b) Swashplate mechanism [45].

The flybar-less (FBL) swashplate mechanism uses an electronic stabilization system to compensate for manageability, thus is less mechanical intricate in structure and lighter in weight [46]. Another benefit of the FBL rotor is that the inputs from the swashplate go straight to the main rotor blades, therefore the response is direct and faster [103]. Bi-copters such as Boeing CH-47 (shown in Figure 4.1a) achieve control over their cyclic pitch by using such kind of flybar-less swashplate



mechanism (shown in [Figure 4.1b](#)).

### 4.3 Working Principle

For small-sized UAVs, the FBL is widely applied for higher maneuverability and lighter weight. [Figure 4.2a](#) shows an example of the FBL swashplate mechanism and its simplified model without a drag arm is shown in [Figure 4.2b](#).

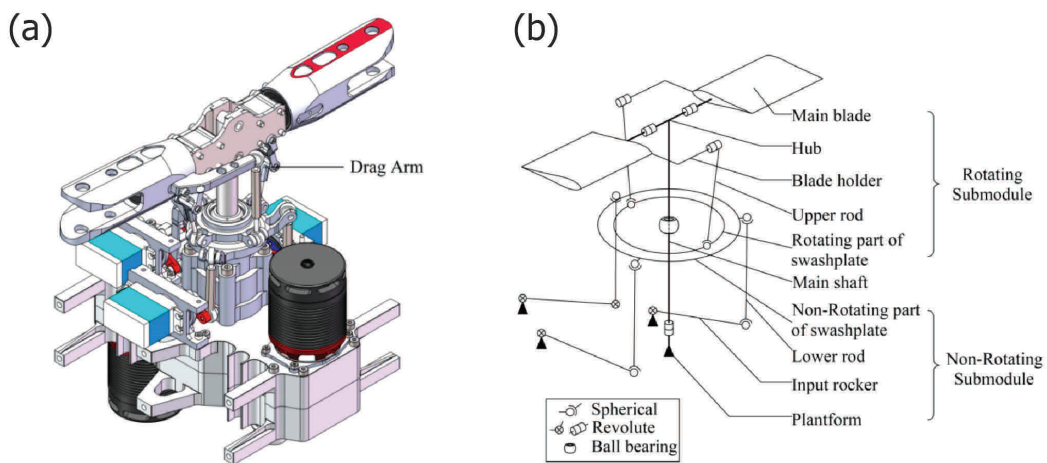


**Figure 4.2** Flybar-less swashplate mechanism **(a)** The assembled flybar-less swashplate mechanism example; **(b)** Simplified schematic of the proposed swashplate mechanism with the essential joints. **Image Source:** [46]

The whole mechanism consists of the Non-Rotating submodule (NR-SM) and the Rotating submodule (R-SM). The NR-SM is a 3-DOF motion platform that controls the attitude of the swashplate. Usually, two or three servo actuators are fixed on the platform of the helicopter body and bonded to the Non-Rotating part of the swashplate in a 180° or 120° arrangement through lower rods and input rockers. The swashplate connects the main rotor shaft through the swashplate ball bearing in the form of spherical and cylindrical joints. The cylindrical components allow a sliding motion to manipulate the collective control (also known as the heave) along the axis of the main shaft and a free rotation around the main shaft. The spherical components allow the swashplate to rotate about two axes in its plane, achieving cyclic controls authorities. The rotating part of the swashplate connects to the non-rotating part



through a revolute. The two propeller blades are attached to the rotating part with blade holders and upper rods. Each propeller blade is mounted to the hub through a revolute joint. The whole R-SM is granted the freedom to rotate with the main rotor shaft.

## 4.4 Hong Sun: Swashplate Bi-copter

The design objective of project Hong Sun is to develop a bi-copter platform that is able to achieve not only hovering for around 30 minutes but also level flight for longer cruising time utilizing only two FBL swashplate propulsion systems (no tilting mechanism as Boeing V-22). The concept of the Hong Sun is shown in [Figure 4.3](#). Note the scissor-shaped stands are the retractable landing gear, and the transparent cone shape is the field of view (FOV) of the LiDAR payload.

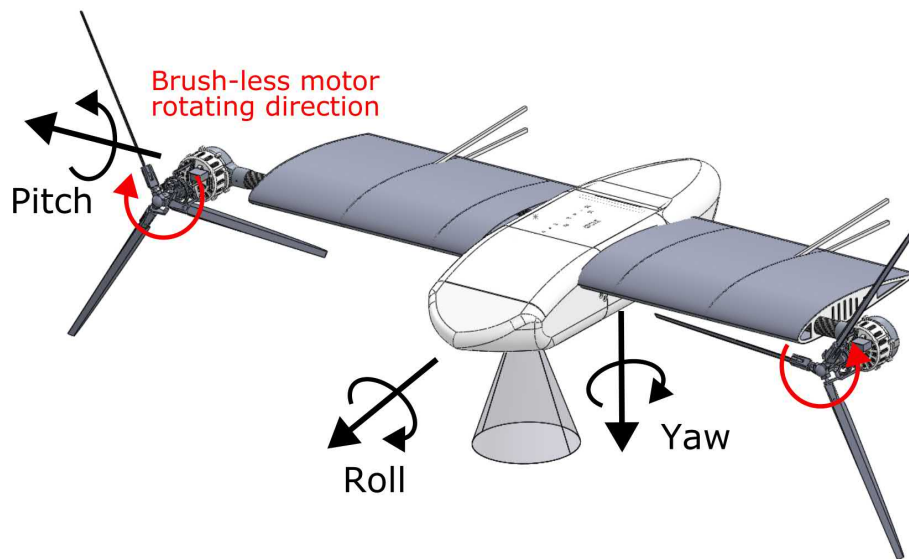
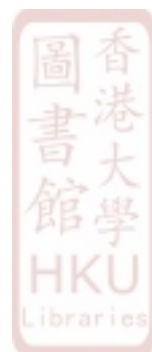


**Figure 4.3** The Hong Sun bi-copter concept. Hong Sun is a bi-copter powered by two FBL swashplate propulsion systems. The Hong Sun has a wingspan of 155 cm and is designed for 5 Kg takeoff weight. With a 50000 mAh 12s battery on board, it is expected to hover for around 30 minutes or level flight for even longer flight efficiency.

[Figure 4.4](#) shows the one propulsion system of Hong Sun. For mechanical simplicity, Hong Sun adopts two servo actuators in a 180° arrangement, and each propulsion system consists of three actuators. The DJI E2000 is a 130KV brushless



motor, and it generates actuator thrust by actuating the propeller. Two ALZRC DM1232s servo motors control the swashplate NR-SM, so that both heave and pitch control authority can be achieved. To be more specific, when two servo motors both pull the pulley down to the bottom of the motor cage, the AOA of the propeller blades will reach maximum (shown in Figure 4.4a), achieving the largest heave. On the other hand, when two servo motors both push the pulley up, the AOA of propeller blades will reach a minimum (shown in Figure 4.4b) with the minimum heave. Large AOA generates higher thrust than smaller AOA under the same rotating speed. The collective control authorities of thrust generating by rotating speed and AOA add redundancy to the system during hovering and yaw control during level flight, increasing the safety at the same time.

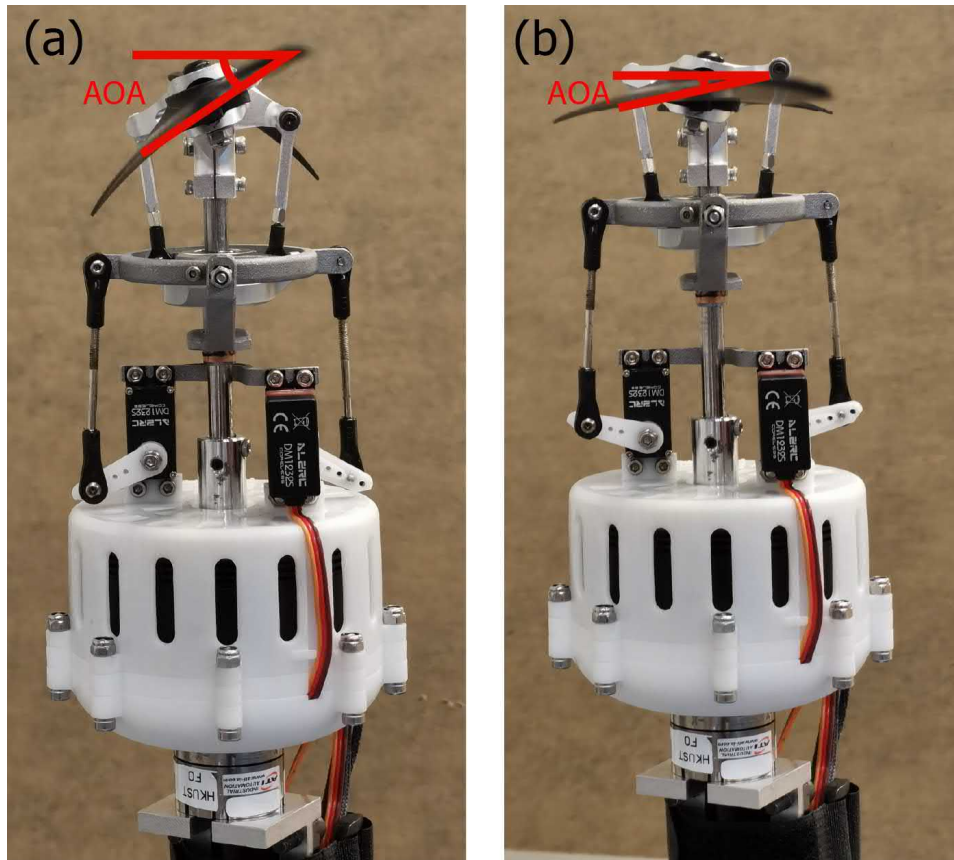


**Figure 4.4** Controlling the Hung Sun propulsion system heave with servo motor **(a)** Maximum AOA for maximum heave; **(b)** Minimum AOA for minimum heave.

When two servo motors pose at different angles, the swashplate cyclic blade pitch system is able to generate component forces to generate torque on the body in



roll and pitch directions, enabling the full attitude control of the bi-copter.

#### 4.4.1 Propulsion System Test

Unlike previous bi-copter projects, which already have specific payload choices, the onboard space is very limited, so deciding the payload and avionics must be the first step. The Hong Sun is a general-purpose UAV that has huge capacity and high thrust generation redundancy. As a result, to build the whole system, the first step is to model the performance of the actuator.

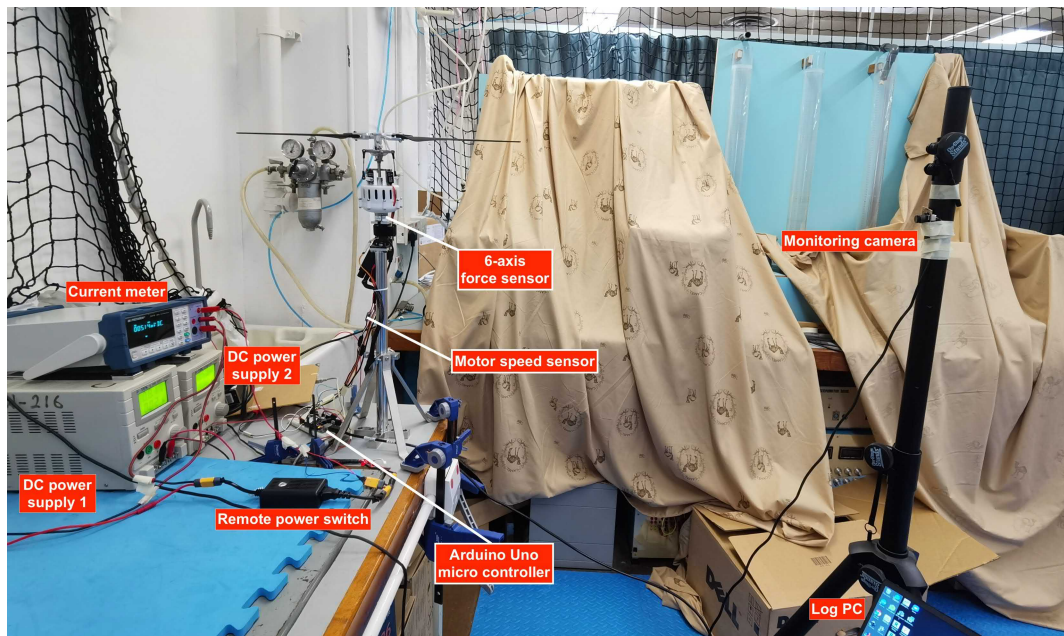


**Figure 4.5** Hong Sun propulsion system test setup. The power consumption and force generation are monitored through this setup.

The propulsion system test setup is shown in [Figure 4.5](#). The goal of this test is to measure the power consumption (including voltage and current), as well as the actuator performance (6-axis force and momentum data) throughout all actuator combinations. The motor demands high voltage (50.2 V DC operating voltage, with an estimated 12A current), and the servo motors are powered with 8.2V DC, so two DC power supplies are used. The current is measured with Keithley high voltage current multimeter, with direct serial port output into the logging PC in MATLAB.



The voltage is measured with a simple voltage divider circuit with Arduino, which is also capable of outputting data directly to MATLAB with Arduino data acquisition extension (DAQ)[104]. The force/torque sensor is ATI mini40, and it is capable of sensing 240 N force on the Z-axis and 80 N on the lateral axes. Besides, it is also able to measure the torque on XYZ axes with the maximum limit of 4 Nm on a single axis. The ATI mini40 sensor generates analog signals, which are picked up by the NI USB 6009 high precision analog to digital converter (ADC). Besides collecting the F/T data, it also measures and interpolates the brushless motor speed from the PPM signal differentials of two branches from the ESC signal. The output of the NI USB 6009 is then directly sent to the MATLAB DAQ, where all the data is collected and synchronized.

Since this experiment contains high voltage and high speed rotating propellers, so for safety concerns, a remote power switch is connected in serial with the brushless motor power supply. In case of emergency, the test conductor is able to kill the main power switch from a maximum of 2 kilometers away. A monitoring camera is placed 1 meter away from the rotating propeller for analysis purposes.

The testing command is a nested for loop where we sweep the throttle from 40 % to 70 % (When the throttle goes above 70 %, even the 3D aluminum structure is usually unable to bear the stress. Besides, the designed working zone shall fall around 50% throttle. For practical and safety reasons, this range is chosen), and the servo angle is swept inside of the loop. Each loop will last for 5 seconds, and then the data is taken from the average of the measurement from 2 seconds to 3s of each step. The test data is shown in [Figure 4.6](#).

During the motor test, huge vibration causes the propeller to make a huge noise, and this phenomenon gets more severe as the rotation speed goes above 3500 RPM. As shown in [Figure 4.7](#), the propulsion system has a 10 centimeters motor shaft which leaves necessary space for the swashplate mechanism. Since the motor shaft is long, its precision, especially the straightness, will be exaggerated with rotational speed. However, the precision shaft shall be customized with high-precision CNC machines. Experientially speaking, 0.01 mm precision CNC part will cost ten times







**Figure 4.7** The long motor shaft in Hong Sun propulsion system. Due to non-ideal factors such as manufacturing error or wastage, the long shaft tends to bend and causes vibrations when rotating at high speed.

more than 0.1 mm parts.

Besides the high manufacturing price, even a precise CNC manufactured shaft is hard to maintain. Due to the heavy propeller head and propeller, the rotational inertia has a relatively high value, and sudden acceleration/deceleration and collision could cause the shaft to bend.

The maintenance is also a highly complex process to replace the shaft and the swashplate mechanism. Not only do the ball bearings need to be replaced, but also constant lubrication is needed. Otherwise, more energy will be required to counteract the friction.

Not only does the brushless motor shaft needs to be constantly checked, but the servo motor also tends to be fragile over time. Due to the nature of servo motors, the gearbox within the servo motor tends to develop bigger gaps as the machine operates, especially under such a heavy load.



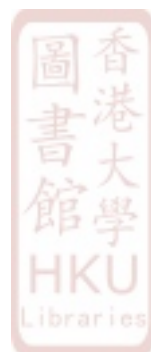
Heat dissipation is another problem as the testing goes on for more than 10 minutes. Since this design mainly utilizes a 3D printed nylon cage to support the servo motors, the heat will be trapped inside the cage. Overheating will potentially cause the enameled wires to melt and short the circuit, making the whole system unstable.

Last but not least, the propulsion system is heavy and oversized. Not only does the swashplate mechanism, servos, and pulleys are gigantic, but the servo motors also need to be powered with a high current DC power supply. The high current DC buck converter usually has huge capacitors and inductors, which seriously jeopardizes the already very limited onboard spaces.

#### 4.4.2 Fuselage Design

As shown in [Figure 4.8](#), the fuselage of Hung Sun mainly consists of three chambers at the center fuselage (transparent). The Top and bottom fuselage is reserved for carrying payload and goods. The center fuselage is for placing the avionics, including LiDAR, a 5000 mAh 12s battery set (with two 5000 mAh 6s battery packs that are connected in series), an on-board PC, etc. Two carbon fiber spars go across the center fuselage and mount with all the avionics, forming a strong “H” shape. A lid is on top of the center fuselage for easy replacement. The wings only have six bone structures and are covered with films to minimize the UAV weight. Two propulsion systems are attached to the carbon fiber rod, which is the strongest part of the UAV.

[Figure 4.9](#) shows the 3D nylon printed fuselage body with carbon fiber rods structure assembled. The intersections between fuselages are connected with countersunk head nylon screws, minimizing both the aerodynamics drag and the UAV weight.



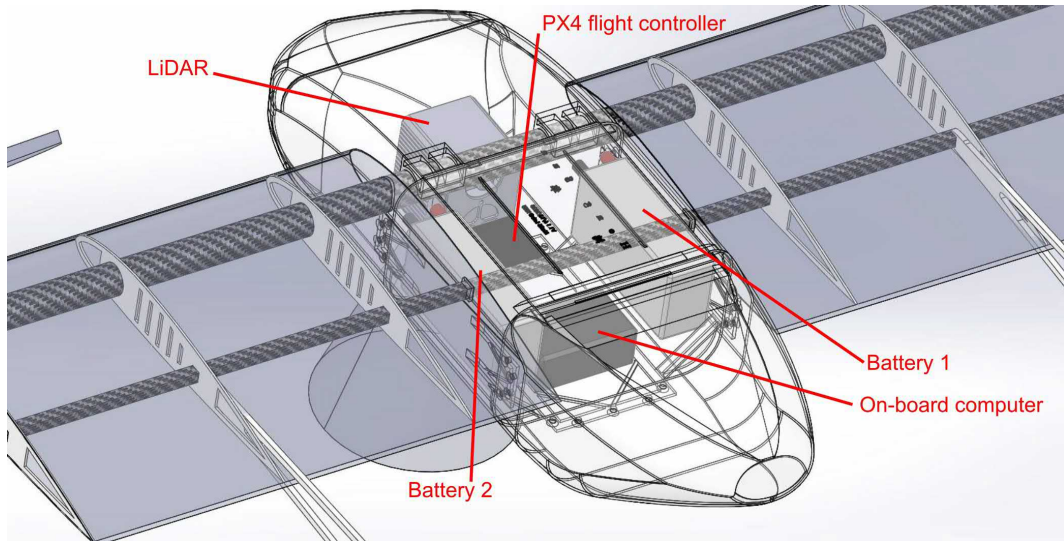


**Figure 4.8** Hong Sun interior avionics.

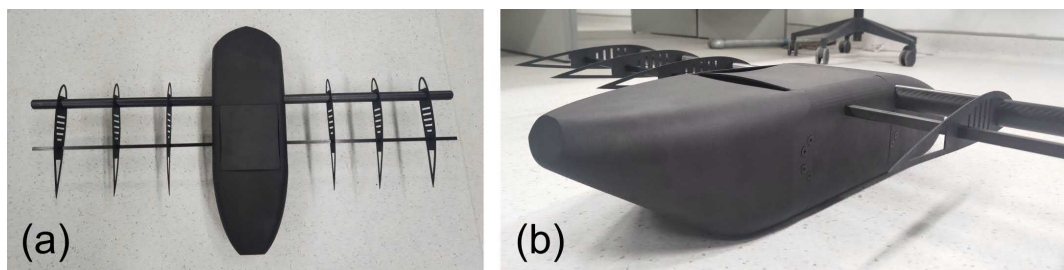


**Figure 4.9** Hong Sun fuselage validation (a) Top view; (b) Side closeup. The fuselage (including 3D printed body, nylon parts and carbon fiber parts) weights 811 g.

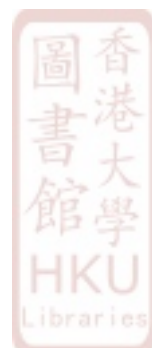
#### 4.4.3 Overall Specification

The following table summarizes Hong Sun's specification:

**Table 4.1** The Hong Sun's Specifications

Width	Length	Power	Takeoff Weight	Hovering Time
1.364 m	0.668 m	395.42 W	4.1 Kg	38.23 min

The hovering flight time estimation is based on the motor test result when the throttle is at the desired operating point of 50%. When both servo motors have the



identical angle command at 72.5 degrees, a single propulsion system generates 2.171 Kg thrust while consuming 197.71 W of power. Under the thrust result above, two propulsion systems can generate 4.342 Kg thrust, enough to support the designed takeoff weight of 4.1 Kg. On the other hand, the 12S 5000 mAh on-board battery can support hovering for 38.23 minutes based on the power consumption result.

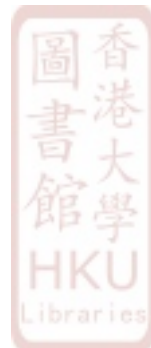
#### 4.4.3.1 Testing

In order to quickly test the feasibility of such a system, we conduct a hovering test flight with only the propulsion system and necessary avionics covered with a protecting foam box, as shown in Figure 4.10a. As shown in Figure 4.10b, the interior of the test rig consists of the flight controller, RC receiver, battery, DC converter, and eight branches of wires (Each propulsion unit consists of two branches of wire, one branch of rotational speed PPM wire, and one branch of brushless motor wire. Each branch consists of one signal wire, a power supply, and a ground wire).



**Figure 4.10** (a) Hong Sun hovering test rig with protecting foam box; (b) Hong Sun test rig interior closeup.

However, during testing, huge vibration starts to take place as the rotational speed increases, resulting in the brushless motor disassembling itself. We believe the reasons behind the vibration could be caused by the imprecision of the rotor shaft, the poor dynamic equilibrium of the propeller, or the wearing of parts. The wrecked part is purchased from the off-the-shelf product [105]. Upon the emergency, the test remotely cut down the power source and took a picture of the wrecked propulsion



system as shown in [Figure 4.11](#). The area that goes torn off belongs to the bottom part of the off-the-shelf DJI E2000 propulsion system. It is supposed to hold the brushless motor (shown in the lower right corner of [Figure 4.11](#)) in place. Such a part is made of high-grade CNC aluminum with anodic oxidation strengthening, a highly rigid material. The failure of this experiment proved the infeasibility of swashplate design again. Besides the high price, precision manufacturing and assembly requirement, and demands for maintenance, the safety concern is another reason why we chose not to keep pursuing the swashplate method.

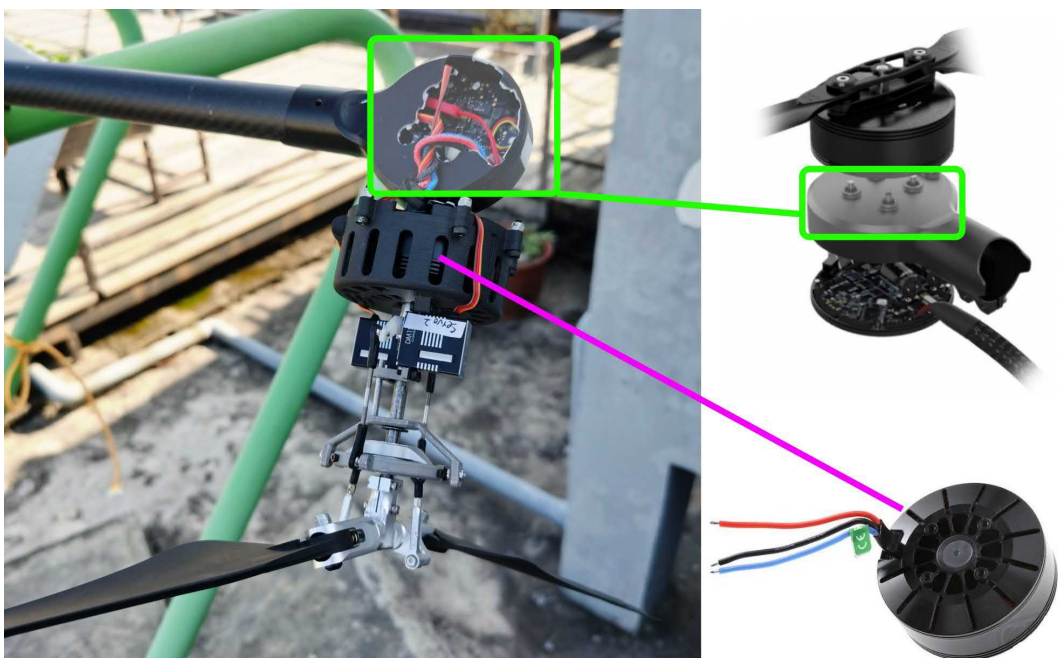


**Figure 4.11** Propulsion system test fails. Huge vibrations of the brush-less motor (shown in the lower right corner) cause the motor base (circled in green) to disassemble itself during testing.

## 4.5 Conclusion

Throughout our failed attempt in the swashplate-based bi-copter, we conclude that adopting a swashplate mechanism for small-size bi-copter is impractical. For the current design, the method of controlling bi-copters with the traditional swashplate method has multiple potential issues.

First and foremost, the swashplate mechanism requires high manufacturing precision, otherwise, the high-speed rotating shaft will cause vibration issues and motor failure very quickly. Even with a commercial product, the E2000 propulsion system cannot withstand vibrations. Moreover, with our chosen aluminum material, frictions can still wear the swashplate parts, causing failures in the long run. Therefore, constant maintenance is mandatory as safety issues have a higher priority for large aircraft.

Secondly, since off-the-shelf servo motors and swashplate designed not dedicated to our specific design, the prototype will unavoidably have a large size, which reduces the efficiency. As the size of the UAV increase, safety issues become more and more severe.

Thirdly, since the swashplate mechanism is highly complicated with multiple parts, the assembling process is a labor-heavy task. The UAV uses four servo motors, and each of them consumes around 25 watts of power, and each servo has three branches of wires. Powering up all the servo motors requires a dedicated high power DC buck converter and 12 branches of wire connections to the servo motors, which is heavy and consumes the precious onboard spaces. Besides avionics assembly, the precision assembling of the swashplate is even more critical. Without the production line level assembling precision, the performance potential will not be able to be maximized, and the flight efficiency will be compromised as a result.

Moreover, for the current design, long-term operation over 10 minutes will unavoidably cause the motor to heat up, and the heat will be trapped inside the motor cage. This issue will be alleviated when the aircraft performs the level flight, but it will be a huge issue upon hovering. Overheating will melt the nylon material, short the circuit, and bring other unstable factors to the system.

In conclusion, the current swashplate bi-copter design is not only expensive but also impractical. For the major reason of safety concerns, we chose not to keep on pursuing such a design.



# Chapter 5

## Gemini II: Swashplate-less Bi-copter

### 5.1 Introduction

By using servo motors to achieve tilting of each individual propeller for yaw and roll control, the tandem tilt-rotor configuration is a more practical solution for indoor applications and has been widely explored by previous chapters and other researchers[25–27, 76–78, 106, 107]. The servo motors, however, are heavy, bulky, hard to maintain, and expensive.

Throughout the failed attempt in the last chapter, we also concluded that the swashplate approach also suffers the issues including expensive, high precision assembling and manufacturing demands, low efficiency, bulky, hard to maintain, safety issues, and other practical concerns.

Towards the goal of making the UAV mechanically simpler, more reliable, cost-effective, meanwhile mitigating the issues of backlash, non-linearity, and non-minimum phase caused by servo motors that existed in previous Gemini mini, we proposed the Gemini II bi-copter. Unlike tandem rotor bi-copters that utilize two servomotors to achieve yaw and roll control, our novel design controls attitude by using cyclic flapping response in hinges that connect the blades. This passive cyclic pitch-varying mechanism makes the UAV no longer depend on two heavy and expensive servo motors or swashplate to vector the thrust. To the best of the



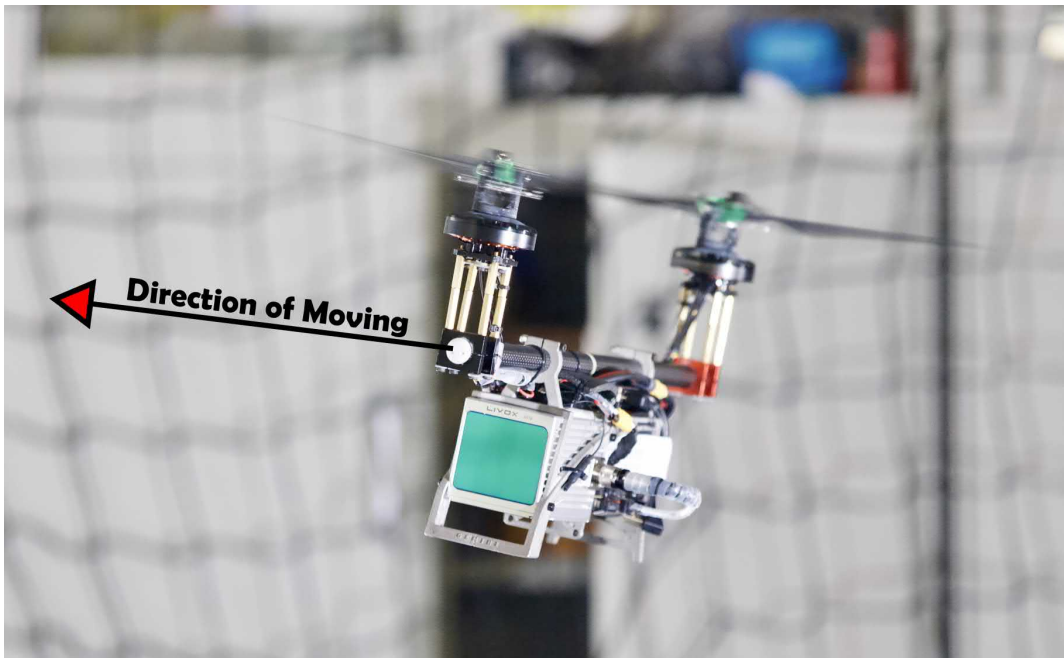


**Figure 5.1** Gemini II servo-less bi-copter performing agile maneuvering (Gemini II achieves 6-DoF with two motors as the only actuators). The propeller size is 13 inches (33.02 cm), and the total system weights 1.87 Kg. It is capable of flying up to 22 minutes. The video is available at: <https://youtu.be/qGhQbPtp7Sw>

authors' knowledge, the Gemini II, built entirely on off-the-shelf electronics, is the first servo-less bi-copter that can precisely control its 3D position and orientation with two actuators only.

Figure 5.1 shows the Gemini II servo-less bi-copter performing agile maneuvering. The propeller size is 13 inches. The Gemini II moves in the direction indicated by the arrow, and it is able to control its attitude with the swashplate-less cyclic blade pitch control technique. It carries a front-facing 3D LiDAR and an on-board computer, which makes it able to perform tasks like real-time 3D LiDAR mapping. With a take-off weight of 1.87 Kg and 13-inch propellers, our exemplary design Gemini II carries a 600 g LiDAR while only consuming 193 watts of power, resulting in 22 minutes of operation time.

In this chapter, we introduce the Gemini II bi-copter, a novel bi-copter approach that controls attitude by using cyclic flapping response in hinges that connect the

blades. This passive cyclic pitch-varying mechanism makes the UAV no longer depend on two heavy and expensive servo motors or swashplate to vector the thrust. This change of propulsion system not only makes the UAV mechanically simpler, more reliable, and cost-effective but also enhances the UAV performance by mitigating the issues of backlash, nonlinearity, and nonminimum phase caused by servo motors. This chapter presents the systematic design, modeling, and control of the Gemini II bi-copter. To demonstrate the flight performance and applications of the proposed novel UAV, we conduct path-following experiments along with manual poking and wind disturbances tests. The main contributions of this work includes:

1. We improve the swashplate-less mechanism and eliminate the dead zone non-linearity in control response at low drive amplitudes compared to [47].
2. Based on this swashplate-less mechanism, we develop a novel servo-less bi-copter configuration Gemini II and a detailed dynamics model.
3. We design an effective cascaded PID controller and control allocation scheme and implement them all on off-the-shelf electronics without using any custom motor controllers as in prior works [47, 48, 108–110] for the Gemini II.
4. We demonstrate the validity and flight performance of Gemini II by conducting a series of flight tests, including a power consumption test, poking disturbance test, gust wind disturbance test, step response test, and agile trajectory tracking

## 5.2 Literature Review

The one thing that all the bi-copters mentioned in the previous chapters have in common is that they all rely on external actuators to provide pitch, roll, and yaw control authority. The servo motors used on tandem rotor configuration always require high torque and quick response, and this will narrow the choice of servo motors options down to relative heavy metal gears, which in turn, adds on weight and lowers its efficiency. Besides, the backlash inside the servo motor gearbox also might increase the system's nonlinearity. Moreover, the control bandwidth is restricted



by the mechanical nature of servo motors. As shown in Li *et al.* [107], the roll dynamics of a servo-driven tandem rotor bi-copter is the non-minimum phase, which fundamentally limits the attainable controller bandwidth [111]. Besides the servo-based approach, our failed attempt in the last chapter taught us that the method of swashplate not only will not solve such problems but also brings up more impractical factors and safety concerns.

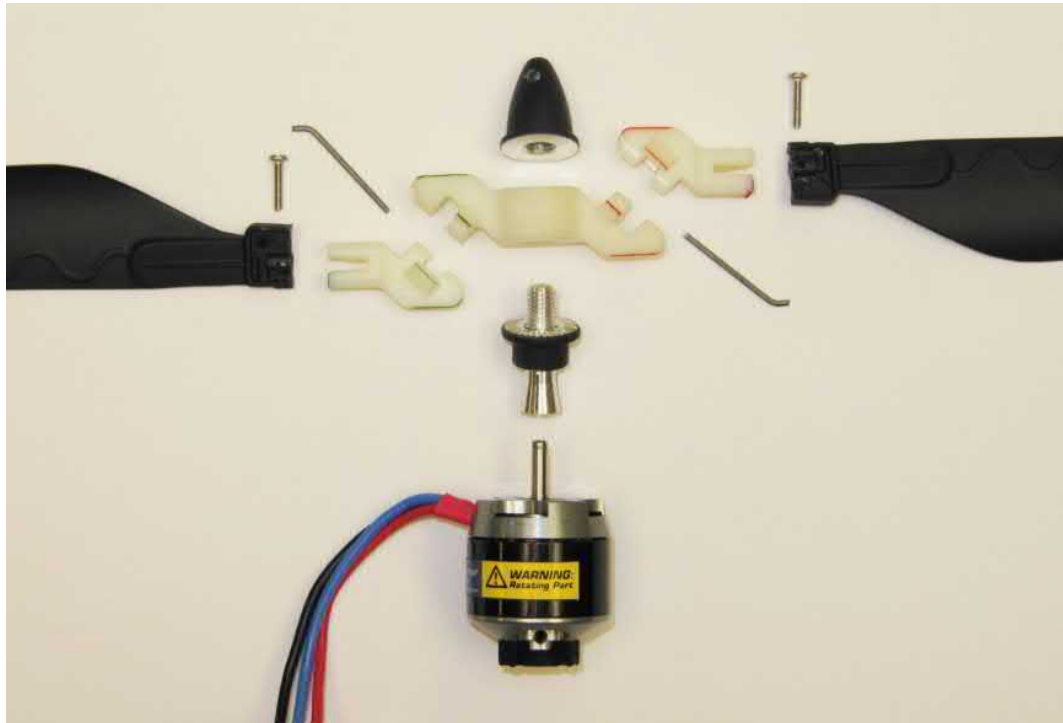


**Figure 5.2** Dual rolls swashplate-less mechanism that is able to generate pitching and rolling torque without extra servo motors. **Image Source:** [47]

To reduce the number of actuators, increase reliability, and reduce cost and weight for MAV, James Paulos and Mark Yim [47] first proposed a dual rolls swashplate-less mechanism (shown in Figure 5.2). By driving the brushless motor through a position-dependent signal, pitching and rolling torque can be generated without requiring neither additional servo motors nor complex linkages like traditional swashplate. The swashplate-less mechanism was applied to a 227 g coaxial helicopter MAV [108], and its performance is validated by closed-loop trajectory tracking.

The subsequent work [48] further introduced flap hinges to the swashplate-less





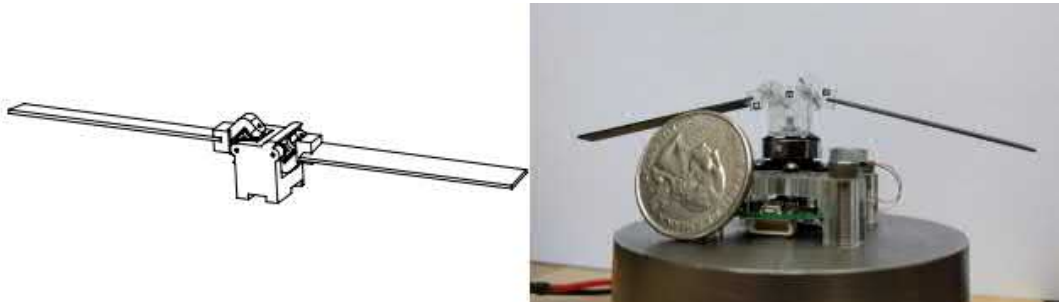
**Figure 5.3** Swashplate-less mechanism with flap hinges to reduce vibrations.  
**Image Source:** [48]

mechanism (shown in Figure 5.3). The detailed kinetics and dynamic models, including hinge losses, are discussed. The author stated that this skewed lag-pitch hinge enables a smoother harmonic flapping response and reduced vibrations.

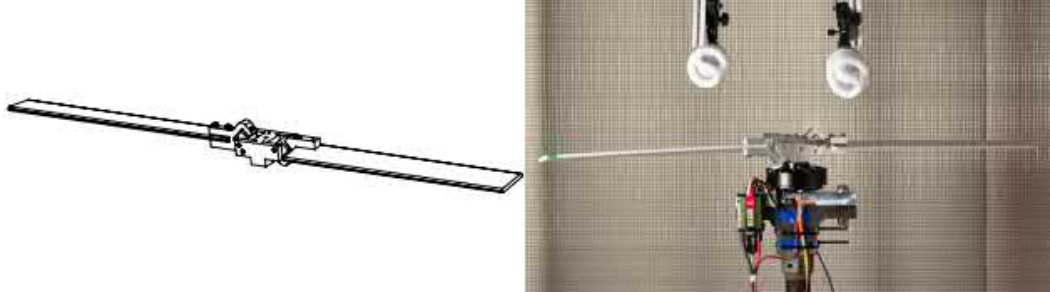
According to [110], the swashplate-less mechanism is highly scalable. The swashplate-less cyclic blade pitch control has been demonstrated in rotors from 10 cm to 1 m, at operating speeds ranging from 300 RPM to 9000 RPM, as shown in. [109] merged two teetering hinges into one. By adopting such a new mechanism, the coaxial helicopter prototype can emulate a fully actuated MAV.

Toward the goal of increasing the control bandwidth, mechanical reliability, efficiency, and mitigating the non-minimum phase behavior brought by servo motors, we adopted a swashplate-less cyclic blade pitch control technique with similar working principles as [109] and combined the benefit of the swashplate-less mechanism and the high efficiency of the bi-copter configuration.

As found in the original work [47], this swashplate-less mechanism has a dead-



(a) 10 cm diameter swashplate-less mechanism. **Image Source:** [109]



(b) 1 m diameter swashplate-less mechanism. **Image Source:** [109]

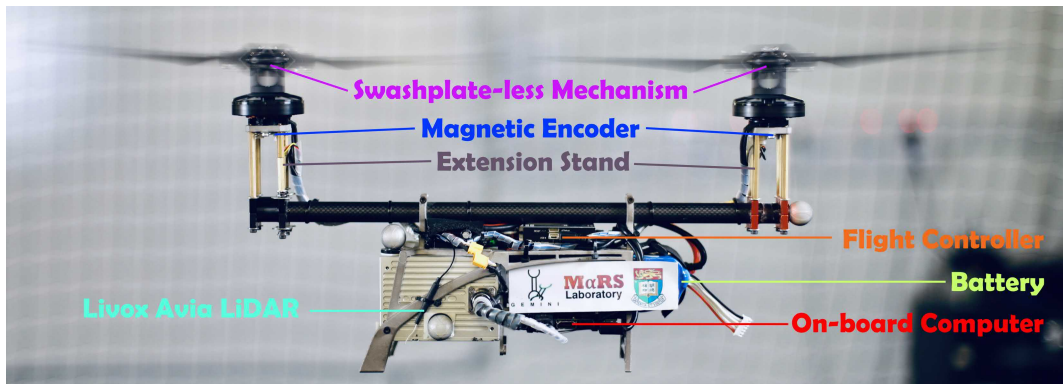
**Figure 5.4** Scalability of swashplate-less mechanism.

zone non-linearity in control response at low drive amplitude ascribed to sliding friction. To avoid this issue, we improve the swashplate-less mechanism by using ball bearings and thrust bearings in the hinges. As a result, our approach is a servo-less bi-copter UAV. Magnetic encoders are placed beneath the center of the brushless motor rotating shaft, providing rotor angle feedback to the flight controller. The motor torque is modulated depending on the angle feedback to excite a lead-lag motion of the swashplate-less mechanism and make a once-per-revolution variation in blade pitch. Instead of depending on servo motors to produce torque in roll (same tilting direction of the two rotor disks) and yaw (different tilting direction of the disks), this bi-copter UAV achieves improved attitude control performance with only passive hinges.



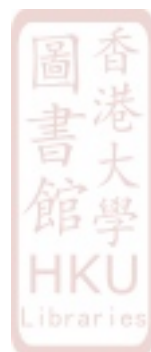
### 5.3 System Architecture and Mechanical Design

Figure 5.5 shows the main components of our developed bi-copter UAV, Gemini II. When compared to our previous tandem rotor bi-copter, Gemini [106], the most apparent difference is the propulsion system. Instead of using servo motors to tilt the propeller disk to gain all four degrees of freedom control authorities, the swashplate-less cyclic blade pitch control technique is utilized. As detailed in Section 5.3.3, this mechanism requires no extra actuator (e.g., servo motor) to tilt the rotor disk. As a consequence, the Gemini II has only two actuators, whose speeds are controlled by a 45 A two-in-one electrical speed controller (ESC). Another obvious difference is the change of payload. Rather than using mechanical 360 degrees LiDAR, the Gemini II uses a Livox Avia non-repetitive scanning front-facing LiDAR module instead. Because this LiDAR faces the same direction as the moving bi-copter, it has the potential of providing obstacle avoidance and autonomous navigation.



**Figure 5.5** Gemini II mechanical design detail and avionics. Each propulsion system consists of only one motor and swashplate mechanism with extension stands augmenting roll and yaw control authorities. Gemini II is also equipped with Livox Avia LiDAR and an on-board computer for future autonomous flying capability.

Extension stands are placed beneath the brushless motors to increase the distance from the propeller to the center of mass (COM), and therefore increase the torque on the roll or yaw direction when the same amount of lateral force is generated (see Section 5.4.2). Since hinges are connecting the blade and motors, due to gravity, propeller blades tend to flap down when the motor stops spinning. The extension stands also serve the function of protecting propellers from hitting the drone's body.



### 5.3.1 Fuselage

The fuselage is made with a 3D-printed aluminum body. Two propulsion units are attached at the two ends of the 41 cm long carbon fiber rod. To minimize the differential thrust between the front and back rotor, we make the fuselage movable on the carbon fiber rod. By adjusting the fuselage position, the center of mass can be manually shifted to the center of the aircraft. Without balancing the center of mass, the propulsion unit will be forced to generate pitch torque while hovering. In the worst-case scenario, one side of the propulsion unit will be close to saturation, leaving little room for sinusoidal manipulation, and making the aircraft lose control ability over yaw and roll. The following subsection is going to further illustrate the process of the design and optimization process.

#### 5.3.1.1 Design and Optimization Process

Similar to Gemini mini, the design process of the Gemini II can be generally divided into two steps. The first step is to clarify the design goals. The design goals contain the function that the bi-copter will have to accomplish, as well as the expected flight performance. As a result, the first step process will determine the list of avionics. The second step is to design the frame structure and optimize it through iterations. As mentioned previously, the Gemini II adopts a similar on-board computer and battery as the Gemini mini except for the LiDAR unit. So the first step is to develop the fuselage with the pre-determined avionics.

After importing all the avionics into CATIA, draw the basic geometric shape that can cover all the avionics at the desired position without the need to worry about excessive material (shown in [Figure 5.6a](#)). Such a shape shall be able to protect all the avionics during crashing as well as reserve spaces for installation holes and easy assembling. The design space is shown in [Figure 5.6b](#). The next step is to determine the load condition. Considering the scenario of both a head crash (refer to [Figure 3.8a](#)) and a hard touchdown (refer to [Figure 3.8b](#)), the support on the LiDAR side will have the highest chance of colliding when compared to other parts. Assume



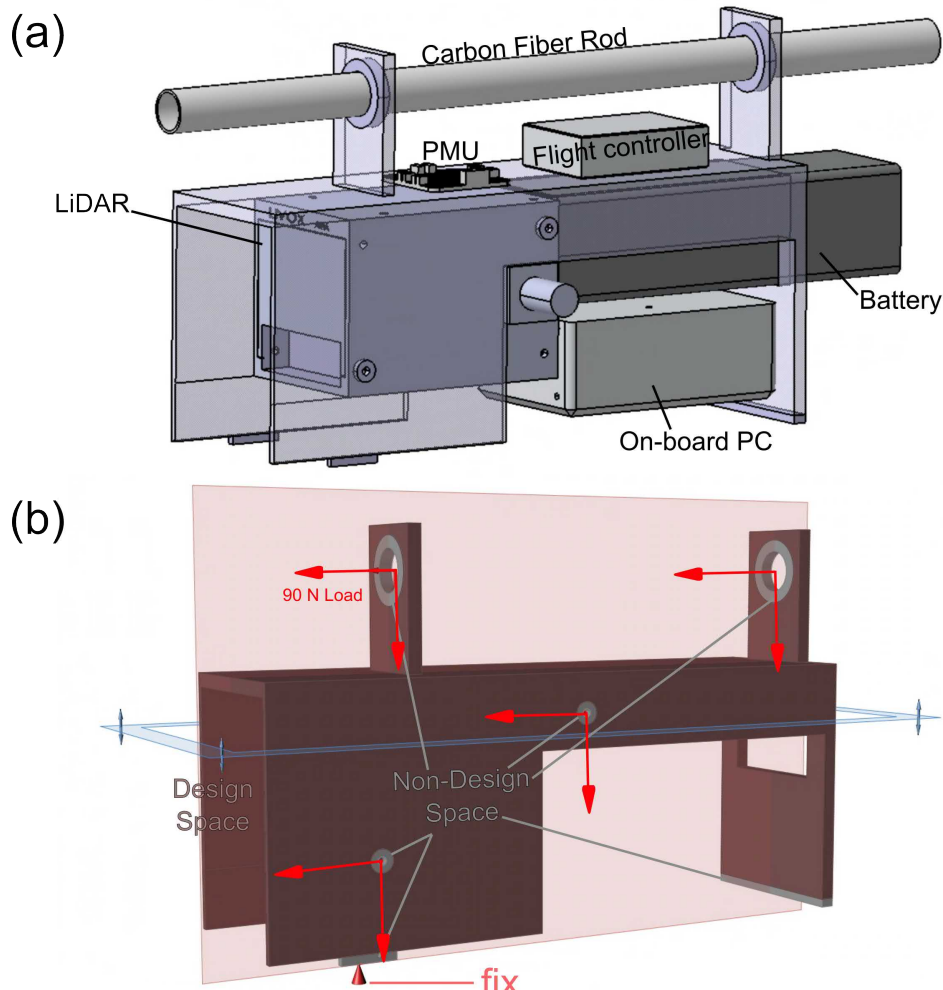


**Figure 5.6** Gemini II design space design **(a)** Avionics layout (LiDAR payload, battery, on-board computer, flight controller, PMU); **(b)** Design space and constraints setting (Draw the basic geometric shape and apply load with assumptions).

the colliding of the UAV and the ground happened at the free-falling body (because the frame structure of the UAV is symmetrical, it only needs to consider the left tilt direction). The lower left part of the fuselage can be regarded as the fixed point when it touches the ground. The inertial force of heavy components such as the battery, controller, and radar are transmitted to the mainframe through the fixed point and contact surface of each component and the mainframe structure. Assume the total mass of the heavy components on the UAV to be 1.7kg. According to the momentum theorem, it can be calculated that the force in three directions of XYZ is 42N (joint force). Select the material as Aluminum (7075-T6) and apply the load condition as shown in [Figure 5.6b](#). Since the fuselage is left-right symmetric, we set the boundary layer (marked in 50% opaque red plane in [Figure 5.6b](#)) in the middle of the design

space in order to lower the calculation load for the solver and half the calculation time.

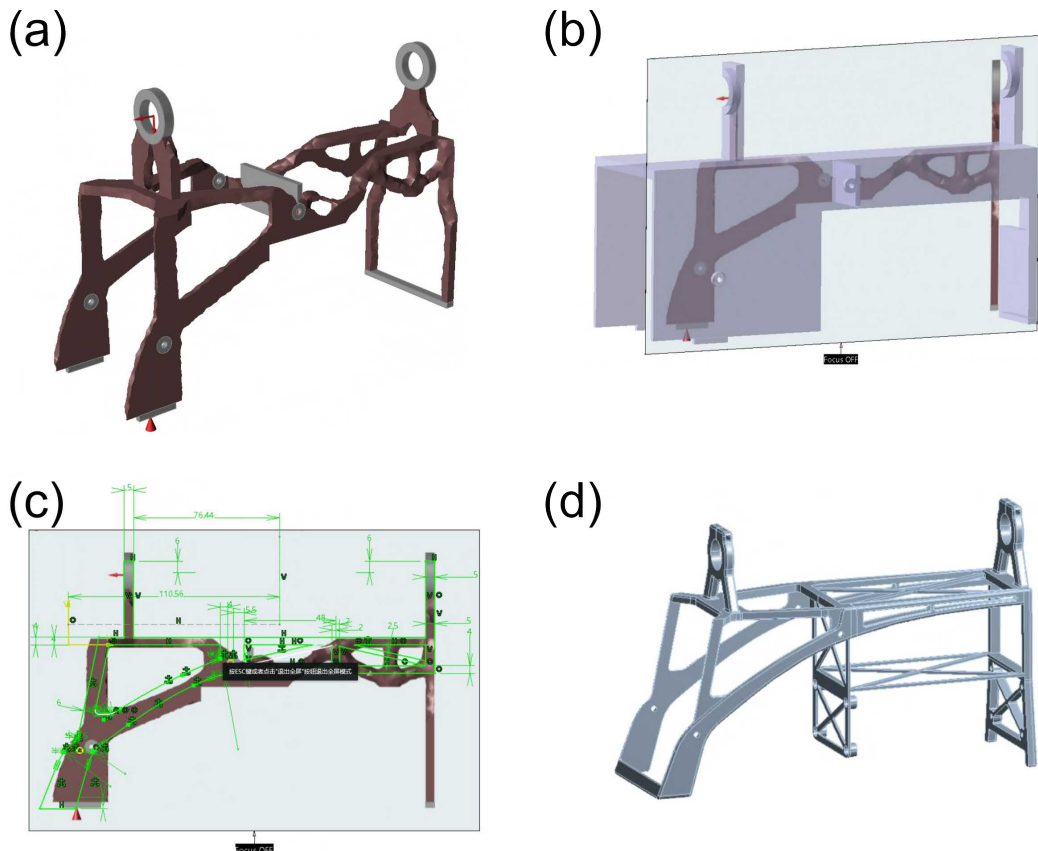


**Figure 5.7** Gemini II fuselage sketching process **(a)** Topology optimization result; **(b)** Importing the result into CATIA; **(c)** Do a new sketch on top of the topology optimization result, and repeat the process for top, side, and front views; **(d)** Fuselage sketch deliverable.

The topology optimized model is displayed in Figure 5.7a. It can be seen that there are two main branches connecting the front of the support to the rest of the fuselage. The rear side of the fuselage is a common truss structure. Since the on-board PC Manifold 2C is covered in an aluminum shell, the lower rear side of the fuselage will be strong even without strengthening. On the other hand, the lower front part of the fuselage is informative, and shall be kept as much as possible. Import the screenshot of the topology optimized result into the CATIA, and draw the Gemini II sketch space as shown in Figure 5.7b. Repeat the process for X, Y, and Z plane. Based on the screenshot, construct the first sketch with smooth curves and structures (shown in Figure 5.7c). Since the manufacturing is going to be using SLS aluminum, there is no need to consider the constraints on the shapes as what is



required by the traditional CNC method, as additive manufacturing does not depend on drills and cutting. After drawing structural draft upon the topology optimization model, installation structure for battery, on-board PC, flight controller, and LiDAR all needs to be considered. The distance between the carbon fiber rod and the upper plane of the lower fuselage body needs to be tall enough for PX4 installation. As a result, the Gemini II first fuselage sketch is constructed as Figure 5.7d.

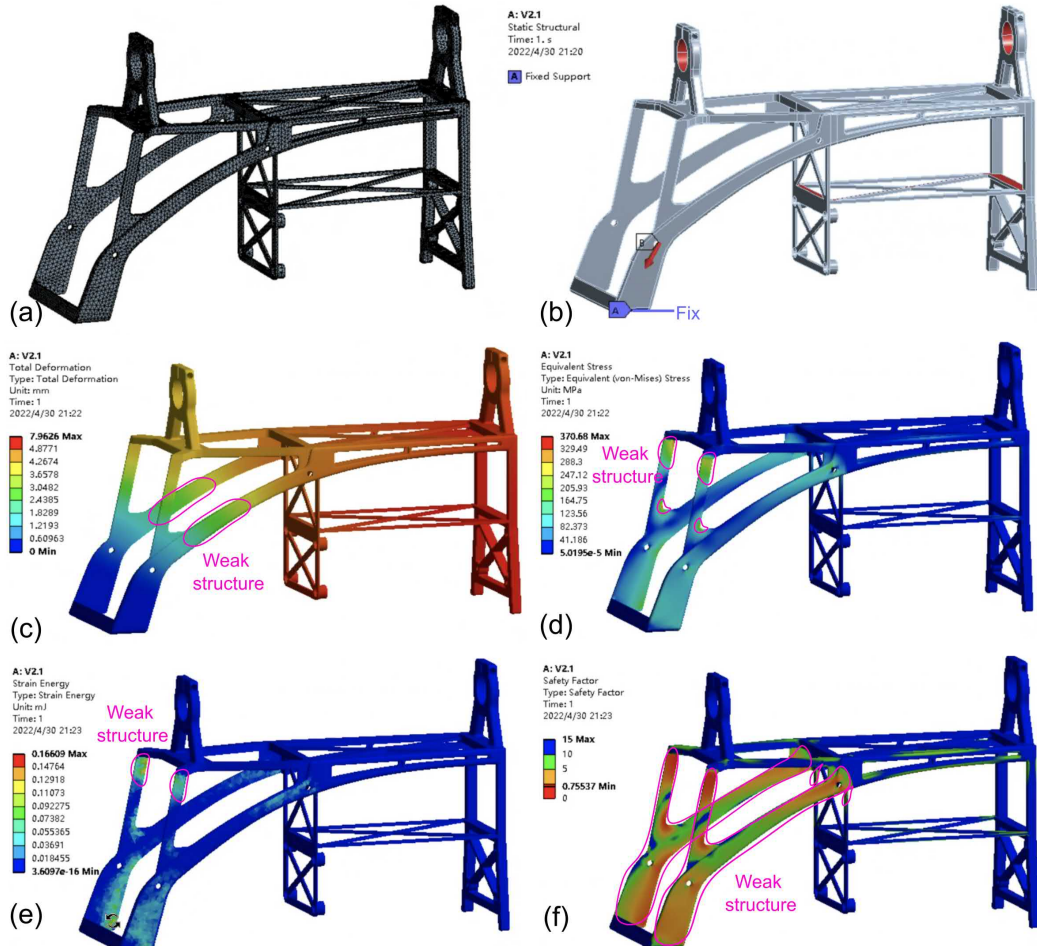
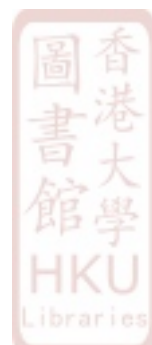


**Figure 5.8** Gemini II fuselage sketch analysis (a) Mesh analysis; (b) Constrains and load condition settings; (c) Total Deformation (The most dramatical change of deformation happens in the weak structure circled in magenta); (d) Equivalent Stress (The weak structure experience the greatest amount of stress, and is circled in magenta); (e) Strain Energy (The weak structure bear the largest amount of strain energy, and is circled in magenta); (f) Safety Factor (The weak structure is a continuous chunk rated with safety factors less than 9, and is circled in magenta).

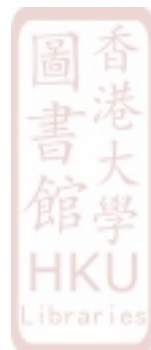
Analysis of the model in ANSYS Workbench by meshing the model with the default parameters as shown in Figure 5.8a. Adjust the meshing element size until



the grid distribution is uniform and fine, and grid quality is high so that the round edges are clearly visible. Next, set the load constraint for the model. As shown in [Figure 5.8b](#), the lower left corner of the model is set to be a fixed constraint as it is contacting the ground, and apply load settings identical to [Figure 5.6b](#). The applied 90N force is located at the contact and bolt connection with the carbon fiber rod, battery, LiDAR load, controller, and the main frame to simulate both head crash and hard touchdown crash scenarios.

After the setup process, the next step is to observe the deformation, equivalent stress, strain energy of the frame, as well as the safety factor of the structure. These observation cloud images are added to the solution module. As shown in the analysis from [Figure 5.8c](#) to [Figure 5.8f](#), we can see some problems. For example, the deformation and stress are mainly concentrated in the front section of the fuselage, which indicates that the stiffness of the front half of the fuselage is not enough. When impacted by an external force, the impact force is not transmitted to the back half of the fuselage, and almost all the energy of the impact force is absorbed by the front half of the fuselage. Therefore, in order to solve this problem, we need to strengthen the structure of the front half of the fuselage.

In view of the structural strengthening of the front half of the fuselage, the method of adding a tendon strengthener is adopted, which can ensure that the stiffness of the structure can be maximized without increasing too much mass. The model safety factor before remedy and improved structure after adding stiffeners is shown in [Figure 5.9a](#). The tendon stiffeners are added in the circle marked in magenta. In addition, the battery cage part of the fuselage is thin and below the safety factor threshold of 9, and is circled in magenta on the left hand side of [Figure 5.9b](#). When the rear of the fuselage is grounded first, the connection area between the fixed fuselage and the front will be stressed. If the connection area is too thin in the relative area, the structure will tend to break. Therefore, strengthening actions shall be taken for this specific area. The measures adopted are to thicken the fixed fuselage in this area and add a reinforcing pillar rib below to connect the fixed fuselage with the front half of the fuselage. The modified model is shown in [Figure 5.9c](#).



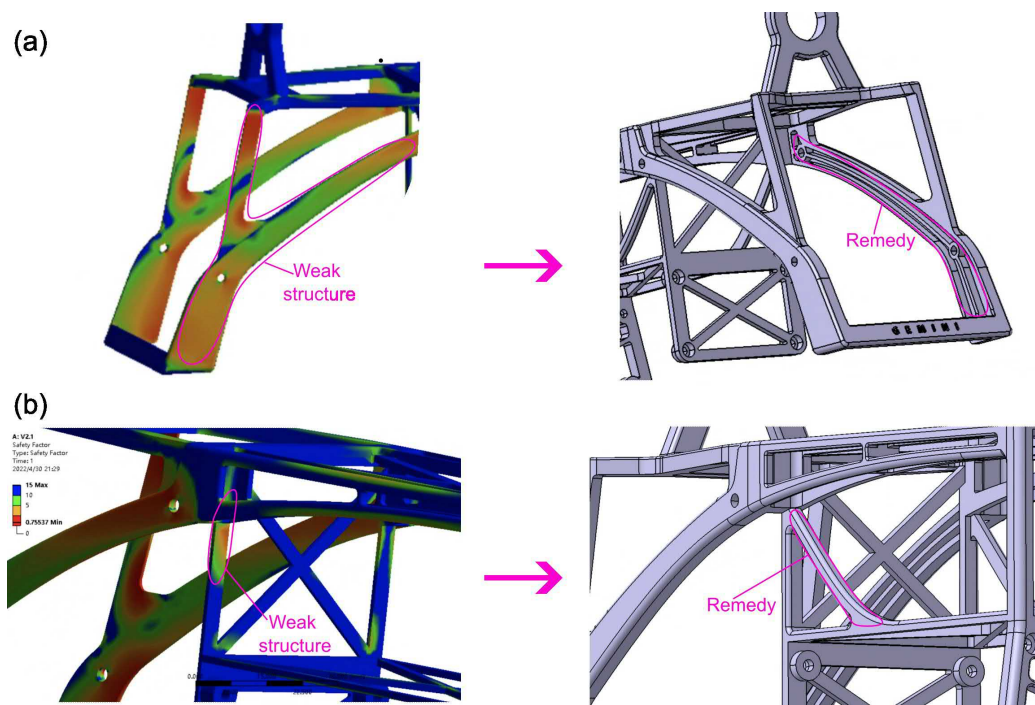


**Figure 5.9** Gemini II fuselage weak structures and corresponding remedy **(a)** Tendon strengthener method; **(b)** Pillar rib strengthener method.

After the above adjustment, the simulation analysis is carried out again, and the constraint is set the same as the load. Each cloud image after analysis is shown in the following group of images. It can be seen from Figure 5.10a to Figure 5.10d that after the adjustment, the stiffness performance of the structure has been greatly improved. In terms of displacement, it can be seen that the displacement of the whole fuselage changes more evenly from front to back, which proves that the stiffness of the front half of the fuselage has been effectively strengthened, and the impact force when falling is successfully transferred from the front half of the fuselage to the rear half. The stress distribution and strain energy distribution are also dispersed. The minimum value of the safety factor is a little higher than before, and it is more than 1, which experimentally indicates that the structure will not fracture or surface crack under this condition.

After unified measurement, only the part with a safety factor of less than three is displayed. According to the author's experience, a structure with a large chunk of structure that has a safety factor of less than one will have a high chance of breaking upon hard crashes, and a structure with a safety factor of less than three is considered



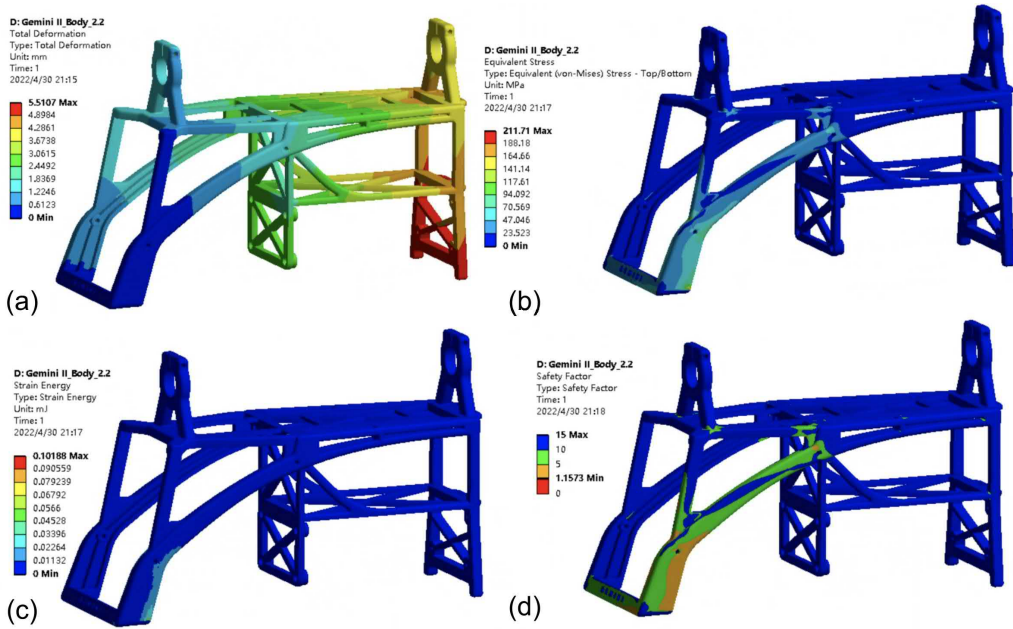


**Figure 5.10** Gemini II fuselage analysis after iteration **(a)** Total Deformation (5.51 mm maximum vs. 7.96 mm maximum previously); **(b)** Equivalent Stress (211.71 MPa maximum vs. 370.68 MPa maximum previously); **(c)** Strain Energy (0.10 mJ maximum vs. 0.17 mJ maximum previously); **(d)** Safety Factor (1.16 minimum vs. 0.76 minimum previously). Every aspect mentioned above suggests the fuselage has higher stiffness against shocks, and is much less likely to break upon crash.

weak structure. It can be found that the volume of the part with a safety factor of less than three is significantly reduced, and the whole structure has a safety factor greater than one, as shown in Figure 5.11a and Figure 5.11b.

### 5.3.2 Avionics

In our bi-copter prototype, PX4 flight controller hardware is used, but the key controller including the mixer is customized as detailed in Section 5.4.2. The on-board computer is an ARM-based single-board computer, and it serves as a relay that transmits the position data from the Vicon motion capture system to the flight controller. In the future, with the onboard Livox Avia LiDAR providing a 3D point cloud, real-time SLAM algorithms can be performed on the on-board computer, yielding position feedback without depending on an external motion capture system.



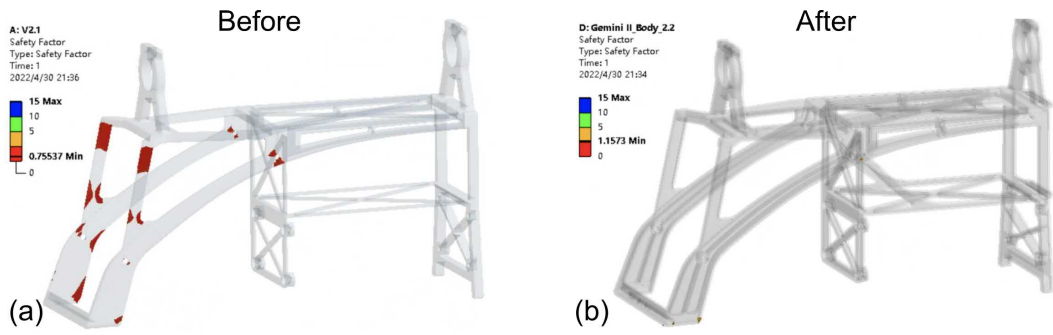


**Figure 5.11** Gemini II fuselage safety factor improvement **(a)** Before iteration, multiple chunks of structures have a safety factor of less than three (circled in red); **(b)** After iteration, safety factor is greatly improved with no risky structure that has safety factor less than one and no huge chunk of structure has safety factor less than three.

The Fuli 5000 mAh 5S HV battery can be charged up to 4.35 V per cell on the daily basis. It provides power for all the on-board electronics, and the actual flight time lasts 22 minutes.

### 5.3.3 Swashplate-less Cyclic Blade Pitch Control Mechanism

Benefiting from the swashplate-less cyclic blade pitch control mechanism proposed in [48], the thrust generated by the propulsion system is able to change direction with the addition of only three passive hinges. Figure 5.12 shows a complete set of swashplate-less cyclic blade pitch control mechanisms, which consists of a set of swashplate-less mechanisms (shown in the upper side of Figure 5.12), a pair of propellers blades, a brushless DC motor, and a magnetic encoder board placed at the bottom of the rotor (shown in the lower right corner of Figure 5.12). The two blades are tightly mounted on their respective side hubs, which are then connected to a teetering hub through two passive lag-pitch hinges. A third passive hinge, the teetering hinge, is further used to connect the teetering hub to the central hub which is firmly attached to the rotor. As a result, the two blades and the teetering hub can freely rotate about their respective hinges, and the whole mechanism is driven by the motor.



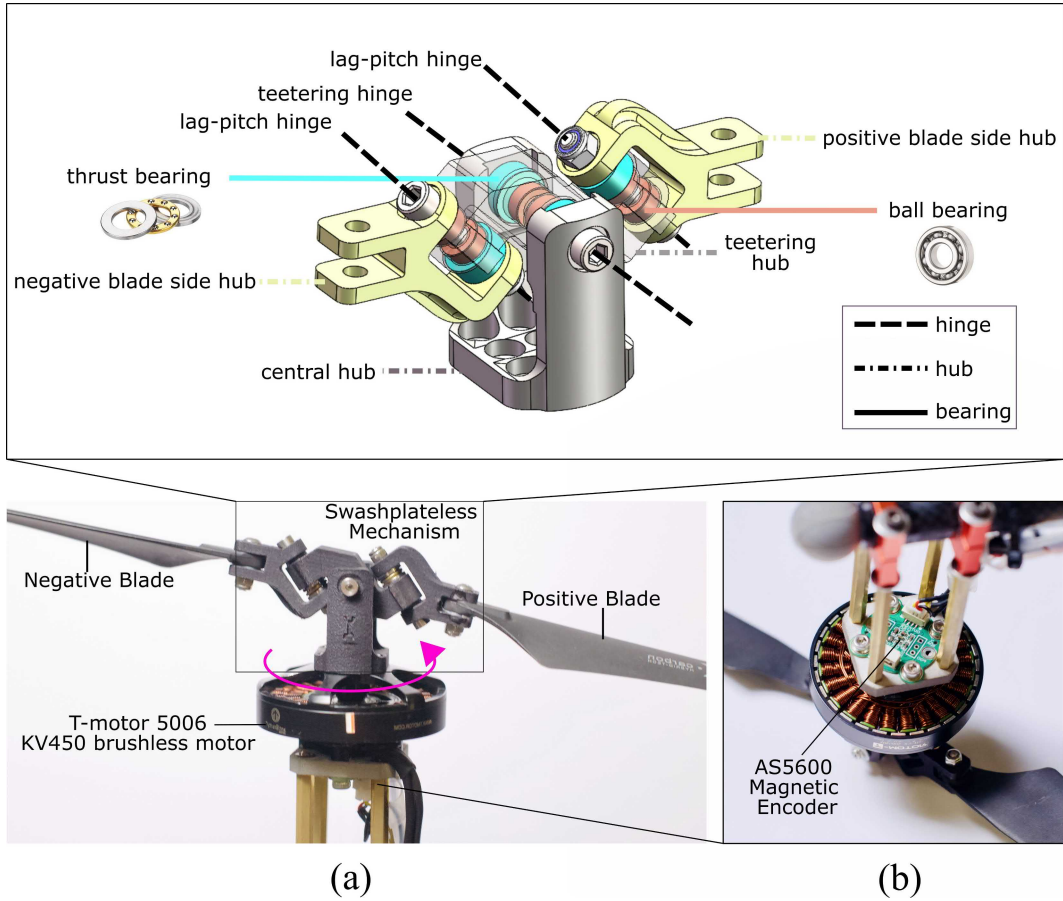


**Figure 5.12** swashplate-less cyclic blade pitch control mechanism **(a)** Mechanism diagram (brush-less motor rotates following the direction indicated by the magenta arrow); **(b)** Magnetic encoder closeup.

### 5.3.3.1 Working Principle

Figure 5.13 illustrates the working principle of the swashplate-less cyclic blade pitch control mechanism. To ease the explanation, a motor frame  $\mathcal{M}$  with its  $z$ -axis along the rotation axis of the motor is introduced. When the motor accelerates at angular location  $\gamma$ , the two blades (colored in green in Figure 5.13(a)) will not accelerate immediately due to blade inertia, causing a lag from their supposed positions (colored in blue). As a consequence, the two blades will further rotate around their respective lag-pitch hinges. Because of the special lag-pitch hinge arrangement, the rotation of the positive blade will lead to an increased pitch angle



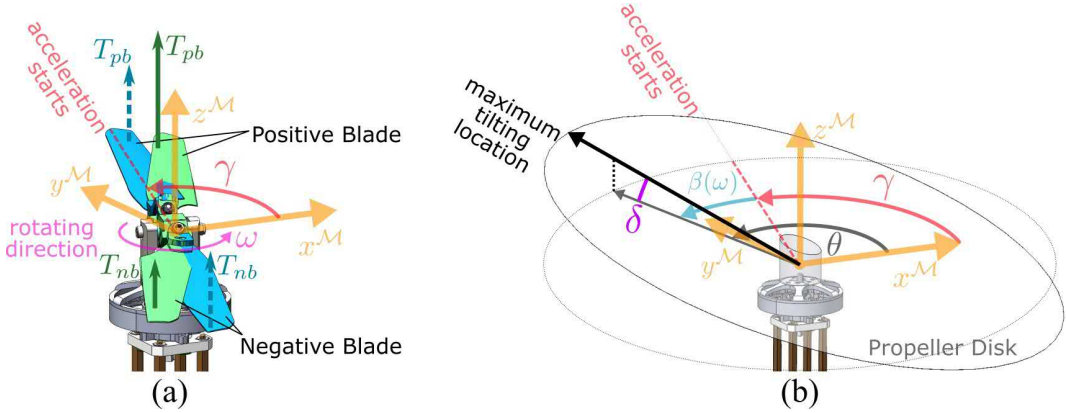


**Figure 5.13** Blade dynamic reaction on the counterclockwise spinning motor  
**(a)** Lagging behavior of the two blades. **(b)** Tilting of the propeller disk.

(hence a larger thrust  $T_{pb}$ ) while the rotation of the negative blade will lead to a decreased pitch angle (hence smaller thrust  $T_{nb}$ ). The thrust difference will then cause the two blades (hence the propeller disk) to rotate around the teetering hinge. The tilting of the propeller disk further causes a tilting of the total thrust  $T = T_{pb} + T_{nb}$ .

In practice, to prevent the possible vibration excited by a sudden jump in the rotor acceleration, a sinusoidal rotor acceleration profile is typically employed [48]. More specifically, the motor throttle command  $U$  is designed as

$$U = C + A \sin(\alpha - \gamma), \quad (5.1)$$

where  $C$  is the nominal throttle (e.g., at hovering) that produces the average motor speed  $\omega$  and total thrust  $T$ ,  $A$  is the amplitude,  $\alpha$  is the current angular location of rotor measured by the magnetic encoder, and  $\gamma$  is the angular location where the motor starts to accelerate. In [48], it is shown that the maximal angle the two blades rotate around the teetering hinge (i.e., the disk tilting angle)  $\delta$  (see Figure 5.13 (b)) is approximately proportional to  $A$  by  $K_a$ , i.e.,

$$\delta = K_a A, \quad (5.2)$$

while the maximal tilting location of the blades (referred from the  $x$ -axis of the motor



frame  $\mathcal{M}$ ) is

$$\theta = \gamma + \beta(\omega), \quad (5.3)$$

where  $\beta$  is a lag angle of the blades' maximal tilting location  $\theta$  relative to the  $\gamma$  due to the tilting dynamic response of the blades. Typically,  $\beta$  depends on the average motor speed  $\omega$  and can be calibrated in experiments.

Changing  $\gamma$  in the motor command Eq. 5.1 will change the maximum tilting location of the propeller disk, thus vectoring the thrust. In practice, we could restrict the range of  $\gamma$  such that  $\theta$  is within  $[0, \pi]$  and flip the sign of  $A$  (hence  $\delta$  by Eq. 5.2) to attain a negative tilting of the disk. As a result, the motor thrust vector expressed in the motor frame  $\mathcal{M}$  is

$$\mathbf{F}^{\mathcal{M}} = \mathbf{R}(\theta \cdot \mathbf{e}_3) \mathbf{R}(\delta \cdot (-\mathbf{e}_2)) \cdot (T \cdot \mathbf{e}_3), \quad (5.4)$$

where  $\mathbf{R}(\mathbf{a})$  denotes the rotation matrix about an axis-angle  $\mathbf{a} \in \mathbb{R}^3$  and  $\mathbf{e}_i \in \mathbb{R}^3$  has its  $i$ -th element is equal to one and other elements are equal to zeroes.

### 5.3.3.2 Implementation Details

Compared to the design from [109], we employed an M3 half-thread hex bolt that was customized with CNC machines instead of using thin steel wire as hinges. Due to the high frequency of rotation caused by the much larger aircraft weight, the plastic hubs in [109] could easily be heated up to their melting point by sliding friction, resulting in a larger gap between the hinges and the hub, causing vibration in the long run. With precisely manufactured CNC bolts and commercial ball bearings, the friction between hinges and hubs is minimized.

Each hinge of our swashplate-less mechanism is clasped by two ball bearings on both ends, ensuring the central hub has a firmer grip over the lag-pitch hinges when counteracting with the lateral component of the centrifugal force while the mechanism is rotating. Two thrust bearings on the teetering hinge aim to transfer the sliding friction between the central hub and the teetering hub into rolling friction, which is significantly smaller than the former. On each side of the lag-pitch hinge,



only one thrust bearing is placed between the side hub and the central hub. The reason behind this is that once the mechanism starts to spin, the lateral component of the centrifugal force will push the side hubs side-way, increasing only the pressure on the contacting surface where the thrust bearing is currently placed. Since manufacturing errors are unavoidable, an even tightness between the lag-pitch hinge is critical to dynamic response excited by modulated shaft torque from the driving motor. Uneven pressures on lag-pitch hinge thrust bearings will result in different pitch angles on two sides of the propeller, generating a high-frequency vibration at the same frequency as the motor rotation. In practice, adjusting the nylon-insert lock nut on the lag-pitch hinge so that it is loose enough to allow the side hubs to rotate freely will avoid such an issue.

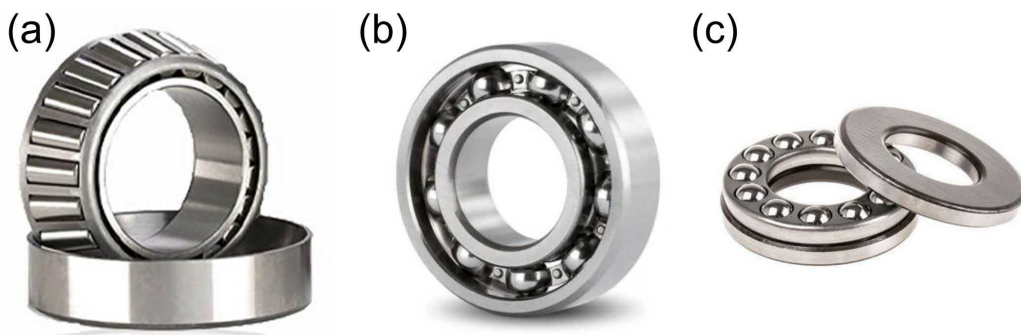


**Figure 5.14** Different mechanical bearings **(a)** Tapered roller bearing **(b)** Ball bearing **(c)** Thrust bearing.

It is also worthwhile to point out that each pair of the thrust bearing and ball bearing could be replaced with a single tapered roller bearing (shown in [Figure 5.14](#)), but miniature thrust bearing and ball bearing are easily available off-the-shelf components while mini single tapered roller bearing is not. Out of practical and cost concerns, the current design is chosen.

For the propeller, T-MOTOR MF1302 propeller blades are made of lightweight polymer, which minimizes the rotational inertia and the torque needed for the motor to frequently change its acceleration. The T-MOTOR MN5006 KV450 brushless motor has both relatively low KV value and resistance, which enables a slower rotational speed and generates less heat when generating high rotational torque. The

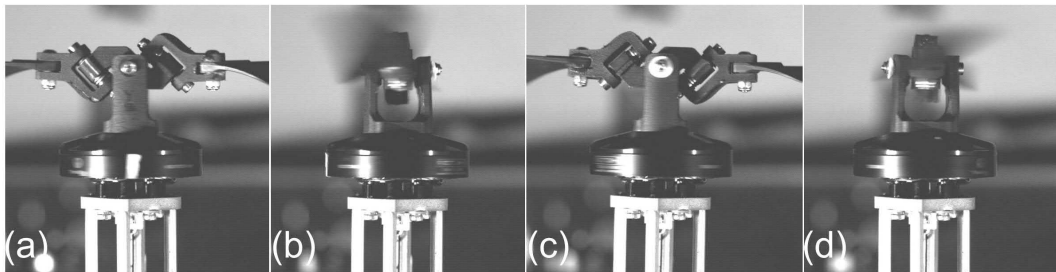


**Figure 5.15** One rotation cycle of the swashplate-less mechanism under high speed camera. The instantaneous pitch at one location is controlled by the phase of the torque modulation **(a)**  $0^\circ$ ; **(b)**  $90^\circ$ ; **(c)**  $180^\circ$ ; **(d)**  $270^\circ$ .

magnetic encoder unit is a customized PCB board with AS5600 placed at the center, as shown in [Figure 5.12\(b\)](#). The AS5600 magnetic encoder interprets rotor position with a resolution of  $2\pi/4096$  by an update frequency at 920 Hz. Note that the experimental maximum rotation speed is about 5000 RPM, which equals 83 Hz. The ESC is running with the OneShot125 protocol, so the motor command is updating at 4 kHz, and at least 48 motor commands can be sent out during each rotation cycle.

To validate the feasibility of the swashplate-less cyclic blade pitch control, we adopted the most direct observation using a high-speed motion camera capturing the image at 3600 frames per second (0.27 ms per frame) rate. As shown in [Figure 5.15](#), the rotation cycle of the swashplate-less mechanism is recorded at four instances. Through the trial and error approach, we adjust mechanical constraints to the teetering hub so that it is enough for the blade to make a cyclic response while making sure the blade won't collide with the carbon fiber rod upon sudden deceleration.

### 5.3.4 Overall Specification

The following table summarizes the Gemini II's specification:

**Table 5.1** The Gemini II's Specifications

Width	Power	Takeoff Weight	Flight Time
41 cm	193 W	1.869 Kg	22 min



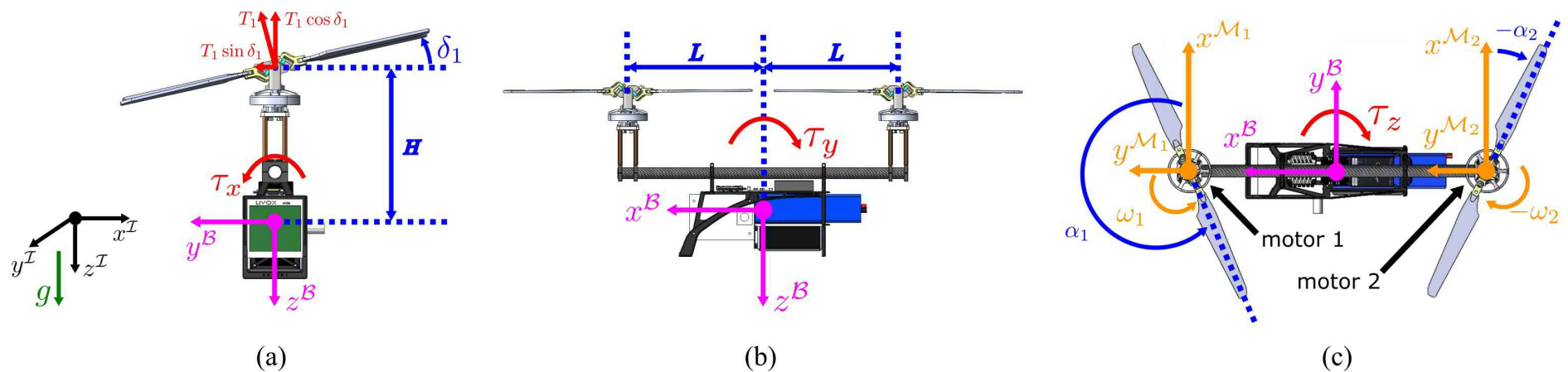


**Figure 5.16** Gemini II's definition of coordinate frames (the black coordinate represents the world frame, the magenta coordinate represents the body frame, and the two orange coordinate represents two motor frames respectively) **(a)** Front view. **(b)** Side view. **(c)** Top view.

## 5.4 System Modeling and Control

The replacement of servo motors changes the controller logic of the bi-copter platform since the roll and yaw commands are coupled with the sinusoidal command instead. The chapter presents the system modeling and control that enables the swashplate-less bi-copter operation.

### 5.4.1 Modeling

#### 5.4.1.1 Coordinate Systems

[Figure 5.16](#) shows the definition of all four right-handed coordinate frames of Gemini II. The North-East-Down (NED) inertia frame  $\mathcal{I}$  is a world-fixed frame whose origin coincides with the origin of the Vicon motion capture system and the direction of the  $z$ -axis is the same as the gravity vector. The Forward-Right-Down (FRD) body frame  $\mathcal{B}$  is a motion frame whose origin coincides with the COM of the Gemini II. Two motor rotor frames,  $\mathcal{M}_1$  and  $\mathcal{M}_2$ , both are origins at the center at two teetering hinges respectively. Motor 1 (the front motor) rotates counterclockwise and motor 2 (the back motor) rotates clockwise from the top view. The motor rotor angle  $\alpha_1, \alpha_2$ , and the disk tilting angle  $\delta_1, \delta_2$  follows the same definition as [Section 5.3.3.1](#).

#### 5.4.1.2 Forces and Moments

To control the four degrees of freedom of the Gemini II (i.e., position and yaw), it is sufficient that the propeller disk is only tilted along the  $y$ -axis of the body frame (i.e.,  $\theta = \pi$ ). Hence, the  $\gamma$  in the motor command [Eq. 5.1](#) is calculated as

$$\gamma = \pi - \beta(\omega), \quad (5.5)$$



and the resultant propeller thrust from Eq. 5.4 is

$$F_y^{\mathcal{B}} = F_x^{\mathcal{M}} = T \sin \delta, \quad (5.6a)$$

$$F_z^{\mathcal{B}} = F_z^{\mathcal{M}} = T \cos \delta, \quad (5.6b)$$

$$F_x^{\mathcal{B}} = F_y^{\mathcal{M}} = 0. \quad (5.6c)$$

Because the Gemini II has two motors, a subscript  $i, i = 1, 2$  is adopted to  $F_y^{\mathcal{B}}$  and  $F_z^{\mathcal{B}}$  for representing which motor the thrust is generated from. According to the geometry of the mechanical structure of Gemini II (see Figure 5.16), we can obtain

$$\begin{bmatrix} f_{T,z}^{\mathcal{B}} \\ \tau_x^{\mathcal{B}} \\ \tau_y^{\mathcal{B}} \\ \tau_z^{\mathcal{B}} \end{bmatrix} = \begin{bmatrix} 1 & 1 & 0 & 0 \\ 0 & 0 & H & H \\ L & -L & 0 & 0 \\ 0 & 0 & L & -L \end{bmatrix} \begin{bmatrix} F_{z,1}^{\mathcal{B}} \\ F_{z,2}^{\mathcal{B}} \\ F_{y,1}^{\mathcal{B}} \\ F_{y,2}^{\mathcal{B}} \end{bmatrix}, \quad (5.7)$$

where  $H$  is the body  $z$ -axis direction distance from the teetering hinge of swashplate-less structure to the COM,  $L$  is the body  $x$ -axis direction distance from the motor mounted position to the COM.  $f_{T,z}^{\mathcal{B}}$  is the total thrust in the body  $z$ -axis.  $\tau_j^{\mathcal{B}}, j = x, y, z$  are three moments along the body  $x$ ,  $y$ , and  $z$  axes, respectively.

#### 5.4.1.3 Dynamics

The dynamics of the Gemini II can be represented in a standard rigid motion with both translation and rotation

$$\begin{bmatrix} m\mathbf{I} & 0 \\ 0 & \mathbf{J}^{\mathcal{B}} \end{bmatrix} \begin{bmatrix} \dot{\mathbf{v}}^{\mathcal{I}} \\ \dot{\boldsymbol{\omega}}^{\mathcal{B}} \end{bmatrix} + \begin{bmatrix} 0 \\ \hat{\boldsymbol{\omega}}^{\mathcal{B}} \mathbf{J}^{\mathcal{B}} \boldsymbol{\omega}^{\mathcal{B}} \end{bmatrix} = \begin{bmatrix} \mathbf{f}_g^{\mathcal{I}} \\ 0 \end{bmatrix} + \begin{bmatrix} \mathbf{R}\mathbf{f}_T^{\mathcal{B}} \\ \boldsymbol{\tau}^{\mathcal{B}} \end{bmatrix} \quad (5.8a)$$

$$\mathbf{R} = \mathbf{R}_z(\psi)\mathbf{R}_y(\lambda)\mathbf{R}_x(\varphi), \quad (5.8b)$$

where  $m$ ,  $\mathbf{I}$ , and  $\mathbf{J}^{\mathcal{B}}$  stand for the mass, the identity matrix in  $\mathbb{R}^{3 \times 3}$  and the inertia matrix in the body frame, respectively.  $\boldsymbol{\omega}^{\mathcal{B}}$  is the angular velocity vector represented in the body frame while  $\hat{\boldsymbol{\omega}}^{\mathcal{B}}$  is the skew-symmetric cross-product matrix of  $\boldsymbol{\omega}^{\mathcal{B}}$ ,



$\mathbf{v}^I$  is the velocity vector represented in the inertial frame.  $\mathbf{f}_g^I = [0 \ 0 \ mg]^T$  stands for the gravity in the inertial frame and the thrust vector in body frame is  $\mathbf{f}_T^B = [0 \ 0 \ f_{T,z}^B]^T$ .  $\boldsymbol{\tau}^B = [\tau_x^B \ \tau_y^B \ \tau_z^B]^T$  is the moment vector.  $\mathbf{R}$  is the rotation matrix from the inertial frame to the body frame following the  $z - y - x$  Tait-Bryan order where  $\psi$ ,  $\lambda$ , and  $\varphi$  stand for the Euler angle yaw, pitch, and roll, respectively.

It should be noted that three simplifications are adopted in the above modeling process. (1) The propeller torques are ignored in  $\boldsymbol{\tau}^B$  as it is usually small when compared to the torques induced by thrust. (2) The gyroscopic torque which comes from the direction change of the angular momentum of the propeller when the rotating plane of propeller tilts by the swashplate-less structure, is also not modeled in  $\boldsymbol{\tau}^B$  because the inertia of rotor and propeller are quite small when compared to the inertia of the whole aircraft. Also, this torque only occurs in the transient response of roll and yaw rotation and is zero when the roll and yaw angle converge to the desired values. (3) In the calculation for the force vector  $\mathbf{f}_T^B$ , due to the tilt angle of the rotating plane of the propeller, the thrust projected to the  $xy$  plane of the body frame is neglected. This force is similar to the gyroscopic torque, only present in the transient response of roll rotation and becomes zero when it converges to the desired value. The neglected torque and force can simplify the dynamic model, however, it will lead to some dynamics remaining unmodeled. In this paper, we focus on designing the baseline controller that aims to stabilize the overall system. For this purpose, the three simplifications are valid, as shown in the actual experiments.

## 5.4.2 Control

### 5.4.2.1 Control System Structure

The whole control structure of the Gemini II is shown in [Figure 5.17](#). The navigation module produces the desired position  $\mathbf{p}_d$  and yaw angle  $\psi_d$  for the



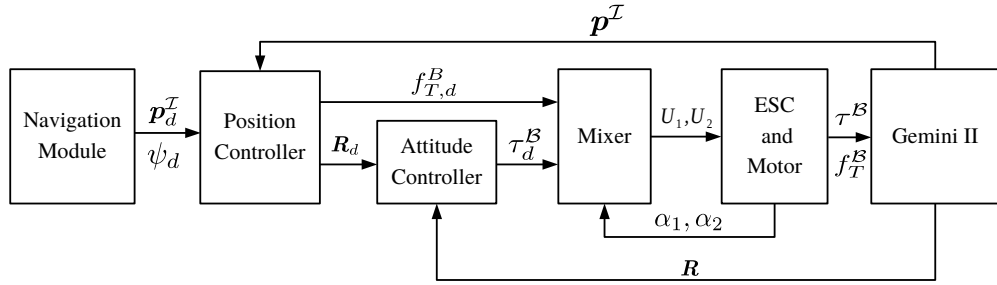


**Figure 5.17** Control system structure of the Gemini II.

position controller to track. The position controller will generate the desired attitude  $\mathbf{R}_d$  and body  $z$ -axis force  $T_d$ . The attitude controller will calculate the desired moment  $\boldsymbol{\tau}_d^B$  based on the desired attitude.  $\alpha_i, i = 1, 2$  is the angular location of motor  $i$  measured by the magnet encoder. The major difference between the swashplate-less bi-copter controller and the previous servo-based bi-copter in [Figure 2.19](#) is addition of real-time angular position feedback and the reduction of command. Instead of relying on the throttle command and servo command to generate moments, the swashplate-less bi-copter is able to generate moments through only the feedback-coupled throttle command. Lastly, according to the  $T_d$ ,  $\boldsymbol{\tau}_d^B$  and real-time angular position of the motor rotor  $\alpha_i$ , the mixer will calculate the motor throttles that will be sent to the electronic speed control (ESC) for controlling the motors to drive propellers.

#### 5.4.2.2 Position Controller

The position controller of the Gemini II is a cascaded controller with proportional gain  $K_p^p$  and an inner velocity loop. The desired velocity  $\mathbf{v}_d^T$  is calculated as follows:

$$\mathbf{v}_d^T = K_p^p \cdot \mathbf{p}_e^T = K_p^p \cdot (\mathbf{p}_d^T - \mathbf{p}^T) , \quad (5.9)$$

where  $\mathbf{p}_e^T$ ,  $\mathbf{p}_d^T$  and  $\mathbf{p}^T$  are the position error, desired position and current position in the inertia frame, respectively.

The velocity loop is a full PID controller and its output is the desired acceleration



$\mathbf{a}_d^{\mathcal{I}}$  that is calculated by the desired velocity and current velocity as

$$\mathbf{v}_e^{\mathcal{I}} = \mathbf{v}_d^{\mathcal{I}} - \mathbf{v}^{\mathcal{I}}, \quad (5.10a)$$

$$\mathbf{a}_d^{\mathcal{I}} = K_p^v \cdot \mathbf{v}_e^{\mathcal{I}} + K_i^v \cdot \int \mathbf{v}_e^{\mathcal{I}} dt + K_d^v \cdot \dot{\mathbf{v}}_e^{\mathcal{I}}, \quad (5.10b)$$

where  $\mathbf{v}_e^{\mathcal{I}}$  and  $\mathbf{v}^{\mathcal{I}}$  are the velocity error and current velocity, respectively,  $K_p^v$ ,  $K_i^v$  and  $K_d^v$  are the gains of PID actions in the velocity loop.

When the desired acceleration is obtained, the desired attitude  $\mathbf{R}_d$  and force  $\mathbf{f}_{T,d}^{\mathcal{B}} = [0 \ 0 \ f_{T,z,d}^{\mathcal{B}}]^T$  can be solved from the below equation following the method in [83]:

$$m\mathbf{a}_d^{\mathcal{I}} = \mathbf{f}_g^{\mathcal{I}} + \mathbf{R}_d \mathbf{f}_{T,d}^{\mathcal{B}}. \quad (5.11)$$

It should be noted that a rotation around the body  $z$ -axis does not affect the force direction, hence the yaw angle can be freely specified. Once the desired yaw angle is specified, the whole desired attitude  $\mathbf{R}_d$  can be uniquely determined and will be used as the input of the attitude controller.

#### 5.4.2.3 Attitude Controller

The attitude controller is also cascaded. The outer loop (i.e., angular loop) is a proportional controller to track the desired attitude  $\mathbf{R}_d$ . The quaternion ( $\mathbf{q} = [w, \mathbf{r}^T]^T$ ) is used to represent the attitude, where  $w$  and  $\mathbf{r}$  denote the scalar and vector part of the quaternion, respectively. With the quaternion representation, the attitude error  $\mathbf{q}_e$  and desired angular velocity  $\boldsymbol{\omega}_d^{\mathcal{B}}$  are calculated based on the “Quaternion linear” method in [84]:

$$\mathbf{q}_e = \mathbf{q}^* \otimes \mathbf{q}_d = [w_e \ \mathbf{r}_e^T]^T \quad (5.12a)$$

$$\eta = 2 \cdot \arctan2(\|\mathbf{r}_e\|, w_e) \quad (5.12b)$$

$$\boldsymbol{\omega}_d^{\mathcal{B}} = K_p^a \cdot \boldsymbol{\xi}_e^{\mathcal{B}} = K_p^a \cdot \text{sign}(w_e) \cdot \frac{\eta}{\sin(\frac{\eta}{2})} \mathbf{r}_e, \quad (5.12c)$$



where  $\mathbf{q}_d$  and  $\mathbf{q}$  are the desired and actual attitude, operator  $*$  and  $\otimes$  denote the conjugate and multiplication operation of quaternion, respectively,  $K_p^a$  is a proportional gain from attitude error  $\xi_e^B$  to desired angular velocity  $\omega_d^B$ .

The inner loop (i.e., angular velocity loop) is a PID controller used to track the desired angular velocity  $\omega_d^B$ , which can be represented as

$$\omega_e^B = \omega_d^B - \omega^B \quad (5.13a)$$

$$\tau_d^B = K_p^w \cdot \omega_e^B + K_i^w \cdot \int \omega_e^B dt + K_d^w \cdot \dot{\omega}_e^B, \quad (5.13b)$$

where  $\omega_e^B$  and  $\omega^B$  are angular velocity error and current angular velocity, respectively.  $K_p^w$ ,  $K_i^w$  and  $K_d^w$  are the gains of PID terms in the angular velocity loop. The output of the inner loop is the desired moment  $\tau_d^B = [\tau_{x,d} \quad \tau_{y,d} \quad \tau_{z,d}]^T$ .

#### 5.4.2.4 Mixer

The mixer is used to calculate the motor throttles ( $U_1$ ,  $U_2$ ) that produce the desired moment  $\tau_d^B$  and force  $f_{T,z,d}^B$ . Combining Eq. 5.6 and Eq. 5.7, because the tilt angles of propeller disks are small during normal operation, the result can be simplified as

$$\begin{bmatrix} f_{T,z}^B \\ \tau_x^B \\ \tau_y^B \\ \tau_z^B \end{bmatrix} = \begin{bmatrix} 1 & 1 & 0 & 0 \\ 0 & 0 & H & H \\ L & -L & 0 & 0 \\ 0 & 0 & L & -L \end{bmatrix} \begin{bmatrix} T_1 \\ T_2 \\ T_1\delta_1 \\ T_2\delta_2 \end{bmatrix}, \quad (5.14)$$

where  $T_i$  and  $\delta_i$  are the motor thrust and tilting angle of the propeller disk of motor  $i, i = 1, 2$ , respectively.

Given the desired moment vector  $\tau_d^B = [\tau_{x,d}^B \quad \tau_{y,d}^B \quad \tau_{z,d}^B]^T$  and force  $f_{T,z,d}^B$ , the desired body  $z$ -axis motor thrust ( $T_{1,d}$ ,  $T_{2,d}$ ) and body  $y$ -axis force ( $T_{1,d}\delta_{1,d}$ ,  $T_{2,d}\delta_{2,d}$ )



can be solved from [Eq. 5.14](#) as below

$$\begin{bmatrix} T_{1,d} \\ T_{2,d} \\ T_{1,d}\delta_{1,d} \\ T_{2,d}\delta_{2,d} \end{bmatrix} = \begin{bmatrix} \frac{1}{2} & 0 & \frac{1}{2L} & 0 \\ \frac{1}{2} & 0 & \frac{-1}{2L} & 0 \\ 0 & \frac{1}{2H} & 0 & \frac{1}{2L} \\ 0 & \frac{1}{2H} & 0 & \frac{-1}{2L} \end{bmatrix} \begin{bmatrix} f_{T,z,d}^{\mathcal{B}} \\ \tau_{x,d}^{\mathcal{B}} \\ \tau_{y,d}^{\mathcal{B}} \\ \tau_{z,d}^{\mathcal{B}} \end{bmatrix}, \quad (5.15)$$

where  $T_{1,d}$  and  $T_{2,d}$  are the desired thrust of the front and rear motor,  $\delta_{1,d}$  and  $\delta_{2,d}$  are the desired tilt angles of the front and rear propeller disks. The motor throttles ( $U_1, U_2$ ) can be calculated as

$$\begin{bmatrix} U_1 \\ U_2 \end{bmatrix} = \begin{bmatrix} K_t & 0 \\ 0 & K_t \\ \sin(\alpha_1 - \gamma_1) & 0 \\ 0 & \sin(\alpha_2 - \gamma_2) \end{bmatrix}^T \begin{bmatrix} T_{1,d} \\ T_{2,d} \\ \frac{\delta_{1,d}}{K_a} \\ \frac{\delta_{2,d}}{K_a} \end{bmatrix}, \quad (5.16)$$

where  $K_t$  and  $K_a$  are positive proportion coefficients from propeller thrust to the corresponding motor throttle, and from sinusoidal amplitude to tilting angle of propeller disk, respectively.  $\gamma_i = \pi - \beta_i(\omega), i = 1, 2$ .

According to [Eq. 5.15](#) and [Eq. 5.16](#), the relation between motor throttles and desired moments and force can be finally derived as

$$U_1 = C_1 + A_1 \sin(\alpha_1 - \gamma_1) \quad (5.17a)$$

$$U_2 = C_2 + A_2 \sin(\alpha_2 - \gamma_2) \quad (5.17b)$$

$$C_1 = \frac{K_t}{2} f_{T,z,d}^{\mathcal{B}} + \frac{K_t}{2L} \tau_{y,d}^{\mathcal{B}}, A_1 = \frac{1}{K_a T_{1,d}} \left( \frac{\tau_{x,d}^{\mathcal{B}}}{2H} + \frac{\tau_{z,d}^{\mathcal{B}}}{2L} \right) \quad (5.17c)$$

$$C_2 = \frac{K_t}{2} f_{T,z,d}^{\mathcal{B}} - \frac{K_t}{2L} \tau_{y,d}^{\mathcal{B}}, A_2 = \frac{1}{K_a T_{2,d}} \left( \frac{\tau_{x,d}^{\mathcal{B}}}{2H} - \frac{\tau_{z,d}^{\mathcal{B}}}{2L} \right). \quad (5.17d)$$

## 5.5 Experiment results

This chapter presents the experiment results. Through monitoring the power performance, force and torque, we first evaluate the power and dynamic performance



of a single swashplate-less actuator. Then, we analyzed the swashplate-less UAV flight performance and compared it to the others.

### 5.5.1 Actuators Evaluation

#### 5.5.1.1 Power Consumption

To verify the feasibility and performance of the servo-less bi-copter design, we first test the actuators on a test bench, as shown in [Figure 5.18](#), then compared the agility among Gemini II , quad-copter, and our previous servo bi-copter, Gemini mini [106].



**Figure 5.18** Actuator evaluation setup. ATI 6-axis force sensor is used along with 3D printed structure for testing.

Using the well-tuned parameters, we identified the external force disturbance rejection model. Then we conduct two disturbance tests, along with a trajectory



tracking experiment on the complete UAV, Gemini II. Videos showing the UAV performance in these tests are available in the supplementary material.

We first study the effect of the swashplate-less mechanism on propeller power consumption. Figure 5.19 shows the power comparison of the original 13.4 inches propeller MF1302 and its modification with the swashplate-less mechanism, which is 1 inch wider due to bearing and hinges, at different thrusts. As can be seen, the power consumption results are very close with and without the swashplate-less mechanism. By the prediction of the ideal disk loading theory, the increase in propeller size should boost efficiency by 7%, but the absence of such behavior indicates the swashplate-less mechanism lowers the efficiency by 7% mainly due to the optimized design of the propeller blade is affected by the slight change of the angle of attack and the increased diameter. Moreover, due to the slightly increased propeller size, the variant with a swashplate-less mechanism obtains a larger maximal thrust. Figure 5.19 also shows the operating point of the propeller at hovering. The operating point is near 50% PWM, reserving a safe margin for the sinusoidal drive command and avoiding saturation.

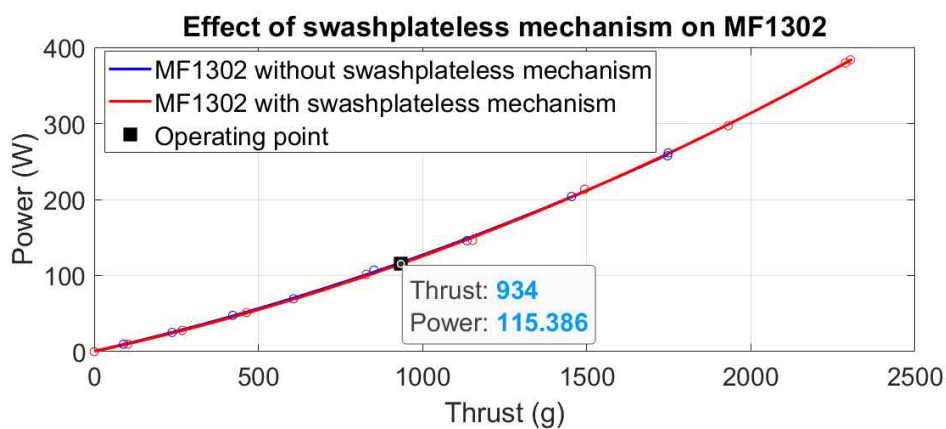


**Figure 5.19** Effect of the swashplate-less mechanism on the power efficiency. The swashplate-less mechanism barely has any effect on the power efficiency.

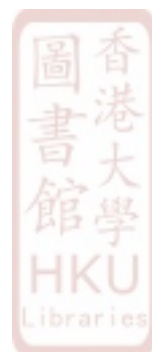
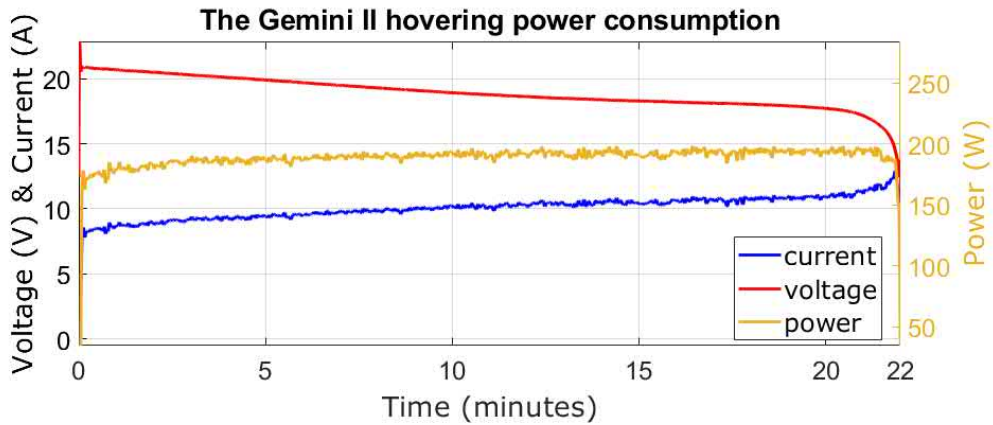


Figure 5.20 shows the power consumption of the Gemini II during the flight endurance test. The average power consumption during hovering is 193 W, which indicates each propulsion system consumes 96.5 W of power. The error between



**Figure 5.20** Gemini II hovering power consumption. The Gemini II consumes around 193 W of power on average while hovering.

the measured power consumption during flight and the prediction (see Figure 5.19) might be due to the imprecision of the on-board power monitoring module. With the 5S 5000 mAh battery onboard, the actual test lasted for 22 minutes and the landing was automatically initiated after the battery voltage is observed below 16.5 V. The Gemini II weighs 1869 g (including a 600 g LiDAR payload), making its hovering efficiency 9.68 g/W.

### 5.5.1.2 Sinusoidal Throttle Command

To verify the assumption we made earlier in Section 5.3.3.1 about the relation between  $\delta$  and  $A$  is proportional, we fixed the voltage to 21 V and conducted a sinusoidal amplitude sweeping command test when the propeller is rotating at the hovering speed. As shown in Figure 5.21a, the relation is highly linear with no clear sign of actuator deadband, and Eq. 5.2 can be a curve fitted into the function shown in the legend.

Previous works in [47] conducted a similar experiment as shown in Figure 5.21b, where the moment magnitude directly reflects the titling angle, and the pulse PWM duty is identical to our definition of sinusoidal amplitude. However, barely any moment magnitude is generated under 5% pulse PWM duty at three different operating speeds. With the addition of bearings in our design, the tilting response no longer



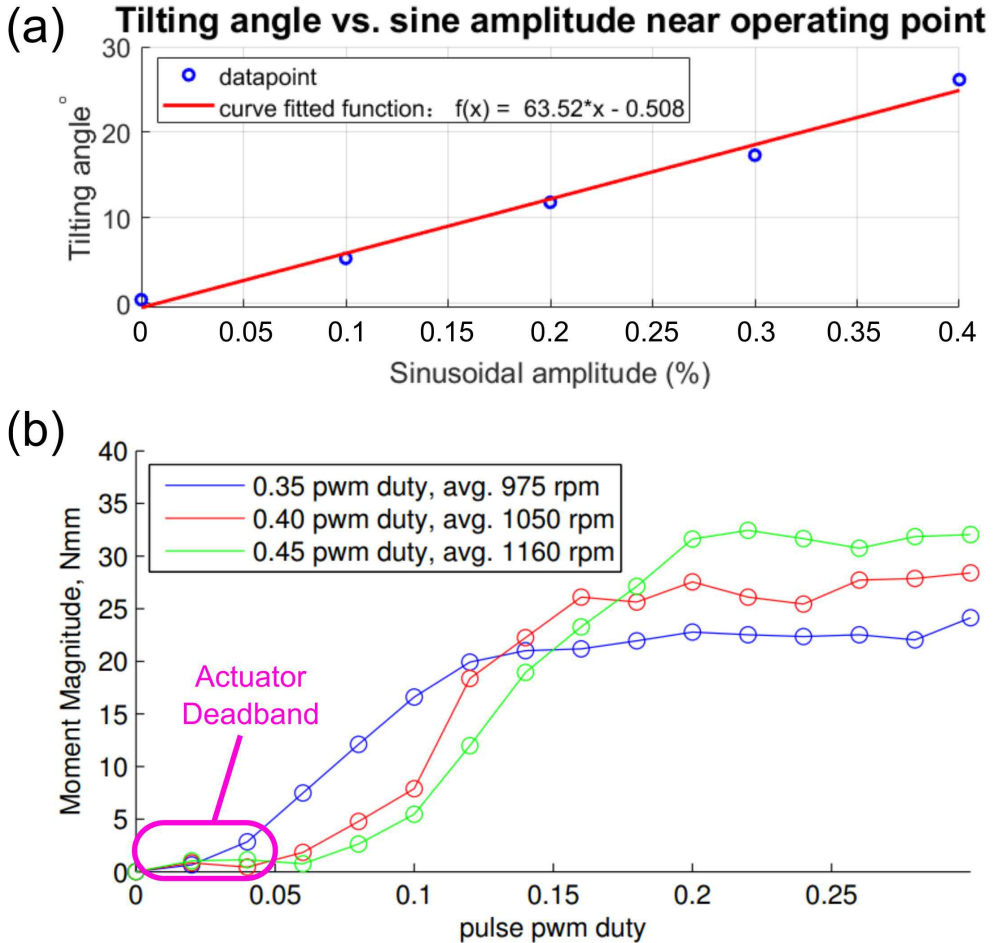


**Figure 5.21** (a) Our improved mechanism: Tilting angle vs. sinusoidal amplitude response near operating point (highly linear with no actuator deadband). (b) Previous swashplate-less work: Moment magnitude vs. sinusoidal amplitude response at three different operating speeds. **Image Source:** [47]

has a dead-zone nonlinearity in control response at low drive amplitudes ascribed to sliding friction and becomes highly linear.

In practice, we limit the sinusoidal amplitude below  $A_{\max} = 26\%$  to ensure the side hubs do not collide with the teetering hub, and the motor does not overheat. Similar to [108], we also calibrated the relation between  $\beta$  and  $\omega$ , and compensated the angle lag in the controller.



### 5.5.1.3 Agility Comparison

To demonstrate the agility of the UAV with the swashplate-less mechanism, step response tests on roll attitude were conducted on Gemini II, our previous servo-based bi-copter, Gemini mini [106], and a quad-copter, all with the same width and weight. The tests on Gemini II and the quad-copter are conducted on actual UAVs, and the test on Gemini mini is performed on a high-fidelity model identified by a sweep sine excitation [107]. Gemini II and the quad-copter UAV are controlled by well-tuned PID controllers and the Gemini mini is controlled by a high-gain optimal controller designed by H-infinity synthesis [107]. The three UAVs were initially hovering without position feedback, at time zero, 20-degree roll angle attitude commands were given to the UAV. As shown in Figure 5.22, the quad-copter quickly reached the attitude target at 110 ms, while the Gemini II has a larger rise time of 174 ms. In contrast, the servo-based bi-copter, Gemini mini, despite its high-gain controller, has a rise time of 339 ms.

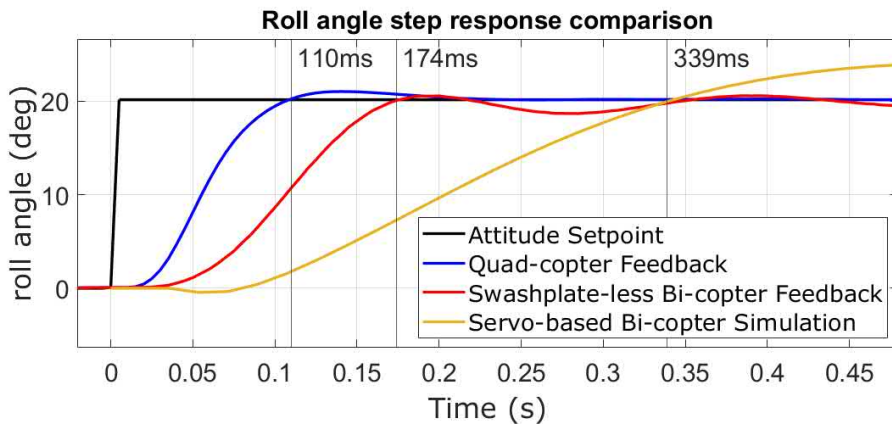


**Figure 5.22** Roll angle step response comparison. The swashplate-less bi-copter Gemini II performs twice as fast as the servo-based bi-copter Gemini mini, and is 64 ms slower than the corresponding quad-copter.

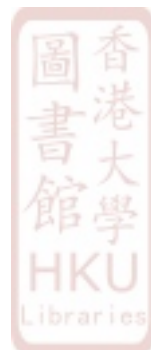
When comparing the actuator time constant  $T$  of the two bi-copters, Gemini II has a  $T$  of 28.5 ms, while the Gemini mini has a  $T$  of 33.2 ms with an additional 30 ms pure time delay (see (6) of [107]). We also notice that the servo-based bi-copter exposes a clear non-minimum phase phenomenon where the response goes first



towards the opposite direction of the command. This phenomenon is much mitigated and almost negligible in Gemini II. The excelsior actuator response and the vanished behavior of the non-minimum phase nature of the Gemini II results in a great improvement in agility when compared to servo bi-copters, yet it is still outmatched by quad-copters at a cost of 55% higher average hovering power consumption.

### 5.5.2 Model Identification and Disturbance Rejection Analysis

In this section, we perform disturbance analysis of the overall aircraft, especially along the roll direction (or  $y$ -axis) which differs the most from the standard quadcopter. [Figure 5.23](#) shows the diagrams of  $y$ -axis position control. The upper diagram inside of the red box represents the closed-loop roll angle control system and the lower diagram indicates the complete closed-loop  $y$ -axis position control system. The closed-loop transfer function of the roll rate loop, roll angle loop,  $y$ -axis velocity loop, and  $y$ -axis position loop are  $G_r$ ,  $G_a$ ,  $G_v$ , and  $G_p$ , respectively. They can be calculated as shown from [Eq. 5.18](#) to [Eq. 5.21](#).



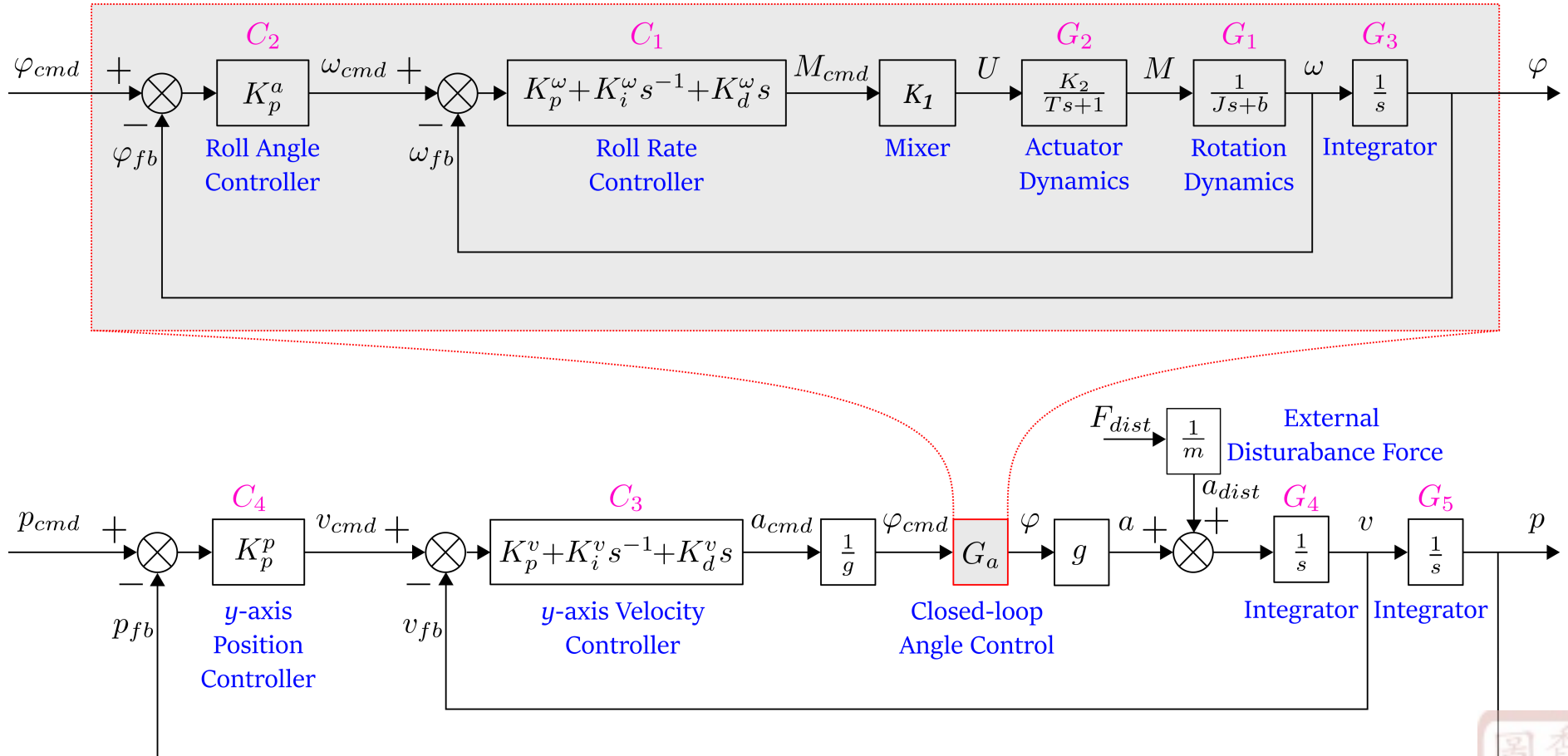


**Figure 5.23** y-axis position control system structure of the Gemini II. The upper diagram inside of the red box represents the closed-loop roll angle control system and the lower diagram indicates the complete closed-loop y-axis position control system.

$$G_r = \frac{\omega_{fb}(s)}{\omega_{cmd}(s)} = \frac{K_1 C_1 G_1 G_2}{1 + K_1 C_1 G_1 G_2}, \quad (5.18)$$

$$G_a = \frac{\varphi_{fb}(s)}{\varphi_{cmd}(s)} = \frac{C_2 G_r G_3}{1 + C_2 G_r G_3}, \quad (5.19)$$

$$G_v = \frac{v_{fb}(s)}{v_{cmd}(s)} = \frac{C_3 G_a G_4}{1 + C_3 G_a G_4}, \quad (5.20)$$

$$G_p = \frac{p_{fb}(s)}{p_{cmd}(s)} = \frac{C_4 G_v G_5}{1 + C_4 G_v G_5} = \frac{C_3 C_4 G_a G_4 G_5}{1 + C_3 G_a G_4 + C_3 C_4 G_a G_4 G_5}. \quad (5.21)$$

The transfer function from the external force disturbance  $F_{dist}$  to the position output  $p$  can be represented as:

$$G_{dist} = \frac{p(s)}{F_{dist}(s)} = \frac{\frac{1}{m} G_4 G_5}{1 + \frac{1}{m} C_3 (C_4 + s) G_a G_4 G_5} = \frac{G_4 G_5}{m + C_3 (C_4 + s) G_a G_4 G_5}. \quad (5.22)$$

**Table 5.2** Gemini II y-axis Control Parameters

Controller	Parameters		
Roll angle ( $C_2$ )		$K_p^a = 13$	
y-axis Velocity ( $C_3$ )	$K_p^v = 1.8$	$K_i^v = 0.4$	$K_d^v = 0.2$
y-axis Position ( $C_4$ )		$K_p^p = 0.95$	

which involves the velocity controller  $C_3$ , position controller  $C_4$ , transfer functions  $G_4$  and  $G_5$ , and the angle loop transfer function  $G_a$ . The transfer functions  $G_4$  and  $G_5$  are both known from Figure 5.23, so as the controllers  $C_3$  and  $C_4$ , which are designed previously and their parameters are shown in Table 5.2. The angle loop response  $G_a$ , according to Eq. 5.19, is dependent on the known angle controller  $C_2$  shown in Table 5.2,  $G_3$ , which is an integrator from Figure 5.23, and the angular rate loop  $G_r$ . We could further breakdown  $G_r$  as in Eq. 5.18, but in practice, we identify  $G_r$  directly from real flight data to obtain higher model accuracy. According to the structure of  $G_r$  in Eq. 5.18, it has three poles and one zero and their values are identified through the MATLAB system identification toolbox. The resultant model is:

$$G_r = \frac{-23.8672s + 35879}{s^3 + 51.6s^2 + 2017.1s + 43762}. \quad (5.23)$$



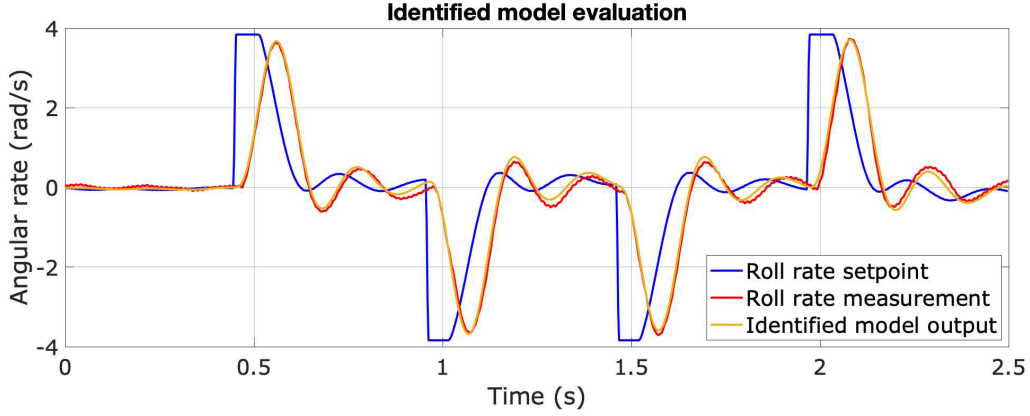


**Figure 5.24** Gemini II identified model evaluation. The roll rate measurement and identified model output comparison are highly overlapping, proving the accuracy of the model.

Figure 5.24 shows the roll rate command, which excites the roll dynamics, the measured roll rate data and the predicted output from the identified model  $G_r$ . As can be seen, the identified model output highly matches the actual roll rate feedback data, indicating the accuracy of the predicted dynamics of the closed-loop roll rate control system.

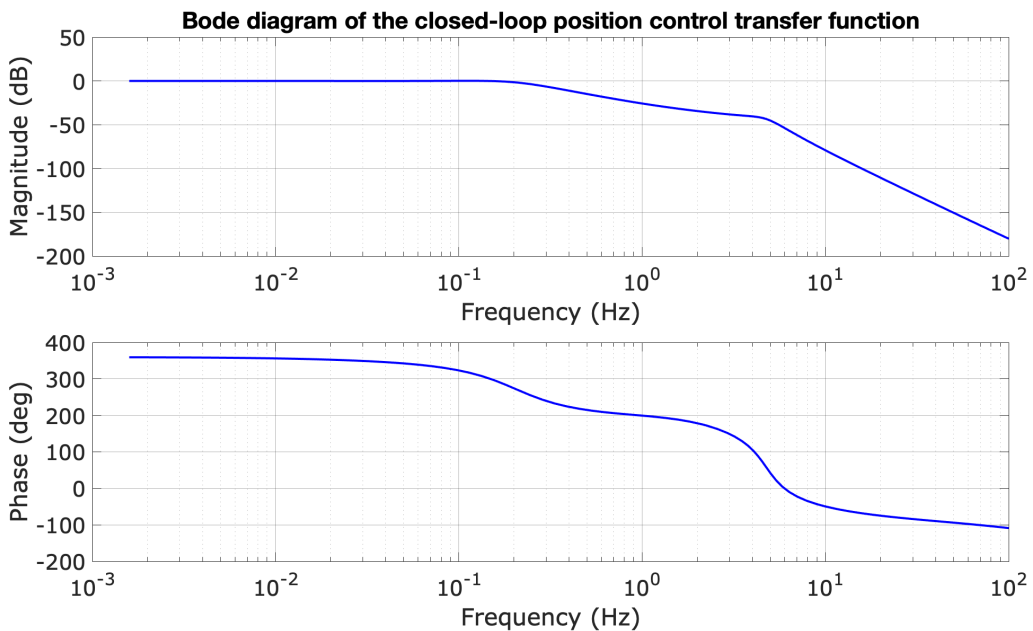
Once  $G_r$  and all outer loop controllers  $C_2$ ,  $C_3$ , and  $C_4$  (shown in Table 5.2) are determined, the  $G_p$  and  $G_{dist}$  can be finally obtained as:

$$G_p = \frac{-58.95s^3 + 88090s^2 + 797500s + 177200}{s^7 + 51.61s^6 + 2017s^5 + 43390s^4 + 559100s^3 + 927500s^2 + 984000s + 177200}, \quad (5.24)$$

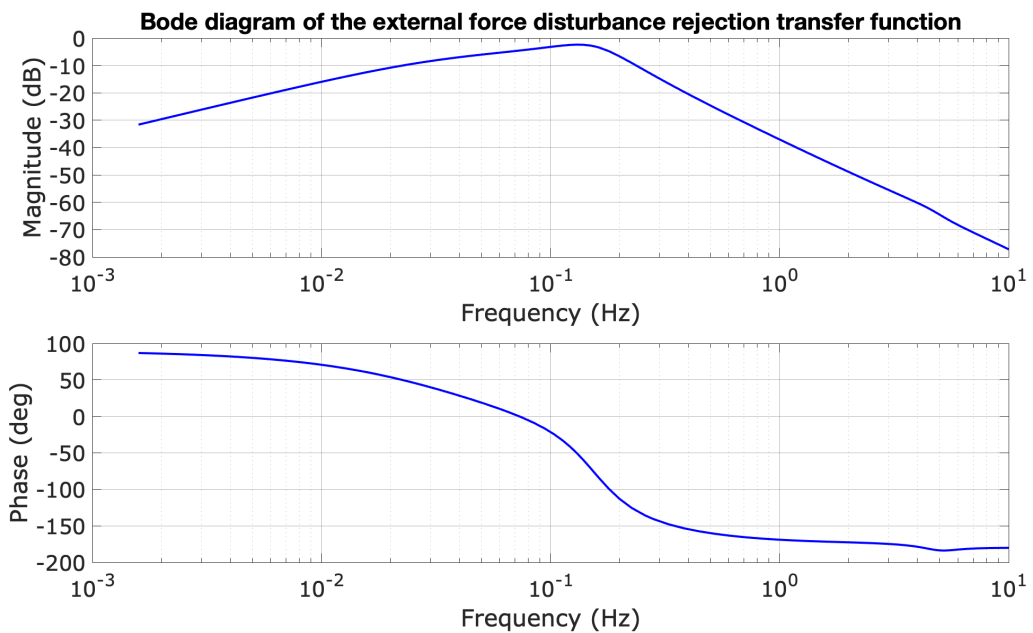
$$G_{dist} = \frac{0.5495s^5 + 28.36s^4 + 1108s^3 + 23870s^2 + 256300s}{s^7 + 51.61s^6 + 2017s^5 + 43420s^4 + 517300s^3 + 509600s^2 + 540700s + 97390}. \quad (5.25)$$

The external disturbance response bode diagram of  $G_p$  and  $G_{dist}$  are shown in Figure 5.25a and Figure 5.25b, respectively. As shown in Figure 5.25b, the external disturbance force can be attenuated in the whole frequency band and the most sensitive frequency of disturbance is around 0.13 Hz with a magnitude of -2.37 dB.





(a) Bode diagram of the closed-loop position control transfer function.



(b) Bode diagram of the external force disturbance rejection transfer function.

**Figure 5.25** Frequency domain analysis of the Gemini II (a) Bode diagram of the closed-loop position control transfer function; (b) Bode diagram of the external force disturbance rejection transfer function.



### 5.5.3 Disturbance Test

#### 5.5.3.1 Poking

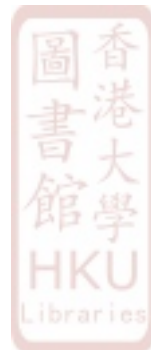
To verify the quality of the position control loop and the robustness of the Gemini II in presence of disturbances, a poking test, and a wind disturbance test are conducted. With the motion capture system providing position feedback, the Gemini II hovers at a fixed point in space and was hit 10 times from 3 different angles as shown in [Figure 5.26a](#).

As shown in in-flight data in [Figure 5.26b](#), the first 4 hits were firmly poked at the front of the aircraft, i.e., the  $x$ -axis of the world frame. From the 29 s to 36 s, 4 consecutive hits result in 4 peaks on the pitch angle, ranging from 3 to 5 degrees, and were all recovered quickly. Notice that each poking also makes about 5 cm displacement on the  $x$ -direction of the world frame, and all of them were recovered within half a second.

The following three firm pokes were made on the front of the right side body, in order to test its yaw disturbance rejection performance. During the actual testing, the first 2 hits made between 38 s to 41 s resulted in spikes on both yaw and roll, and the last hit made on 43 s only pushed the roll to tilt instead of having an impact on the yaw as well. From the data, we can see that both yaw and roll recovered quickly as well.

The last 3 hits were gentle pushes made on the center of the right side body. The purpose of the last 3 hits is to test the roll attitude control ability. From 48 s to 55 s, 3 even pushes were made, resulting in 5 to 10 cm displacement on the  $x$ -direction world frame as well as 5 degrees tilt on the roll angle.

To examine the inner controller loop, we take a closer look at the first poke. From [Figure 5.27a](#), a clear sign of disturbance happens around 31.2 s (boxed in green), resulting in  $-0.6 \text{ m/s}^2$  angular rate differences between the desired and actual pitch rate,  $1.2 \text{ m/s}^2$  angular rate differences between the desired and actual roll



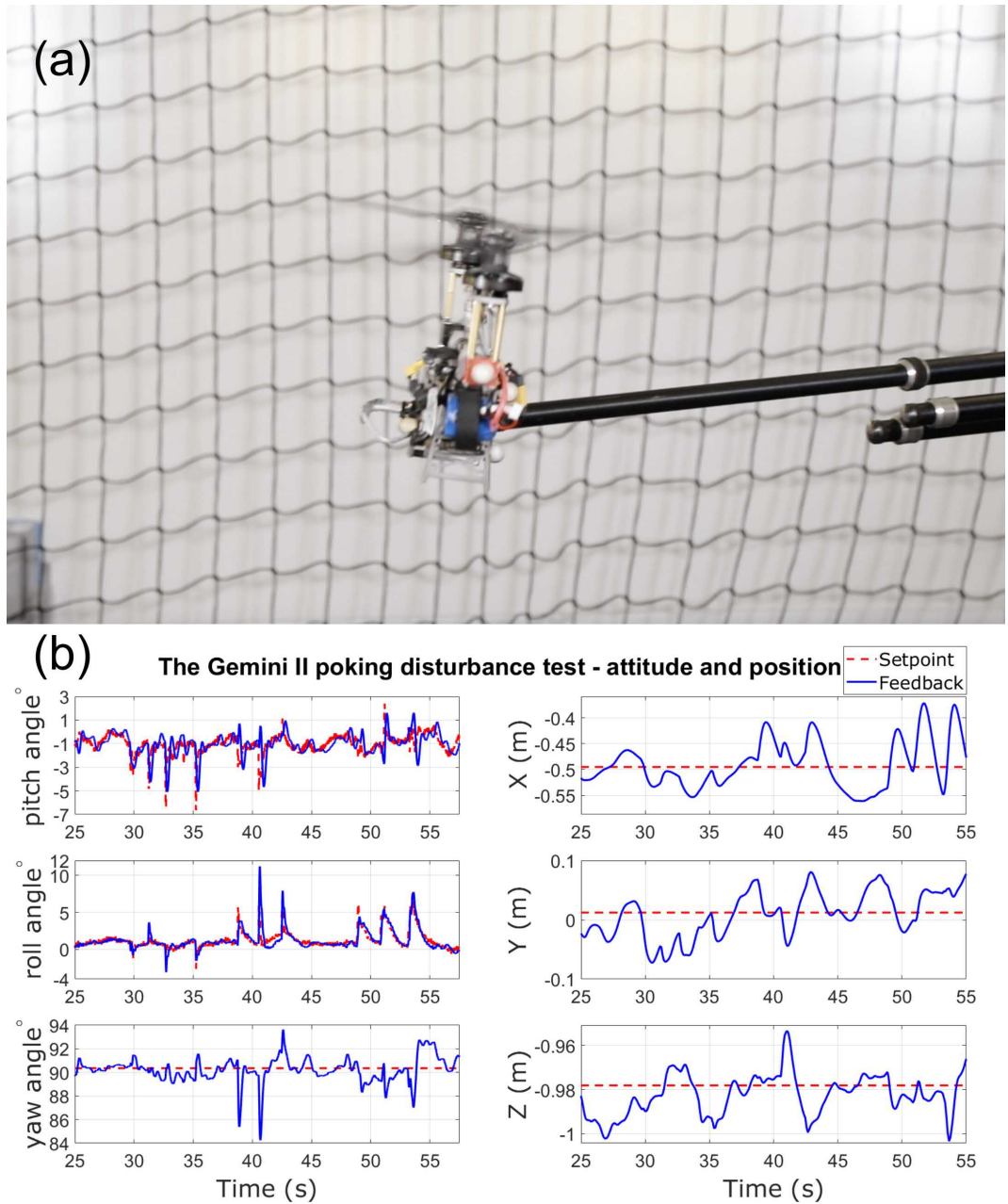


**Figure 5.26** Gemini II poking test (a) Test setup (b) The attitude and position setpoint vs. feedback during the poking test.



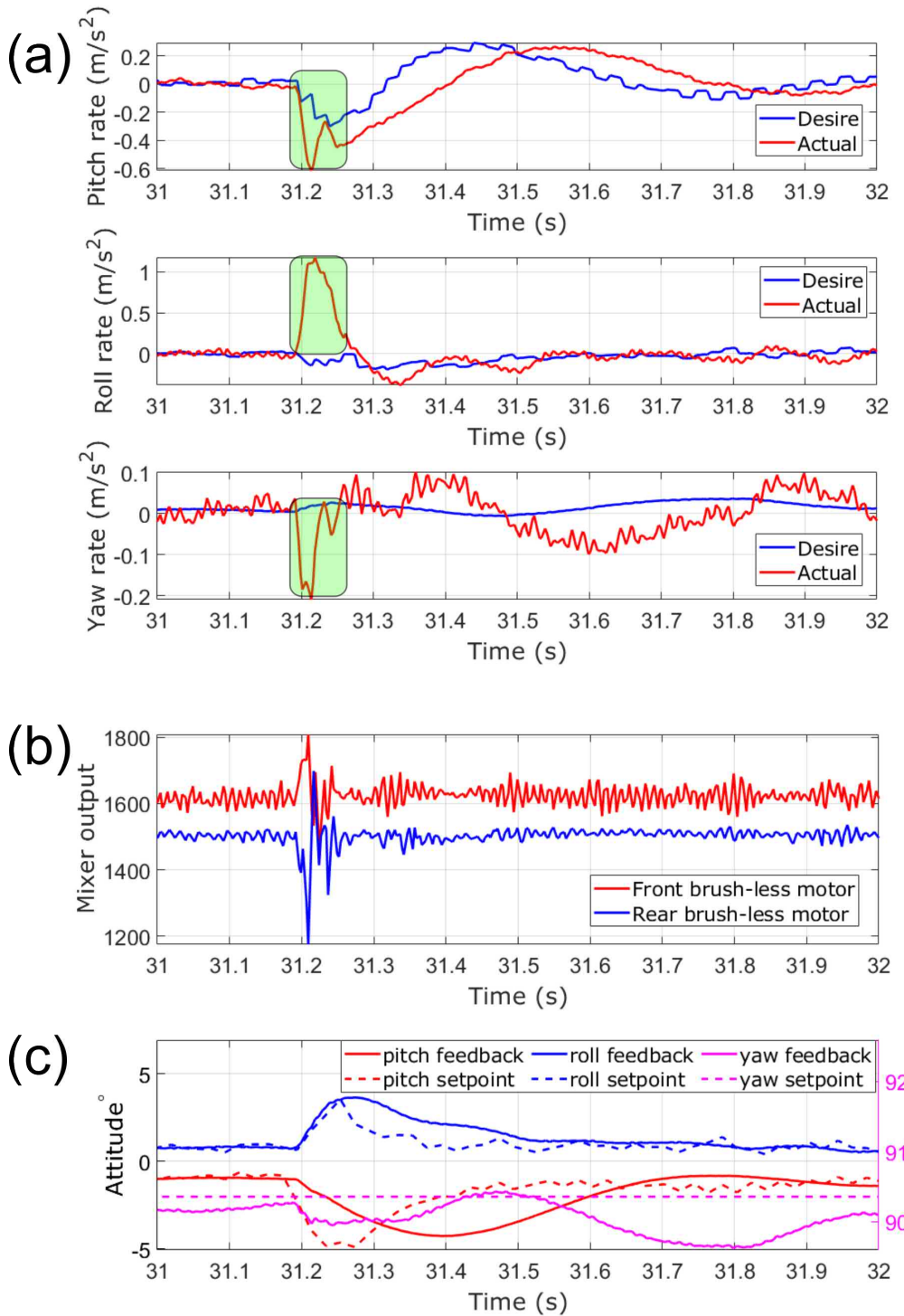


**Figure 5.27** Closeup data during the first poke **(a)** Desired angular rate vs. actual angular rate during the first poke (boxed in green); **(b)** Mixer output during the first poke; **(c)** Attitude setpoint vs. feedback during the first poke.



rate, and  $-0.2 \text{ m/s}^2$  angular rate differences between the desired and actual yaw rate. When facing such disturbance, the yaw and pitch quickly recovered back to the desired angular rate within 0.05 s. On the other hand, the angular roll rate converged to the desired value within 0.1 seconds. As shown in Figure 5.27b, upon a negative pitch disturbance, the rear brush-less motor lowers the output, and the front brush-less motor increases the output to generate a thrust resulting in a positive pitch command. Meanwhile, the high-frequency sinusoidal waves indicate that the cyclic blade control is constantly adjusting the attitude. Note that a motor command offset of roughly 100 constantly exists between the front and rear brush-less motors when no disturbances are applied. This phenomenon is because the center of gravity is not perfectly located in between the two actuators, resulting in a need for constant pitching torque generation. Figure 5.27c shows a closeup of the attitude setpoint vs. feedback during the first poke, indicating that each displacement disturbance was recovered within half a second. The success of this experiment marks the robustness of the controller.

### 5.5.3.2 Wind Disturbance

When the UAVs are deployed in the field, gust wind will cause complicated aerodynamic disturbances to the UAV body and the propellers. Since the Gemini II uses a similar differential rotation speed to control the pitch as that of the quad-copters, which has been extensively studied, the disturbance rejection performance on the roll is of particular interest to us. In order to simulate wind disturbance on the roll, the Gemini II is tested at hovering where two electric fans provide operating wind speeds ranging from 4.5 m/s to 5 m/s. As shown in Figure 5.28a, the direction of the wind blows along the  $x$ -axis direction of the world frame, hitting on the left side of the vehicle. Figure 5.28b shows the attitude and position control performance.

At first, the Gemini II was hovering at a fixed point. The electric fan was turned on at 37 s and turned off at 57 s. The fan came to a complete stop at 70 s. The roll attitude data clearly shows a 1-degree disturbance while the fan got turned on and



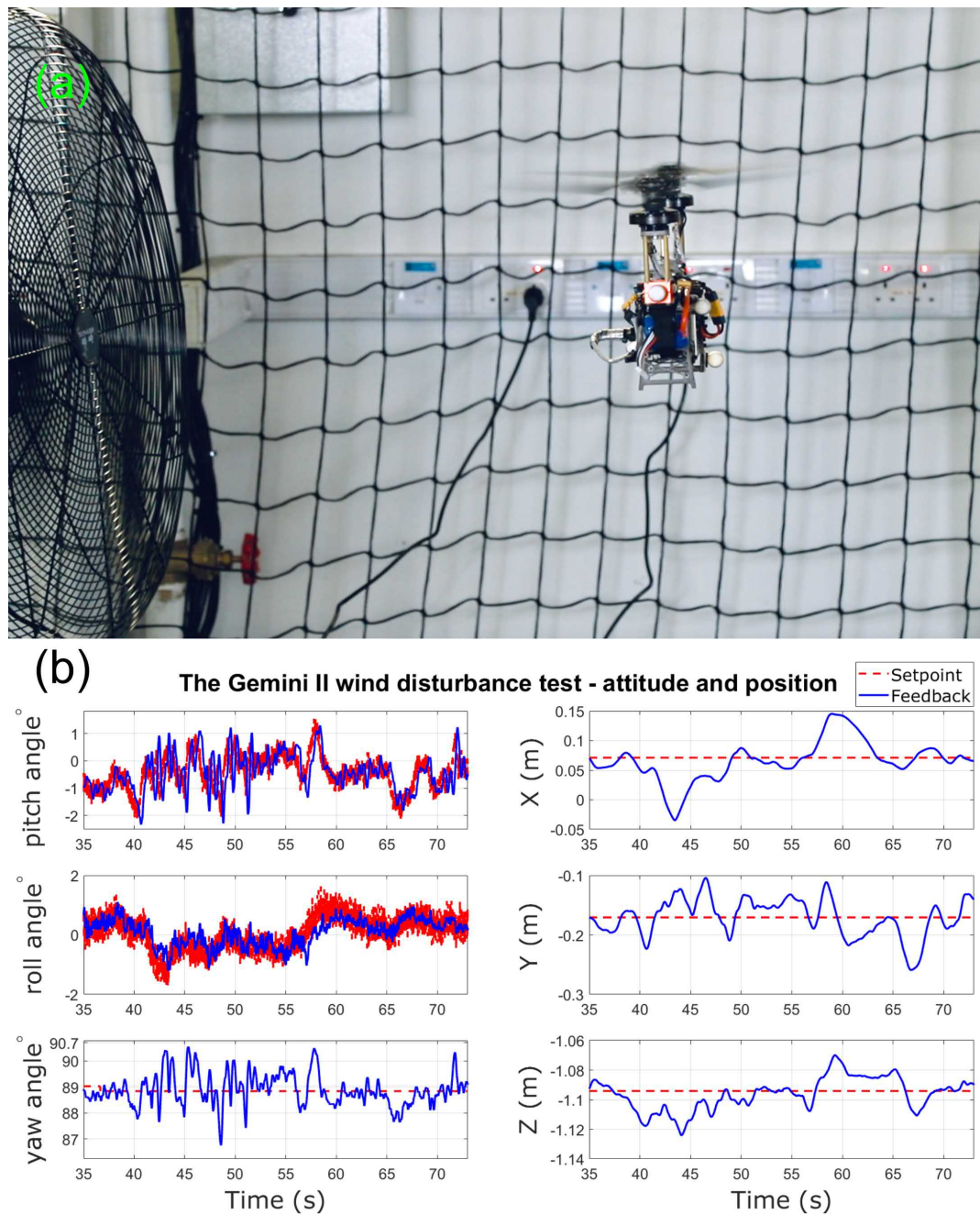


**Figure 5.28** Gemini II wind disturbance test **(a)** Test setup **(b)** attitude and position setpoint vs. feedback during the gust wind disturbance test.



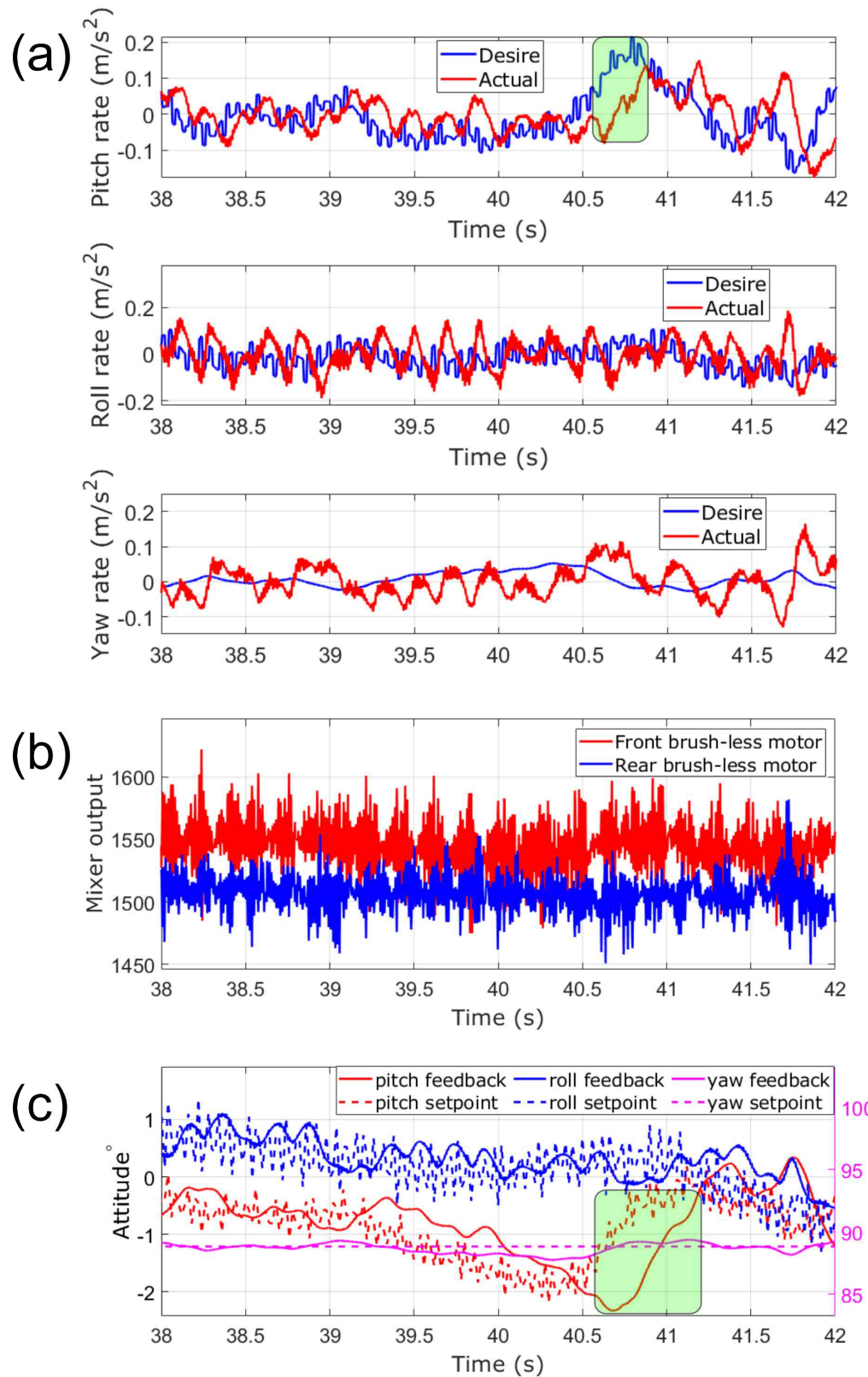


**Figure 5.29** Closeup data of a gust of wind hit (a) Desired angular rate vs. actual angular rate of a gust of wind hit (boxed in green); (b) Mixer output of a gust of wind hit; (c) Attitude setpoint vs. feedback of a gust of wind hit.



off. During fan operation, disturbances of a similar frequency got reflected on the yaw and pitch angle. The response time on both pitch and roll channels is usually within 0.35 s, and the overall attitude control quality is good.

The on and off of the gusting wind are responsible for the -10 cm and 7 cm position drift on  $x$  at 43 s and 58 s respectively. The position drift on the  $y$  and  $z$  axes are within 8 cm and 3 cm respectively, which are within a reasonable range.

Stepping into the close-up data upon a gust of wind hit, [Figure 5.29a](#) shows the angular rate response. After the fan tuned on at 37 s, the angular rate loop has been suffering wind disturbance with increasing frequency. The zoom-in view between 30 s to 42 s indicates the frequency to be around 12 Hz (equivalent to 900 RPM), affecting all the pitch, roll, and yaw angular rates. At around 40.5 s, a clear sign of a  $0.15 \text{ m/s}^2$  gap between the desired and actual pitch angle rate (boxed in green) marks a gusting wind hitting the propeller blade. The noisy 12 Hz frequency mixer output in [Figure 5.29b](#) is also an indicator of the controller compensating against the disturbance. [Figure 5.29b](#) suggests that after the gusting wind hits the blade, an attitude mismatch in pitch lasts for around 1 second until it stabilizes back to the desired setpoint.

Note that during the gust wind test, the UAV has to adjust the desired attitude and rate setpoint to maintain a stationary position in space, so the desired setpoints are fluctuating. It is the differences between the desired setpoint and the actual feedback that indicates the control quality. According to the test data, all the rate, attitude, and position loops show good rejection to disturbance, indicating the robustness of the complete UAV system.

#### 5.5.4 Trajectory Tracking Following a “3D Figure 8” Pattern

In order to test the maneuverability and trajectory tracking performance of the Gemini II, we challenged it to fly following a “3D Figure 8” pattern, as shown in [Figure 5.30a](#) and [Figure 5.30b](#). Velocity and position with respect to time are shown in [Figure 5.30c](#). It indicates that the lag between the setpoint and feedback are 1 s



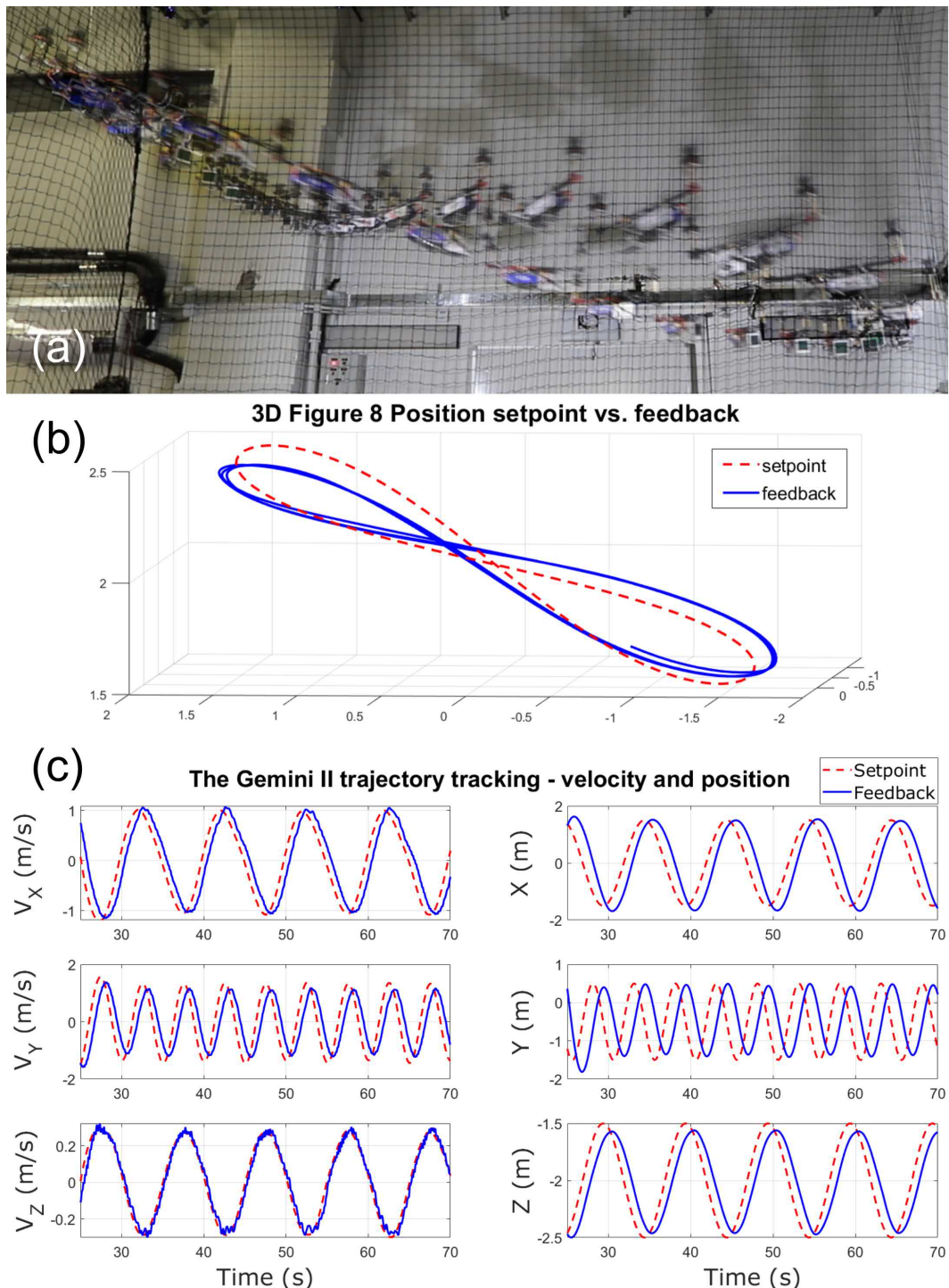


**Figure 5.30** Gemini II trajectory test (a) following a “3D Figure 8” pattern trajectory (b) “3D Figure 8” trajectory track setpoint vs. feedback (c) Velocity and position setpoint vs. feedback while following a “3D Figure 8” pattern.



and 0.65 s respectively. The success of the trajectory tracking validates the feasibility and performance of the novel bi-copter design.

## 5.6 Conclusion and Discussion

Even though Froude scaling of aircraft systems shows that the dynamics are insensitive to the gross scale of the aircraft[110], but in practice, rotor rotation-dependent vibration will be unavoidably generated due to the asymmetry of the hub mechanism. This phenomenon will be more severe as the sinusoidal amplitude  $A$  in the throttle command increases, body length  $H$  or  $L$  increases, or the inertia of the swashplate-less mechanism increases. The vibration can potentially affect the accuracy of the flight controller IMU sensor or even cause resonance between the two motors and damage the UAV body.

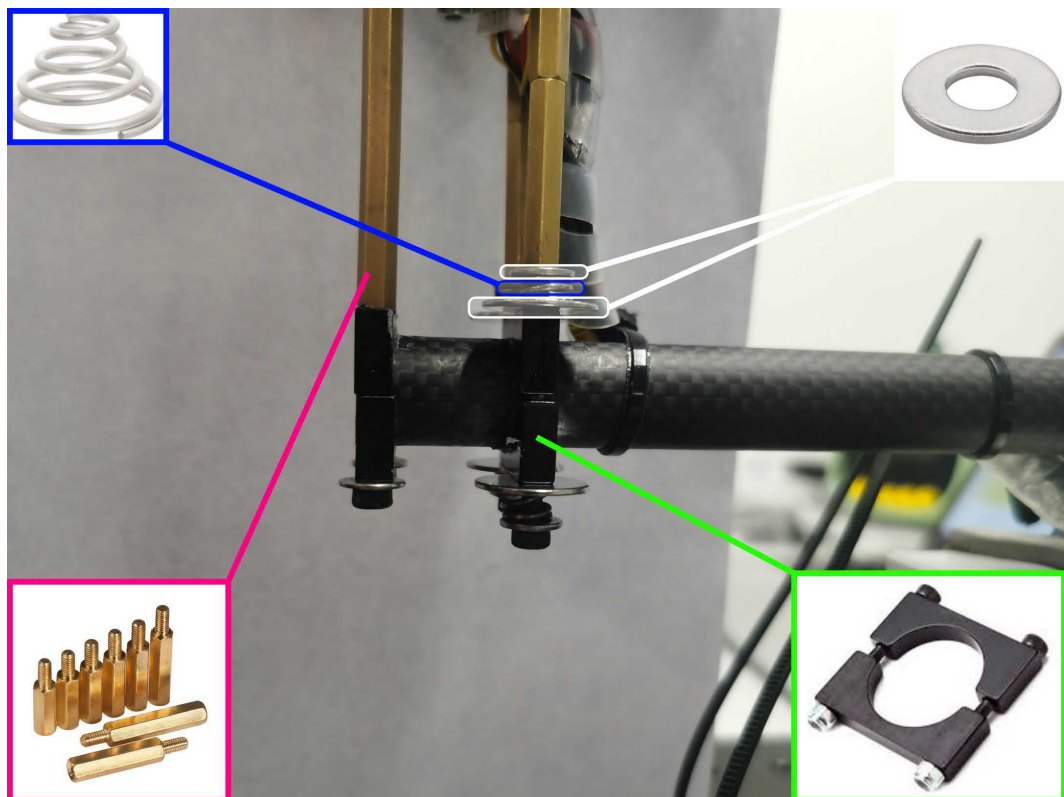


**Figure 5.31** Gemini II two-way spring-damper mechanism for alleviating vibration issues.

Adopting a two-way spring-damper mechanism or rubber buffer can alleviate such a problem. As shown in [Figure 5.31](#), the mechanism mainly consists of four parts. Washers and cone springs act as the main suspension system, while the right-hand side carbon-fiber clamp and the female end of the carbon pillar fix the mechanism except for the vertical direction, and the left-hand side carbon fiber rod act as a fixed mounting point.

This section proposed a novel servo-less bi-copter that uses a swashplate-less cyclic blade pitch control technique. The design, implementation details, modeling, and control are presented. Various flight and disturbance tests proved its ability to carry a heavy payload and stably hover while subject to various disturbances. Our prototype, Gemini II, proved the feasibility of the bi-copter adopting a swashplate-less cyclic blade pitch control technique to achieve roll and yaw control without depending on heavy and expensive servo motors. There are still a few future works that could improve the current design: improving the flight performance more by using more advanced control techniques such as model predictive control and robust control, increasing swashplate-less mechanism efficiency by reducing its aerodynamic resistance, etc. Exploiting the scalability of the swashplate-less bi-copter is also an interesting future work topic. In addition, using the LiDAR SLAM to provide position feedback and adding planning algorithms to the platform could enable the Gemini II to perform autonomous flight tasks.

## 5.7 Related Publication

[Qin Y.](#), Chen N., Cai Y., Xu W., and Zhang F., “Gemini II: Design, Modeling, and Control of a Compact Yet Efficient Servo-less Bi-copter,” *IEEE/ASME Transactions on Mechatronics*, doi: 10.1109/TMECH.2022.3153587, 2022.



# Chapter 6

## Conclusion and Future Works

### 6.1 Conclusion

This thesis theoretically proved that bi-copters are a more power-efficient yet practical solution for indoor applications and systematically presents the design, modeling, control, and implementation of servo-based bi-copter, swashplate-based bi-copter, and swashplate-less bi-copter.

As demonstrated by multiple flights and disturbance tests, both servo-based and swashplate-less bi-copter platforms are capable of carrying a significant payload hover stably while subject to various disturbances. The servo-based Gemini mini achieves similar levels of efficiency and maneuverability common amongst quad-copters and multi-rotor while allowing it to perform stable flight through small gaps. The implementation of the swashplate bi-copter encountered issues of severe vibrations, which were caused by the lack of precision by the manufacturing. For practical reasons and safety concerns, the method was aborted, and the swashplate-less method was adopted instead. The success of the novel swashplate-less Gemini II proves the feasibility of the bi-copter adopting a swashplate-less cyclic blade pitch control technique to achieve roll and yaw control without depending on heavy and expensive servo motors.

Besides, this thesis also proposes novel aerial-ground hybrid locomotion with a



single passive wheel. Unlike previous works that sacrifice weight for heavy chassis to achieve hybrid locomotion, our approach achieves great power efficiency advantages of the ground locomotion with the minimal addition of a single wheel that weighs only 1% of the total takeoff weight. Flight experiments validated the feasibility and efficiency of our proposed method.

In conclusion, this thesis systematically presents the process of design, modeling, control, and implementation of three different types of bi-copter UAVs, as well as the aerial-ground locomotion of the servo-based bi-copter.

## 6.2 Future Works

Some future works include improving flight performance by using more advanced control techniques such as model predictive control and robust control, increasing swashplate-less mechanism efficiency by reducing its aerodynamic resistance, etc. The scalability of the swashplate-less bi-copter is also an interesting future work topic to be explored. In addition, utilizing LiDAR SLAM to provide position feedback, adding planning algorithms to the platform, and performing autonomous flight tasks are also interesting topics to study.

Further exploration of these UAVs' efficiency and flight performance will enlarge UAV application potentials. Building robust, small, heavy-duty, and long cruising bi-copter UAVs will resolve the existing application gaps and enhance the tools available for human beings. Pushing the limit of UAVs is a consistent target of interest to me, and I hope the bi-copter UAVs can help humans fight against natural disasters, replace repetitive routines of indoor inspection, map the infinity of nature, explore the abyss of the unknown, and more.

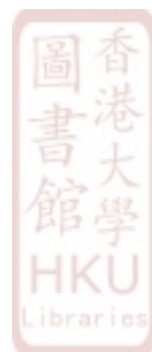


# References

- [1] R. Naughton. Remote piloted aerial vehicles: an anthology. [Online]. Available: [https://ctie.monash.edu.au/hargrave/rpav\\_home.html](https://ctie.monash.edu.au/hargrave/rpav_home.html)
- [2] “Kettering aerial torpedo bug,” April 2015. [Online]. Available: [https://en.wikipedia.org/wiki/Kettering\\_Bug](https://en.wikipedia.org/wiki/Kettering_Bug)
- [3] N. S. Sakamoto, “UAV development and history at Northrop Grumman Corporation Ryan Aeronautical Center.” [Online]. Available: <https://nps.edu/documents/103424733/107333295/August+26+2004+History+of+UAVs.pdf/58d359c9-6b39-49fe-aba7-34dd708c66a5>
- [4] “Lockheed D-21,” Feb 2022. [Online]. Available: [https://en.wikipedia.org/wiki/Lockheed\\_D-21](https://en.wikipedia.org/wiki/Lockheed_D-21)
- [5] “Northrop grumman RQ-4 global hawk,” Mar 2022. [Online]. Available: [https://en.wikipedia.org/wiki/Northrop\\_Grumman\\_RQ-4\\_Global\\_Hawk](https://en.wikipedia.org/wiki/Northrop_Grumman_RQ-4_Global_Hawk)
- [6] M. Moon, “Harvard’s RoboBee X-Wing can fly under its own power,” *Engadget*, 2019.
- [7] V. Chamola, P. Kotesh, A. Agarwal, N. Gupta, M. Guizani, and N. Naren, “A comprehensive review of unmanned aerial vehicle attacks and neutralization techniques,” *Ad Hoc Networks*, vol. 111, 10 2020.
- [8] Unmanned 5G-enabled airship completes test flight in southwest China. [Online]. Available: <https://m.yunnan.cn/system/2021/09/13/031662808.shtml>
- [9] Engineers developed a low-cost, open-source, indoor robotic airship. [Online]. Available: <https://www.inceptivemind.com/>



- [engineers-developed-a-low-cost-open-source-indoor-robotic-airship/  
13044/](https://en.wikipedia.org/wiki/Engineers_developed_a_low-cost_open-source_indoor_robotic_airship/13044/)
- [10] General atomics MQ-1 predator. [Online]. Available: [https://en.wikipedia.org/wiki/General\\_Atomics\\_MQ-1\\_Predator](https://en.wikipedia.org/wiki/General_Atomics_MQ-1_Predator)
- [11] Airbus to supply SMDM Aliaca fixed-wing UAV to the French navy. [Online]. Available: <https://www.navalnews.com/naval-news/2021/02/airbus-to-supply-smdm-aliaca-fixed-wing-uav-to-the-french-navy/>
- [12] S. Bouabdallah, P. Murrieri, and R. Siegwart, “Design and control of an indoor micro quadrotor,” in *IEEE International Conference on Robotics and Automation, 2004. Proceedings. ICRA '04. 2004*, vol. 5, 2004, pp. 4393–4398 Vol.5.
- [13] China takes surveillance to new heights with flock of robotic doves, but do they come in peace? [Online]. Available: <https://www.scmp.com/news/china/society/article/2152027/china-takes-surveillance-new-heights-flock-robotic-doves-do-they>
- [14] Harvard researchers create insect-sized robot that can both fly and swim. [Online]. Available: <https://www.yahoo.com/news/harvard-researchers-create-insect-sized-robot-both-fly-195546372.html>
- [15] Firefighting drones extinguish 10-story blaze in China demonstration. [Online]. Available: <https://dronedj.com/2020/04/03/firefighting-drones-extinguish-10-story-blaze-china/>
- [16] Mooc: Drones for agriculture: Prepare and design your drone (UAV) mission. [Online]. Available: <https://www.fao.org/e-agriculture/news/moocdrones-agriculture-prepare-and-design-your-drone-uav-mission>
- [17] Inspection drones: No. 1 task for commercial drones. [Online]. Available: <https://dronerush.com/inspection-drones-18200/>
- [18] Joint 3-d positioning and power allocation for UAV relay aided by geographic information. [Online]. Available: <https://www.catalyzex.com/author/Liang%20Zhu>



- [19] “DJI Matrice 100 user manual,” 2016. [Online]. Available: [On-line:https://dl.djicdn.com/downloads/m100/M100\\_User\\_Manual\\_EN.pdf](https://dl.djicdn.com/downloads/m100/M100_User_Manual_EN.pdf)
- [20] W. Giernacki, M. Skwierczyński, W. Witwicki, P. Wroński, and P. Kozierski, “Crazyflie 2.0 quadrotor as a platform for research and education in robotics and control engineering,” in *2017 22nd International Conference on Methods and Models in Automation and Robotics (MMAR)*. IEEE, 2017, pp. 37–42.
- [21] J. Lin, L. Wang, F. Gao, S. Shen, and F. Zhang, “Flying through a narrow gap using neural network: an end-to-end planning and control approach,” in *2019 IEEE/RSJ International Conference on Intelligent Robots and Systems (IROS)*, 2019, pp. 3526–3533.
- [22] D. Falanga, K. Kleber, S. Mintchev, D. Floreano, and D. Scaramuzza, “The foldable drone: A morphing quadrotor that can squeeze and fly,” *IEEE Robotics and Automation Letters*, vol. 4, no. 2, pp. 209–216, 2018.
- [23] N. Bucki and M. W. Mueller, “Design and control of a passively morphing quadcopter,” in *2019 International Conference on Robotics and Automation (ICRA)*. IEEE, 2019, pp. 9116–9122.
- [24] Unmanned aerial systems (UAS) applications: Gap analysis. [Online]. Available: [https://www.researchgate.net/publication/353123011\\_Unmanned\\_Aerial\\_Systems\\_UAS\\_Applications\\_Gap\\_Analysis](https://www.researchgate.net/publication/353123011_Unmanned_Aerial_Systems_UAS_Applications_Gap_Analysis)
- [25] Y. Qin, Y. Li, X. Wei, and F. Zhang, “Hybrid aerial-ground locomotion with a single passive wheel,” in *2020 IEEE/RSJ International Conference on Intelligent Robots and Systems (IROS)*, 2020, pp. 1371–1376.
- [26] A. Sanchez, J. Escareno, O. Garcia, and R. Lozano, “Autonomous hovering of a noncyclic tiltrotor UAV: Modeling, control and implementation,” *IFAC Proceedings Volumes*, vol. 41, no. 2, pp. 803–808, 2008.
- [27] L. Hrečko, J. Slačka, and M. Halás, “Bi-copter stabilization based on IMU sensors,” in *2015 20th International Conference on Process Control (PC)*. IEEE, 2015, pp. 192–197.



- [28] C. Blouin and E. Lanteigne, “Pitch control of an oblique active tilting bi-rotor,” in *2014 International Conference on Unmanned Aircraft Systems (ICUAS)*. IEEE, 2014, pp. 791–799.
- [29] K. Siddhardha, “A novel bi-rotor configuration and its control,” *IFAC-PapersOnLine*, vol. 51, no. 1, pp. 456–461, 2018.
- [30] J. Leishman, “Principles of helicopter aerodynamics, Cambridge University,” *Press, New*, 2000.
- [31] J. A. Detore and S. Conway, “Technology needs for high speed rotorcraft (3),” 1991.
- [32] E. Davis, W. McKay-Lowndes, D. Gonano, S. Hansen, and P. Pounds, “Towards the stackrotor: Aerodynamics, construction, dynamics and control of a vertical stacked-rotor configuration for indoor heavy-lift helicopter robots,” in *Australasian Conference on Robotics and Automation, ACRA*, vol. 2016. Australasian Robotics and Automation Association, 2016, pp. 81–88.
- [33] S. Driessens and P. Pounds, “The triangular quadrotor: a more efficient quadrotor configuration,” *IEEE Transactions on Robotics*, vol. 31, no. 6, pp. 1517–1526, 2015.
- [34] S. Salazar, H. Romero, R. Lozano, and P. Castillo, “Modeling and real-time stabilization of an aircraft having eight rotors,” in *Unmanned Aircraft Systems*. Springer, 2008, pp. 455–470.
- [35] M. Zhao, T. Anzai, F. Shi, X. Chen, K. Okada, and M. Inaba, “Design, modeling, and control of an aerial robot dragon: A dual-rotor-embedded multilink robot with the ability of multi-degree-of-freedom aerial transformation,” *IEEE Robotics and Automation Letters*, vol. 3, no. 2, pp. 1176–1183, 2018.
- [36] K. Hang, X. Lyu, H. Song, J. A. Stork, A. M. Dollar, D. Kragic, and F. Zhang, “Perching and resting—a paradigm for UAV maneuvering with modularized landing gears,” *Science Robotics*, vol. 4, no. 28, p. eaau6637, 2019.



- [37] J. Thomas, M. Pope, G. Loianno, E. W. Hawkes, M. A. Estrada, H. Jiang, M. R. Cutkosky, and V. Kumar, “Aggressive flight with quadrotors for perching on inclined surfaces,” *Journal of Mechanisms and Robotics*, vol. 8, no. 5, 2016.
- [38] A. Kalantari, K. Mahajan, D. Ruffatto, and M. Spenko, “Autonomous perching and take-off on vertical walls for a quadrotor micro air vehicle,” in *2015 IEEE International Conference on Robotics and Automation (ICRA)*. IEEE, 2015, pp. 4669–4674.
- [39] S. Morton and N. Papanikolopoulos, “A small hybrid ground-air vehicle concept,” in *2017 IEEE/RSJ International Conference on Intelligent Robots and Systems (IROS)*, Sep. 2017, pp. 5149–5154.
- [40] R. Adarsh and M. M. Dharmana, “Multi-terrain multi-utility robot,” *Procedia computer science*, vol. 133, pp. 651–659, 2018.
- [41] W. Wang, C. y. Li, L. h. Chu, and C. y. Qu, “Study on air-ground amphibious agricultural information collection robot,” in *2016 13th International Conference on Ubiquitous Robots and Ambient Intelligence (URAI)*, Aug 2016, pp. 938–944.
- [42] K. Tanaka, D. Zhang, S. Inoue, R. Kasai, H. Yokoyama, K. Shindo, K. Matsuhiro, S. Marumoto, H. Ishii, and A. Takanishi, “A design of a small mobile robot with a hybrid locomotion mechanism of wheels and multi-rotors,” in *2017 IEEE International Conference on Mechatronics and Automation (ICMA)*, Aug 2017, pp. 1503–1508.
- [43] J. Goldman, “Parrot minidrone rolling spider review,” Aug 2014. [Online]. Available: <https://www.cnet.com/reviews/parrot-minidrone-rolling-spider-review/>
- [44] [Online]. Available: <https://www.boeing.com/defense/ch-47-chinook/#/technical-specifications>
- [45] Helifreak full-size chinook. [Online]. Available: <https://www.helifreak.com/showthread.php?t=57712>



- [46] J. Liu, R. Guan, Y. Yao, H. Wang, and L. Hu, “A novel comprehensive kinematic and inverse dynamic model for the flybar-less swashplate mechanism: Application on a small-scale unmanned helicopter,” *Symmetry*, vol. 12, p. 1849, 11 2020.
- [47] J. Paulos and M. Yim, “An underactuated propeller for attitude control in micro air vehicles,” *2013 IEEE/RSJ International Conference on Intelligent Robots and Systems (IROS)*, pp. 1374–1379, 2013. [Online]. Available: [⟨GotoISI⟩://WOS:00031367401070](https://doi.org/10.1109/IROS-Demo50000.2013.6740107)
- [48] ——, “Cyclic blade pitch control without a swashplate for small helicopters,” *Journal of Guidance Control and Dynamics*, vol. 41, no. 3, pp. 689–700, 2018. [Online]. Available: [⟨GotoISI⟩://WOS:000425053600008](https://doi.org/10.2514/1.G004250)
- [49] V. Prisacariu, “The history and the evolution of UAVs from the beginning till the 70s,” *Journal of defense resources management*, vol. 8, no. 1, pp. 181–189, 2017.
- [50] S. Yuqing and S. Haijun, “Chinese ancient aircraft,” *China awards for science and technology*, no. 8, pp. 76–78, 2020.
- [51] Leonardo da Vinci’s helicopter: 15th-century flight of fancy led to modern aeronautics. [Online]. Available: <https://tinyurl.com/ThesisReferenceList1>
- [52] Weapons and warfare. [Online]. Available: <https://weaponsandwarfare.com/2019/06/17/1845-austria-drops-balloon-bombs-on-venice/>
- [53] Smithsonian national air and space museum. [Online]. Available: <https://airandspace.si.edu/exhibitions/wright-brothers/online/>
- [54] Cold war. [Online]. Available: [https://en.wikipedia.org/wiki/Cold\\_War](https://en.wikipedia.org/wiki/Cold_War)
- [55] S. Pop, A. Luchian, R. G. Zmădu, and E. Olea, “The evolution of unmanned aerial vehicles,” *Review of the Air Force Academy*, no. 3, pp. 125–132, 2017, copyright - Copyright Henri Coanda Air Force Academy 2017; Last updated - 2020-02-06; SubjectsTermNotLitGenreText - North Vietnam; United States-US; Romania; Vietnam; United Kingdom-UK;



- China. [Online]. Available: <http://eproxy.lib.hku.hk/login?url=https://www.proquest.com/scholarly-journals/evolution-unmanned-aerial-vehicles/docview/2052768585/se-2?accountid=14548>
- [56] K. Nonami, F. Kendoul, D. Nakazawa, S. Suzuki, and W. Wang, *Autonomous Flying Robots: Unmanned Aerial Vehicles and Micro Aerial Vehicles*, 1st ed. Tokyo: Springer Japan, 2010.
- [57] Z. Liu, R. Sengupta, and A. Kurzhanskiy, “A power consumption model for multi-rotor small unmanned aircraft systems,” 06 2017, pp. 310–315.
- [58] What makes the quadcopter design so great for small drones. [Online]. Available: <https://www.forbes.com/sites/quora/2013/12/23/what-makes-the-quadcopter-design-so-great-for-small-drones/?sh=60e55e92654f>
- [59] U. Ozdemir, Y. O. Aktas, A. Vuruskan, Y. Dereli, A. F. Tarhan, K. Demirbag, A. Erdem, G. D. Kalaycioglu, I. Ozkol, and G. Inalhan, “Design of a commercial hybrid VTOL UAV system,” *Journal of Intelligent & Robotic Systems*, vol. 74, no. 1-2, pp. 371–393.
- [60] X. Lyu, H. Gu, Y. Wang, Z. Li, S. Shen, and F. Zhang, “Design and implementation of a quadrotor tail-sitter VTOL UAV,” in *2011 IEEE International Conference on Robotics and Automation (ICRA)*. IEEE, 2011, pp. 3924–3930.
- [61] “Autopilot design of tilt-rotor UAV using particle swarm optimization method.” [Online]. Available: [https://www.researchgate.net/figure/Tilt-Rotor-Unmanned-Aerial-Vehicle-Smart-UAV\\_fig1\\_4300732](https://www.researchgate.net/figure/Tilt-Rotor-Unmanned-Aerial-Vehicle-Smart-UAV_fig1_4300732)
- [62] E. Mitka and S. G. Mouroutsos, “Classification of drones,” *Am J Eng Res*, vol. 6, no. 7, pp. 36–41, 2017.
- [63] Projected civil drone market size worldwide from 2019 to 2027. [Online]. Available: <https://www.statista.com/statistics/1048962/global-civil-drone-market-size/>



- [64] Y. Khosiawan and I. Nielsen, “A system of UAV application in indoor environment,” *Production & Manufacturing Research*, vol. 4, no. 1, pp. 2–22, 2016.
- [65] F. Nex and F. Remondino, “UAV for 3D mapping applications: a review,” *Applied geomatics*, vol. 6, no. 1, pp. 1–15, 2014.
- [66] V. Baiocchi, D. Dominici, and M. Mormile, “UAV application in post-seismic environment,” *International Archives of the Photogrammetry, Remote Sensing and Spatial Information Sciences*, vol. 1, p. W2, 2013.
- [67] J. Senthilnath, M. Kandukuri, A. Dokania, and K. Ramesh, “Application of UAV imaging platform for vegetation analysis based on spectral-spatial methods,” *Computers and Electronics in Agriculture*, vol. 140, pp. 8–24, 2017.
- [68] D. Falanga, E. Mueggler, M. Faessler, and D. Scaramuzza, “Aggressive quadrotor flight through narrow gaps with onboard sensing and computing using active vision,” in *2017 IEEE International Conference on Robotics and Automation (ICRA)*. IEEE, 2017, pp. 5774–5781.
- [69] V. Riviere, A. Manecy, and S. Viollet, “Agile robotic fliers: A morphing-based approach,” *Soft robotics*, vol. 5, no. 5, pp. 541–553, 2018.
- [70] K. Kawasaki, Y. Motegi, M. Zhao, K. Okada, and M. Inaba, “Dual connected bi-copter with new wall trace locomotion feasibility that can fly at arbitrary tilt angle,” in *2015 IEEE/RSJ International Conference on Intelligent Robots and Systems (IROS)*, 2015, pp. 524–531.
- [71] R. Bulaga and T. Worley, “UAV with control and stability system,” Nov. 15 2007, US Patent App. 11/746,628.
- [72] M. W. Moshier and R. W. Bulaga, “SoloTrek XFV(Exo-skeletor Flying Vehicle)- an inside look,” in *Vertical Lift Aircraft Design Conference, San Francisco, CA*, 2000.
- [73] R. Stone and G. Clarke, “The T-wing: a VTOL UAV for defense and civilian applications,” *University of Sydney*, 2001.



- [74] B. NORDWALL, “Boeing unveils heliwing UAV,” *AVIATION WEEK & SPACE TECHNOLOGY*, vol. 140, no. 14, pp. 34–34, 1994.
- [75] B. Settle and T. Wise, “Bell Eagle Eye TR-911X–Tiltrotor unmanned aerial vehicle: Recent developments, autoland integration, and flight test demonstrations,” in *Annual Forum Proceedings-American Helicopter Society*, vol. 56, no. 1. American Helicopter Society, Inc., 2000, pp. 306–319.
- [76] C. Papachristos, K. Alexis, G. Nikolakopoulos, and A. Tzes, “Model predictive attitude control of an unmanned tilt-rotor aircraft,” in *2011 IEEE International Symposium on Industrial Electronics*. IEEE, 2011, pp. 922–927.
- [77] Q. Zhang, Z. Liu, J. Zhao, and S. Zhang, “Modeling and attitude control of bi-copter,” in *2016 IEEE International Conference on Aircraft Utility Systems (AUS)*. IEEE, 2016, pp. 172–176.
- [78] F. 015Gonçalves, J. Bodanese, R. Donadel, G. Raffo, J. Normey-Rico, and L. Becker, “Small scale UAV with bi-rotor configuration,” in *2013 International Conference on Unmanned Aircraft Systems (ICUAS)*. IEEE, 2013, pp. 761–768.
- [79] E. Davis, J. Spollard, and P. Pounds, “Passive height stability and trajectory repeatability of a quadrotor maneuvering in ground effect with regulated voltage bus,” in *Australasian Conference on Robotics and Automation (ACRA 2015)*, 2015.
- [80] “APC propeller performance data,” 2019. [Online]. Available: <https://www.apcprop.com/technical-information/performance-data/>
- [81] B. Theys, G. Dimitriadis, P. Hendrick, and J. De Schutter, “Influence of propeller configuration on propulsion system efficiency of multi-rotor unmanned aerial vehicles,” in *2016 International Conference on Unmanned Aircraft Systems (ICUAS)*. IEEE, 2016, pp. 195–201.
- [82] “Snail racing drone propulsion system - DJI.” [Online]. Available: <https://www.dji.com/hk-en/snail>



- [83] D. Mellinger and V. Kumar, “Minimum snap trajectory generation and control for quadrotors,” in *2011 IEEE International Conference on Robotics and Automation (ICRA)*. IEEE, 2011, pp. 2520–2525.
- [84] X. Lyu, H. Gu, J. Zhou, Z. Li, S. Shen, and F. Zhang, “A hierarchical control approach for a quadrotor tail-sitter VTOL UAV and experimental verification,” in *2017 IEEE/RSJ International Conference on Intelligent Robots and Systems (IROS)*. IEEE, 2017, pp. 5135–5141.
- [85] H. V. Abeywickrama, B. A. Jayawickrama, Y. He, and E. Dutkiewicz, “Empirical power consumption model for UAVs,” in *2018 IEEE 88th Vehicular Technology Conference (VTC-Fall)*, Aug 2018, pp. 1–5.
- [86] Y. Qin, W. Xu, A. Lee, and F. Zhang, “Gemini: A compact yet efficient bi-copter UAV for indoor applications,” *IEEE Robotics and Automation Letters*, pp. 1–1, 2020.
- [87] M. Kovac, “Learning from nature how to land aerial robots,” *Science*, vol. 352, no. 6288, pp. 895–896, 2016.
- [88] M. Graule, P. Chirarattananon, S. Fuller, N. Jafferis, K. Ma, M. Spenko, R. Kornbluh, and R. Wood, “Perching and takeoff of a robotic insect on overhangs using switchable electrostatic adhesion,” *Science*, vol. 352, no. 6288, pp. 978–982, 2016.
- [89] H. Zhang, J. Sun, and J. Zhao, “Compliant bistable gripper for aerial perching and grasping,” in *2019 International Conference on Robotics and Automation (ICRA)*, May 2019, pp. 1248–1253.
- [90] H. Jiang, M. T. Pope, M. A. Estrada, B. Edwards, M. Cuson, E. W. Hawkes, and M. R. Cutkosky, “Perching failure detection and recovery with onboard sensing,” in *2015 IEEE/RSJ International Conference on Intelligent Robots and Systems (IROS)*. IEEE, 2015, pp. 1264–1270.
- [91] H. Jiang, M. T. Pope, E. W. Hawkes, D. L. Christensen, M. A. Estrada, A. Parlier, R. Tran, and M. R. Cutkosky, “Modeling the dynamics of perching



- with opposed-grip mechanisms,” in *2014 IEEE International Conference on Robotics and Automation (ICRA)*. IEEE, 2014, pp. 3102–3108.
- [92] L. Daler, A. Klaptoč, A. Briod, M. Sitti, and D. Floreano, “A perching mechanism for flying robots using a fibre-based adhesive,” in *2013 IEEE International Conference on Robotics and Automation*. IEEE, 2013, pp. 4433–4438.
- [93] Understanding KV ratings. [Online]. Available: <https://www.rotordronepro.com/understanding-kv-ratings/#:~:text=The%20Kv%20rating%20of%20a,voltage%20is%20applied%20to%20it>.
- [94] M. Bendsøe and O. Sigmund, *Topology optimization. Theory, methods, and applications. 2nd ed., corrected printing*, 01 2004.
- [95] ANSYS fluent gradient-based optimization. [Online]. Available: <https://tinyurl.com/ThesisReferenceList>
- [96] ANSYS workbench. [Online]. Available: <https://www.ansys.com/products/structures/ansys-mechanical>
- [97] HV1220 MKS servos USA. [Online]. Available: <https://www.mksservosusa.com/product.php?productid=163>
- [98] G. Shi, X. Shi, M. O’Connell, R. Yu, K. Azizzadenesheli, A. Anandkumar, Y. Yue, and S.-J. Chung, “Neural lander: Stable drone landing control using learned dynamics,” in *2019 International Conference on Robotics and Automation (ICRA)*. IEEE, 2019, pp. 9784–9790.
- [99] B. Xian and W. Hao, “Nonlinear robust fault-tolerant control of the tilt trirotor UAV under rear servo’s stuck fault: Theory and experiments,” *IEEE Transactions on Industrial Informatics*, vol. 15, no. 4, pp. 2158–2166, 2019.
- [100] F. Ranjbaran, J. Angeles, G. Goritschnig, *et al.*, “The kinematics of the swashplate mechanism of a VTOL unmanned aerial vehicle,” *Multibody System Dynamics*, vol. 3, no. 4, pp. 333–365, 1999.



- [101] C. Lange, J. Angeles, F. Ranjbaran, and G. Goritschnig, “The dynamics of the swashplate mechanism of a VTOL unmanned aerial vehicle,” *Multibody System Dynamics*, vol. 5, no. 2, pp. 105–131, 2001.
- [102] L.-W. Tsai, “Solving the inverse dynamics of a Stewart-Gough manipulator by the principle of virtual work,” *J. MECH. Des.*, vol. 122, no. 1, pp. 3–9, 2000.
- [103] B. Ren, S. S. Ge, C. Chen, C.-H. Fua, and T. H. Lee, *Modeling, control and coordination of helicopter systems*. Springer Science & Business Media, 2012.
- [104] Matlab Arduino support. [Online]. Available: <https://ww2.mathworks.cn/help/supportpkg/arduinoio/ug/connect-to-arduino-hardware.html>
- [105] DJI E2000. [Online]. Available: <https://www.dji.com/hk/e2000/info>
- [106] Y. Qin, W. Xu, A. Lee, and F. Zhang, “Gemini: A compact yet efficient bi-copter UAV for indoor applications,” *IEEE Robotics and Automation Letters*, vol. 5, no. 2, pp. 3213–3220, 2020.
- [107] Y. Li, Y. Qin, W. Xu, and F. Zhang, “Modeling, identification, and control of non-minimum phase dynamics of bi-copter UAVs,” in *2020 IEEE/ASME International Conference on Advanced Intelligent Mechatronics (AIM)*, 2020, pp. 1249–1255.
- [108] J. Paulos and M. Yim, “Flight performance of a swashplateless micro air vehicle,” *2015 IEEE International Conference on Robotics and Automation (ICRA)*, pp. 5284–5289, 2015. [Online]. Available: [⟨GotoISI⟩://WOS:000370974905033](https://doi.org/10.1109/ICRA.2015.7148533)
- [109] J. Paulos, B. Caraher, and M. Yim, “Emulating a fully actuated aerial vehicle using two actuators,” *2018 IEEE International Conference on Robotics and Automation (ICRA)*, pp. 7011–7016, 2018. [Online]. Available: [⟨GotoISI⟩://WOS:000446394505048](https://doi.org/10.1109/ICRA.2018.8433800)



- [110] J. J. Paulos and M. Yim, “Scalability of cyclic control without blade pitch actuators,” in *2018 AIAA Atmospheric Flight Mechanics Conference*, Conference Proceedings, p. 0532.
- [111] K. Åström, *Fundamental Limitations of Control System Performance*. Germany: Springer, 1997.

